AUS Repository

Deep Neural Networks for Electromagnetic Inverse Scattering Problems in Microwave Imaging

Item Type	Thesis
Authors	Maricar, Mohammed Farook
Download date	2026-02-14 01:54:44
Link to Item	http://hdl.handle.net/11073/25464

DEEP NEURAL NETWORKS FOR ELECTROMAGNETIC INVERSE SCATTERING PROBLEMS IN MICROWAVE IMAGING

by

Mohammed Farook Maricar

A Thesis Presented to the Faculty of the
American University of Sharjah
College of Engineering
in Partial Fulfillment
of the Requirements
for the Degree of

Master of Science in
Electrical Engineering

Sharjah, United Arab Emirates

November 2023

Declaration of Authorship

I declare that this thesis is my own work and, to the best of my knowledge and belief, it does not contain material published or written by a third party, except where permission has been obtained and/or appropriately cited through full and accurate referencing.

Signed……Mohammed Farook Maricar…….

Date……23/11/2023……

The Author controls copyright for this report.

Material should not be reused without the consent of the author. Due acknowledgement should be made where appropriate.

© Year 2023

Mohammed Farook Maricar

ALL RIGHTS RESERVED

Approvals

We, the undersigned, approve the Master's Thesis written

by: Mohammed Farook Maricar

Thesis Title: Deep Neural Networks for Electromagnetic Inverse Scattering Problems in Microwave Imaging

Date of Defense: November 22, 2023

Name, Title and Affiliation	**Signature**
Dr. Amer Zakaria Associate Professor Department of Electrical Engineering Thesis Advisor	
Dr. Nasser Qaddoumi Professor Department of Electrical Engineering Thesis Co-advisor	
Dr. Usman Tariq Associate Professor Department of Electrical Engineering Thesis Examiner	
Dr. Salam Dhou Associate Professor Department of Computer Science and Engineering Thesis Examiner	

Accepted by:

Dr. Fadi Aloul
Dean
College/School of Engineering

Dr. Mohamed El-Tarhuni
Vice Provost for Research and Graduate Studies Office
of Research and Graduate Studies

Acknowledgment

I extend my deepest gratitude to the American University of Sharjah (AUS) for generously providing the necessary resources that facilitated the completion of this thesis. Their support has been instrumental in helping me achieve this significant milestone in my academic career. Additionally, I am thankful to the Department of Electrical Engineering for offering me Graduate Research and Teaching Assistantships, which played a crucial role in the successful completion of my thesis.

I would like to express my sincere gratitude to my supervisor, Dr. Amer Zakaria, for his unwavering support, patience, and generous sharing of knowledge and expertise. His guidance and training have been instrumental in shaping this work, and I appreciate the valuable insights he provided throughout the entire process. I also extend my heartfelt thanks to my co-advisor and mentor, Prof. Nasser Qaddoumi, for his guidance, motivation, and most importantly, his unwavering belief in me. Returning to academia after 17 years, Prof. Nasser's confidence in my abilities was a driving force that propelled me forward. His steadfast support and belief have been instrumental in the successful completion of this thesis, and for that, I am sincerely thankful. Both were not just my advisors, but also my friends, and their passion and commitment gave me the courage to undertake this difficult but worthwhile thesis work.

To my family, friends, and all those who supported me throughout every phase of my thesis research, I express my sincere gratitude. Without your support, reaching this point would not have been possible, and I couldn't have asked for more.

A special thanks is reserved for my wife, whose steadfast support and motivation were the driving forces behind this achievement. Her sacrifices played an indispensable role, and I am profoundly grateful for her love, encouragement, and unwavering presence throughout this journey.

I extend a special thanks to the Vice Provost, Dr. Mohamed El -Tarhuni, whose vision and support were instrumental in initiating and inspiring this entire endeavor. I would also like to express my gratitude to Dr. Abdulrahman Al-Ali for his continuous positive support throughout this journey.

Last and foremost, I express my gratitude to Allah for guiding me and providing strength throughout this endeavor.

Abstract

Microwave imaging, due to its non-invasive and non-destructive nature of detection, is of interest in various applications such as biomedical imaging, geophysical surveying, and non-destructive testing. The most common technique for microwave imaging is by solving an electromagnetic inverse scattering (EMIS) problem. The high nonlinearity and ill-posedness of these EMIS problems have led researchers to develop various inversion algorithms, such as the distorted Born iteration method (DBIM), the contrast source inversion (CSI) method, and the sub-space optimization method (SOM). Though these conventional nonlinear inversion algorithms provide acceptable results in many applications with moderate size and contrast, their computational costs are usually very high. In addition, for high-contrast targets, the performance is generally degraded. To tackle these issues, various deep-learning techniques have been proposed in recent years. In this thesis, the EMIS problem will be solved using deep neural networks (DNNs), with a focus on solving two-dimensional (2D) microwave imaging problems. Different DNN architectures are tested with three types of complex inputs: the measured scattered field $\vec{E}^{\,sct}_{\text{meas}}$; an input image obtained from backpropagating (BP) the measured scattered field; or the novel physics-incorporated input (ITER10) obtained from the output image from the tenth iteration of CSI. For the purpose of training, validation, and testing the networks, 10000 samples from the well-known MNIST dataset are used. In the initial phase, two encoder-decoder-based convolutional neural networks (CNNs) are designed and implemented; the Baseline-AE, and the deep convolutional encoder-decoder network (DCEDnet). These models were tested in the two different input scenarios: $\vec{E}^{\,sct}_{\text{meas}}$ and BP. The BP-DCEDnet provided improved results than the CSI at a much lesser time when tested within the MNIST database. In the next phase, three additional networks namely the Unet-Lite, Unet and the Attention-Unet (ATTN-Unet) together with DCEDnet were trained with BP and tested with complex profiles under different noise levels and permittivity range. The BP-ATTN-Unet outperformed the rest. However, the real component still needed to improve in comparison with the CSI. Thereby, the ATTN-Unet was trained with the ITER10 input to produce more stronger results. The optimized ITER10-ATTN-Unet was then successfully tested with experimental data and the results obtained were as expected.

Search Terms: Deep Learning, convolutional neural network, Unet, attention, complex inputs, inverse scattering, microwave imaging, backpropagation, CSI.

Table of Contents

List of Figures

List of Tables

List of Abbreviations

2D	Two-dimensional
AE	Autoencoder
AG	Attention Gate
AI	Artificial intelligence
ANN	Artificial Neural Network
ATTN	Attention
BP	Backpropagation
CNN	Convolutional Neural Network
CSI	Contrast source inversion
CT	Computed Tomography
DBIM	Distorted born iterative method
DNN	Deep neural network
EMIS	Electromagnetic inverse scattering
FEM	Finite-element method
GAN	Generative adversarial network
GPU	Graphics Processing Unit
IMD	Imaging Domain
ITER10	Iteration ten
MNIST	Modified National Institute of Standards and Technology
MSE	Mean squared error
OI	Object of Interest
PGAN	Perceptual generative adversarial network
RAM	Random Access Memory
SOM	Sub-space optimization method
TM	Transverse magnetic
UM	University of Manitoba
VRAM	Video Random Access Memory

Chapter 1. Introduction

1.1 Motivation

Over the years, microwave imaging has been gaining much interest in various applications such as biomedical imaging [1], [2], geophysical surveying [3], through-wall imaging [4], and non-destructive testing [5]. This is mainly due to its non-invasive and non-destructive nature of detection [6]. The modeling of the microwave imaging (MWI) system as an electromagnetic inverse scattering (EMIS) problem is the most effective technique for solving such systems [7]. In EMIS, electromagnetic signals are radiated onto an object of interest, and then the scattered fields are measured at different locations around the object. The scattered data are then used as input to an inversion algorithm to detect the shape, size and/or electrical properties of the object [8].

Over the last few decades, several inversion algorithms have been proposed and implemented to solve the EMIS problem [6]. The most typical inversion algorithms include the distorted Born iterative method (DBIM) [9], the contrast source inversion (CSI) method [10], and the sub-space optimization method (SOM) [11]. Though these conventional inversion algorithms achieve high-quality reconstruction results in several applications involving moderate size and contrast, their performance usually degrades for high-contrast scatterers [12]. Moreover, their computational costs are usually very high [12]. Their time-consuming characteristic due to high computational complexity makes it extremely challenging to realize microwave imaging in real-time, especially for high-contrast scatterers [6], [13].

Recently, deep learning methods have been largely implemented in image and computer vision and have seen much success. Due to this, many researchers have applied several deep learning techniques to solve the EMIS problems [14], [15]. Though these techniques have led to a significant improvement in reconstruction quality, there is still much room for improvement [12]. Furthermore, much of the work done is on non-complex problems where the input to the neural network contains only the real component and the network's output is for lossless targets with real electrical properties (or permittivity). However, the EMIS problem is typically a complex problem, with both real and imaginary field components and lossy targets with complex electrical properties (permittivity and conductivity) [16].

1.2 Objectives

The objective is to solve the complex two-dimensional (2D) EMIS problem with the use of state-of-the-art deep neural networks and integrate it together with the

conventional imaging technique such as the contrast source inversion (CSI) method. In order to achieve this aim, the following goals are set:

- Create different types of complex input datasets for the EMIS problem from the readily available Modified National Institute of Standards and Technology (MNIST) handwritten digits.
- Develop and test a complex-input deep convolutional encoder-decoder neural network and compare the results with a conventional inversion algorithm result such as CSI for 2D-transverse magnetic (TM) problem.
- Develop and test a more advanced and recent deep neural network model such as the U-Net for the EMIS problem and compare its results.
- Test the developed DNN models using cross-database synthetic samples.
- Test the developed DNN models using experimental data.
- Design and implement a novel technique to enhance the performance of the DNN to obtain results of higher quality.

1.3 Outline

The proposal is structured as follows. Chapter 2 discusses the recent research work done on the use of artificial intelligence in microwave imaging. Different artificial neural network (ANN) architectures ranging from the fully connected (FC) to the convolutional neural networks (CNNs) have been discussed. As CNNs are well known for their outstanding performance on object classification and image segmentation [15], much work has been done using this type of architecture. Within the CNNs, there are popular architectures such as the Encoder-Decoder, U-Net, and GAN, which has been implemented by many researchers to solve the EMIS problem. These architectures along with their results have been discussed in Chapter 2.

Chapter 3 discusses the mathematical formulation of the EMIS problem, where the forward problem and the inverse problem are explained. In Chapter 4, the proposed deep neural networks and their methodology has been explained, which includes the electromagnetic (EM) problem configuration, the generation of the complex datasets from the measured scattered field obtained from the forward solver, and the different deep neural network (DNN) architectures and its hyperparameters. Chapter 5 displays the results obtained from the DNNs for both synthetic and experimental data, and compares these results with each other and with the conventional CSI results. Finally, Chapter 6 concludes the work done in this thesis.

Chapter 2. Literature Review

Over the recent years, deep learning techniques have been widely implemented in image processing and segmentation. Deep neural networks have proved successful in building nonlinear mappings. To solve the EMIS problem, the requirement is to build a nonlinear mapping between the scattered field and the unknown parameters of the scatterers [13]. Since DNNs are powerful nonlinear mappers, there has been lot of interest in using DNNs to solve the typical EMIS problem in recent years. The use of artificial neural networks (ANNs) to solve the EMIS problem goes back to the late 90's [17], [18]. The major drawback of these early shallow fully-connected methods was that they largely depended on the prior knowledge of the scatterers [13]. Recently, with the emergence of the deep convolutional neural networks (CNNs), the image processing and segmentation field has seen much progress and success [15]. Due to this success, researchers began using the CNNs to solve the EMIS problems. These deep learning techniques to solve the inverse scattering problems is denoted as DL-IS [13]. The DL-IS method can be divided in different parts: target scatterers, DNN Input/Output, DNN Architecture, DNN Training, Testing, and DNN Results.

2.1 Targets

Since the CNNs require large datasets for optimal performance, many of the researchers have used the handwritten digits in MNIST database as the targets in the imaging domain [6], [12], [13], [19], while few have generated their own randomly shaped objects as targets [20]. All of the works have considered the 2D-TM case of the EMIS problem in free space background with the targets assumed to be lossless dielectric in the training stage.

2.1.1 Dataset

2.1.1.1 MNIST

As the MNIST dataset is readily available, many researchers have opted for it. In [12], Huang *et al.* randomly selected 5000 MNIST samples as training data, 2500 for validation, and 1500 for testing. To improve the capacity of the model and represent multiple targets, Huang *et al.* also added random circles to the imaging domain. Wang *et al.* [16] uses 8000 MNIST samples for training and 2000 for testing. In [13], Song *et al.* randomly selected 5000 MNIST images for training, 2500 as validation, and 1500 for testing purpose. Yao *et al.* [6] selected 8000 samples randomly in MNIST to train the DL model, while choosing another 1000 samples for testing. In [19], Li *et al.*

randomly selected 7000 MNIST images for training, 1000 for validation, and 2000 for testing.

2.1.1.2 Non-MNIST

While most of the work done is using MNIST dataset, some researchers have preferred to train their models using their own generated datasets. For example, Shao and Du in [20] have generated virtual objects by software to serve as targets in the electromagnetic (EM) simulation. Objects of basic shapes (ring, square, triangle, and eclipse of different sizes and locations) were randomly generated by a software tool to create 32000 sample images. From this, 25600 images (80%) were used for training, 3200 images (10%) for validation, and remaining 3200 (10%) for testing.

2.1.2 Relative Permittivity

All the research work studied assumed the targets to be lossless dielectrics in free space background to generate the measured scattered field data. In [12], Huang *et al.* the target's relative permittivity, $\epsilon_{r,}$ was randomly distributed between 1.5 and 2.5 for the MNIST handwritten digit targets. Wang *et al.* [16] set $\epsilon_{r,}$ value of all the targets for the digits to be 3. In [13], Song *et al.* the ϵ_r values for the targets in the training stage were randomly distributed to be between 1.5 and 2.5. Li *et al.* [19] set the ϵ_r for the targets to be 3. Yao *et al.* [6] set an extremely high relative permittivity ϵ_r of 8 to all the MNIST digit-shaped targets, which is a challenging problem for the conventional inversion methods due to the target's high-contrast relative to the background. In [20], Shao and Du assigned their shaped objects with ϵ_r values ranging from 2 to 6 randomly.

2.2 DNN Input/Output

The output of all the architectures is the reference ground truth image of either the permittivity or contrast profile which is obtained from the forward problem. As for the input of the DNN, some have used the measured scattered field data, $\vec{E}^{sct}_{\text{meas}}$, directly as the input to the DNN, while others have preferred to use the rough image reconstructed from the measured scattered field by the non-iterative BP method.

2.2.1 Measured Scattered Field Data

In [6], Yao *et al.* used $\vec{E}^{sct}_{\text{meas}}$ as the input to their DConvNet. In doing so, Yao *et al.* splits the real and imaginary parts of the $\vec{E}^{sct}_{\text{meas}}$ into two channels of the input. On the other hand, Shao and Du in [20] used the magnitude and phase of $\vec{E}^{sct}_{\text{meas}}$ as the input to their DNN.

2.2.2 Input from BP method

In Huang *et al.* [12], rather than applying $\vec{E}_{\text{meas}}^{sct}$ directly to their U-Net architecture, they first mapped $\vec{E}_{\text{meas}}^{sct}$ to a coarse input image by using a non-iterative model-based inversion method known as the backpropagation (BP) method. Due to this, Huang *et al.* name their network 'BP-U-net.' It is also worth noting that Huang *et al.* use only the real component of the coarse image obtained by BP as their input. Hence, both input and output are of a single channel representing the only the real component. However, in [19], Li *et al.* used the BP method to obtain a complex-valued input containing the real and imaginary parts of the BP image. This represented a 2D multiple-input-multiple-output measurement configuration as stated in [19].

2.3 DNN Architecture

Due to the convolutional neural networks (CNNs) powerful imaging readability and image processing capability, most of the researchers have preferred to work with architectures based on the CNNs such as the Encoder-Decoder architecture, the U-Net, and the more recently the GAN architecture.

2.3.1 Encoder-Decoder

In [6], Yao *et al.* have proposed a deep convolutional encoder-decoder structure called the DConvNet to transform the $\vec{E}_{\text{meas}}^{sct}$ into contrast profiles of the targets. The proposed DConvNet included three parts: encoder, fully connected layer, and decoder. The encoding layer convolved the $\vec{E}_{\text{meas}}^{sct}$ layer-by-layer refining it into chunks of information fragments, while the decoding layer deconvolved and extracted these chunks of information fragments layer-by-layer until the target contrast, χ, is generated. The middle fully connected layer acted as bridge between the encoder and decoder. Yao *et al.* used repeated 2×2 convolution and up-convolution with a stride of 2, rectified linear unit (ReLU) activation function, and batch normalization (BN) in the proposed DConvNet architecture. Shao and Du [20] have also proposed a similar autoencoder (AE) architecture beginning with encoder, two fully connected layers in the middle, followed by a decoder; each network layer had its own configuration parameters.

2.3.2 U-Net

Huang *et al.* [12] proposed the well-known U-net architecture due to its proven powerful nonlinear fitting ability to build complicated one-to-one mappings between the input and output images [21]. Huang *et al.* implemented the U-net to build the nonlinear mapping between the rough input BP image and the ground truth image. Like

the AE, the U-net consisted of an encoder on the left and the decoder to the right; the encoder is used to extract various levels of feature maps, and the decoder utilized to reconstruct the image through layer by layer up convolutions. The additional feature of the U-net in comparison the AE, is that it has skip connections that concatenate the feature maps of the encoding blocks to the corresponding decoding blocks. This additional inputs at the decoder from the corresponding encoding blocks help the U-net learn more precise output based on this information [21].

2.3.3 GAN

In [13], Song *et al.* have proposed the perceptual generative adversarial network (PGAN) which is composed of two parts: the generator and the discriminator. The rough BP image is taken as input for the generator which tries to generate realistic profiles. The discriminator's job was to learn to distinguish between the reconstructed image and the ground truth. The PGAN consisted of a U-net [21] in the generator, while the discriminator was simply a classifier like the one used in [22]. One point of significance is that GANs not only solved the EMIS problems, but they can also help improve the generalization capabilities of the DL-IS network, which has always been a challenge to the DL network.

2.4 DNN Training

All the models in the research works have been trained without noise.

2.5 DNN Testing

All the works under review tested their DL-IS networks with synthetic data, while some further tested the robustness of their networks using experimental data. Synthetic data are those generated by solving an electromagnetic problem numerically using a forward solver. An example of such solver is the finite-element method (FEM), which is used in this thesis.

2.5.1 Synthetic Data Testing

This can be explained in two parts: Within-database and Cross-database.

2.5.1.1 Within-database

After training and validating the models with the respective training/validation datasets, all the researchers initially tested their trained models against the same database. In [6], Yao *et al.* performed the model testing with 1000 randomly selected MNIST images. Similarly, in [16] and [19][16], the DL-IS trained models were tested with 2000 MNIST images each. However, in [12] and [13] the models were tested with

1500 MNIST images, with 10% white Gaussian noise added to all of the testing scattered field samples, prior to the testing. From the non-MNIST trained model, Shao and Du [20] tested their trained DNN with 3200 test scattered-signal datasets with 5% random noise added.

2.5.1.2 Cross-database

In addition to the same database testing, some researchers have gone a step further to test their trained models against different databases to verify their trained model's generalization capabilities. For example, in [12] Huang *et al.* tested their trained U-net model using the well-known 'Austria' profile under different noise levels ranging from 10% up to 25%. The 'Austria' profile had a $\epsilon_r = 1.5$. Song *et al.* [13] not only tested with different noise levels of 'Austria' profile, but also tested their trained PGAN model with more complex profiles like double rings, double circles, and letter P with $\epsilon_r = 2$. In addition, to ensure the generalization ability of the trained model, they used a star profile with large permittivity range of 1.5, 2.0, 2.5 and 3.0 to test the PGAN model. In [19], Li *et al.* conducted the testing with objects of dielectric shapes in the form of English letters, whose $\epsilon_r = 3$.

2.5.2 Experimental Data Testing

To validate the effectiveness and generalization capabilities of the trained DL-IS models, many researchers [6], [12], [13], [19] have also tested their trained networks with a real experimental data namely, the Fresnel experiment data: the "FoamDielExt" profile [23]. However, Shao and Du [20] tested using their own experimental data from their previously developed electromagnetic imaging system [24].

2.6 DNN Result Comparison Metric

To quantify the performance of the networks, all the works reviewed used the structural similarity index (SSIM) together with the different forms of the mean squared error (MSE) such as root mean square error (RMSE) and normalized mean square error (NMSE). While MSE calculates the mean square error between each pixel of the two images under comparison, SSIM looks for the similarities within the pixels. This means an acceptable performance is achieved when MSE is low, and SSIM is high. The lowest possible MSE is zero, while the maximum value of SSIM can be 1. For example, in [12], the BP-U-net with full configuration obtained a SSIM of 0.88 while the conventional SOM algorithm got only 0.778. Similarly, the RMSE was only 0.119 while for SOM it is 0.142. These results were for the MNIST 1500 testing images.

Similarly, [12], [13] also compare results using the SSIM and RMSE metric, where the PGAN obtained better results than the conventional algorithms and other neural networks like the U-net. In [6], Yao *et al.* employed two quantitative indicators: the SSIM and the NMSE to evaluate the test results of the reconstructed images. For their DConvNet, the SSIM average of the reconstructed images reached an approximate value of 0.8 while the NMSE average was close to 0.08. On the other hand, the conventional BIM could not provide acceptable results due to high-contrast target. Additionally, in [19], the DeepNIS reconstructed images had a higher SSIM and lower MSE than the conventional CSI and BP methods.

Chapter 3. Mathematical Formulation

3.1 Microwave Imaging System

Microwave Imaging (MWI) is a field which uses electromagnetic waves ranging between 300 MHz to 300 GHz to evaluate hidden or embedded objects inside a structure.

In a MWI system, an object of interest (OI) is placed within a bounded chamber as shown in Figure 1. The chamber is illuminated by each of the T transmitters successively, and the resulting field from the OI is measured at each of the R receiver positions for each transmitter. Both the transmitters and receivers are located on a measurement surface S. A transmitter t produces an incident field $\vec{E}_t^{inc}$ in the absence of the OI. With the presence of the OI in the imaging domain D, the transmitter t produces the total field $\vec{E}_t^{tot}$. Thus, the scattered field due to the presence of OI is defined as [8]

$$\vec{E}_t^{sct} \triangleq \vec{E}_t^{tot} - \vec{E}_t^{inc}. \tag{3.1}$$

The OI along with the imaging domain D, are immersed in a background medium and contained within a problem domain, Ω. This domain Ω is further surrounded by a boundary Γ that can be of any particular shape and size depending on the imaging problem setup. The OI has a complex relative permittivity of ϵ_r, whose corresponding electric contrast X is defined as

$$X \triangleq \frac{\epsilon_r - \epsilon_b}{\epsilon_b}. \tag{3.2}$$

where ϵ_b is the relative complex permittivity of the background medium. Each quantity in this chapter is a function of the two-dimensional position vector $r = (x, y)$.

Further, the contrast source variable $\vec{w}_t$ is defined as

$$\vec{w}_t = X\vec{E}_t^{tot}. \tag{3.3}$$

3.2 Forward Problem

The MWI problem can be split into two parts: the forward problem and the inverse problem. The main purpose of the forward problem is to obtain the behavior of the scattered field of a known OI surrounded by a known background medium. The forward problem is governed by Maxwell's equations for electromagnetic fields [8]. There are several possible configurations for a forward problem. In this thesis, a two-dimensional model with transverse magnetic polarization (2D-TM) is considered.

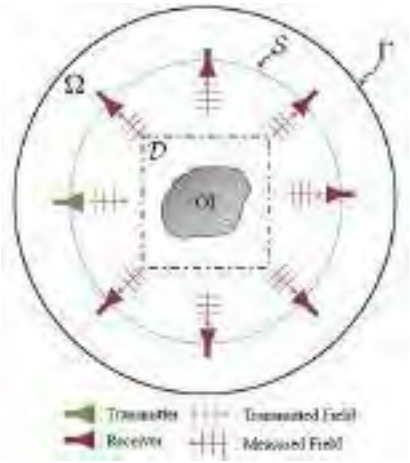

Figure 1. Two-dimensional (2D) model for the MWI problem [8].

The forward problem is solved numerically using the finite-element method (FEM) developed in [8]. The FEM solver is used to calculate the measured scattered field data $\vec{E}_{\text{meas}}^{\,sct}$ of the simulated OI at the receivers on the measurement surface S. Hereafter, the simulated OI in imaging domain D is referred to as the *target*.

3.3 Electromagnetic Inverse Scattering (EMIS) Problem

The objective of the EMIS problem is to estimate the electric contrast X within the imaging domain D, using the measured scattered field $\vec{E}_{\text{meas}}^{\,sct}$ of the target obtained from the FEM solver. This is represented as

$$\vec{E}_{\text{meas}}^{\,sct} = G_S\{X(I - G_D^X)^{-1}(\vec{E}^{\,inc})\}. \tag{3.4}$$

where I is the identity operator, G_S is the linear data operator that returns the electric field values on the measurement surface S, and G_D^X is the linear domain operator that returns the field values within the imaging domain D [8]. The aforementioned operators are based on Maxwell's equations for electromagnetic fields [8]. In (3.4), the incident field $\vec{E}^{\,inc}$ is assumed to be known, while the operator G_D^X similar to contrast X is unknown. Although both G_S and $G_D{}^X$ are linear, the inverse operation within (3.4) is non-linear, making the EMIS problem a non-linear one.

In order to solve this non-linear EMIS problem, there are several inversion algorithms that has been implemented over the years. The most typical ones include the DBIM, SOM, and CSI [8], [9], [11].

3.3.1 The Inversion Algorithm – Contrast Source Inversion (CSI)

In this thesis, the CSI method from [8], [10] is used to solve the EMIS problem, which is formulated using the finite-element method. The CSI algorithm formulates the

MWI optimization problem in terms of the two variables, the contrast X and the contrast source $\vec{w}_t$. The CSI cost functional in terms of these variables are expressed as

$$C^{CSI}(X, \vec{w}_t) = \frac{\sum_{t=1}^{T} \| \vec{E}^{sct}_{t,meas} - G_S\{\vec{w}_t\} \|_S^2}{\sum_{t=1}^{T} \| \vec{E}^{sct}_{t,meas} \|_S^2} + \frac{\sum_{t=1}^{T} \| X\vec{E}^{inc}_t - \vec{w}_t + XG_D\{\vec{w}_t\} \|_D^2}{\sum_{t=1}^{T} \| X\vec{E}^{inc}_t \|^2} \tag{3.5}$$

where $\|\cdot\|$ notation represents the L_2-norm (or the Euclidean norm) of the argument.

The contrast and the contrast source variables are successively updated by a conjugate gradient (CG) method. In the first step, the contrast source variables $\vec{w}_t$ are updated by a CG method with Polak-Ribière search directions, while keeping the contrast variables X constant. In the second step, $\vec{w}_t$ is maintained constant, and a modified form of the function in (3.5) is minimized in an iterative manner until a desired minimum is reached. The optimization process ends upon reaching the desired minimum [8], [10].

3.3.2 Artificial Intelligence - Neural Networks

Due to high computational complexity of the CSI and other inversion algorithms, this thesis aims to solve the nonlinear EMIS problem using deep neural networks (DNNs) and compare the results. As CNNs have seen much success in image classification and processing, different deep CNN architectures ranging from simple to more complex ones have been designed, implemented and tested in this thesis. The architecture and methodology of these DNNs will be discussed in the following chapter. The flowchart of the EMIS-DNN methodology is shown in Figure 2.

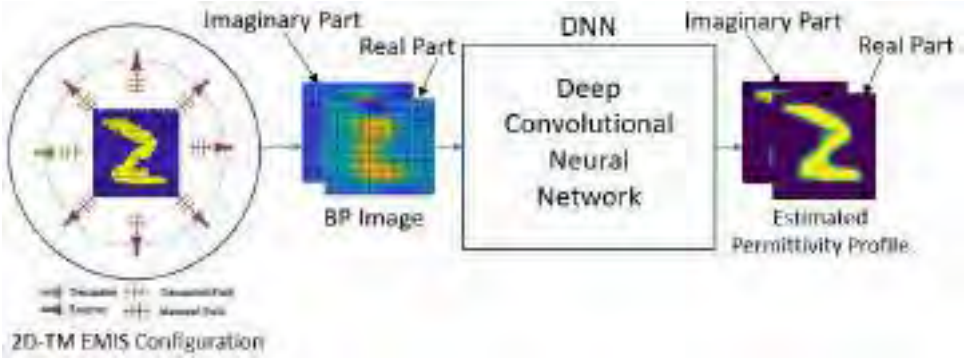

Figure 2. The flowchart of the EMIS – DNN methodology with a sample BP input.

Chapter 4. Deep Neural Networks

The deep learning techniques to solve the EMIS problem involves different parts: the Input Layer, Output Layer, and Architecture.

4.1 Input Layer

As CNNs require large input for training, the readily available MNIST hand-written digits are selected as the targets in imaging domain D, in the forward problem. The MNIST digit-like targets are assigned a static or dynamic relative complex permittivity ϵ_r based on the configuration setup. The imaging domain D is surrounded by a homogeneous lossless background medium with relative permittivity ϵ_b. Upon executing the FEM Solver, the $\vec{E}^{sct}_{\text{meas}}$ of the target is obtained which leads to three different input types to the DNNs.

4.1.1 Input Type 1 – Measured Scattered Field Data

In this input type, the measured scattered field $\vec{E}^{sct}_{\text{meas}}$ data obtained from the FEM forward problem is directly used as input to the DNNs. Further, $\vec{E}^{sct}_{\text{meas}}$ is complex, so the input to the DNNs consists of two channels: one for the real component and the other for the imaginary component.

4.1.2 Input Type 2 – Backpropagation Estimates

The second type of input is calculated by backpropagating (BP) the measured scattered field $\vec{E}^{sct}_{\text{meas}}$ generated using the FEM forward problem. The detail of performing the backpropagation is given as [8], [10]

$$\vec{w}_{t,BP} = \frac{\text{Re}\langle G_S[G_{S^*}(\vec{E}^{sct}_{\text{t,meas}})], \vec{E}^{sct}_{\text{t,meas}} \rangle_S}{\| G_S[G_{S^*}(\vec{E}^{sct}_{\text{t,meas}})] \|^2_S} [G_{S^*}(\vec{E}^{sct}_{\text{t,meas}})] \tag{4.1}$$

where G_{S^*} is the adjoint operator of G_S and $\langle\,\rangle$ is the inner product [8], [10].

The backpropagation results are two images that represent the estimates of the real and imaginary relative permittivity of the target. This means that for simulating K number of MNIST targets, leads to K pairs of input BP images consisting of real and imaginary components. A sample of a BP result is shown in Figure 3. Since DNNs work with square grids, the K BP image pairs obtained in FEM triangular mesh [8], are interpolated into square grids of size $N \times N$ as shown in Figure 4. These square grid BP image pairs are provided as the input to the DNNs. Since the BP images have two parts, real and imaginary, the input to the neural network has two channels, where channel 1 represents the real component and channel 2 represents the imaginary

component. Furthermore, in this thesis the input is referred to as complex-input with dimensions $K \times N \times N \times 2$.

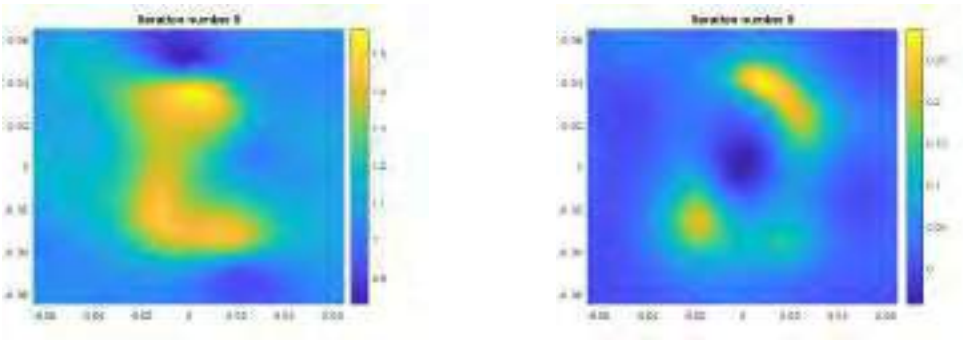

(a) BP Image Real ϵ_r *(b) BP Image Imaginary ϵ_r*

Figure 3. (a) Real and (b) imaginary estimates of the relative permittivity calculated using backpropagation.

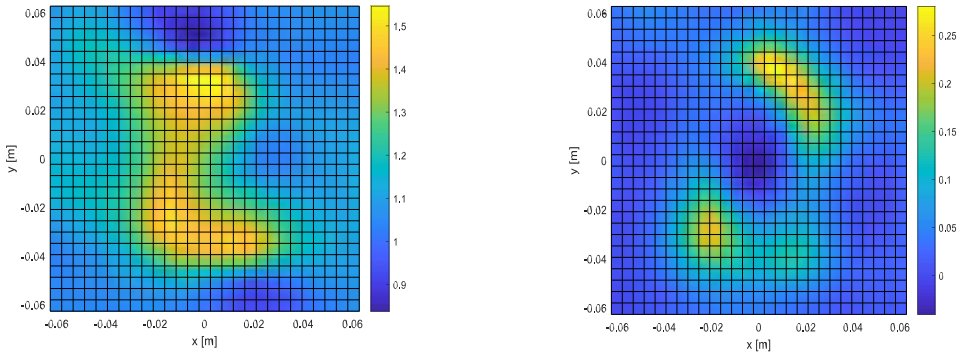

(a) BP Image Real ϵ_r *(b) BP Image Imaginary ϵ_r*

Figure 4. (a) Real and (b) imaginary BP estimates interpolated into a square grid.

4.1.3 Input Type 3 – Tenth Iteration of CSI 'ITER10'

DNNs are mostly data-driven and lack physics, due to which they are widely known in the scientific world as 'Black Box' approximators that lack inner reasoning [25]-[28]. Though DNNs have proven to outperform the conventional algorithms in terms of reconstruction speed and quality, their performance degrades considerably when the testing target is largely different from the training ones. This is because the governing physical laws are only partially satisfied in these DL-based models, unlike the conventional iterative algorithms [26].

To address this issue and incorporate more physics into our models, a novel input type has been introduced in this thesis which is obtained from the output image of the tenth iteration of the CSI that is referred as 'ITER10'. ITER10 not only incorporates more of the governing physical law of the EMIS problem in the input, it

is also obtained at a significantly much lesser computational time when compared to the fully-iterated CSI method.

By running the CSI algorithm through to its tenth iteration, ITER10 is produced. [8], [10]. Similar to the BP, its input dimensions are $K \times N \times N \times 2$.

4.2 Output Layer

As with every supervised learning, the training stage includes two parts: the DNN output and the test label. In this thesis, the DNN output is the reconstructed relative permittivity profile, whereas the test label is the ground truth relative permittivity profile. An example of the ground truth which is the same as the exact complex relative permittivity profile for a single MNIST sample target in the problem domain is shown in Figure 5.

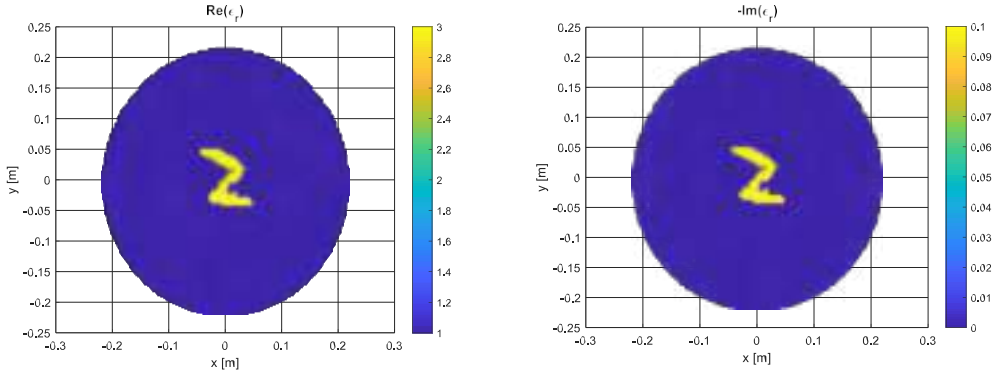

(a) Exact Real ϵ_r *(b) Exact Imaginary ϵ_r*

Figure 5. (a) Real and (b) imaginary components of the relative permittivity for the exact profile of a sample MNIST target.

Since the exact profile serves as the ground truth data for the DNN, they are interpolated from the FEM triangular mesh into a square grid of size $N \times N$ in order for them to be used with the DNN. The square grid conversion of the sample given in Figure 5 is shown in Figure 6. These square grid ground truth image pairs are provided as the output labels to the DNNs. Moreover, the output to the neural network also has two channels similar to the inputs making the output's dimensions $K \times N \times N \times 2$.

The main goal of the DNN training is to minimize as much as possible the error gap between the reconstructed profile and the ground truth without overfitting. Further, unlike the training phase, the output layer of the testing stage includes only the reconstructed relative permittivity profile.

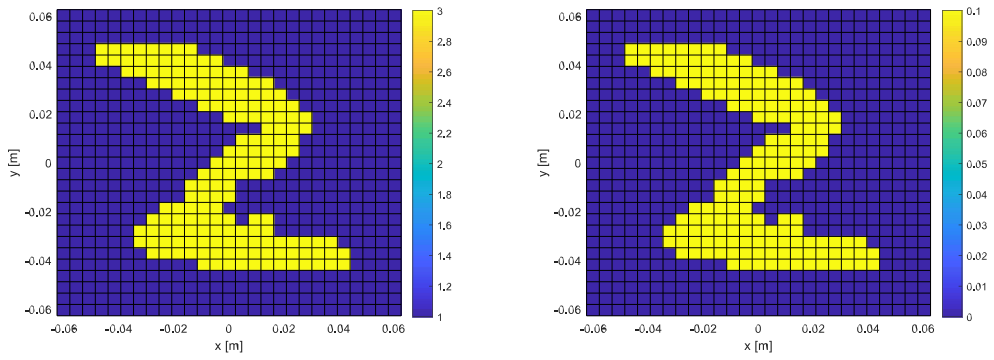

(a) Exact Real ϵ_r *(b) Exact Imaginary* ϵ_r

Figure 6. (a) Real and (b) imaginary components of the relative permittivity for the ground truth sample interpolated into a square grid.

4.3 Architecture

Different CNN architectures have been designed and implemented in this thesis.

4.3.1 Baseline-AE Model

This is a simple baseline model designed for functionality testing purpose with a simple autoencoder (AE) architecture consisting of a convolutional encoder-decoder as seen in Figure 7 [6].

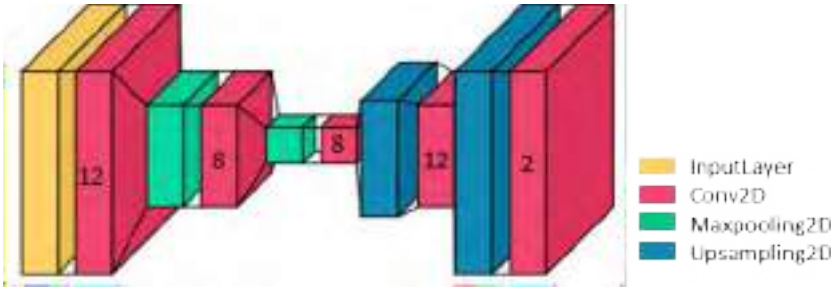

Figure 7. Baseline-AE architecture.

4.3.2 DCEDnet

The Deep Convolutional Encoder Decoder Network (DCEDnet) in Figure 8 is a much deeper version of the Baseline-AE that includes two parts: the encoder and decoder [6]. The encoding layer convolves the input image pair layer-by-layer to extract different levels of the feature map, while the decoding layer deconvolves the extracted features to reconstruct the relative permittivity profile. A repeated two-dimensional convolution together with batch normalization (BN) and max pooling is implemented in the encoder, while the decoder uses a repeated two-dimensional convolution together with up-sampling and BN. The activation function used in all the hidden layers is the rectified linear unit (ReLU), except for output layer which uses the non-linear sigmoid activation function.

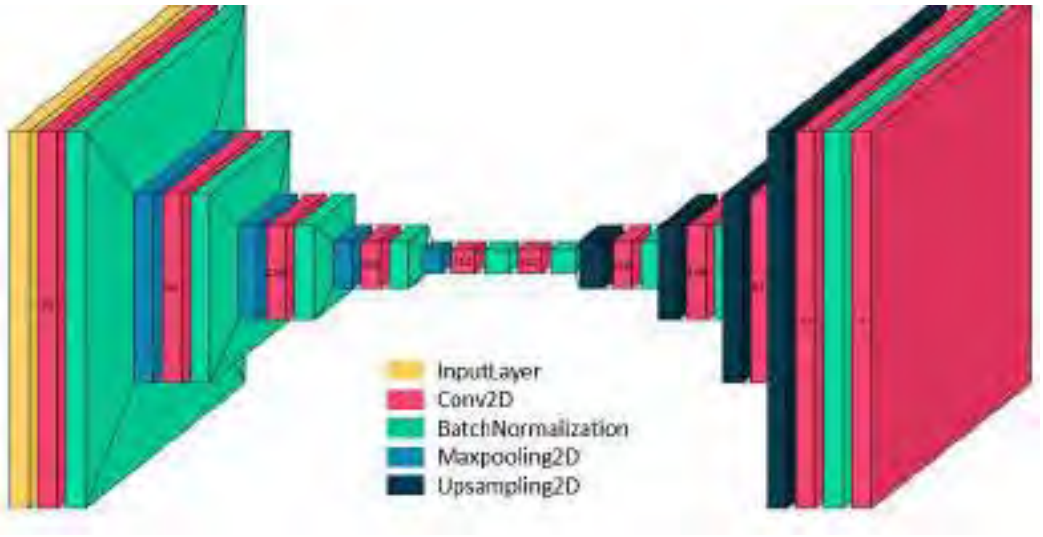

Figure 8. DCEDnet architecture.

4.3.3 Unet & Unet-Lite

In this thesis, the well-known Unet [21] is implemented with slight variations. The implemented Unet architecture as illustrated in Figure 9 consists of a contracting path on the left side and an expansive path on the right side. The contracting path has several levels with each level containing two successive 3×3 convolutional layer, wherein each convolution is followed by BN and ReLU activation. This is followed with 2×2 max pooling with a stride of 2 that down-samples the feature map by half. At each down-sampling, the number of feature channels are also doubled. On the contrary, every level in the expansive path involves 2×2 upsampling of the feature maps doubling its size, while the number of feature channels are halved. A skip connection is used at every level to concatenate the upsampled output with the corresponding similar-sized high resolution feature map from the contracting path. As this contracting path feature map contains additional spatial information, concatenating it with the more feature represented upsampled output enhances the localization capability of the network [21]. This concatenated output is then convolved with the two 3×3 convolutions that are followed by BN and ReLU. The successive convolutional layers can now learn to reconstruct more precise output based on the concatenated information obtained both from the contracting path as well as the expansive path [21]. The final output layer includes a 1×1 convolution which is followed by the non-linear sigmoid activation. The Unet in total has 19 convolutional layers.

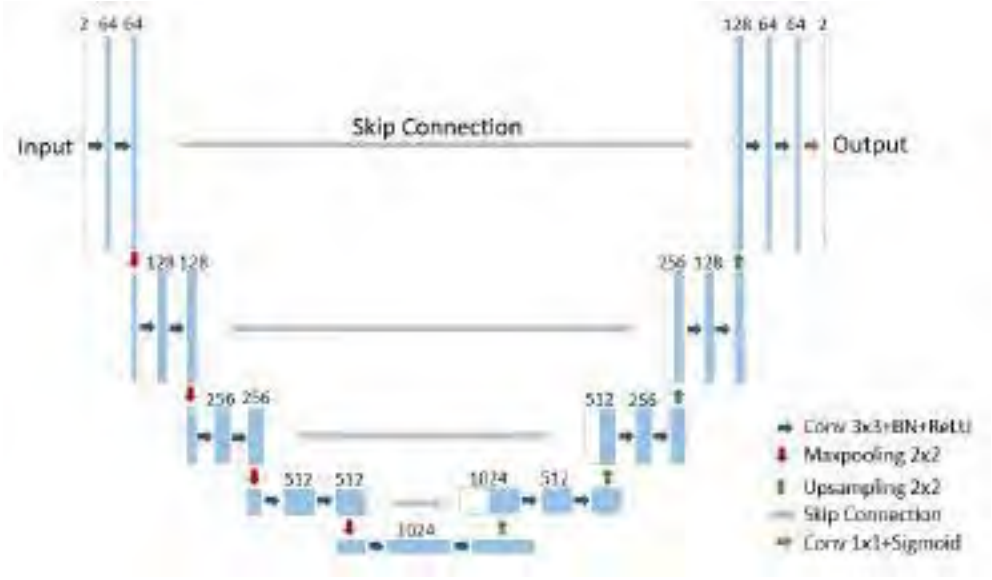

Figure 9. Unet architecture. Each blue box corresponds to a multi-channel feature map with the number of channels labeled at the top of each box.

Further, a lighter version of the Unet named 'Unet-Lite' has also been introduced in this thesis. The only difference in the lighter version is that it has one less convolutional layer at each level, thus reducing the total number of convolutional layers to just 10. The main reason for experimenting the Unet-Lite is to measure the performance difference while reducing the trainable parameters by almost half. Since the Unet-Lite has only half the parameters, it occupies much lesser memory than the Unet. So, in scenarios with memory limitation, Unet-Lite can be an option provided the results are acceptable.

4.3.4 Attention-Unet

4.3.4.1 Attention Mechanism

As the name suggest, attention mechanisms are a neural network layer that allows the model to focus more on a particular part of input, which is of more significance than others by assigning different weights to different parts of the input. They have been widely used in natural image analysis, natural language processing, and knowledge graphs for machine translation [29], [30], in image captioning [31], and in classification tasks [32]-[34]. Trainable attention comes in two types: hard attention and soft attention. In hard attention [35], the relevant regions have to be first highlighted by cropping as only one region at a time can be 'paid' attention. This makes it non-differentiable and requires reinforcement learning for parameter updates, thus making it difficult to train. Moreover, backpropagation can't be used in hard attention. On the contrary, soft attention performs the attention by weighting different parts of the region

differently. The more relevant parts of the image get more weights while the less relevant gets lesser weights. During the training, these weights also get trained enabling the model to pay more attention to the relevant regions. Soft attention is trained using the standard back-propagation [29]. Due to the use of back-propagation and ease of training, soft attention is more widely used than hard attention.

4.3.4.2 Attention Gate (AG) in Unet

Attention-Unet [36] is a customized version of the well-known Unet which uses attention gates (AGs) to highlight only the relevant activations during the Unet training. AGs uses the soft attention mechanism. Attention-Unet trained with AGs intuitively learn to highlight the prominent features that are useful for a particular task while suppressing irrelevant regions in an input image [36]. This reduces the computational resources wasted on irrelevant activations and enhances the generalization capability of the network. Additionally, the AGs don't add a lot of computing complexity or call for a lot of model parameters. Without any additional supervision, they naturally learn to focus on the target structure [36].

In this thesis, an Attention-Unet (ATTN-Unet) similar to the one used in [36] with minor modifications has been designed and implemented to solve the EMIS problem. Though Attention-Unet itself isn't novel as it has been already applied to medical image segmentation in Computed Tomography (CT) abdominal scan for locating pancreas by Oktay *et al.* [36], it has yet to be implemented in field of microwave imaging or inverse scattering. To my best of knowledge, this thesis will be the first to propose and implement the Attention-Unet to solve the EMIS problem. Figure 10 illustrates the Attention-Unet architecture that has been implemented in this thesis. The architecture is very much similar to the implemented Unet architecture in Figure 9 except for the inclusion of the attention gates at every level.

In the Unet, the upsampled output in the expansive path is concatenated directly with the corresponding high resolution feature map from the contracting path. Though this direct concatenation helps in improving the spatial information, it brings along poor feature representation from the initial layers, as these layers are known to have low feature representation. So, there needs to be some additional layer that ensures to keep only the relevant spatial information while ignoring or minimizing the irrelevant feature representations from the contracting layers. To address this issue, soft attention mechanism is introduced at the skip connection in form of attention gates. Rather than

concatenating the upsampled output in the expansive path directly to the corresponding feature map from the contracting path, an attention gate is implemented prior to the concatenation as shown in Figure 10.

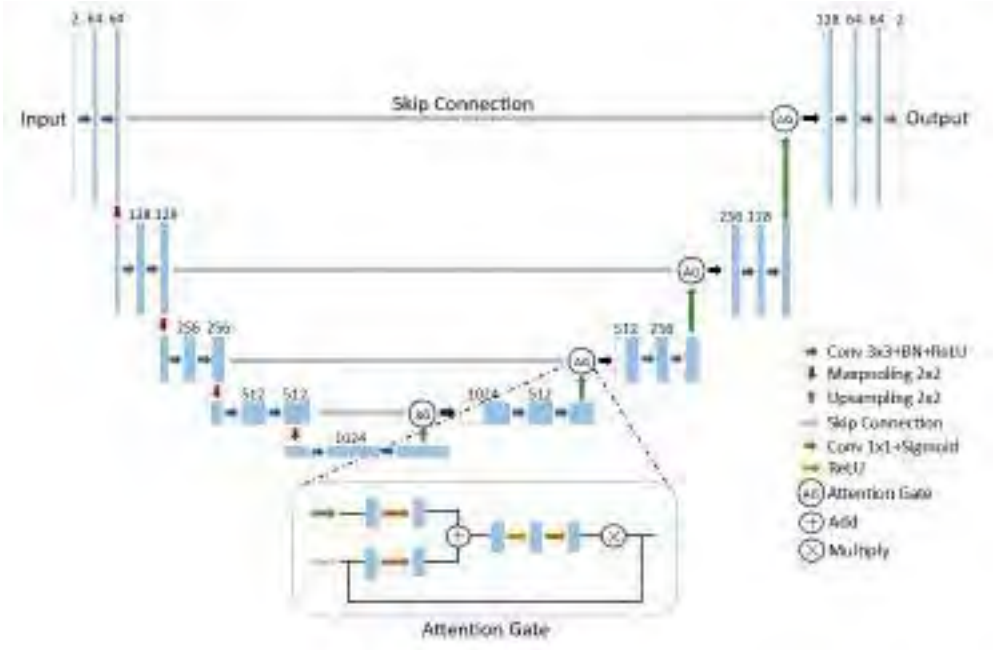

Figure 10. Attention-Unet architecture.

4.3.4.3 AG Methodology

In the AG, the upsampled output and the corresponding feature map goes through a 1×1 convolution with F number of filters that correspond to the particular level. Through this convolution, the dimensions of these attention gate inputs are matched which then get added together. As the feature map has more spatial information and the upsampled output has more feature representation, adding both helps obtain the best of the two paths. After the addition, the aligned weights get larger while the unaligned weights get significantly smaller. These combined weights then go through a ReLU activation followed by a 1×1 convolution and a sigmoid activation function. The main purpose of the sigmoid function is to scale the attention weights between [0,1]. These scaled weights are then multiplied to the feature map output from the contracting path to perform the soft attention of highlighting the significant regions with higher weights while suppressing the irrelevant regions with lower weights. This weighted feature map then gets concatenated with the upsampled output from the expansive path which then goes through similar convolution process as in the standard Unet. One important thing to note is that the AG weights also get trained during the training process. This way the AG weights keep improving with every training epoch to provide better attention [36].

Chapter 5. Numerical and Experimental Results

In order to solve the EMIS problem using DNNs, in this section four different configurations were implemented and tested. The complexity of the configurations was progressively enhanced by incorporating more complex inputs from more general ones, adding more advanced and deeper neural networks, and transitioning from a generic forward problem configuration to the desired one, which is the forward problem configuration of the University of Manitoba's (UM) experimental data [37]. All of these configurations are ultimately meant to lead to the optimal DNN model and input type so that it may be tested using the experimental data from the University of Manitoba to produce high quality reconstructions.

The summary of the different configurations is given below:

- Configuration 1: The Baseline-AE and the DCEDnet both were trained and tested with both the $\vec{E}_{\text{meas}}^{sct}$ and BP estimates that were obtained from simple lossless MNIST targets assigned with a static permittivity at a frequency of 1 GHz. The primary goal was to determine which input-trained DCEDnet produced the best results after initially reconstructing the permittivity profiles using the basic Baseline-AE.
- Configuration 2: With the BP-DCEDnet successful reconstructions with MNIST testing data in configuration 1, it is then trained and tested with a more complex-input BP that was obtained from lossy targets assigned with a static permittivity at a frequency of 3 GHz. The main goal was to verify the BP-DCEDnet performance in the reconstruction of the imaginary component of the complex relative permittivity profile.
- Configuration 3: Since, the ultimate goal is to use the UM experimental data to test the optimal DNN to produce high quality reconstructions, the same forward problem configuration of the experimental data is used to produce the DNN inputs from the MNIST targets, in order to avoid retraining the DNN models for the experimental data testing. Further, to enhance reconstruction testing accuracy of the DNN outputs, more advanced networks namely the Unet-Lite, Unet and ATTN-Unet were added to the already tested DCEDnet. In order to incorporate more physics into the models, the novel ITER10 input was also introduced to these models in addition to the BP. These inputs were obtained from lossy targets assigned with a low dynamic range (LDR) of relative

permittivity values. In order to test the generalization capacity and durability of the models, they were tested with more challenging cross-database complex profiles under different noise levels and large permittivity ranges. All this was done to select the best performing DNN architecture along with its input type. The models were tested with increasingly challenging cross-database complex profiles under various noise levels and large permittivity range in order to assess their generalization ability and durability. All of this was done in order to determine the input type and DNN architecture that performed the best, which was then selected to test the UM experimental data.

- Configuration 4: Having successfully tested both synthetic and experimental data in the LDR setup, the optimal DNN model along with its input is re-trained in the high dynamic range (HDR) of complex relative permittivities in order to handle the experimental data with high permittivity value.

Sections 5.1 to 5.4 explain the different configuration details prior to displaying and discussing their corresponding synthetic results. Section 5.5 depict the results of the experimental data.

5.1 Configuration 1: Lossless Targets with Static Relative Permittivity

In this configuration setup, lossless targets with static permittivity have been implemented.

5.1.1 Configuration of the Forward Problem

The target is positioned inside a square imaging domain D with side-length of 15 cm. The imaging domain is centered in the middle of the microwave imaging system and is illuminated by 32 transmitters at a frequency of 1 GHz. For each transmitter, the scattered data are collected at 32 receivers. The transmitting and receiving points are co-located and evenly spaced on a circular surface S of radius of 10 cm. The problem domain is bounded and enclosed by a circular absorbing boundary with a radius of 15 cm.

Since deep CNNs training requires a large number of input samples, the first 10000 MNIST handwritten digits were selected as targets. The scattered data are obtained for these 10000 MNIST digit-like targets that are assigned a real relative permittivity $\epsilon_r = 3$. The target is surrounded in a homogeneous lossless background medium with relative permittivity $\epsilon_b = 1$. Both the input and the ground truth image pairs are interpolated into square grids of 28×28.

5.1.2 Training Details

For this configuration setup, two DNN architectures (the Baseline-AE and DCEDnet) were trained and tested with two different input types separately: $\vec{E}_{\text{meas}}^{sct}$ and BP estimates.

Out of the 10000 samples, 7000 (70%) were selected as training data, 1000 (10%) for validation, and 2000 (20%) as testing data. The input data for training and validation were either the calculated complex-input $\vec{E}_{\text{meas}}^{sct}$ or BP estimates, while the corresponding complex ground truth pairs served as the output data for training and validation labels in the encoder-decoder architecture of both the DNNs.

The loss function used is the standard mean-square error (MSE). Furthermore, the Adaptive moment estimation (Adam) optimizer is used for optimizing the MSE loss function. As for the hyperparameters, the model is trained for 100 epochs with a batch size of 32.

The code is developed with Python 3 in Google Colab and the model is trained and tested using the T4 GPU provided by Google Colab.

5.1.3 Quality Metric – Mean Squared Error

In order to quantitatively evaluate the DNN models reconstruction accuracy, the mean squared error (MSE) is chosen as the quality metric. Mean Squared Error (MSE) is a commonly used metric to measure the average squared difference between the ground truth (actual) values and the reconstructed (predicted) values. It is a measure of the overall model performance and is widely used in various fields, including statistics, machine learning, and signal processing. The MSE is formulated as

$$MSE = \frac{1}{n}\sum_{i=1}^{n}(y_i - \hat{y}_i)^2 \tag{5.1}$$

where n is the number of samples, y_i is the ground truth value for the i^{th} sample and $\hat{y}_i$ is the reconstructed value for the i^{th} sample [38].

The MSE is calculated by taking the average of the squared differences between the ground truth and reconstructed values. Squaring the differences ensures that both positive and negative errors contribute to the overall metric, and taking the average normalizes the error across all data points [38].

A lower MSE indicates better model performance, as it means that the reconstructed values are closer to the ground truth values [38].

5.1.4 Results

The results obtained from the two DNNs are presented for the two forward problem configurations and using different types of inputs. Furthermore, the forward problem configuration and type of complex-input for DNN are indicated in the section's heading.

Moreover, in the next sections, for each figure with colormaps, the first row shows the ground truth, the middle row is the reconstructed image by the respective DNN model, and the last row is the input.

5.1.4.1 BP-Baseline-AE Model

5.1.4.1.1 Training Results

Upon successful training of the BP-Baseline-AE model for 100 epochs, the training results are shown in Figure 11 and Figure 12.

Moreover, the MSE losses achieved for training and validation are, respectively, 0.0140 and 0.0139. The loss curves for training and validation are shown in Figure 13.

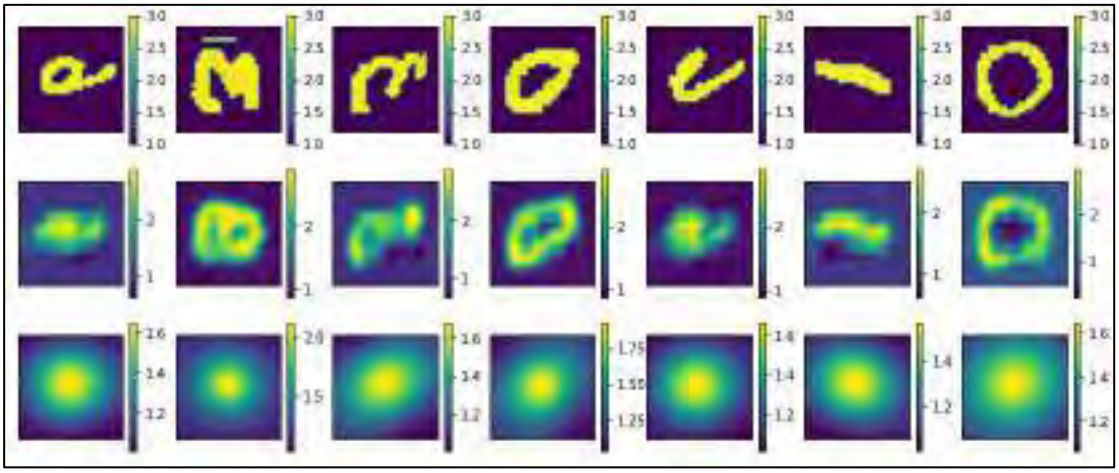

Figure 11. Training results of the BP-Baseline-AE model for the real component of ϵ_r.

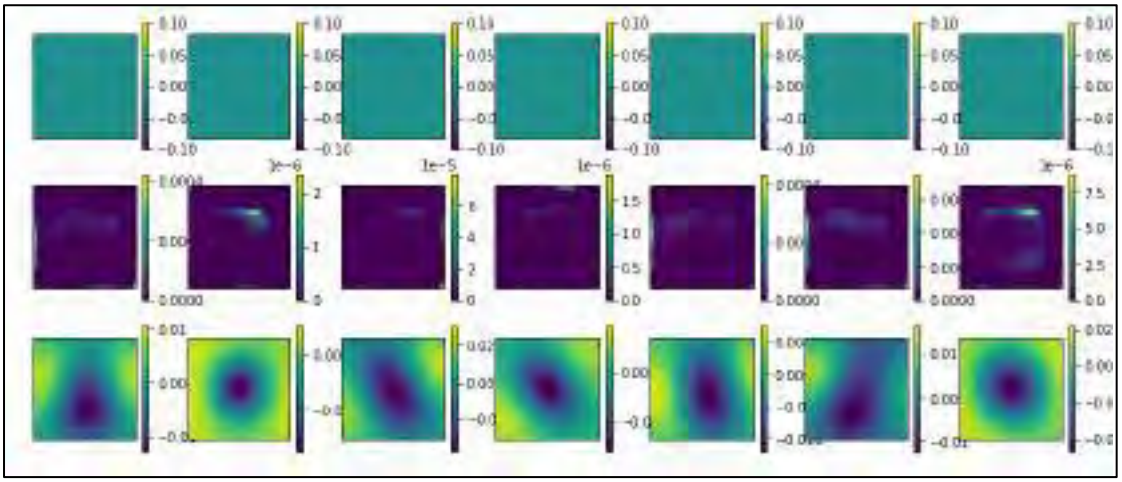

Figure 12. Training results of the BP-Baseline-AE model for the imaginary component of ϵ_r.

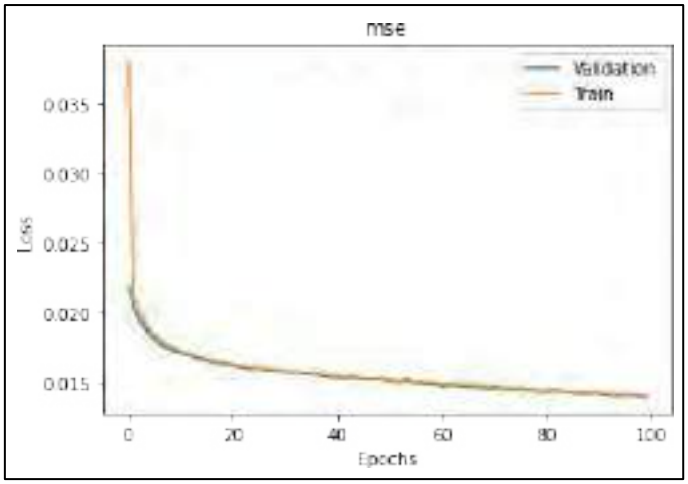

Figure 13. MSE loss curves for training and validation.

5.1.4.1.2 Test Results

The trained model was tested with the unknown 2000 test BP image pairs. Upon evaluation, the model achieved an MSE of 0.0140 for the entire testing set. The testing results are shown in Figure 14 and Figure 15.

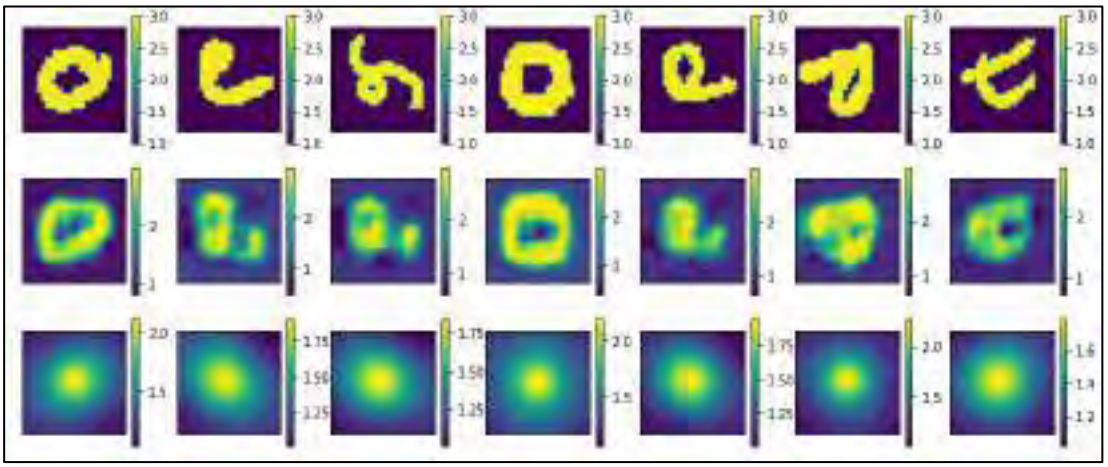

Figure 14. Test results of the BP-Baseline-AE model for the real component of ϵ_r.

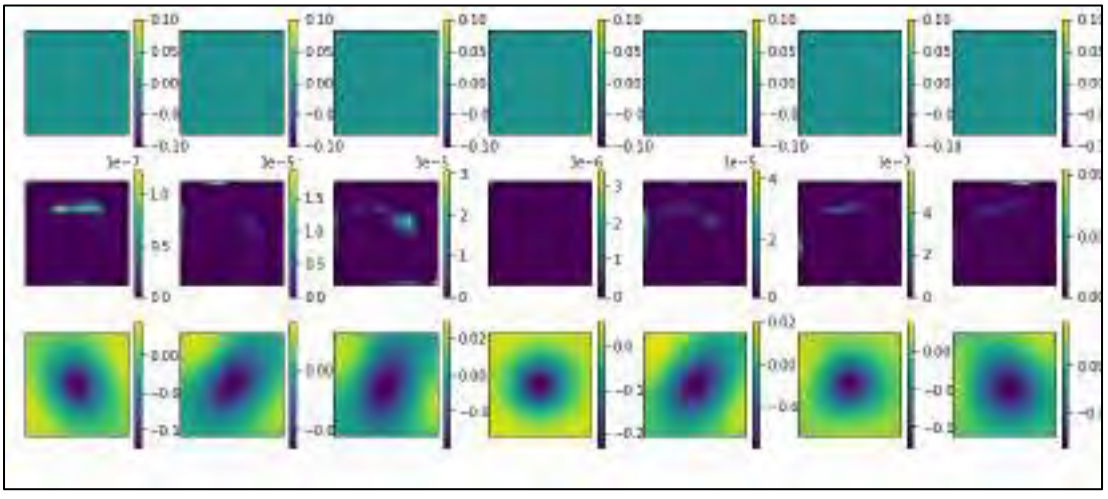

Figure 15. Test results of the BP-Baseline-AE model for the imaginary component of ϵ_r.

5.1.4.2 BP-DCEDnet Model

5.1.4.2.1 Training Results

Upon successful training of the BP-DCEDnet model for 100 epochs, the training results are shown in Figure 16 and Figure 17.

Moreover, the MSE losses achieved for training and validation are, respectively, 0.009 and 0.0105. The loss curves for training and validation are shown in Figure 18.

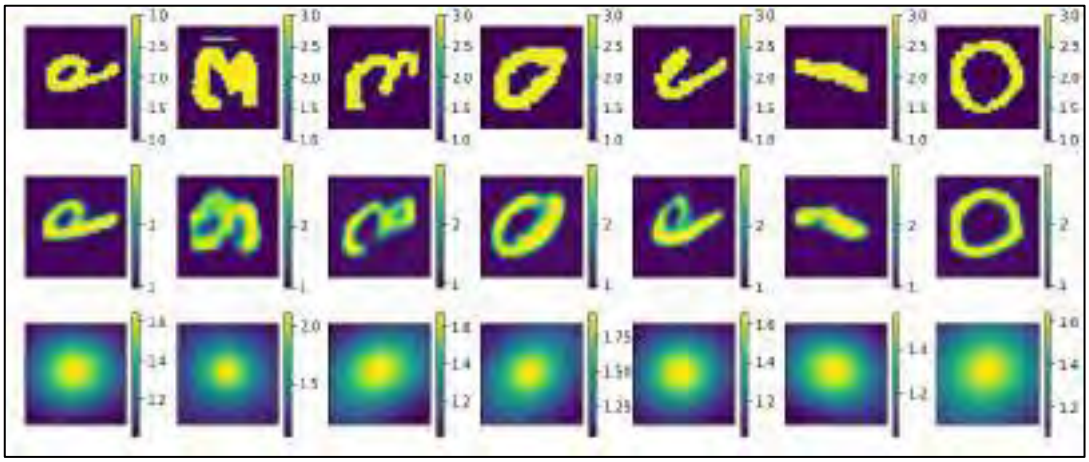

Figure 16. Training results of the BP-DCEDnet model for the real component of ϵ_r.

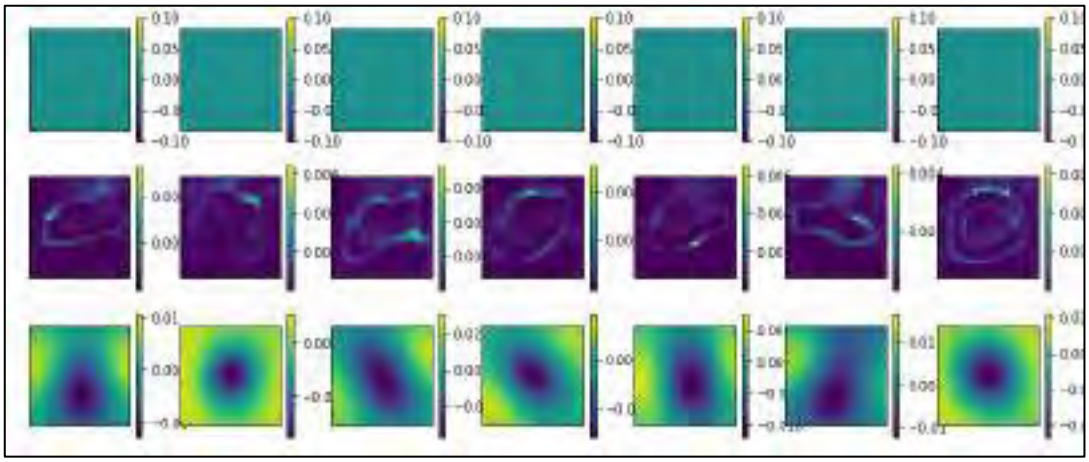

Figure 17. Training results of the BP-DCEDnet model for the imaginary component of ϵ_r.

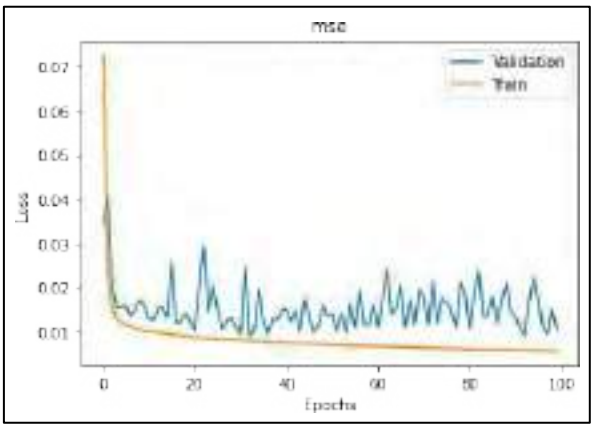

Figure 18. MSE loss curves for training and validation.

5.1.4.2.2 Test Results

The trained model was tested with the unknown 2000 test BP image pairs. Upon evaluation, the model achieved an MSE of 0.0108 for the entire testing set. The testing results are shown in Figure 19 and Figure 20.

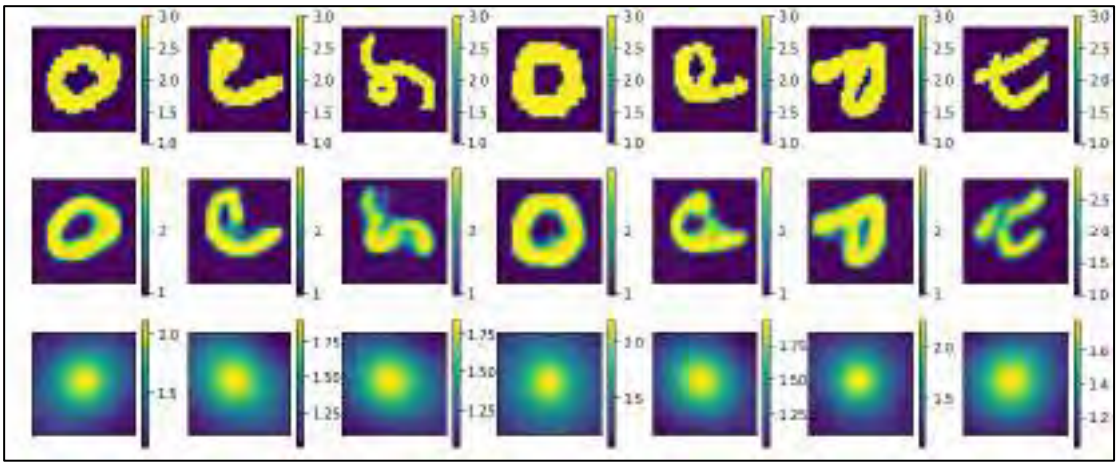

Figure 19. Test results of the BP-DCEDnet model for the real component of ϵ_r.

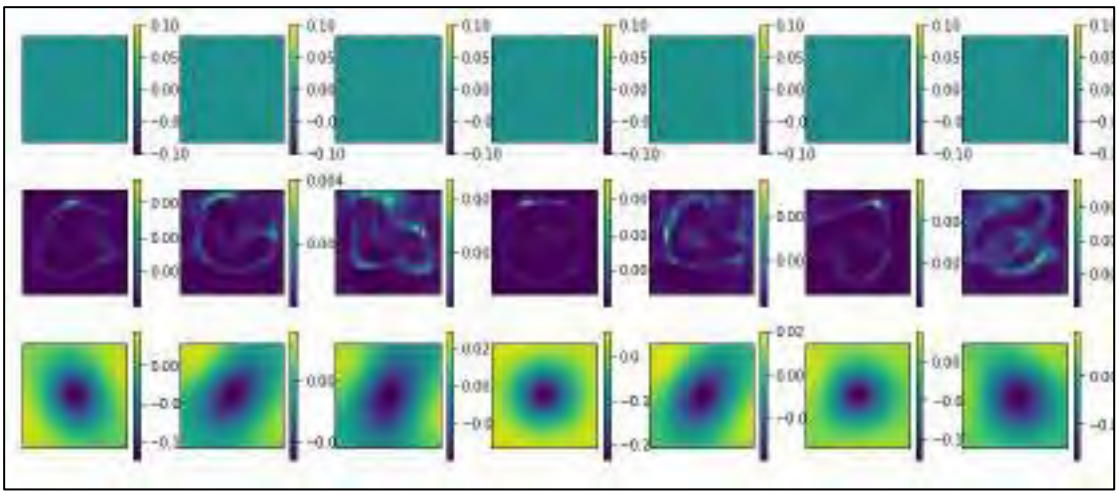

Figure 20. Test results of the BP-DCEDnet model for the imaginary component of ϵ_r.

5.1.4.3 $\vec{E}^{sct}_{meas}$-Baseline-AE Model

5.1.4.4 Training Results

Upon successful training of the $\vec{E}^{sct}_{meas}$-Baseline-AE model for 100 epochs, the training results are shown in Figure 21 and Figure 22.

Moreover, the MSE losses achieved for training and validation are, respectively, 0.0135 and 0.0136. The loss curves for training and validation are shown in Figure 23.

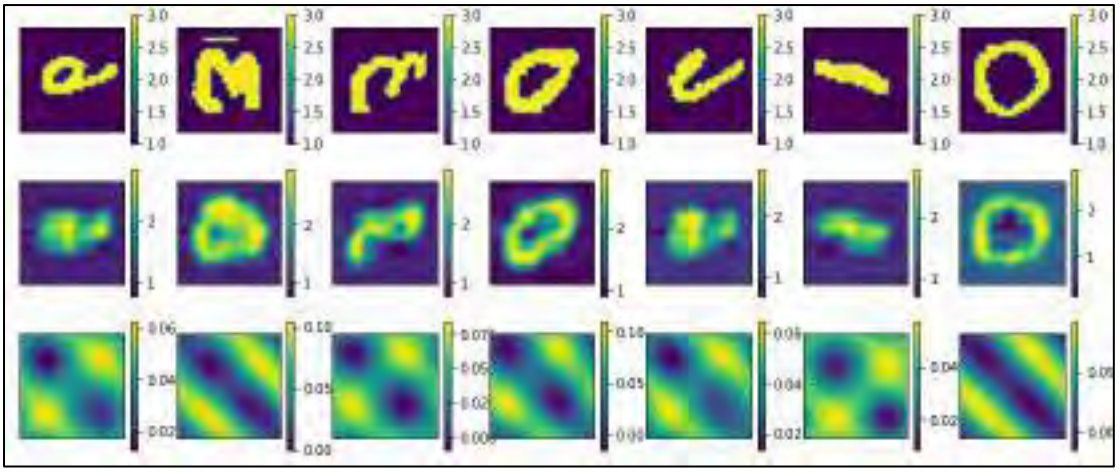

Figure 21. Training results of the $\vec{E}^{sct}_{meas}$ -Baseline-AE model for the real component of ϵ_r.

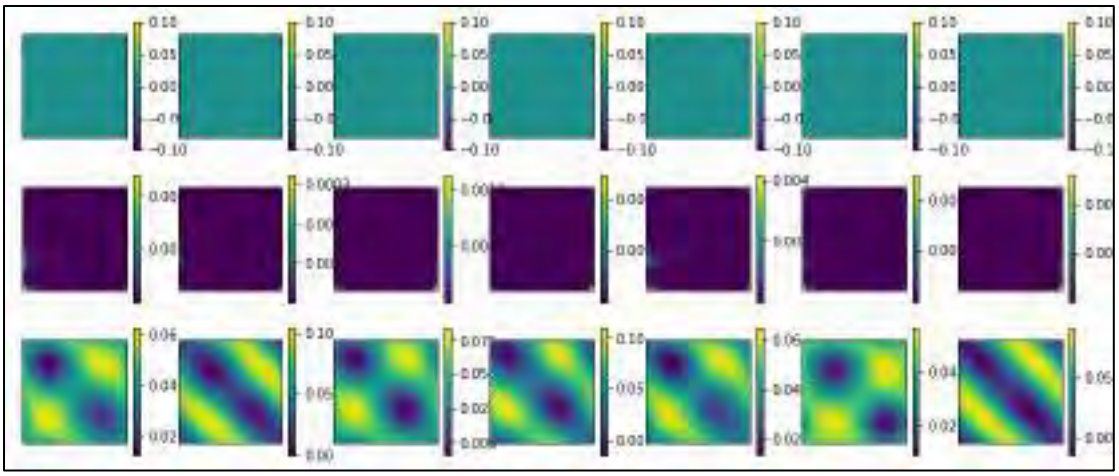

Figure 22. Training results of the $\vec{E}^{sct}_{meas}$ -Baseline-AE model for the imaginary component of ϵ_r.

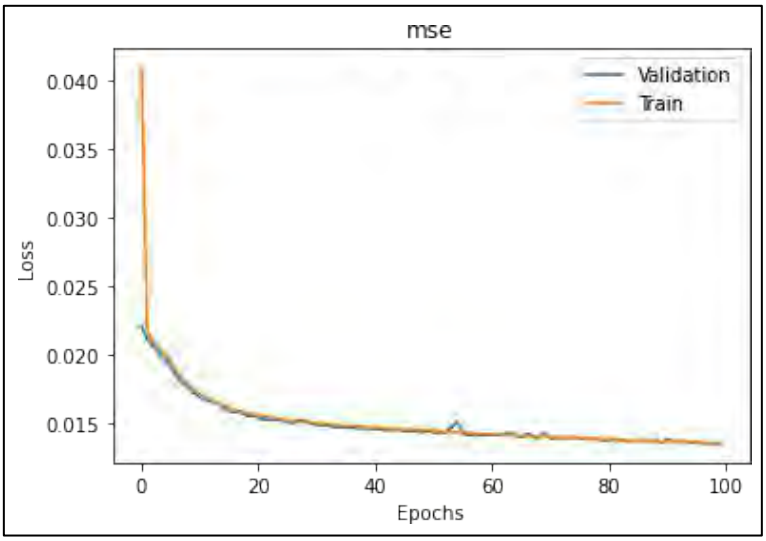

Figure 23. MSE loss curves for training and validation.

5.1.4.5 Test Results

The trained model was tested with the unknown 2000 test $\vec{E}_{meas}^{sct}$ datasets. Upon evaluation, the model achieved a MSE of 0.0137 for the entire testing set. The testing results are shown in Figure 24 and Figure 25.

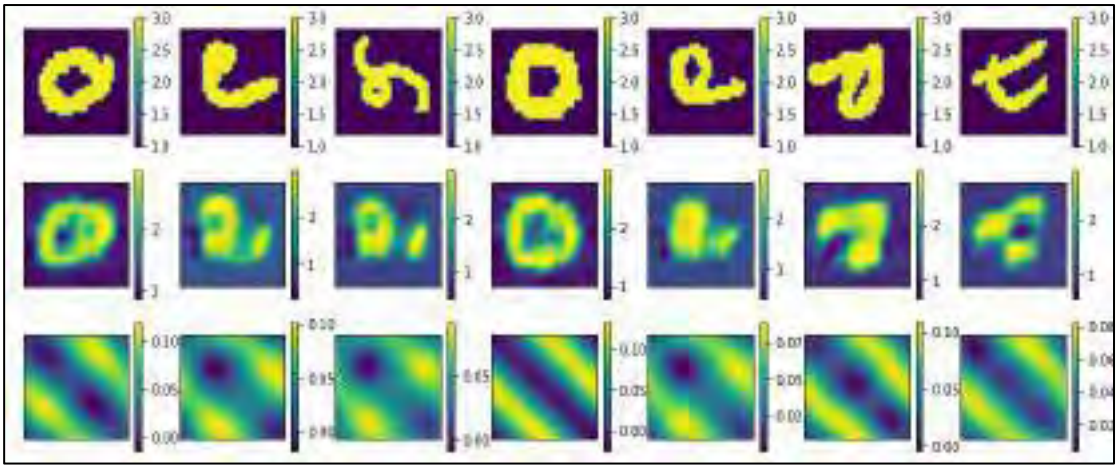

Figure 24. Testing results of the $\vec{E}_{meas}^{sct}$ -Baseline-AE model for the real component of ϵ_r.

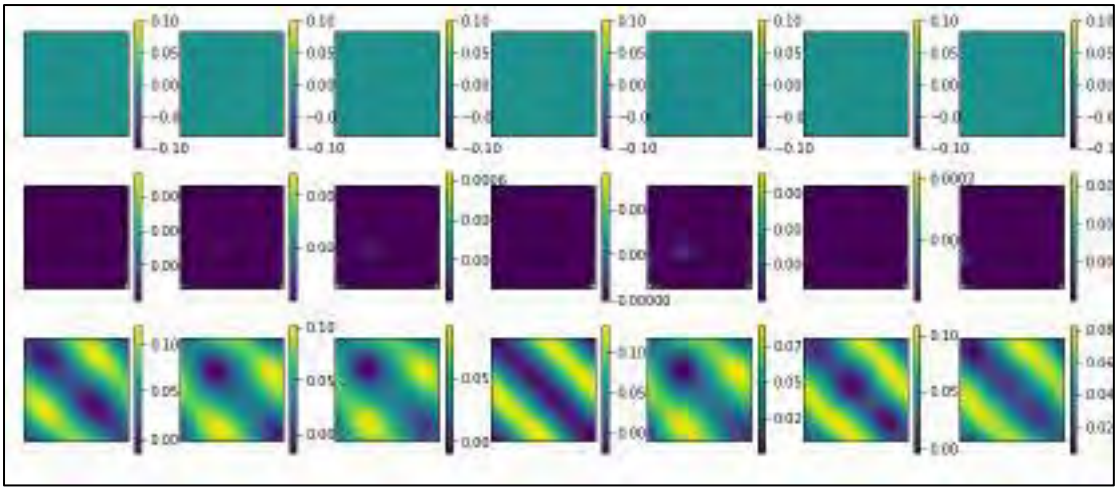

Figure 25. Testing results of the $\vec{E}_{meas}^{sct}$ -Baseline-AE model for the imaginary component of ϵ_r.

5.1.5 $\vec{E}_{meas}^{sct}$-DCEDnet Model

5.1.5.1 Training Results

Upon successful training of the model for 100 epochs, the training results are shown in Figure 26 and Figure 27.

Moreover, the MSE losses achieved for training and validation are, respectively, 0.0061 and 0.0091. The loss curves for training and validation are shown in Figure 28.

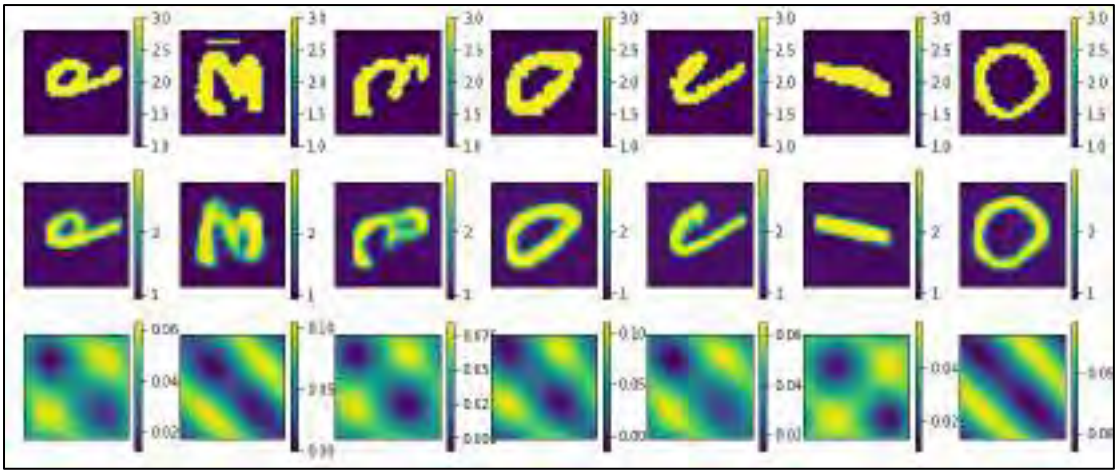

Figure 26. Training results of the E^{sct}_{meas} -DCEDnet model for the real component of ϵ_r.

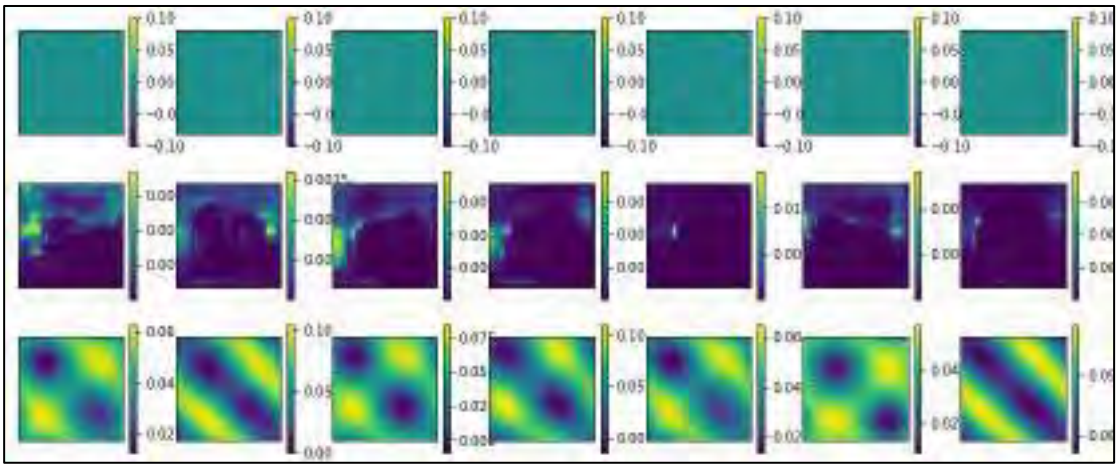

Figure 27. Training results of the E^{sct}_{meas} -DCEDnet model for the imaginary component of ϵ_r.

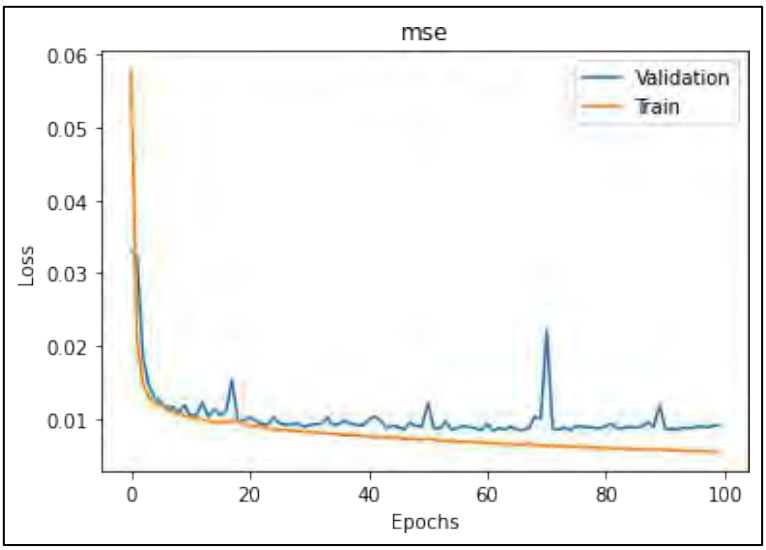

Figure 28. MSE loss curves for training and validation.

5.1.5.2 Test Results

The trained model was tested with the unknown 2000 test $\vec{E}_{meas}^{sct}$ datasets. Upon evaluation, the model achieved a MSE of 0.0094 for the entire testing set. The testing results are shown in Figure 29 and Figure 30.

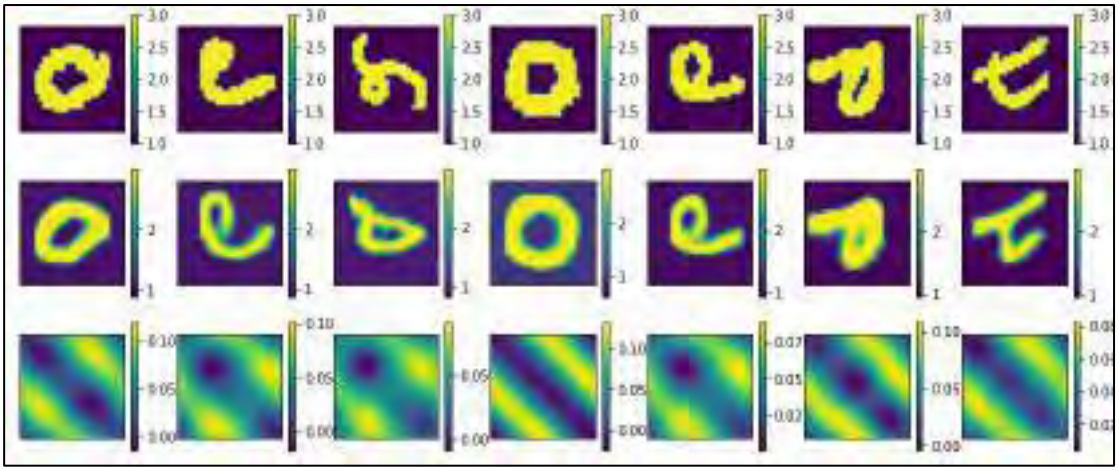

Figure 29. Testing results of $\vec{E}_{meas}^{sct}$ -DCEDnet model for the real component of ϵ_r.

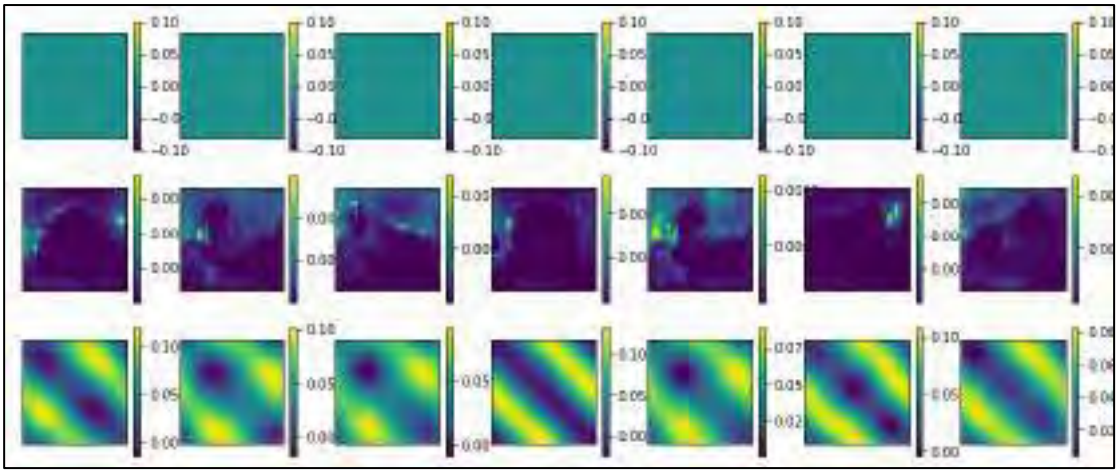

Figure 30. Testing results of the $\vec{E}_{meas}^{sct}$ -DCEDnet model for the imaginary component of ϵ_r.

5.1.5.3 Results Comparison

The reconstructions results estimated by the DNN models for different types of complex-input are compared against each other. Additionally, the DNN results are compared against the ground truth and the results calculated by the conventional inversion algorithm the contrast source inversion (CSI).

The ground truth and the results for the different reconstruction methods are shown in Figure 31 and Figure 32, respectively, for the real and imaginary components of the complex relative permittivity.

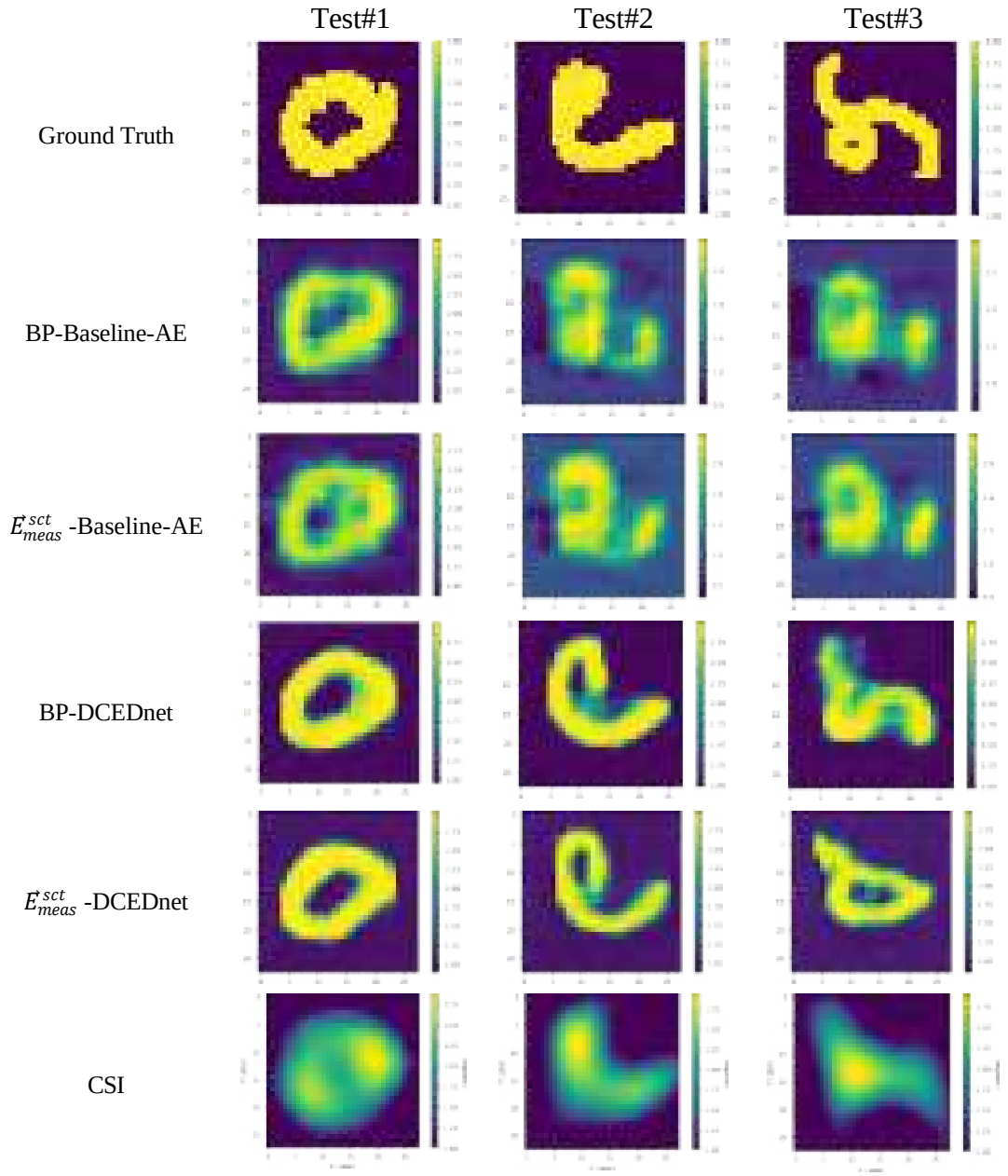

Figure 31. The reconstruction results of Baseline-AE, DCEDnet and CSI for the real component of ϵ_r in comparison with the ground truth.

5.1.5.3.1 Baseline-AE and DCEDnet Comparison

When comparing the Baseline-AE with DCEDnet, the DCEDnet reconstruction results for the real component of ϵ_r are clearly better than the Baseline-AE model, as shown in Figure 31. This is mainly due to the increased depth of the DCEDnet, which has considerably more hidden layers leading to better learning and performance.

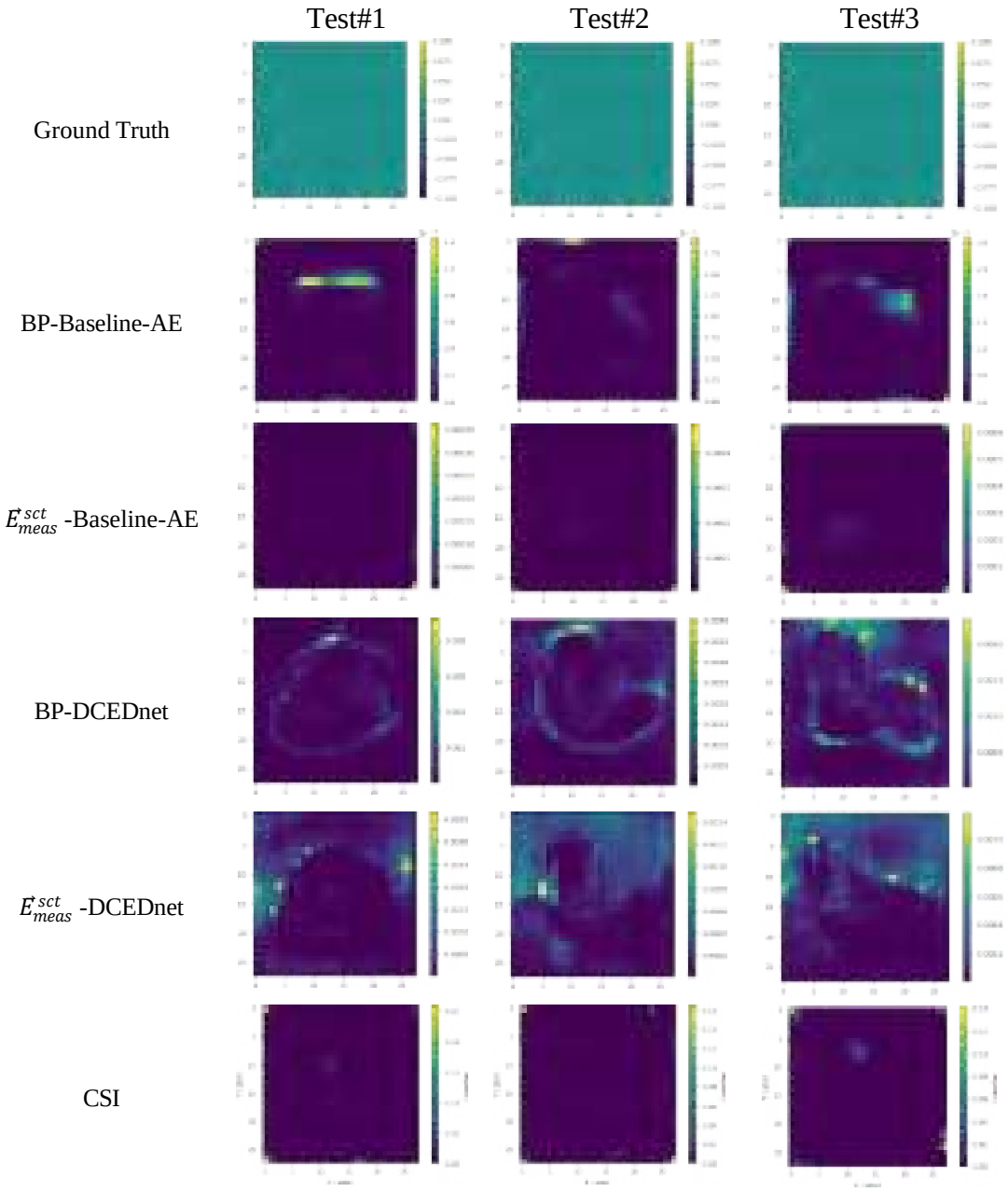

Figure 32. The reconstruction results of Baseline-AE, DCEDnet and CSI for the imaginary component of ϵ_r in comparison with the ground truth.

5.1.5.3.2 BP-DCEDnet and $\vec{E}_{meas}^{sct}$--DCEDnet Comparison

The reconstructions of the DCEDnet with both the BP and $\vec{E}_{meas}^{sct}$ complex-inputs are considerably of similar quality with the BP-DCEDnet having a slight edge over its counterpart $\vec{E}_{meas}^{sct}$-DCEDnet. This can be visualized especially from Test# 3 result in Figure 31. The results of both these models in this test case tend to deviate from the ground truth considerably, however, the BP-DCEDnet reconstruction seems

to be closer to the ground truth than the reconstruction of $\vec{E}^{sct}_{meas}$-DCEDnet whose result clearly misses the ground truth target by a good margin.

5.1.5.3.3 DCEDnet and CSI Comparison

The DCEDnet models produce reconstructions of much higher precision and quality than the CSI, as shown in Figure 31. All test cases 1, 2, and 3 verify this point. In addition to higher quality, the computational time for the DCEDnet results was significantly much less than for CSI.

5.1.5.3.4 Imaginary component of ϵ_r reconstructions

Since configuration 1 is of lossless targets, there is no imaginary component for the ϵ_r as shown in Figure 32. Thereby, there is no valid comparison applicable in this section.

5.1.5.3.5 Mean Squared Error - MSE

The normalized MSE between the ground truth and reconstructions for the DNN models are shown in Table 1. As it can be seen, the BP-DCEDnet has the smallest MSE values for all the tests.

Table 1. Normalized MSE between Ground Truth and Reconstructions for different models

Test	MSE			
	Baseline-AE		DCEDnet	
	BP	E^s_{meas}	BP	E^s_{meas}
#1	0.0123	0.0122	0.0099	0.0090
#2	0.0184	0.0170	0.0116	0.0131
#3	0.0247	0.0229	0.0116	0.0231
MNIST (2000)	0.0140	0.0137	0.0108	0.0094

5.2 Configuration 2: Lossy Targets with Static Relative Permittivity

In this configuration setup, lossy targets with static permittivity have been implemented.

5.2.1 Configuration of the Forward Problem

A lossy target is positioned inside a square imaging domain D with side-length of 13 cm. The imaging domain is centered in the middle of the microwave imaging system and is illuminated by 24 transmitters at a frequency of 3 GHz. For each transmitter, the scattered data are collected at 24 receivers. The transmitting and receiving points are co-located and evenly spaced on a circular surface S of radius of

13 cm. The problem domain is bounded and enclosed by a circular absorbing boundary with a radius of 22 cm.

Since deep CNNs training requires a large number of input samples, the first 10000 MNIST handwritten digits were selected as targets. The scattered data are obtained for these 10000 MNIST digit-like targets that are assigned a complex relative permittivity $\epsilon_r = 3 - j\ 0.1$. The target is surrounded in a homogeneous lossless background medium with relative permittivity $\epsilon_b = 1$. Both the input and the ground truth image pairs are interpolated into square grids of 28×28.

5.2.2 Training Details

For this configuration setup, two DNN architectures: the Baseline-AE and DCEDnet were trained and tested with only the BP input type. As it was clearly observed from configuration 1 results, that BP-DCEDnet reconstructions were of much better quality than the $\vec{E}^{sct}_{\text{meas}}$-DCEDnet, this configuration was trained and tested only with BP estimates input type.

From the 10000 pairs generated using the MNIST targets, 7000 pairs were selected as training data, 1000 for validation, and 2000 as testing data. The input data for training and validation were the BP estimates, while the corresponding complex ground truth pairs served as the output data for training and validation labels in the encoder-decoder architecture of both the DNNs.

The loss function used is the standard mean-square error (MSE). Furthermore, the Adaptive moment estimation (Adam) optimizer is used for optimizing the MSE loss function. As for the hyperparameters, the model is trained for 100 epochs with a batch size of 32.

The code is developed with Python 3 in Google Colab and the model is trained and tested using the T4 GPU provided by Google Colab.

In order to quantitatively evaluate the reconstruction accuracy, the MSE in Equation (5.1) is calculated between the ground truth and the reconstruction for all the numerical samples.

5.2.3 Results

The results obtained from the two DNNs are presented for the two forward problem configurations and using the BP input. Furthermore, the forward problem configuration and type of complex-input for DNN are indicated in the section's heading.

Moreover, in the next sections, for each figure with colormaps, the first row shows the ground truth, the middle row is the reconstructed image by the respective DNN model, and the last row is the input.

5.2.4 BP-Baseline-AE Model

5.2.4.1 Training Results

Upon successful training of the model for 100 epochs, the training results are shown in Figure 33 and Figure 34.

Furthermore, the MSE loss achieved for both training and validation is 0.0107. The loss curves for training and validation are given in Figure 35.

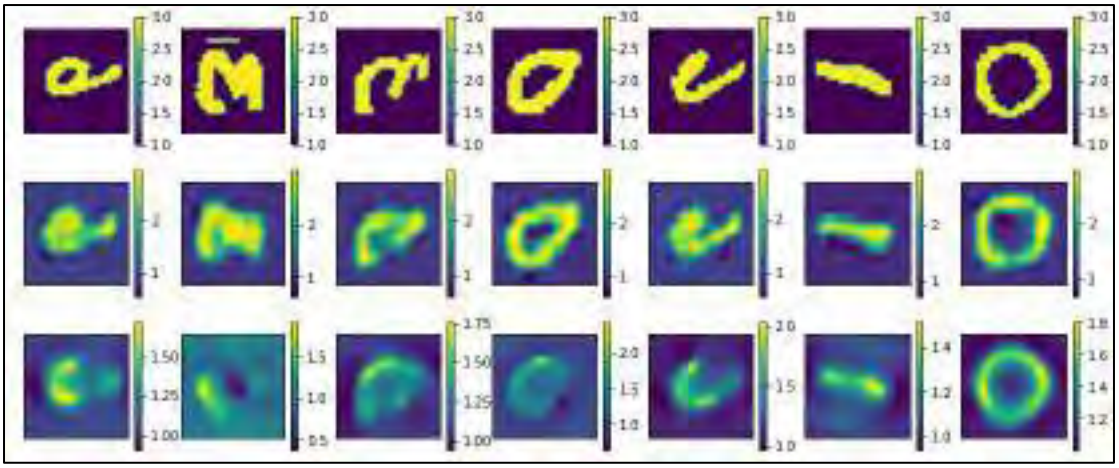

Figure 33. Training results of the BP-Baseline-AE model for the real component of ϵ_r.

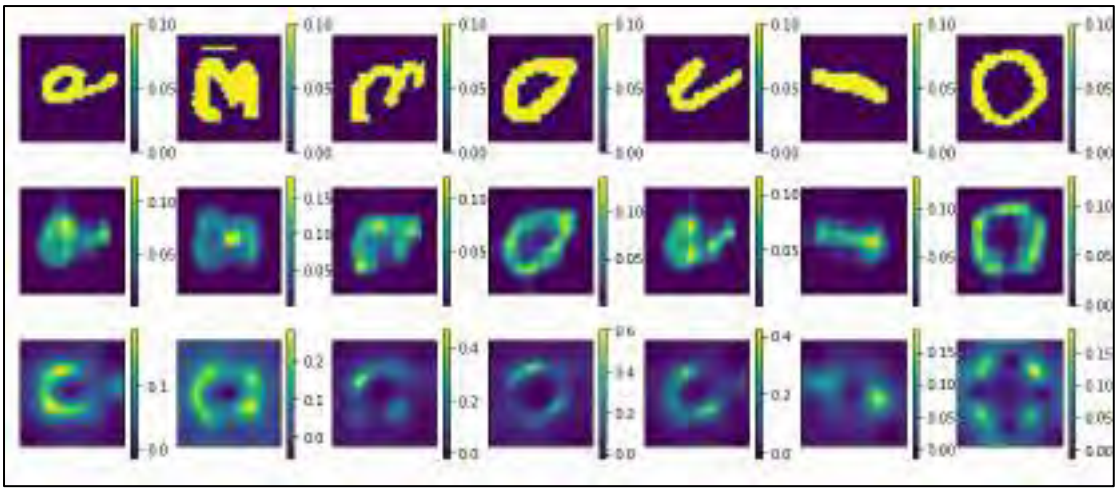

Figure 34. Training results of the BP-Baseline-AE model for the imaginary component of ϵ_r.

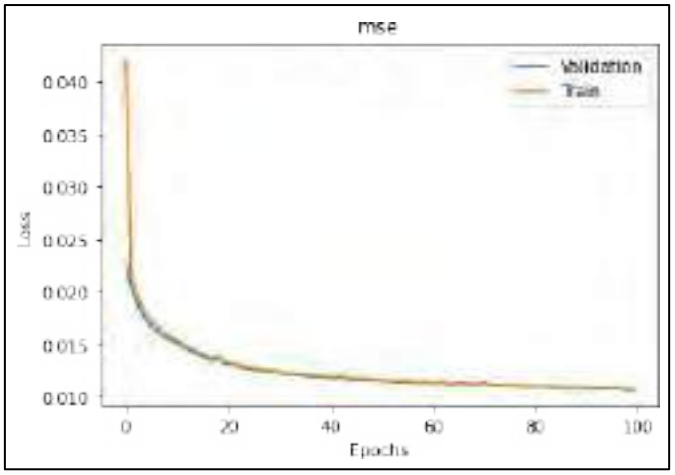

Figure 35. MSE loss curves for training and validation.

5.2.4.2 Test Results

The trained model was tested with the unknown 2000 test BP image pairs. Upon evaluation, the model achieved a MSE of 0.0109 for the entire testing set. The testing results are shown in Figure 36 and Figure 37.

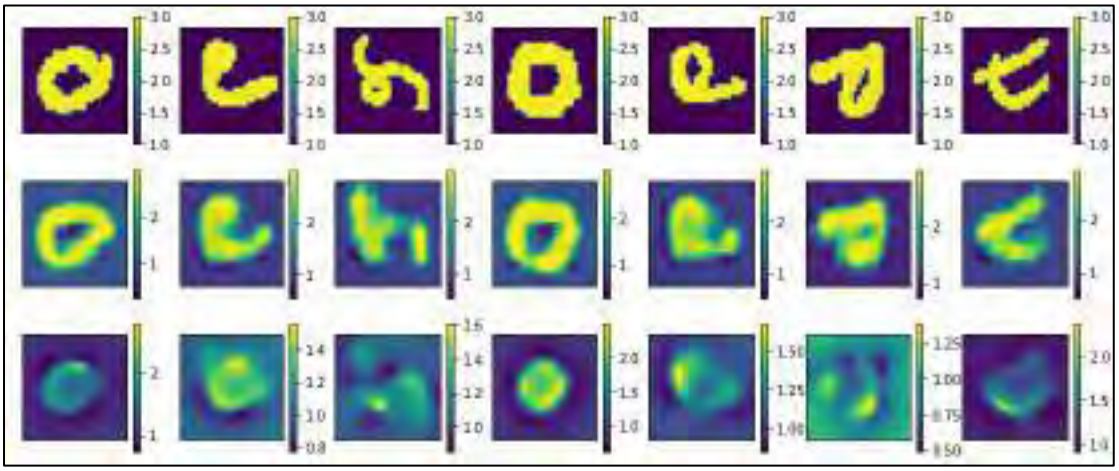

Figure 36. Testing results of the BP-Baseline-AE model for the real component of ϵ_r.

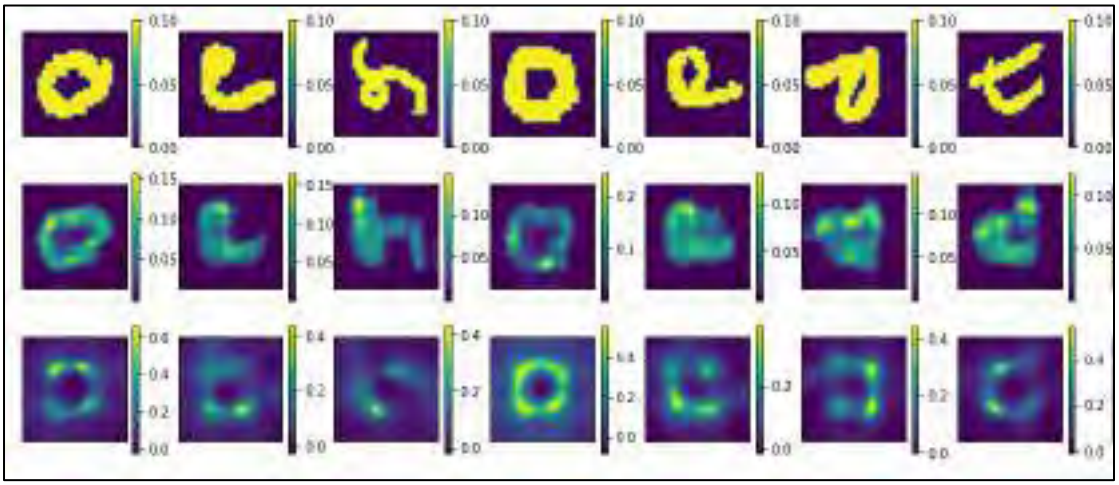

Figure 37. Testing results of the BP-Baseline-AE model for the imaginary component of ϵ_r.

5.2.5 BP-DCEDnet Model

5.2.5.1 Training Results

Upon successful training of the model for 100 epochs, the training results are shown in Figure 38 and Figure 39.

Moreover, the MSE losses achieved for training and validation, respectively, are 0.0029 and 0.0054. The loss curves for training and validation are given in Figure 40.

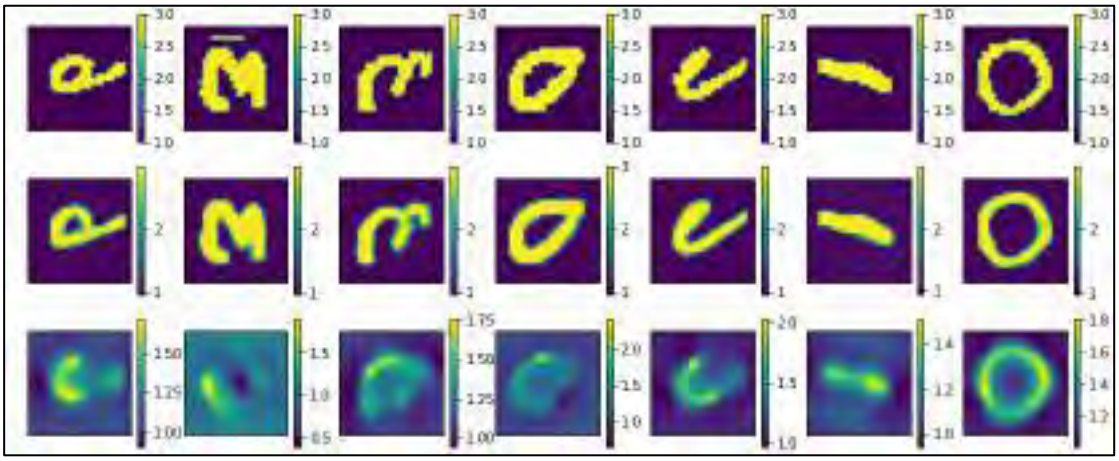

Figure 38. Training results of the BP-DCEDnet model for the real component of ϵ_r.

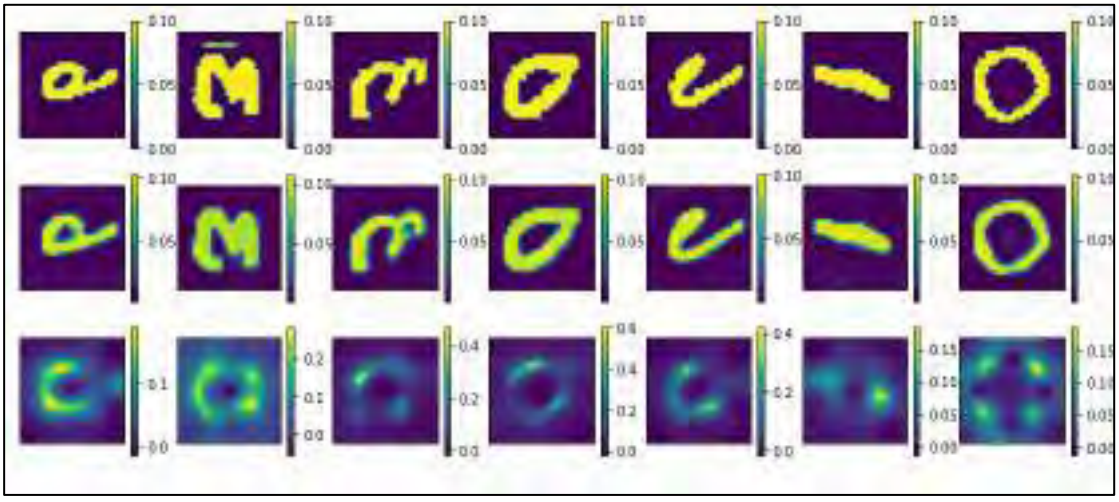

Figure 39. Training results of the BP-DCEDnet model for the imaginary component of ϵ_r.

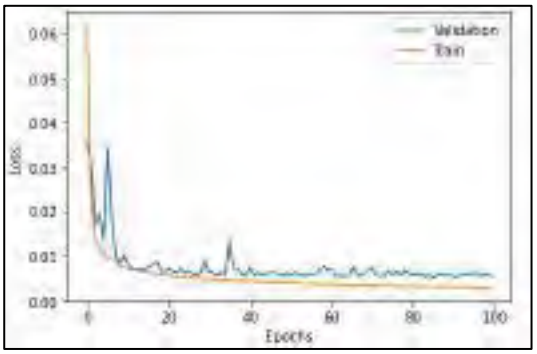

Figure 40. MSE loss curves for training and validation.

5.2.5.2 Test Results

The trained model was tested with the unknown 2000 test BP image pairs. Upon evaluation, the model achieved a MSE of 0.0057 for the entire testing set. The testing results are shown in Figure 41 and Figure 42.

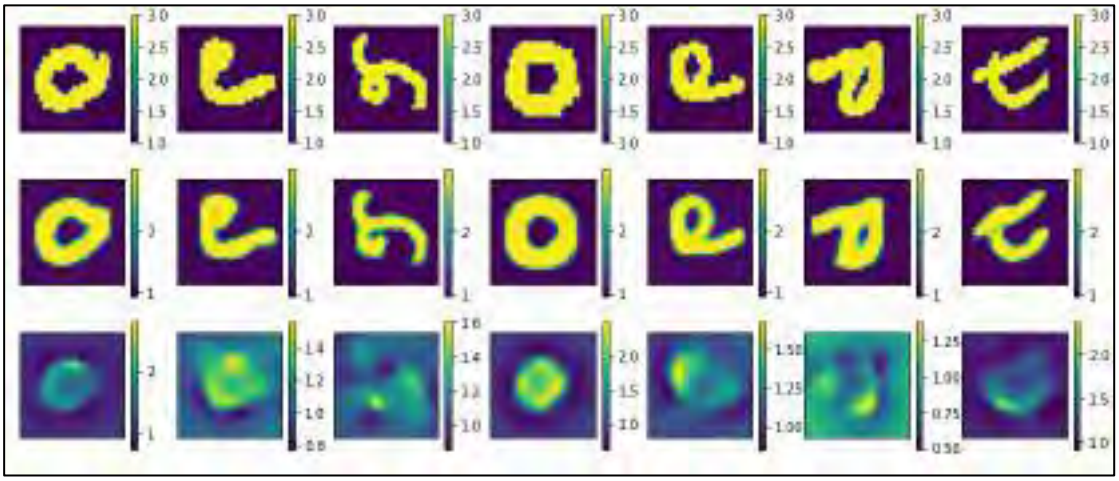

Figure 41. Testing results of the BP-DCEDnet model for the real component of ϵ_r.

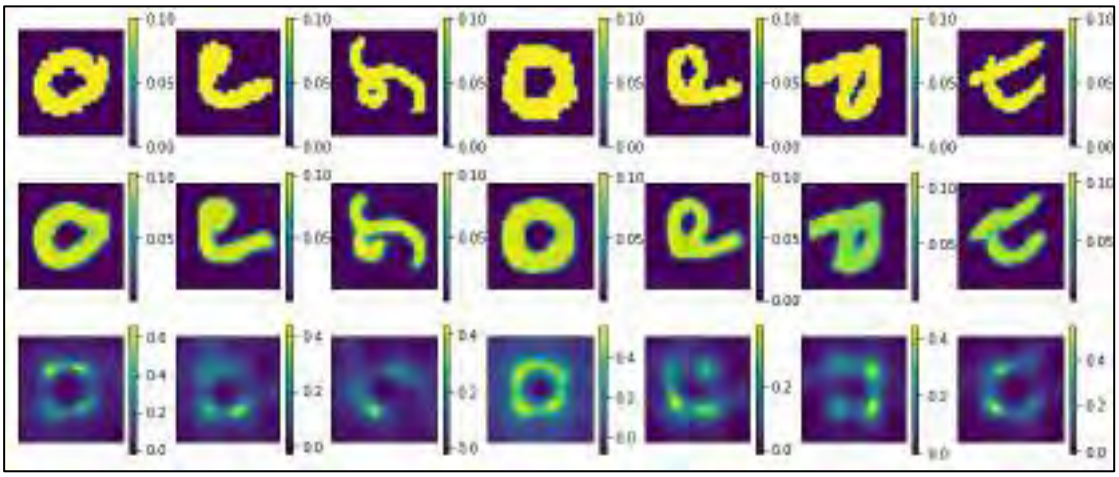

Figure 42. Testing results of the BP-DCEDnet model for the imaginary component of ϵ_r.

5.2.5.3 Results Comparison

The reconstructions results estimated by the DNN models for the complex-input BP estimates are compared against each other. Additionally, the DNN results are compared against the ground truth and the results calculated by the conventional inversion algorithm the contrast source inversion (CSI). The ground truth and the results for the different reconstruction methods are shown in Figure 43 and Figure 44, respectively, for the real and imaginary components of the complex relative permittivity.

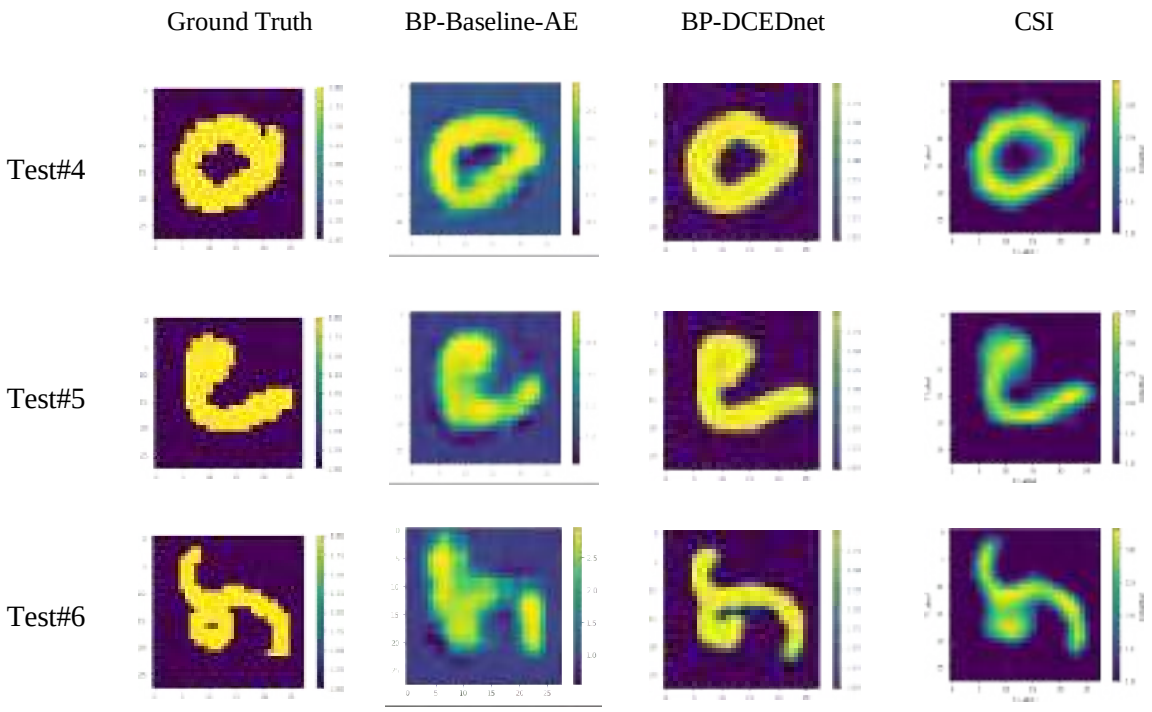

Figure 43. The reconstruction results of Baseline-AE, DCEDnet and CSI for the real component of ϵ_r in comparison with the ground truth.

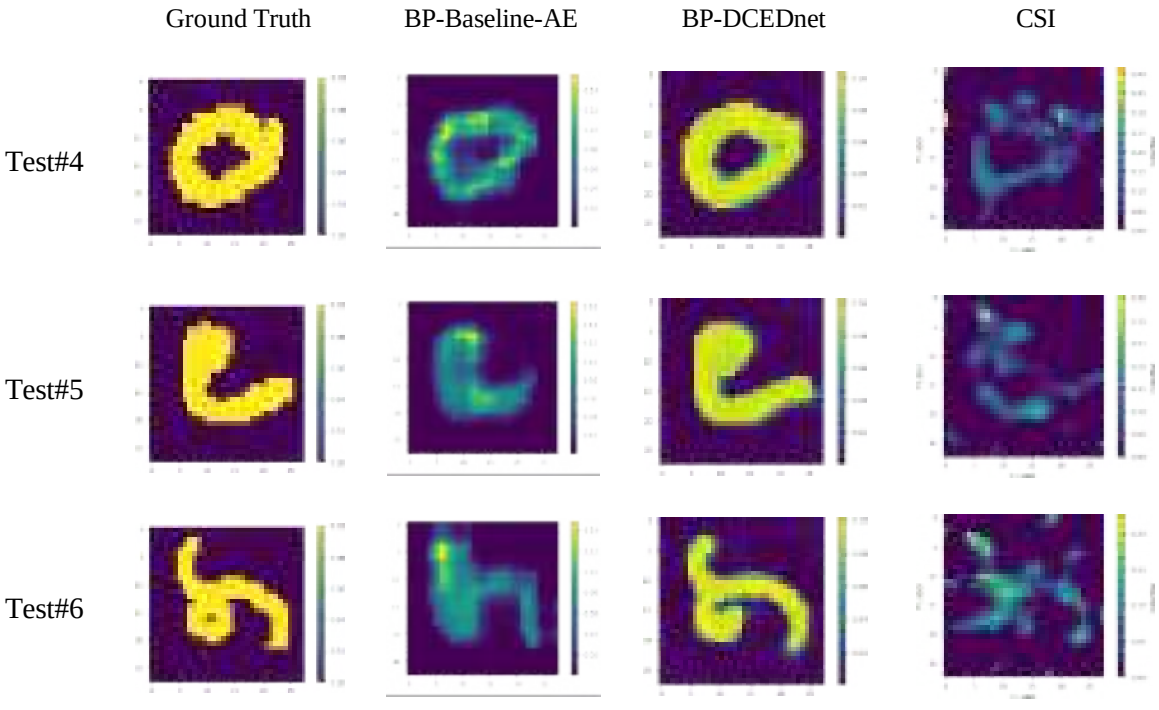

Figure 44. The reconstruction results of Baseline-AE, DCEDnet and CSI for the imaginary component of ϵ_r in comparison with the ground truth

Like configuration 1, the BP-DCEDnet reconstruction results for the real component of ϵ_r are clearly better than the BP-Baseline-AE model, as shown in Figure 43. For the imaginary component of ϵ_r, the BP-DCEDnet reconstruction results are clearly better than the BP-Baseline-AE model as can be seen in Figure 44.

Unlike in configuration 1 results, the CSI reconstructions are more accurate and closer to the ground truth in configuration 2 reconstructions. However, comparing with the BP-DCEDnet results, the BP-DCEDnet reconstructions for the real component of ϵ_r is closer to the ground truth than the CSI results. For the imaginary component of ϵ_r, the BP-DCEDnet reconstruction results are of much higher precision than the conventional CSI. Though the BP-DCEDnet had only a slightly superior precision than the CSI in the real component reconstructions, the difference in the imaginary component is much larger with the BP-DCEDnet clearly outperforming the CSI.

5.2.5.3.1 Mean Squared Error - MSE

The normalized MSE between the ground truth and reconstructions for the DNN models are shown in Table 2. As it can be seen, the BP-DCEDnet has the smallest MSE values for all the tests.

Table 2. Normalized MSE between Ground Truth and Reconstructions for different models

Test	MSE	
	Baseline-AE	**DCEDnet**
	BP	**BP**
#4	0.0108	0.0053
#5	0.0111	0.0051
#6	0.0164	0.0079
MNIST (2000)	0.0109	0.0057

5.3 Configuration 3: Lossy Targets with Relative Permittivity of Low Dynamic Range

In this configuration setup, lossy targets with relative permittivity of low dynamic range (LDR) have been implemented.

5.3.1 Configuration of the Forward Problem

The target is positioned inside a square imaging domain D with side-length of 17 cm. The imaging domain is centered in the middle of the microwave imaging system and is illuminated by 24 transmitters at a frequency of 3 GHz. For each transmitter, the scattered data are collected at 24 receivers. The transmitting and receiving points are

co-located and evenly spaced on a circular surface S of radius of 13 cm. The problem domain is bounded and enclosed by a circular absorbing boundary with a radius of 18 cm.

Since deep CNNs training requires many input samples, the first 10000 MNIST handwritten digits are selected as targets. The scattered data are obtained for these 10000 MNIST digit-like targets in the imaging domain *D* that are randomly assigned a complex relative permittivity ϵ_r of low dynamic range (LDR). The LDR for the real component is from 1 to 4 and the imaginary component is from 0 to 1. The target is surrounded in a homogeneous lossless background medium with relative permittivity $\epsilon_b = 1$. Both the input and the ground truth image pairs are interpolated into square grids of 128×128.

5.3.2 Training Details

For this configuration setup, the four DNN architectures: the DCEDnet, Unet, Unet-Lite and ATTN-Unet are trained and tested with the BP input type initially. After cross-testing the trained models, the best model from the four is chosen to be trained and tested with the ITER10 input type to compare the results with its corresponding BP trained model.

Similar to configurations 1 and 2, from the 10000 pairs generated using the MNIST targets, 7000 pairs are selected as training data, 1000 for validation, and 2000 as testing data. The input data for training and validation are the BP estimates, while the corresponding complex ground truth pairs served as the output data for training and validation labels for the DNNs.

The loss function used is the standard mean-square error (MSE). Furthermore, the Adaptive moment estimation (Adam) optimizer is used for optimizing the MSE loss function. Early stopping with a patience parameter of 10 is implemented during the training. The BP-DCEDnet with a batch size of 32 effectively trained for 58 epochs that took about 0.75 hours, while BP-Unet and BP-Unet-Lite both with batch size 8 trained for 41 and 64 epochs effectively that took about 14.6 and 6.5 hours respectively. Further, the BP-ATTN-Unet trained effectively for 24 epochs with a batch size of 4, which took about 5.45 hours.

The code is developed using Python 3.7 within the Conda environment in the Spyder IDE version 5.3.3. The machine for training and testing the models is equipped

with an Intel(R) Xeon(R) E-2124 CPU operating at 3.30 GHz, equipped with 32GB of RAM and an NVIDIA Quadro P620 GPU with 2GB of VRAM.

5.3.3 Synthetic Data Results

After the models are trained, they are tested both within the MNIST database as well as with cross-database samples that include synthetic complex profiles. In the cross-database testing, the models are tested for robustness against noise as well as permittivity range. To quantitatively evaluate the reconstruction accuracy, the MSE in Equation (5.1) is calculated between the ground truth and the reconstruction for all the numerical samples.

5.3.3.1 Within-Database Test

All the four trained models with BP input are first tested with 2000 MNIST testing data. Test#7 and Test#8 in Figure 44 and Figure 45 show the reconstruction results of two test MNIST targets, while their MSEs for the real, imaginary and combined parts are shown in Table 3, Table 4, and Table 5 respectively.

From the figures and tables, the first clear observation that can be made, much like in configurations 1 and 2, is that the imaginary reconstructions of all the four DNN models outperform the FEMCSI results. Additionally, the DNN reconstructions for the real component of ϵ_r are closer to the ground truth than the FEMCSI results.

Secondly, the reconstructions of BP-DCEDnet are of lower quality than the Unet based model reconstructions. This is self-explanatory for the fact that Unet is much deeper with more convolutional layers and trainable parameters than the DCEDnet, which leads to better training and reconstructions.

When comparing the three Unet based models, the reconstructions of Unet and ATTN-Unet are slightly better than the Unet-Lite. As for the Unets with and without attention, the results are very much similar and both are close to the ground truth.

Moreover, it significantly took much lesser computational time to obtain the DNN results than the FEMCSI. It only took about 10 seconds to obtain a single reconstruction in the testing phase. In detail, the BP took about 8 seconds, while the DNN took about 2 seconds. On the other hand, running the FEMCSI for 300 iterations to reconstruct a single testing sample took about 56 seconds.

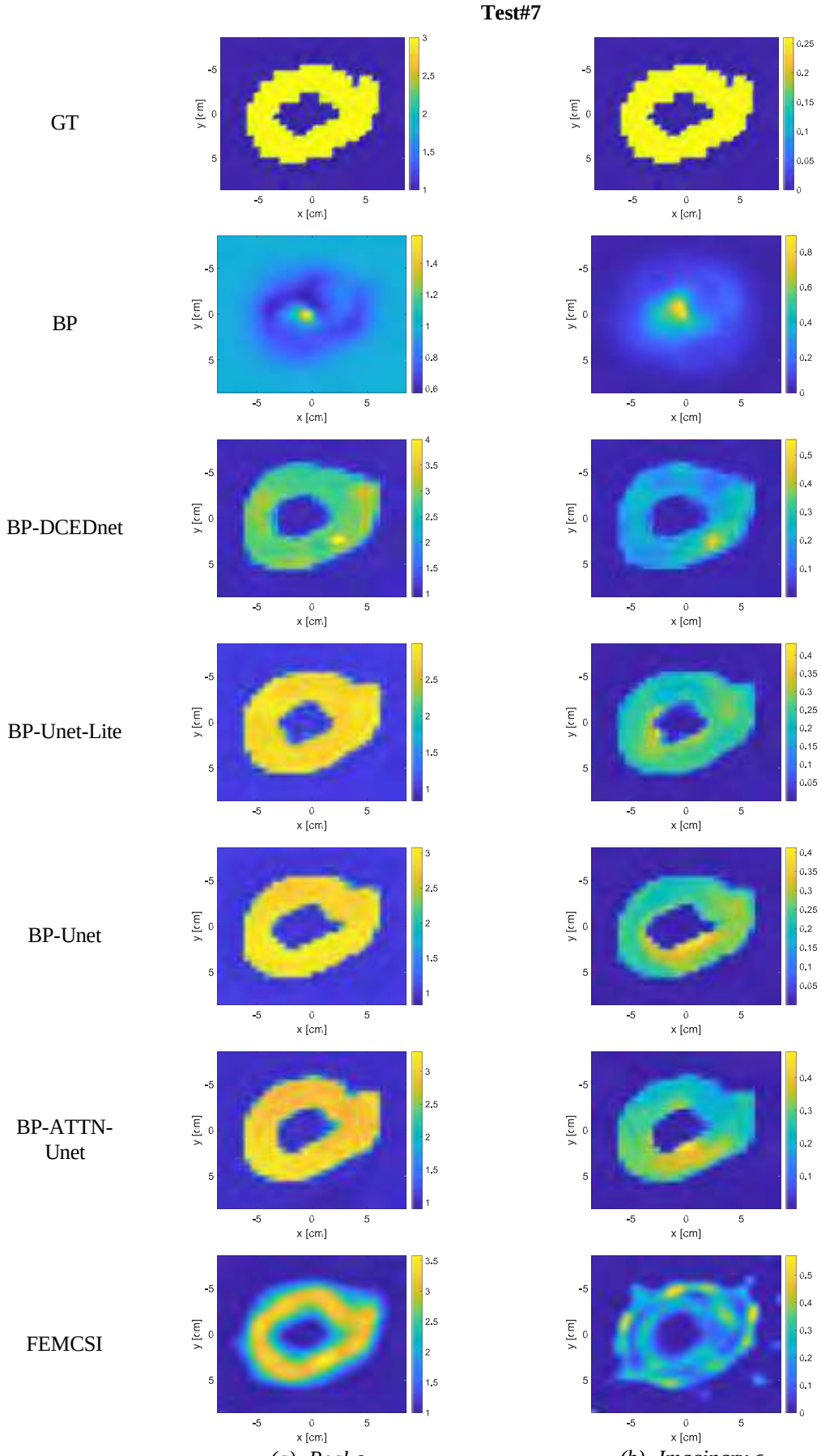

(a) Real ϵ_r *(b) Imaginary ϵ_r*

Figure 45. Reconstruction results of (a) real and (b) imaginary components of ϵ_r of Test#7.

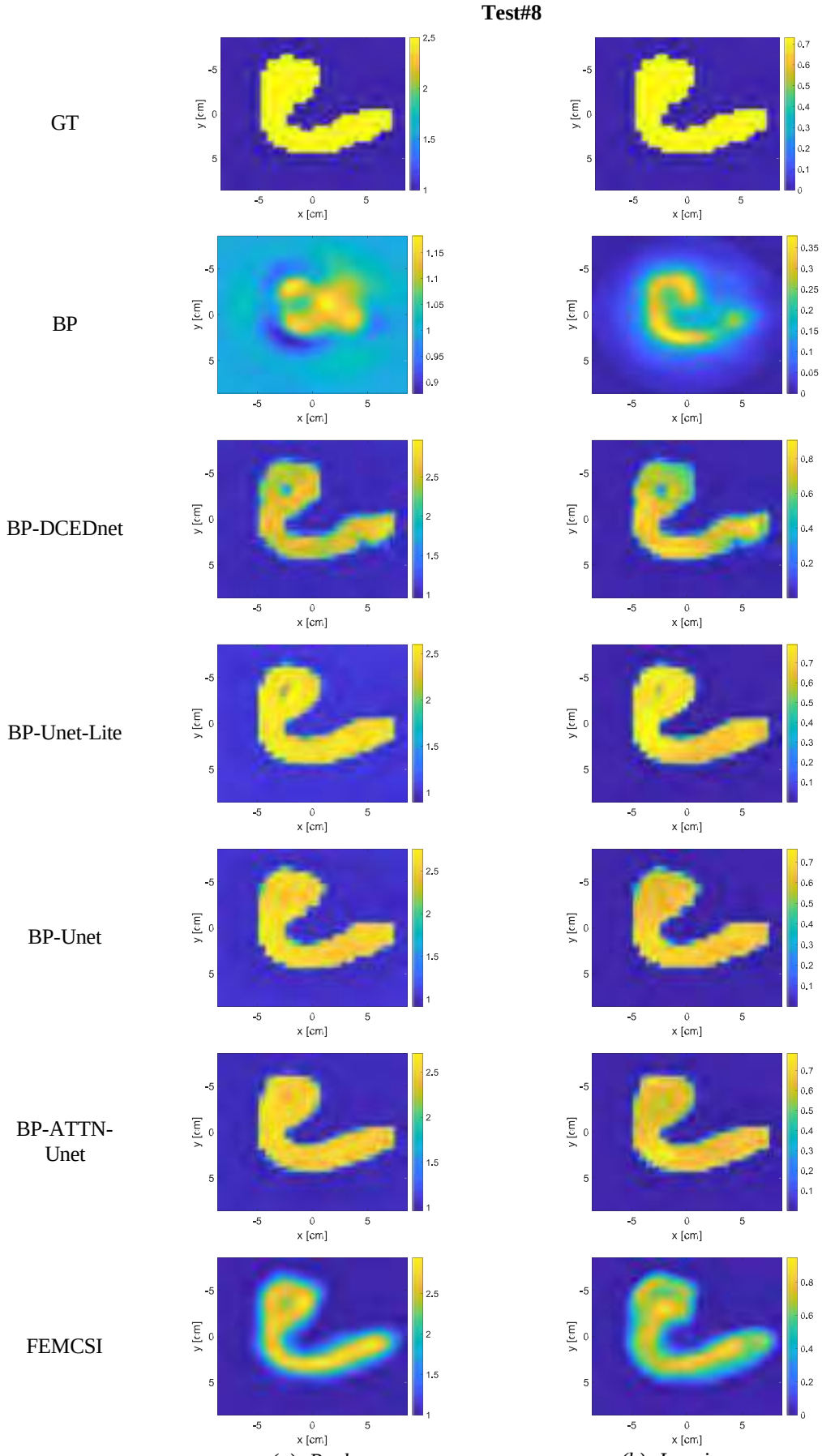

(a) Real ϵ_r *(b) Imaginary ϵ_r*

Figure 46. Reconstruction results of (a) real and (b) imaginary components of ϵ_r of Test#8.

Table 3. MSE between Ground Truth and Reconstructions of the real ϵ_r for Test#7-Test#8

Method	MSE-Real	
	Test#7	Test#8
BP-DCEDnet	0.1526	0.0322
BP-Unet-Lite	0.0917	0.0193
BP-Unet	0.0812	0.0190
BP-ATTN-Unet	0.1039	0.0256
FEMCSI	0.0984	0.0442

Table 4. MSE between Ground Truth and Reconstructions of the imaginary ϵ_r for Test#7-Test#8

Method	MSE-Imaginary	
	Test#7	Test#8
BP-DCEDnet	0.0031	0.0082
BP-Unet-Lite	0.0021	0.0049
BP-Unet	0.0016	0.0059
BP-ATTN-Unet	0.0031	0.0072
FEMCSI	0.0063	0.0107

Table 5. MSE between Ground Truth and Reconstructions for the ϵ_r for Test#7-Test#8

Method	MSE	
	Test#7	Test#8
BP-DCEDnet	0.0778	0.0202
BP-Unet-Lite	0.0469	0.0121
BP-Unet	0.0414	0.0125
BP-ATTN-Unet	0.0535	0.0164
FEMCSI	0.0524	0.0275

5.3.3.2 Cross-Database Test

In order to validate the generalization capability of the trained DNN models, more challenging complex profiles with shapes different from training samples are created and introduced to test the models.

5.3.3.2.1 Complex Profiles

Two differently shaped complex profiles namely the 'Tilted-F' and '2-Circles' are created as shown in Figure 47 and Figure 48 respectively. The 'Tilted-F' profile is assigned a complex relative permittivity of $\epsilon_r = 3.0 - j0.1$ while for the '2-Circles', the larger circle with radius 3.5 cm is assigned a $\epsilon_r = 3.4 - j0.1$ and the smaller circle with radius 2 cm is assigned a $\epsilon_r = 2.3 - j0.4$. All the other forward problem configurations setup are kept the same. Their respective BP estimates for the DNN inputs are obtained in the same procedure that is used to obtain the BP estimates for the 10000 MNIST targets.

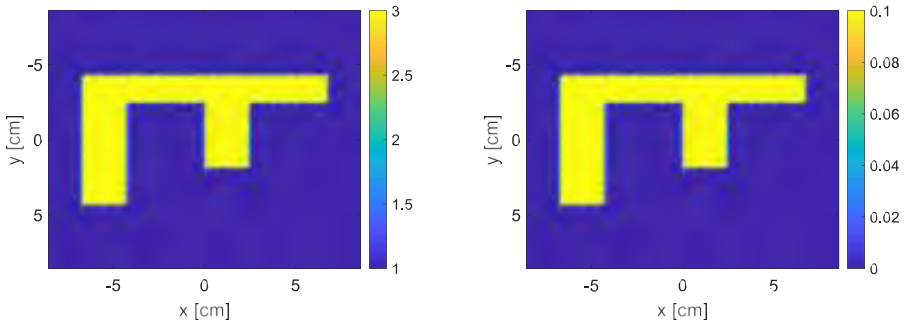

(a) GT-Real ϵ_r *(b) GT-Imaginary ϵ_r*

Figure 47. (a) Real and (b) imaginary components of the relative permittivity for the ground truth of Tilted-F.

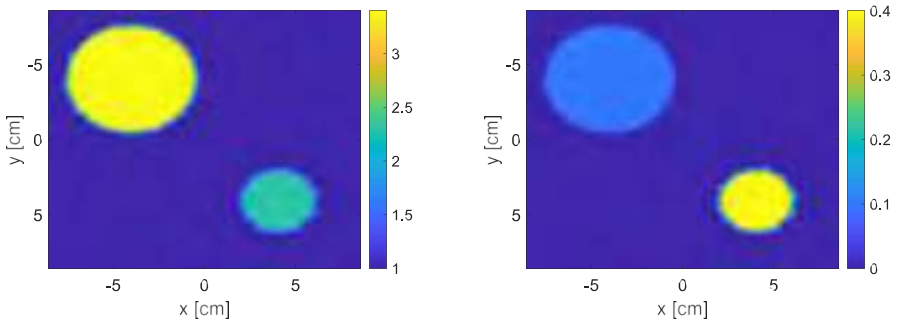

(a) GT-Real ϵ_r *(b) GT-Imaginary ϵ_r*

Figure 48. (a) Real and (b) imaginary components of the relative permittivity for the ground truth of 2-Circles.

Test#9 and Test#10 shown in Figure 49 and Figure 50 display the reconstruction test results of the two complex profiles obtained from the four trained DNN models along with their ground truths, BP inputs, and the FEMCSI results. Their MSE values are summarized in Table 6, Table 7, and Table 8. As seen with Test#1 and Test#2 results, the DCEDnet reconstructions are of lower quality when compared with the other Unet based models. Similarly, though the Unet-Lite reconstructions are better than the DCEDnet, it is still not as good as the complete Unet model. However, the results achieved by Unet-Lite are close to the ground truth and fairly acceptable considering the fact that it used much lesser memory space and training time in comparison with the Unet. So, in scenarios with memory limitation, Unet-Lite can be a suitable option that can be implemented to provide acceptable results in a much lesser training time as well. While comparing the results of Unet and ATTN-Unet, ATTN-Unet performs slightly better providing more accurate reconstructions. When compared with the FEMCSI results, the imaginary reconstruction of the ATTN-Unet in Test#9 is visibly better than that of FEMCSI. However, the same can't be said in Test#10.

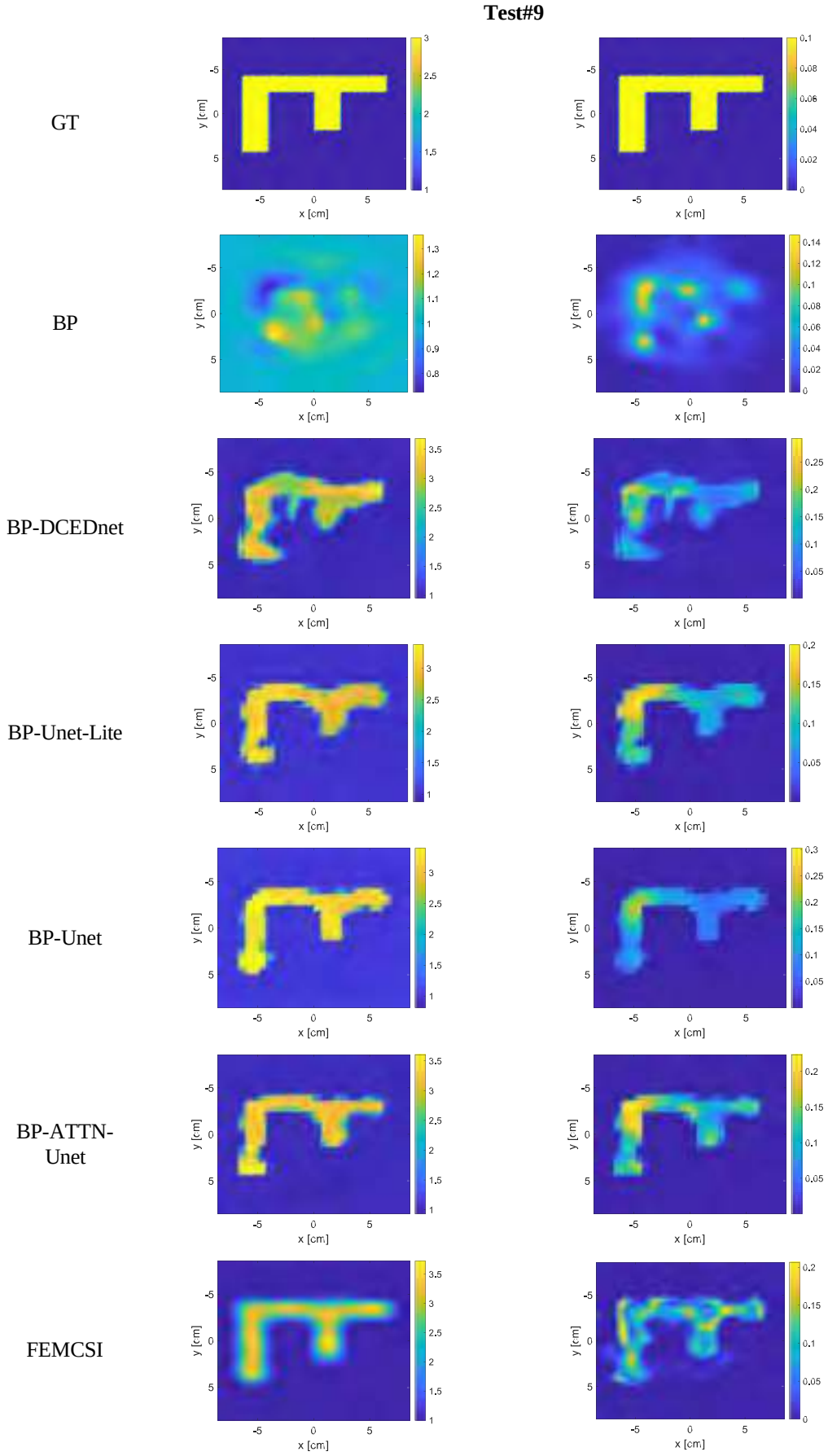

(a) Real ϵ_r *(b) Imaginary ϵ_r*

Figure 49. Reconstruction results of (a) real and (b) imaginary components of ϵ_r of Tilted-F.

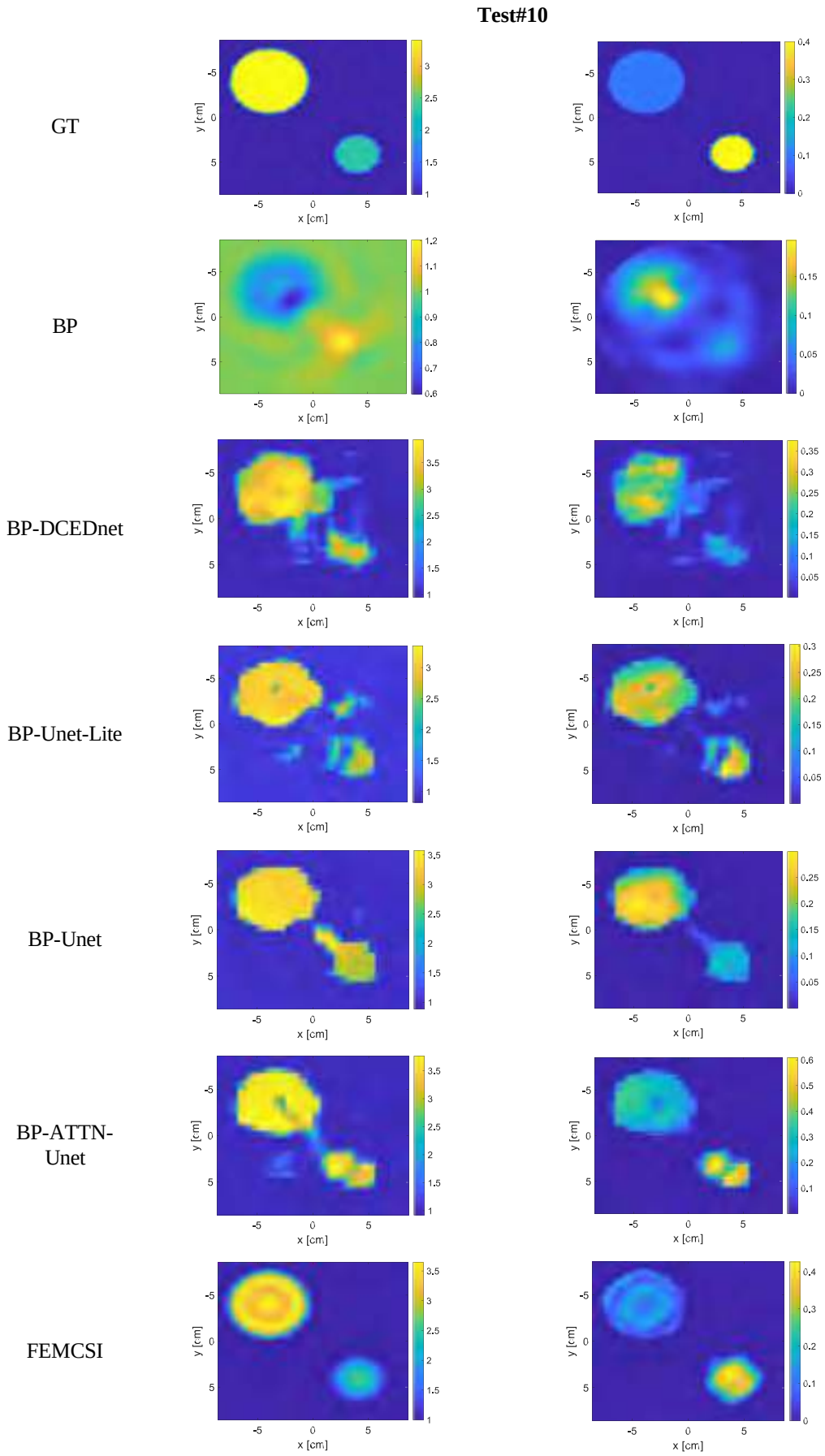

(a) Real ϵ_r *(b) Imaginary ϵ_r*

Figure 50. Reconstruction results of (a) real and (b) imaginary components of ϵ_r of 2-Circles.

Table 6. MSE between Ground Truth and Reconstructions of the real ϵ_r for Test#9-Test#10

Method	**MSE-Real**	
	Test#9	Test#10
BP-DCEDnet	0.2533	0.4347
BP-Unet-Lite	0.1565	0.2568
BP-Unet	0.1565	0.2961
BP-ATTN-Unet	0.1551	0.3224
FEMCSI	0.0491	0.0160

Table 7. MSE between Ground Truth and Reconstructions of the imaginary ϵ_r for Test#9-Test#10

Method	**MSE-Imaginary**	
	Test#9	Test#10
BP-DCEDnet	0.0010	0.0080
BP-Unet-Lite	0.0006	0.0054
BP-Unet	0.0006	0.0064
BP-ATTN-Unet	0.0006	0.0088
FEMCSI	0.0004	0.0007

Table 8. MSE between Ground Truth and Reconstructions for the ϵ_r for Test#9-Test#10

Method	**MSE**	
	Test#9	Test#10
BP-DCEDnet	0.1272	0.2213
BP-Unet-Lite	0.0785	0.1311
BP-Unet	0.0785	0.1512
BP-ATTN-Unet	0.0779	0.1656
FEMCSI	0.0248	0.0083

5.3.3.2.2 High Noise Interference

To further test the robustness of the DNNs, these trained models are tested with high-level noise interferences on the measurements. Both the complex profiles in Figure 47 and Figure 48 are tested under different noise levels. The measured scattered field data $\vec{E}^{sct}_{\text{meas}}$ of these profiles are added with 5%, 10%, 15%, 20%, 25%, and 30% white Gaussian noises respectively prior to the BP estimate generation for testing. Test#11 to Test#22 represent the tests with the different noise levels whose reconstruction results are shown from Figure 51 to Figure 62, along with their respective ground truths, BP inputs, and FEMCSI results. Table 9 to Table 14 summarizes the MSE values of these reconstructions.

From the figures and tables, the first thing that can be clearly seen is that the imaginary component of the FEMCSI degrades significantly with just 5% added noise and almost vanishes completely with 10% added noise. However, both the real and imaginary components of the DNNs reconstructions remain almost unaffected till 15% added noise. Beyond that, both DCEDnet and Unet-Lite reconstructions begin to break while Unet and ATTN-Unet still stay strong. The Unet continues to produce good results up to 20% noise beyond which its reconstructions begin to break. However, the ATTN-Unet which has a slight dip in performance at 20% noise level similar to the Unet, surprisingly rebounds back with better performance at 25% and 30% noise level. This extraordinary robustness to noise feature of the ATTN-Unet due to its attention mechanism serves as the separator making it the best performing DNN model amongst the others.

These tests demonstrate that the suggested DNN trained models retain a good degree of resilience and generalization ability under significant noise interference, with the ATTN-Unet being the best among them.

Furthermore, it significantly took much lesser computational time to obtain the DNN results than the FEMCSI. It only took about 10 seconds to obtain a single reconstruction in the testing phase. In detail, the BP took about 8 seconds, while the DNN took about 2 seconds. On the other hand, running the FEMCSI for 300 iterations to reconstruct a single testing sample took about 58 seconds.

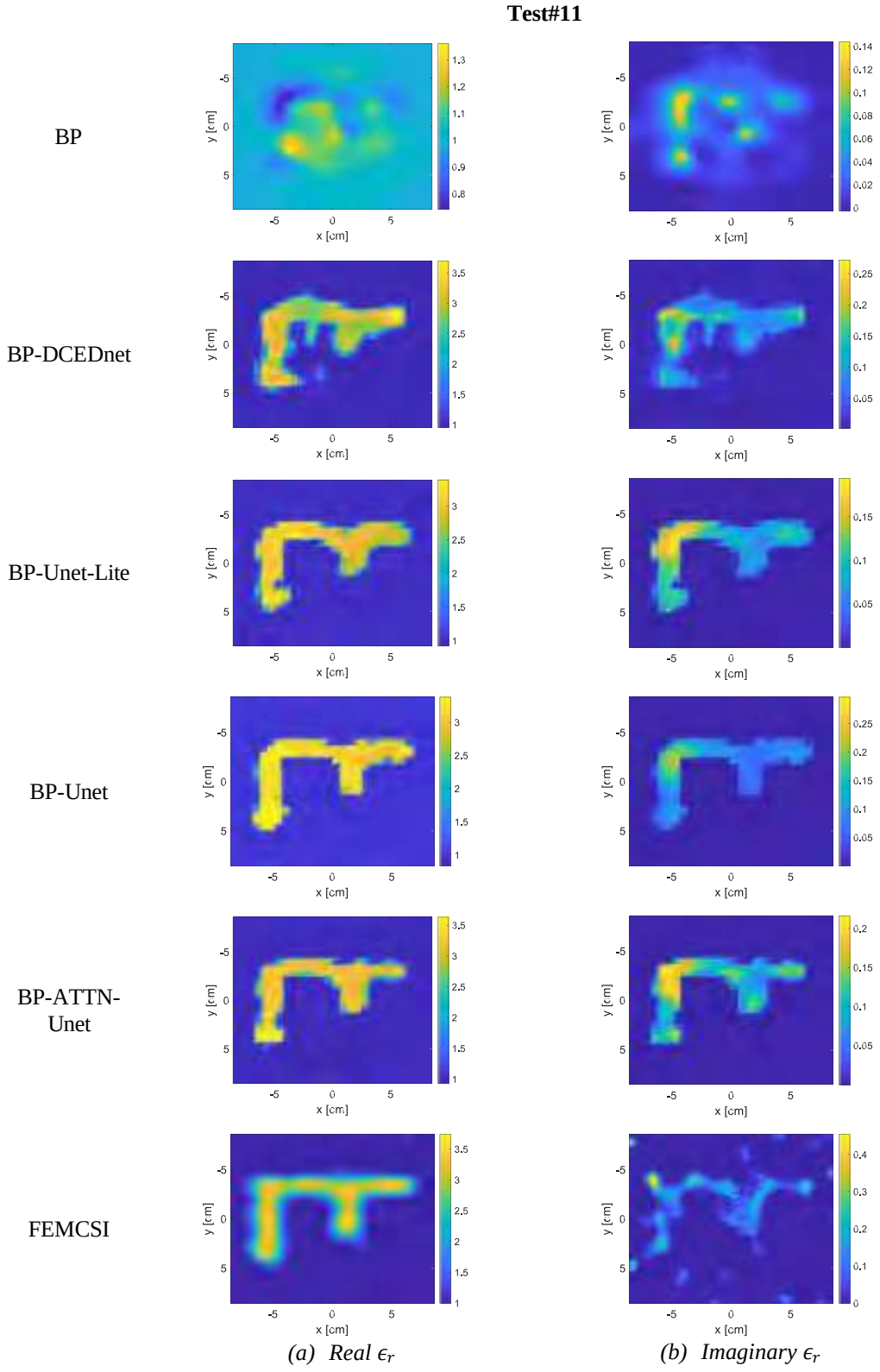

Figure 51. Reconstruction results of (a) real and (b) imaginary components of relative permittivity ϵ_r of Tilted-F with 5% added noise.

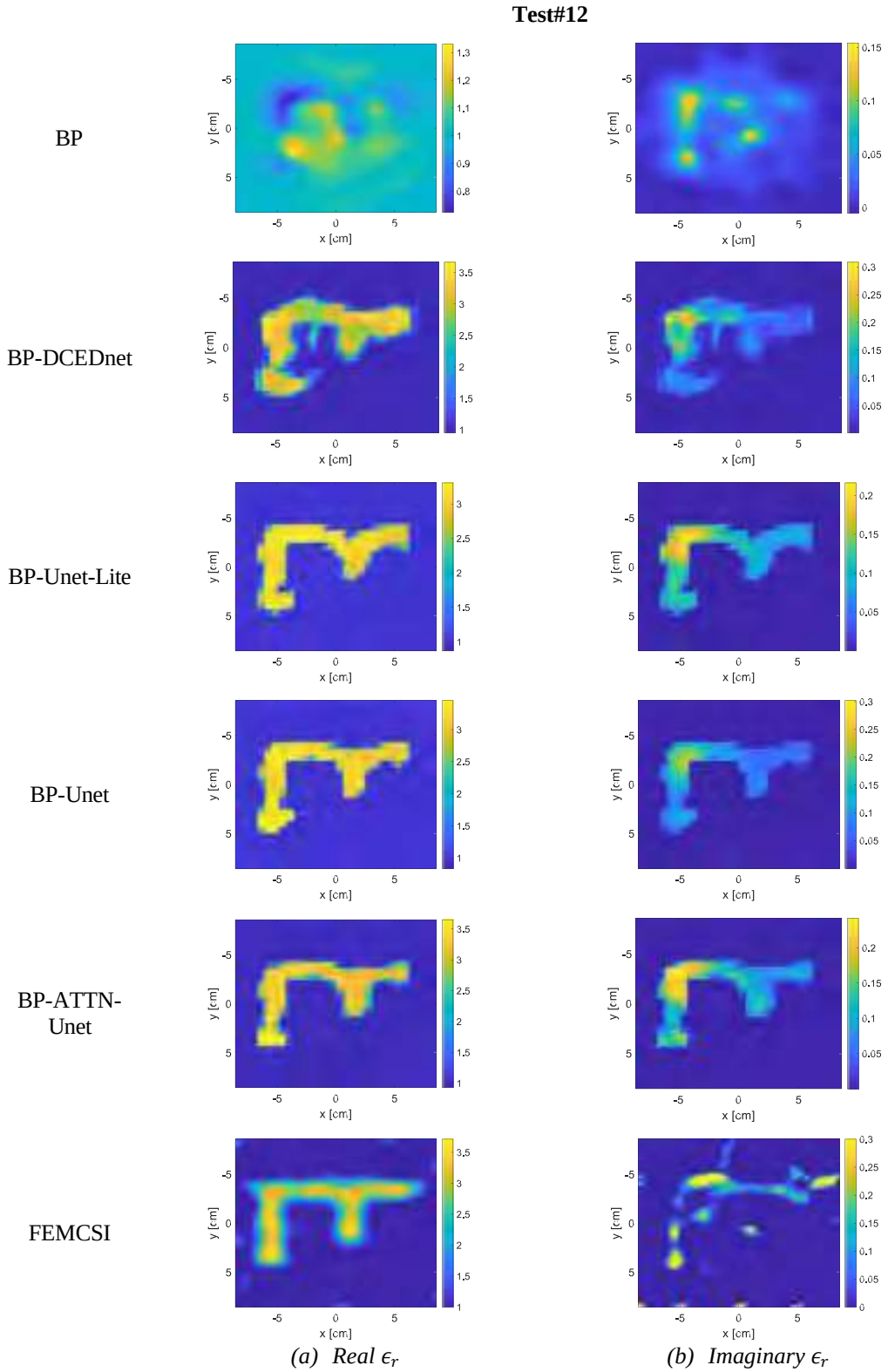

Figure 52. Reconstruction results of (a) real and (b) imaginary components of relative permittivity ϵ_r of Tilted-F with 10% added noise.

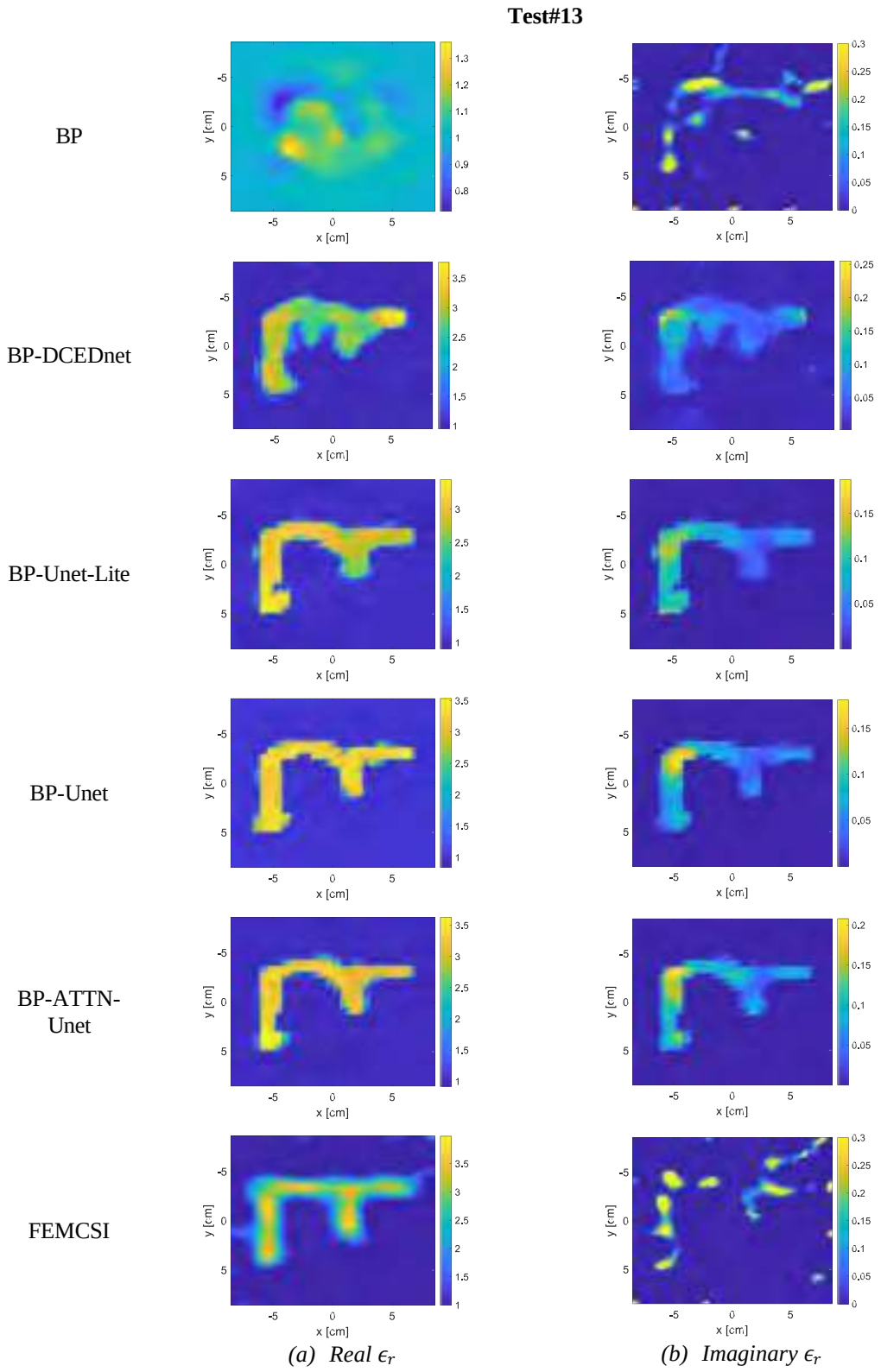

Figure 53. Reconstruction results of (a) real and (b) imaginary components of relative permittivity ϵ_r of Tilted-F with 15% added noise.

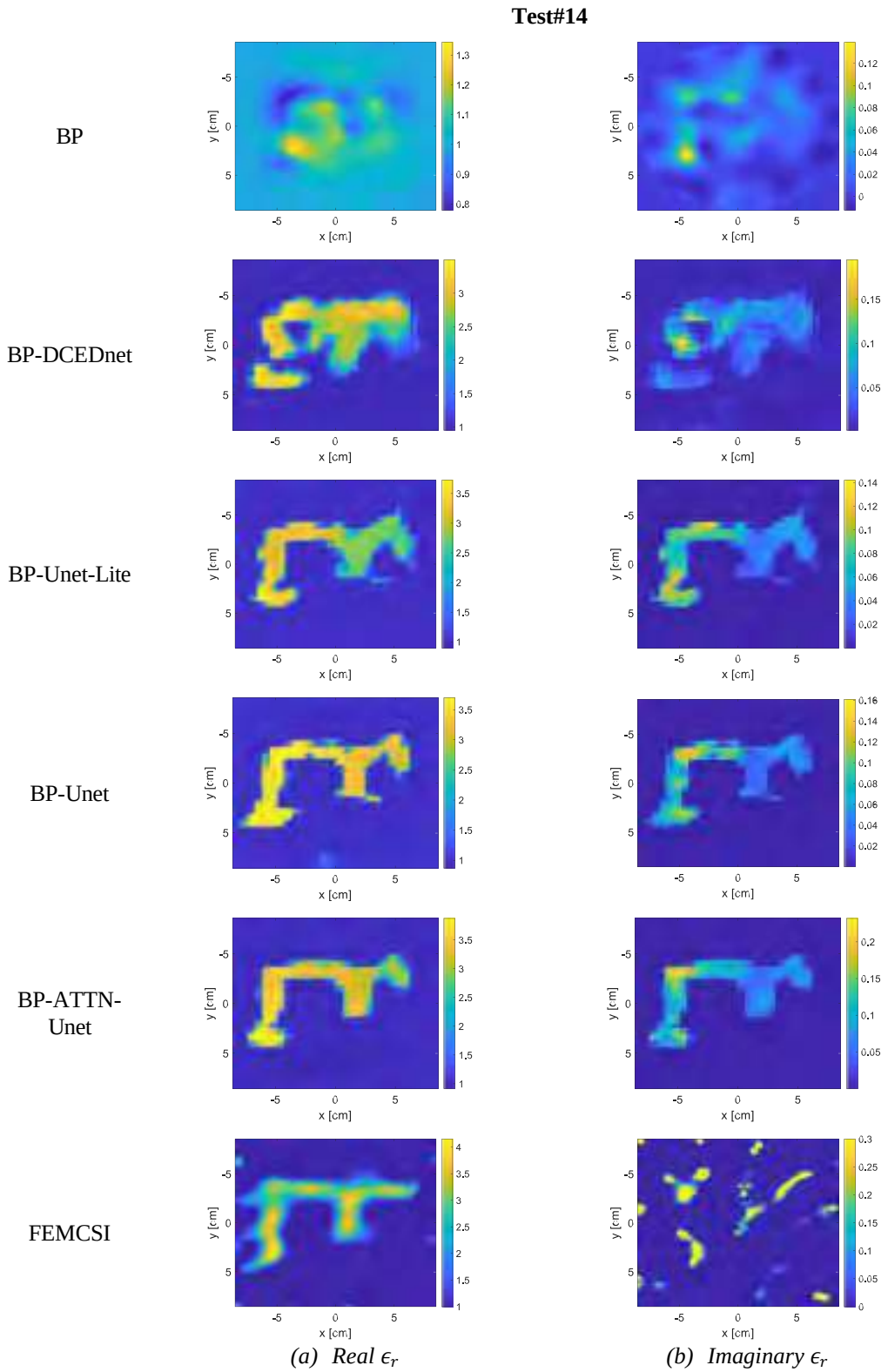

Figure 54. Reconstruction results of (a) real and (b) imaginary components of relative permittivity ϵ_r of Tilted-F with 20% added noise.

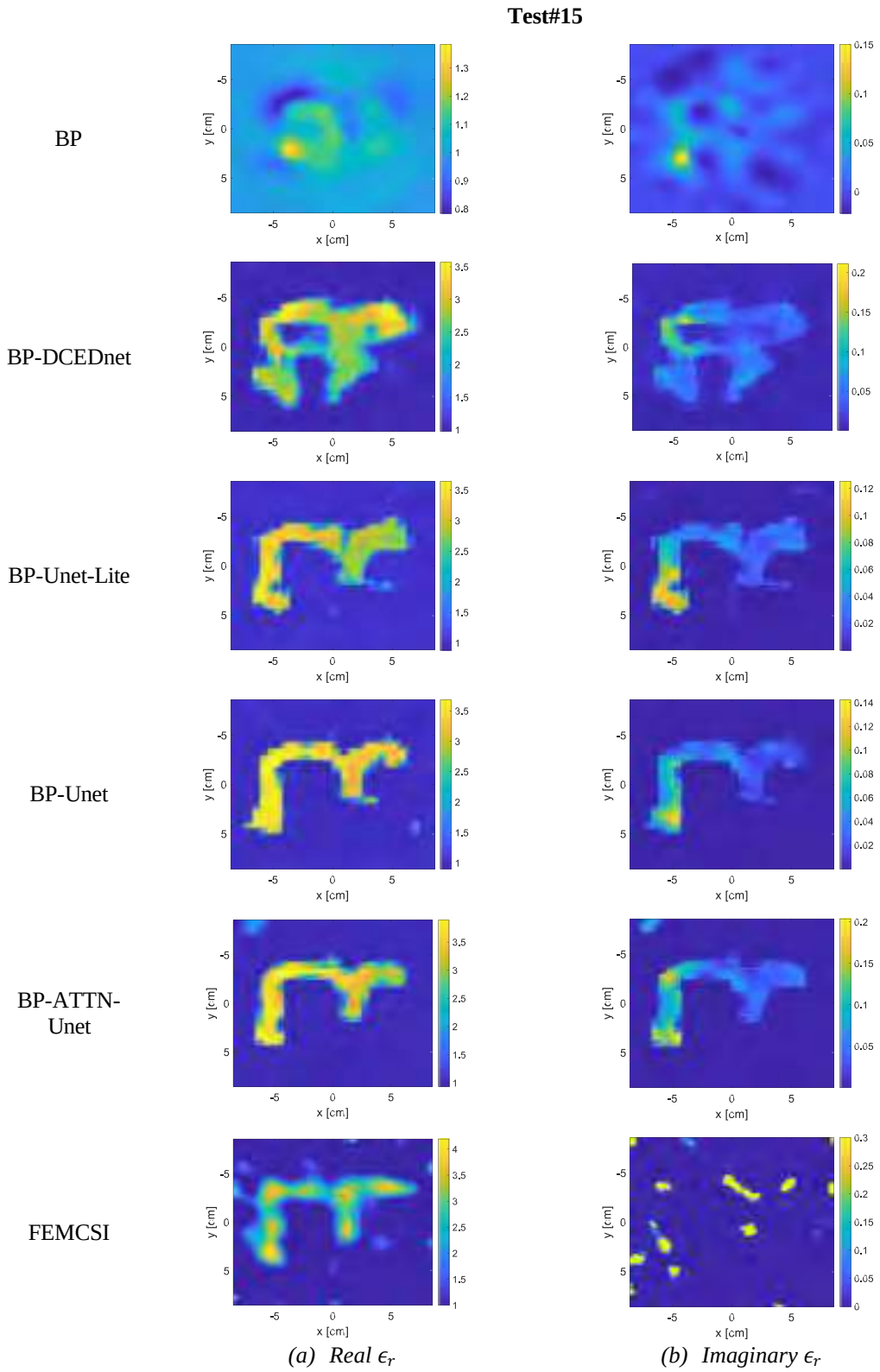

Figure 55. Reconstruction results of (a) real and (b) imaginary components of relative permittivity ϵ_r of Tilted-F with 25% added noise.

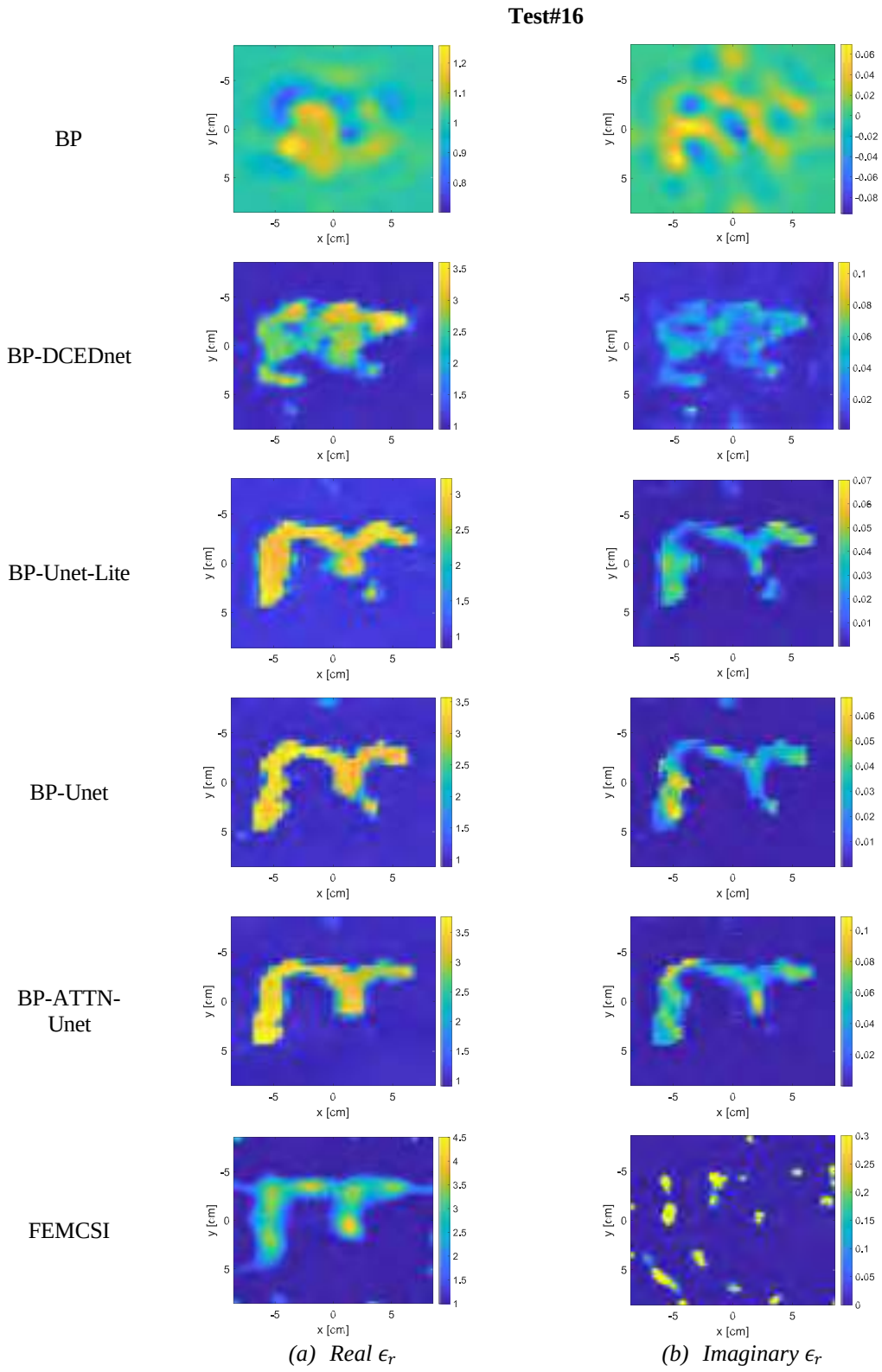

Figure 56. Reconstruction results of (a) real and (b) imaginary components of relative permittivity ϵ_r of Tilted-F with 30% added noise.

Table 9. MSE of the real ϵ_r Reconstructions for Test#11-Test#16 under different Noise levels

Method	MSE-Real					
	Test#11	Test#12	Test#13	Test#14	Test#15	Test#16
BP-DCEDnet	0.2652	0.3076	0.2678	0.2904	0.3684	0.3135
BP-Unet-Lite	0.1716	0.1722	0.2195	0.2113	0.2049	0.2336
BP-Unet	0.1614	0.1737	0.1979	0.2668	0.2094	0.2794
BP-ATTN-Unet	0.1580	0.1604	0.2190	0.2083	0.1969	0.1765
FEMCSI	0.0519	0.0596	0.0643	0.1066	0.1303	0.0987

Table 10. MSE of the imaginary ϵ_r Reconstructions for Test#11-Test#16 under different Noise levels

Method	MSE-Imaginary					
	Test#11	Test#12	Test#13	Test#14	Test#15	Test#16
BP-DCEDnet	0.0009	0.0012	0.0008	0.0008	0.0009	0.0010
BP-Unet-Lite	0.0006	0.0006	0.0007	0.0006	0.0009	0.0011
BP-Unet	0.0006	0.0007	0.0007	0.0007	0.0009	0.0011
BP-ATTN-Unet	0.0006	0.0008	0.0006	0.0006	0.0007	0.0007
FEMCSI	0.0016	0.0047	0.0073	0.0109	0.0136	0.0102

Table 11. MSE of the ϵ_r Reconstructions for Test#11-Test#16 under different Noise levels

Method	MSE					
	Test#11	Test#12	Test#13	Test#14	Test#15	Test#16
BP-DCEDnet	0.1331	0.1544	0.1343	0.1456	0.1847	0.1573
BP-Unet-Lite	0.0861	0.0864	0.1101	0.1060	0.1029	0.1173
BP-Unet	0.0810	0.0872	0.0993	0.1338	0.1051	0.1403
BP-ATTN-Unet	0.0793	0.0806	0.1098	0.1045	0.0988	0.0886
FEMCSI	0.0267	0.0322	0.0358	0.0588	0.0719	0.0545

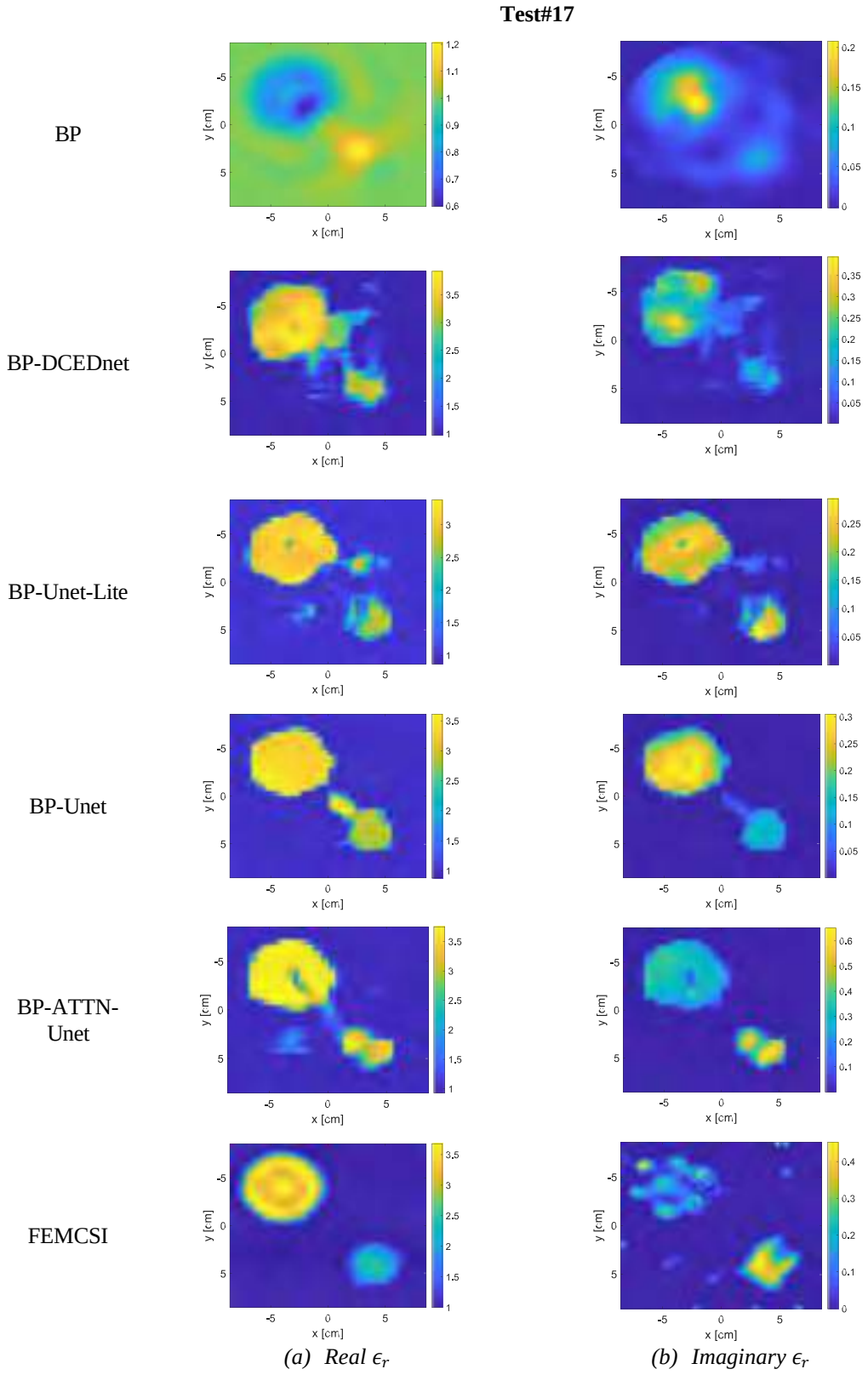

Figure 57. Reconstruction results of (a) real and (b) imaginary components of relative permittivity ϵ_r of 2-Circles with 5% added noise.

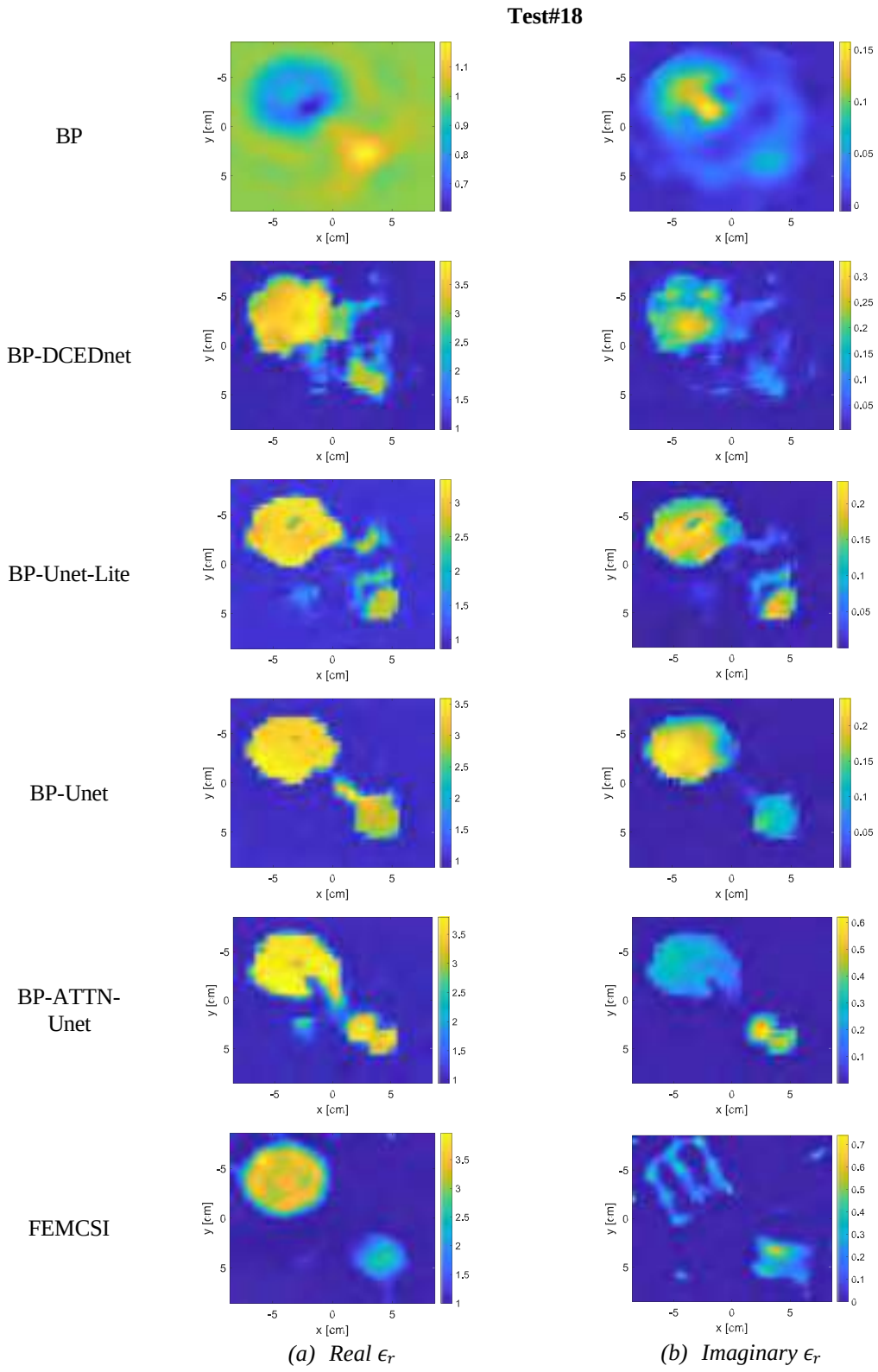

Figure 58. Reconstruction results of (a) real and (b) imaginary components of relative permittivity ϵ_r of 2-Circles with 10% added noise.

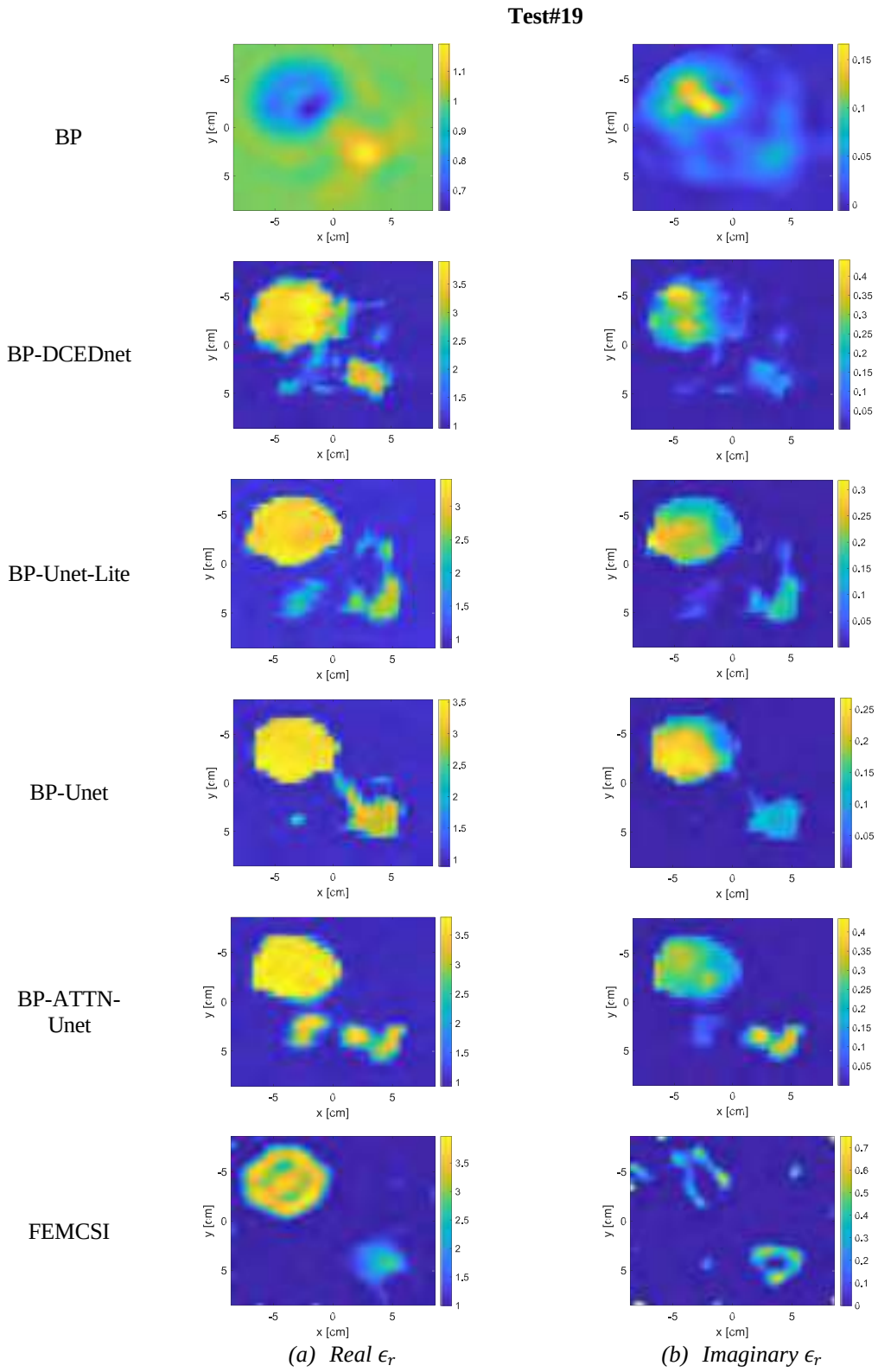

Figure 59. Reconstruction results of (a) real and (b) imaginary components of relative permittivity ϵ_r of 2-Circles with 15% added noise.

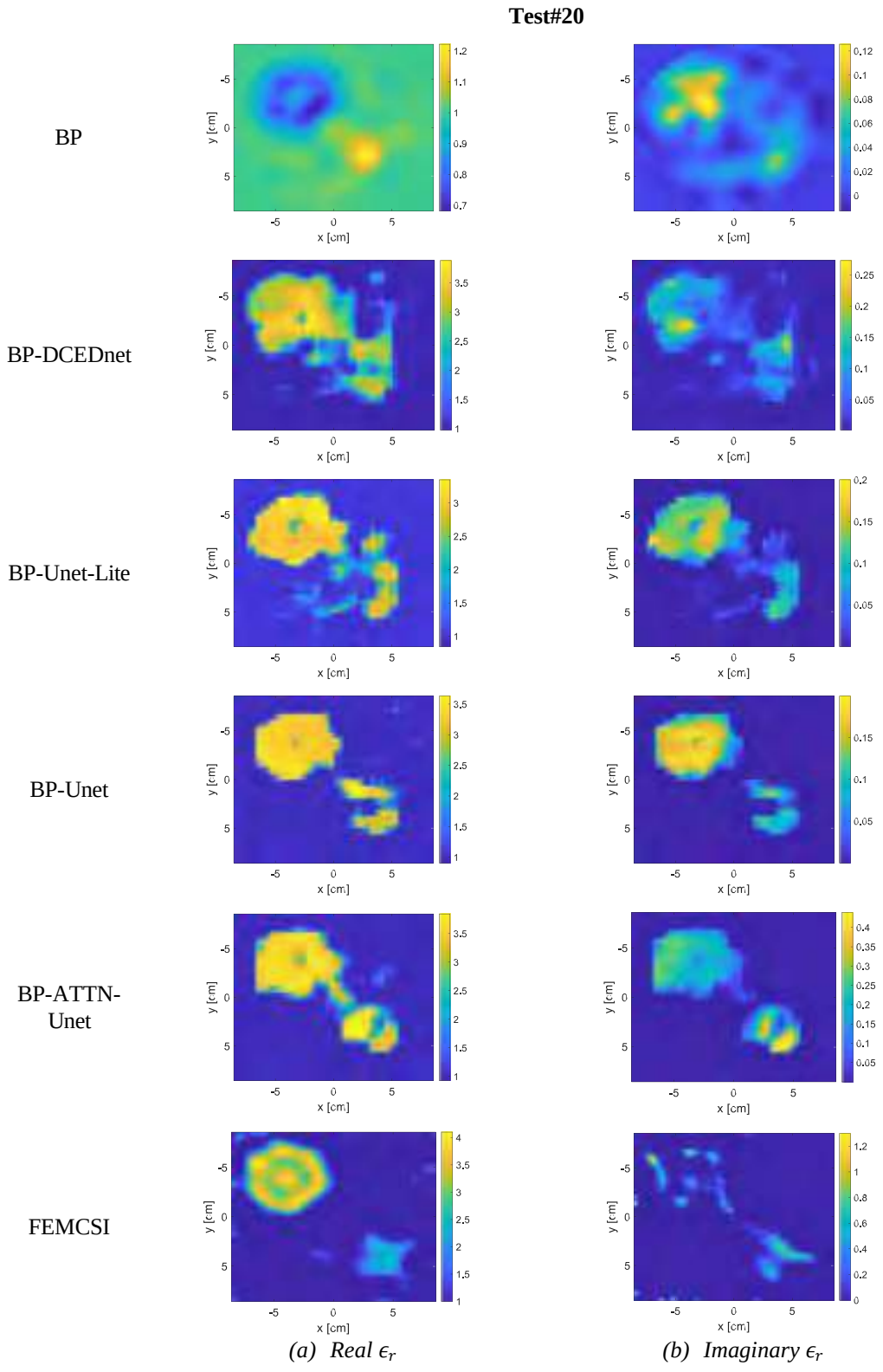

Figure 60. Reconstruction results of (a) real and (b) imaginary components of relative permittivity ϵ_r of 2-Circles with 20% added noise.

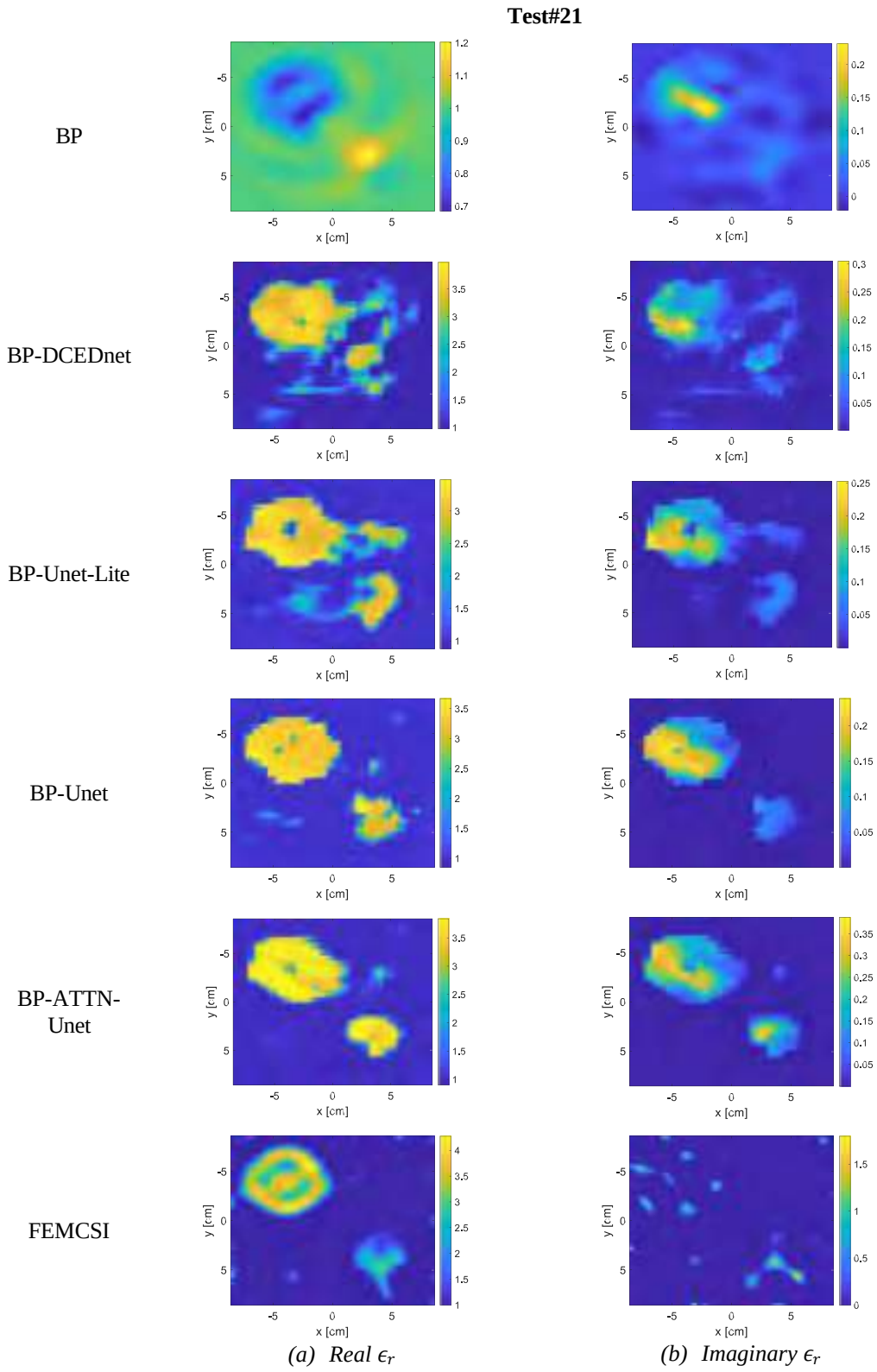

Figure 61. Reconstruction results of (a) real and (b) imaginary components of relative permittivity ϵ_r of 2-Circles with 25% added noise.

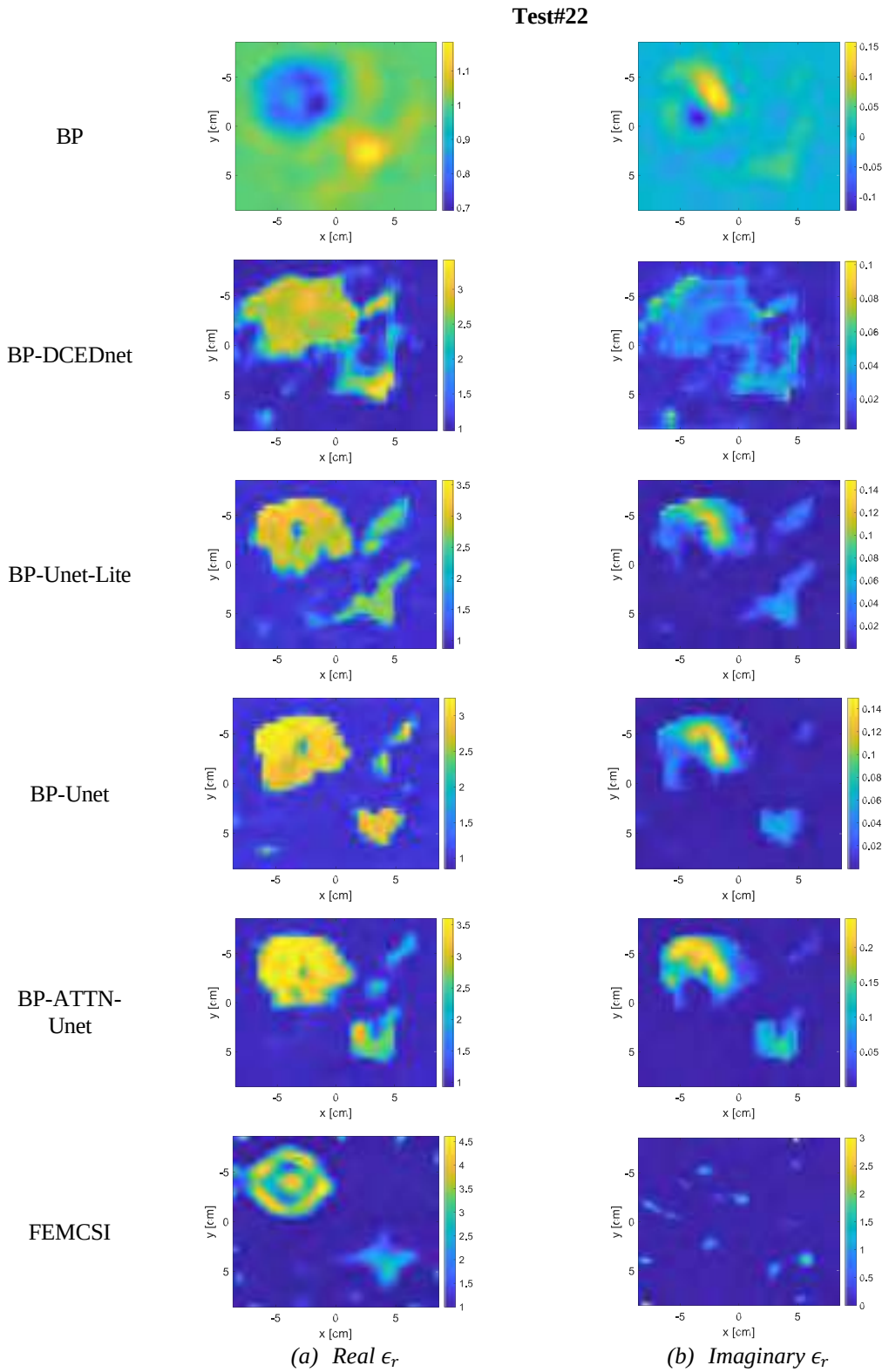

Figure 62. Reconstruction results of (a) real and (b) imaginary components of relative permittivity ϵ_r of 2-Circles with 30% added noise.

Table 12. MSE of the real ϵ_r Reconstructions for Test#17-Test#22 under different Noise levels

Method	MSE-Real					
	Test#17	Test#18	Test#19	Test#20	Test#21	Test#22
BP-DCEDnet	0.4344	0.4354	0.4417	0.2400	0.5855	0.4802
BP-Unet-Lite	0.2521	0.2501	0.2649	0.3627	0.4113	0.4111
BP-Unet	0.2904	0.2627	0.2726	0.3329	0.2603	0.3281
BP-ATTN-Unet	0.3059	0.3498	0.4067	0.4161	0.3875	0.3393
FEMCSI	0.0172	0.0273	0.0398	0.0439	0.0678	0.1280

Table 13. MSE of the imaginary ϵ_r Reconstructions for Test#17-Test#22 under different Noise levels

Method	MSE-Imaginary					
	Test#17	Test#18	Test#19	Test#20	Test#21	Test#22
BP-DCEDnet	0.0077	0.0071	0.0086	0.0059	0.0070	0.0064
BP-Unet-Lite	0.0055	0.0049	0.0058	0.0054	0.0061	0.0061
BP-Unet	0.0069	0.0053	0.0057	0.0058	0.0062	0.0060
BP-ATTN-Unet	0.0096	0.0068	0.0062	0.0051	0.0064	0.0054
FEMCSI	0.0020	0.0046	0.0085	0.0111	0.0194	0.0369

Table 14. MSE of the ϵ_r Reconstructions for Test#17-Test#22 under different Noise levels

Method	MSE					
	Test#17	Test#18	Test#19	Test#20	Test#21	Test#22
BP-DCEDnet	0.2210	0.2212	0.2251	0.4741	0.2962	0.2433
BP-Unet-Lite	0.1288	0.1275	0.1353	0.1841	0.2087	0.2086
BP-Unet	0.1487	0.1340	0.1391	0.1693	0.1333	0.1671
BP-ATTN-Unet	0.1577	0.1783	0.2065	0.2106	0.1969	0.1723
FEMCSI	0.0096	0.0160	0.0242	0.0275	0.0436	0.0825

5.3.3.2.3 Large Permittivity Range

Further to the high-noise testing, the models endured large permittivity range test to validate the generalization capabilities. To achieve this, the complex profile 'Tilted-F' is assigned three different relative permittivity; 'minimum' $\epsilon_r = 1.2 - j0.02$, 'maximum' $\epsilon_r = 4.0 - j1.0$, and 'out of range' $\epsilon_r = 4.4 - j1.1$ as shown in Figure 63 to Figure 65. All the other forward problem configurations setup are kept the same. Their respective BP estimates for the DNN inputs are obtained in the same procedure that is used to obtain the BP estimates for the 10000 MNIST targets. Test#23 to Test#25 as shown in Figure 66 to Figure 68 display their reconstruction test results obtained from the four trained DNN models along with their corresponding ground truths, BP inputs, and the FEMCSI results. Their MSE values are summarized in Table 15 to Table 17. Comparing the trained models results, the Unet-Lite provided slightly better results to the Unet especially for Test#24 and Test#25.

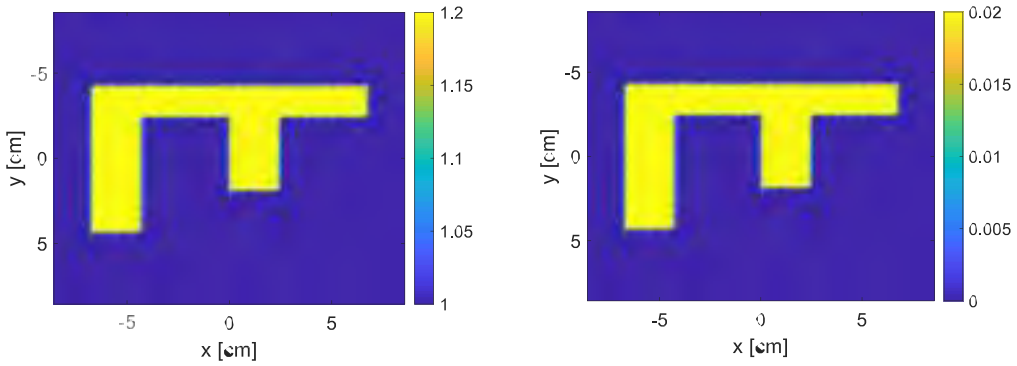

(a) GT-Real ϵ_r *(b) GT-Imaginary ϵ_r*

Figure 63. (a) Real and (b) imaginary components of the 'minimum' relative permittivity for the ground truth of Tilted-F.

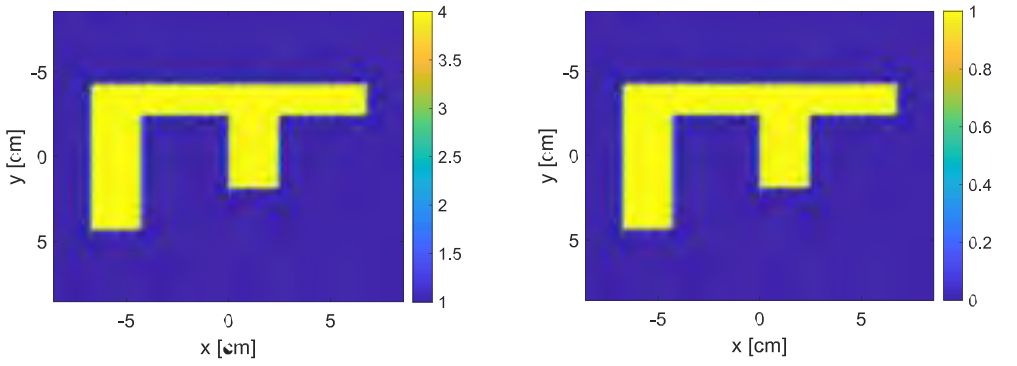

(a) GT-Real ϵ_r *(b) GT-Imaginary ϵ_r*

Figure 64. (a) Real and (b) imaginary components of the 'maximum' relative permittivity for the ground truth of Tilted-F.

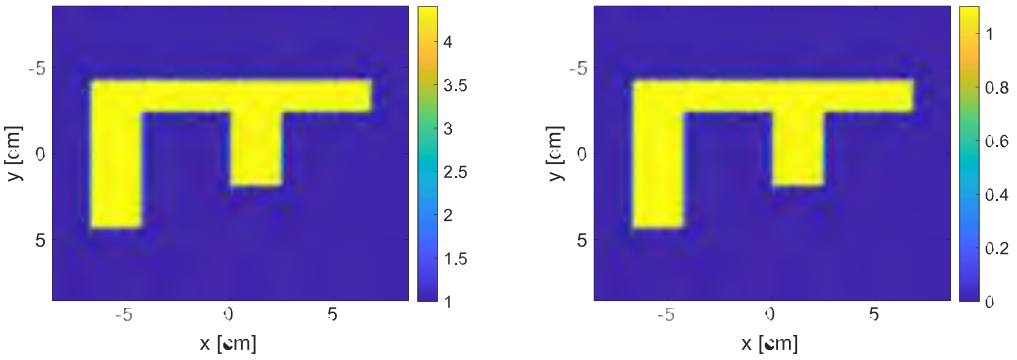

(a) GT-Real ϵ_r *(b) GT-Imaginary ϵ_r*

Figure 65. (a) Real and (b) imaginary components of the 'out of range' relative permittivity for the ground truth of Tilted-F.

.

This is a good case for Unet-Lite against Unet as it used much lesser memory to produce these results. However, the Unet-Lite couldn't outperform the ATTN-Unet whose reconstructions are of better accuracy in all the three-permittivity range. As for the FEMCSI results, the imaginary component for Test#23 with minimum permittivity is considerable better than the ATTN-Unet's. However, with the larger permittivity in Test#24 and Test#25, the FEMCSI's imaginary component reconstruction accuracy severely fades with respect to the ATTN-Unet's.

A crucial observation regarding Test#25 results with 'out of range' relative permittivity is that DNN reconstruction results are all capped off at the maximum training permittivity value for both the real and imaginary components. As all the models are trained with MNIST targets with a maximum $\epsilon_r = 4.0 - j1.0$, the reconstruction results for Test#25 with $\epsilon_r = 4.4 - j1.1$, are capped off at 4.0 and 1.0 for the real and imaginary components respectively. This clearly shows that the neural networks which can very well interpolate between the given training range, can't extrapolate beyond the range. For that reason, the DNN models couldn't produce the permittivity value of $\epsilon_r = 4.4 - j1.1$ for Test#25. So, in order to test profiles with higher relative permittivity exceeding the LDR, a separate DNN model needs to been trained with MNIST targets assigned a higher dynamic range (HDR) of complex relative permittivity. This has been discussed and implemented in configuration 4 in section 5.4.

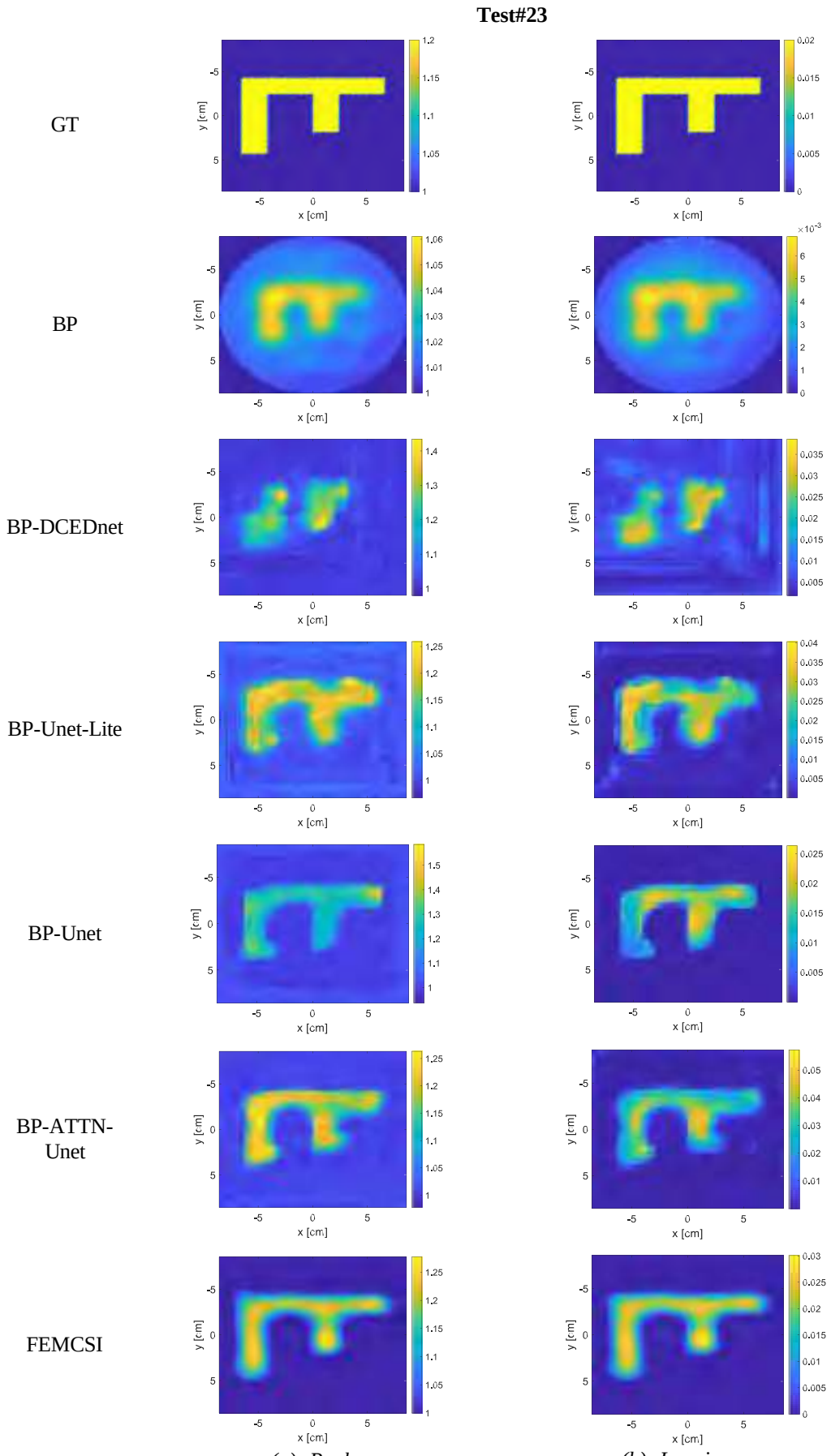

(a) Real ϵ_r *(b) Imaginary ϵ_r*

Figure 66. Reconstructions of (a) real and (b) imaginary components of 'minimum' ϵ_r of Tilted-F.

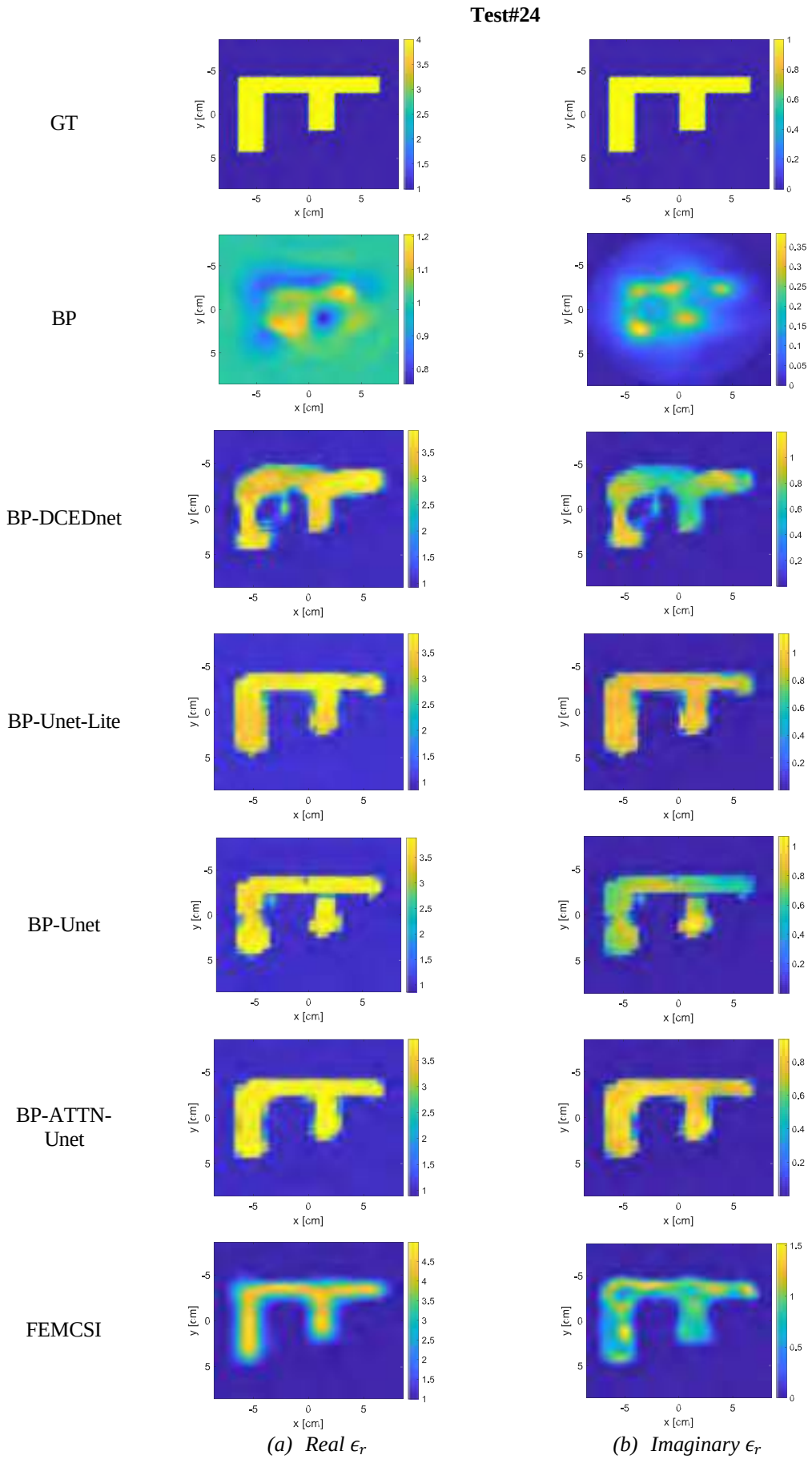

(a) Real ϵ_r *(b) Imaginary ϵ_r*

Figure 67. Reconstructions of (a) real and (b) imaginary components of 'maximum' ϵ_r of Tilted-F.

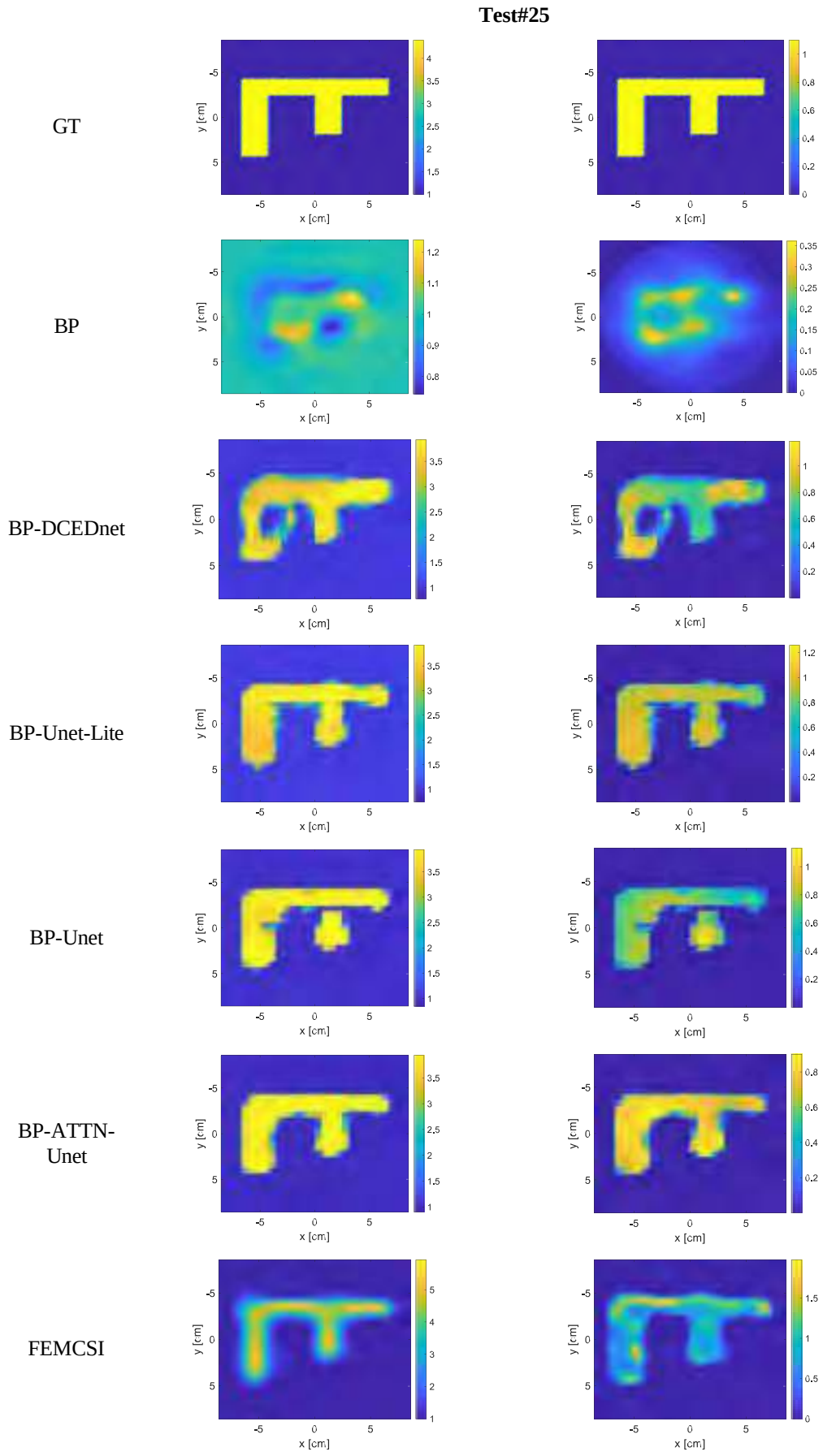

(a) Real ϵ_r *(b) Imaginary ϵ_r*

Figure 68. Reconstructions of (a) real and (b) imaginary components of 'out of range' ϵ_r of Tilted-F.

Table 15. MSE of the real ϵ_r Reconstructions for Test#23-Test#25 with different Permittivity

Method	**MSE-Real**		
	Test#23	Test#24	Test#25
BP-DCEDnet	0.0054	0.3730	0.5267
BP-Unet-Lite	0.0025	0.1574	0.2378
BP-Unet	0.0033	0.1851	0.3196
BP-ATTN-Unet	0.0016	0.1570	0.2633
FEMCSI	0.0005	0.1353	0.1921

Table 16. MSE of the imaginary ϵ_r Reconstructions for Test#23-Test#25 with different Permittivity

Method	**MSE-Imaginary**		
	Test#23	Test#24	Test#25
BP-DCEDnet	0.0007	0.0433	0.0575
BP-Unet-Lite	0.0005	0.0185	0.0289
BP-Unet	0.00002	0.0327	0.0499
BP-ATTN-Unet	0.0006	0.0240	0.0388
FEMCSI	0.000005	0.0284	0.0572

Table 17. MSE of the ϵ_r Reconstructions for Test#23-Test#25 with different Permittivity

Method	**MSE**		
	Test#23	Test#24	Test#25
BP-DCEDnet	0.0027	0.2082	0.2921
BP-Unet-Lite	0.0013	0.0879	0.1513
BP-Unet	0.0016	0.1089	0.1847
BP-ATTN-Unet	0.0008	0.0905	0.1511
FEMCSI	0.0002	0.0818	0.1246

5.3.3.3 Summary of Results

To summarize BP-trained models, the ATTN-Unet provided the best results and significantly outperformed the other networks in terms of precision, generalization, noise resistance, and durability over a wide permittivity range. However, when comparing with FEMCSI results, though the ATTN-Unet largely outperformed the FEMCSI in the imaginary component, it didn't not do as well in the real component. The real reconstructions of the FEMCSI are better than that of the ATTN-Unet especially at low noise levels. Therefore, there is need for improvement.

5.3.4 ITER-10

To further optimize the ATTN-Unet performance, it is re-trained with the novel physics-incorporated input 'ITER10'. All the other forward problem configurations are kept the same.

The 10000 MNIST targets selected for producing the BP training and testing data, are also selected to produce the ITER10 training and testing data as well. The ITER10 data is obtained from the output images from the tenth iteration of CSI. From the 10000 pairs generated using the MNIST targets, 7000 pairs are selected as training data, 1000 for validation, and 2000 as testing data. The input data for training and validation are the ITER10 data, while the corresponding complex ground truth pairs served as the output data for training and validation labels in the ATTN-Unet architecture.

The loss function used is the standard mean-square error (MSE). Furthermore, the Adaptive moment estimation (Adam) optimizer is used for optimizing the MSE loss function. Early stopping with a patience parameter of 10 is implemented during the training. The ITER10-ATTN-Unet with a batch size of 4 effectively trained for 30 epochs that took about 6.75 hours.

The code is developed using Python 3.7 within the Conda environment in the Spyder IDE version 5.3.3. The machine for training and testing the models is equipped with an Intel® Xeon® E-2124 CPU operating at 3.30 GHz, equipped with 32GB of RAM and an NVIDIA Quadro P620 GPU with 2GB of VRAM.

5.3.5 Synthetic Data Results

After the models are trained, they are tested with cross-database samples that include synthetic complex profiles. In the cross-database testing, the models are tested for robustness against different levels of noise. In order to quantitatively evaluate the

reconstruction accuracy, the MSE in Equation (5.1) is calculated between the ground truth and the reconstruction for all the numerical samples.

5.3.5.1 Complex Profiles

After the ITER10-ATTN-Unet is trained, it is tested with the 'Tilted-F' and '2-Circles' complex profiles in Figure 47 and Figure 48 respectively to validate the generalization capability of the network. Test#26 and Test#2 shown in Figure 69 and Figure 70 display the reconstruction results of the two complex profiles obtained from the trained ITER10-ATTN-Unet along with their ground truths, ITER10 input, and FEMCSI results. Additionally, the BP-ATTN-Unet results along with their BP inputs from the previous section has also been included for comparison purposes. The MSE values are summarized in Table 18 to Table 20.

Both the figures and tables of Test#26 and Test#27 clearly show that the ITER10-ATTN-Unet reconstructions are more accurate and closer to the ground truth than that of the BP-ATTN-Unet. In terms of FEMCSI comparison, the ITER10-ATTN-Unet performs significantly better in the imaginary section of the network than the FEMCSI, similar to the BP-ATTN-Unet. However, the primary difference between the BP-ATTN-Unet and the ITER10-ATTN-Unet is that the real component reconstruction greatly improves, getting extremely near to the real component reconstruction found by the FEMCSI as well as the ground truth. This clearly shows the benefit of training the ATTN-Unet with a physics-incorporated input such as the ITER10.

Further, it significantly took much lesser computational time to obtain the ITER10-ATTN-Unet results than the FEMCSI. It only took about 13 seconds to obtain a single reconstruction in the testing phase. In detail, the ITER10 took about 11 seconds, while the ATTN-Unet took only about 2 seconds. On the other hand, running the FEMCSI for 300 iterations to reconstruct a single testing sample took about 58 seconds.

5.3.5.2 High Noise Interference

To further test the robustness of the DNNs, the trained ITER10-ATTN-Unet model is tested with high-level noise interferences on the measurements. The complex profiles in Figure 47 is tested under different noise levels. The measured scattered field data $\vec{E}^{sct}_{\text{meas}}$ of these profiles are added with 5%, 10%, 15%, 20%, 25%, and 30% white Gaussian noises respectively prior to the ITER10 input data generation for testing. Test#28 to Test#33 represent the tests with the different noise levels whose reconstruction results are shown from Figure 69 to Figure 76, along with their

respective ground truths, ITER10 input, and FEMCSI results. The corresponding BP-ATTN-Unet results along with its BP inputs are also shown for comparison purposes. Table 21 to Table 23 summarizes the MSE values of these reconstructions.

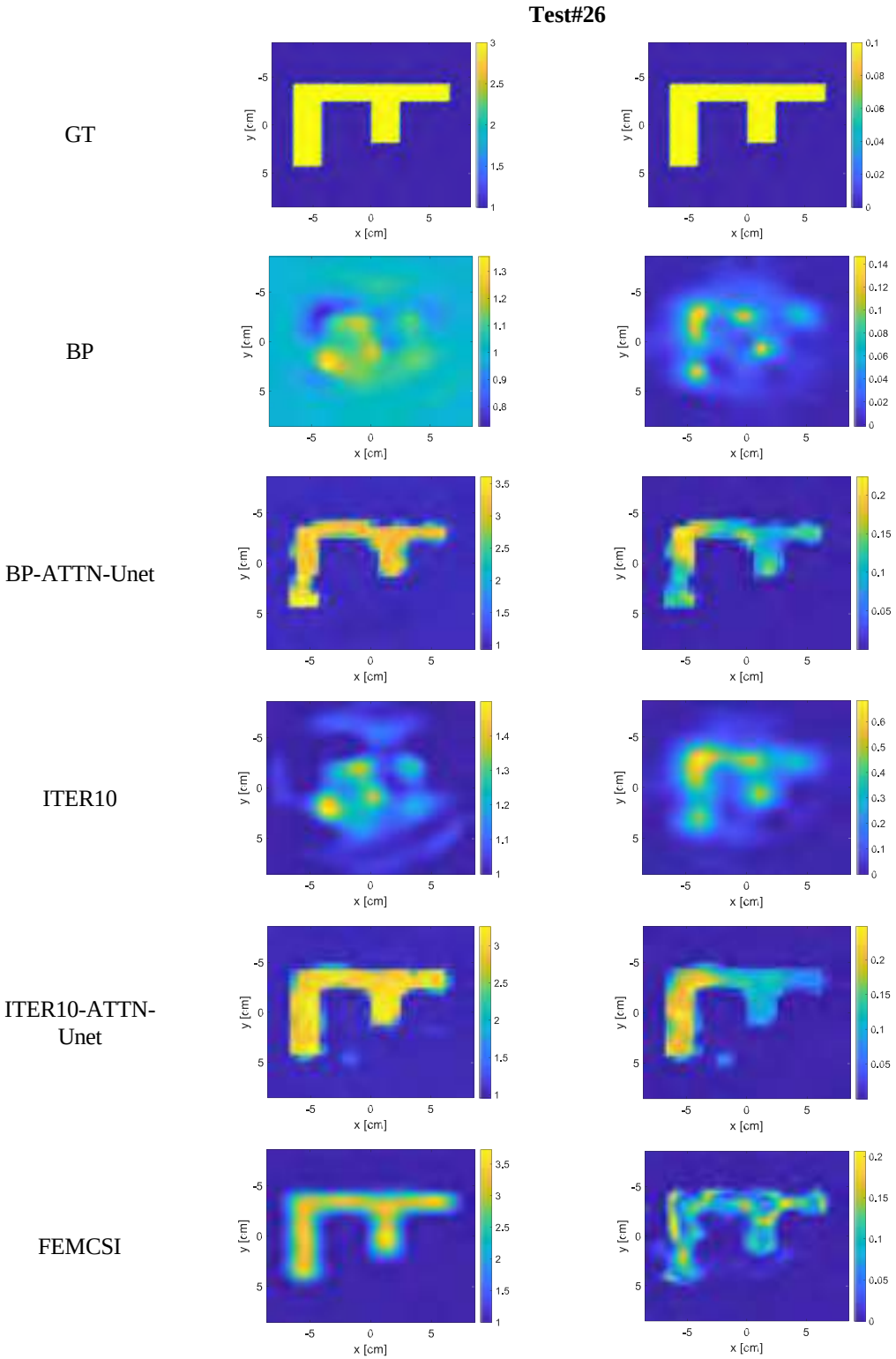

Figure 69. Reconstruction results of (a) real and (b) imaginary components of ϵ_r of Tilted-F.

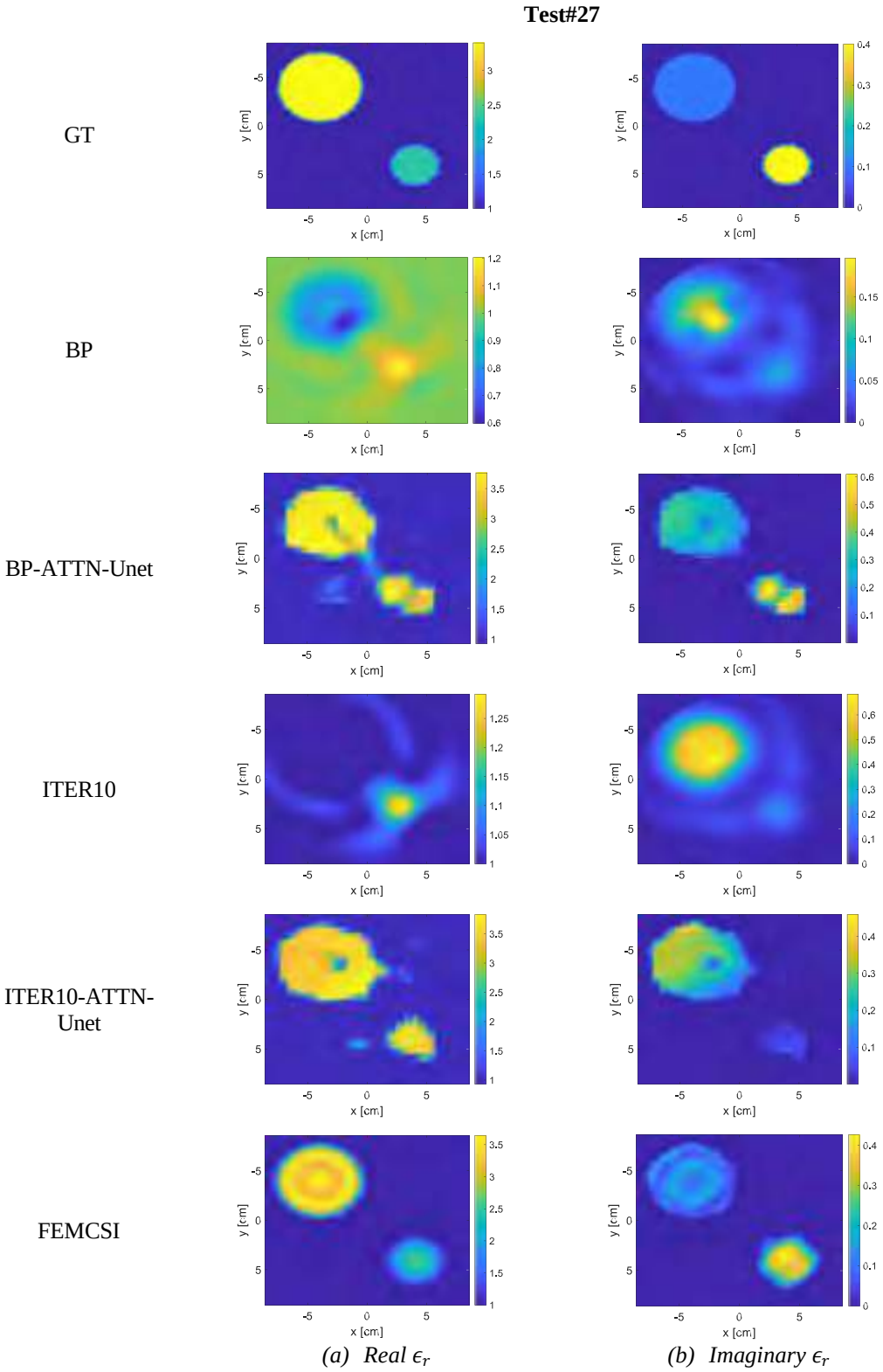

Figure 70. Reconstruction results of (a) real and (b) imaginary components of ϵ_r of 2-Circles.

Table 18. MSE between Ground Truth and Reconstructions of the real ϵ_r for Test#26-Test#27

Method	**MSE-Real**	
	Test#26	Test#27
BP-ATTN-Unet	0.1551	0.3224
ITER10-ATTN-Unet	0.0562	0.3193
FEMCSI	0.0491	0.0160

Table 19. MSE between Ground Truth and Reconstructions of the imaginary ϵ_r for Test#26-Test#27

Method	**MSE-Imaginary**	
	Test#26	Test#27
BP-ATTN-Unet	0.0006	0.0088
ITER10-ATTN-Unet	0.0009	0.0110
FEMCSI	0.0004	0.0007

Table 20. MSE between Ground Truth and Reconstructions of the ϵ_r for Test#26-Test#27

Method	**MSE**	
	Test#26	Test#27
BP-ATTN-Unet	0.0779	0.1656
ITER10-ATTN-Unet	0.0286	0.1652
FEMCSI	0.0248	0.0083

The results for Test#28 to Test#33 clearly shows that the ITER10-ATTN-Unet is affected significantly much lesser compared to both the FEMCSI as well as the BP-ATTN-Unet. The ITER10-ATTN-Unet reconstructions significantly outperform the FEMCSI and remain robust up to a 30% noise level without exhibiting significant quality changes. This is largely due to the physics introduced to the model through the novel physics-incorporated input ITER10.

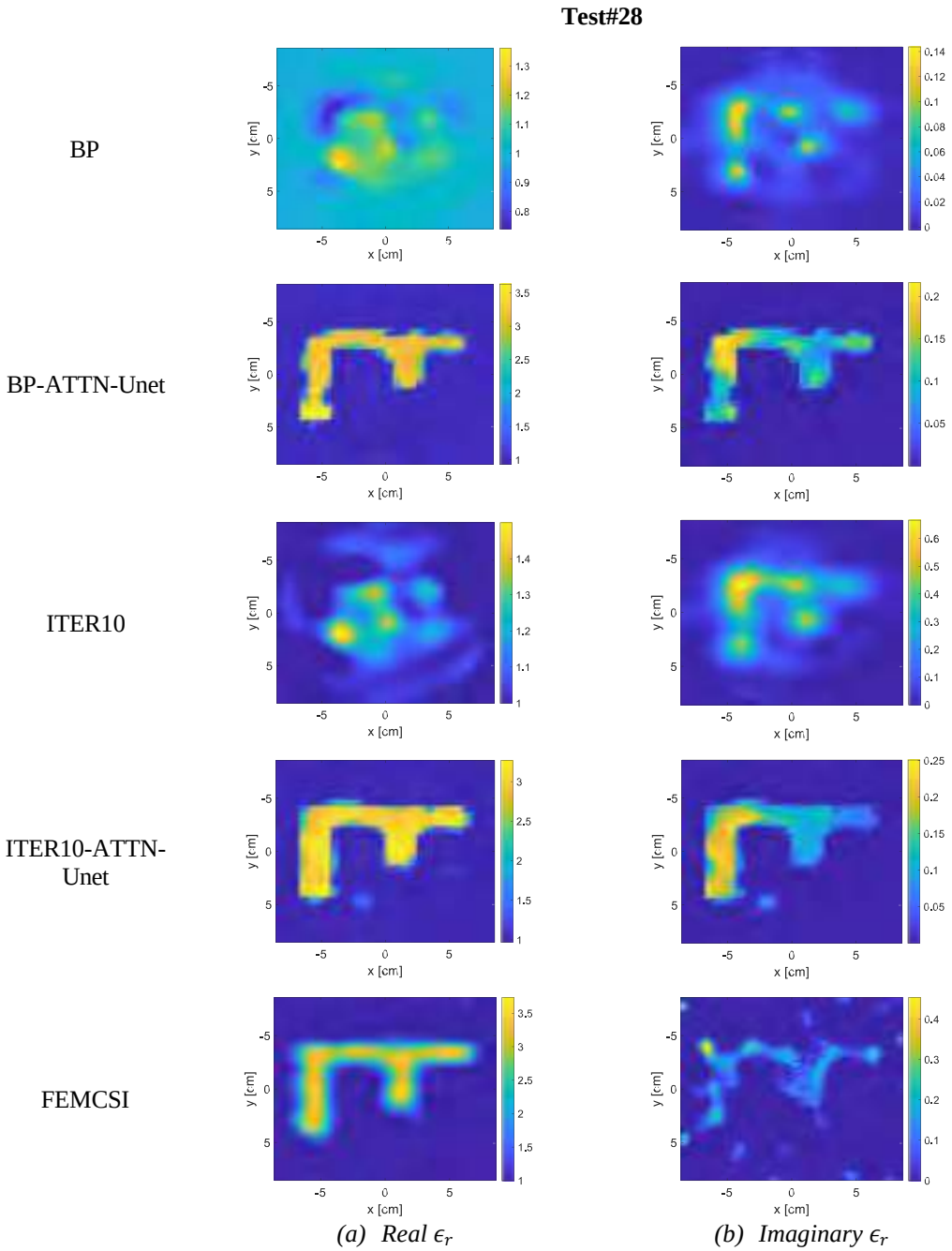

Figure 71. Reconstruction results of (a) real and (b) imaginary components of relative permittivity ϵ_r of Tilted-F with 5% added noise.

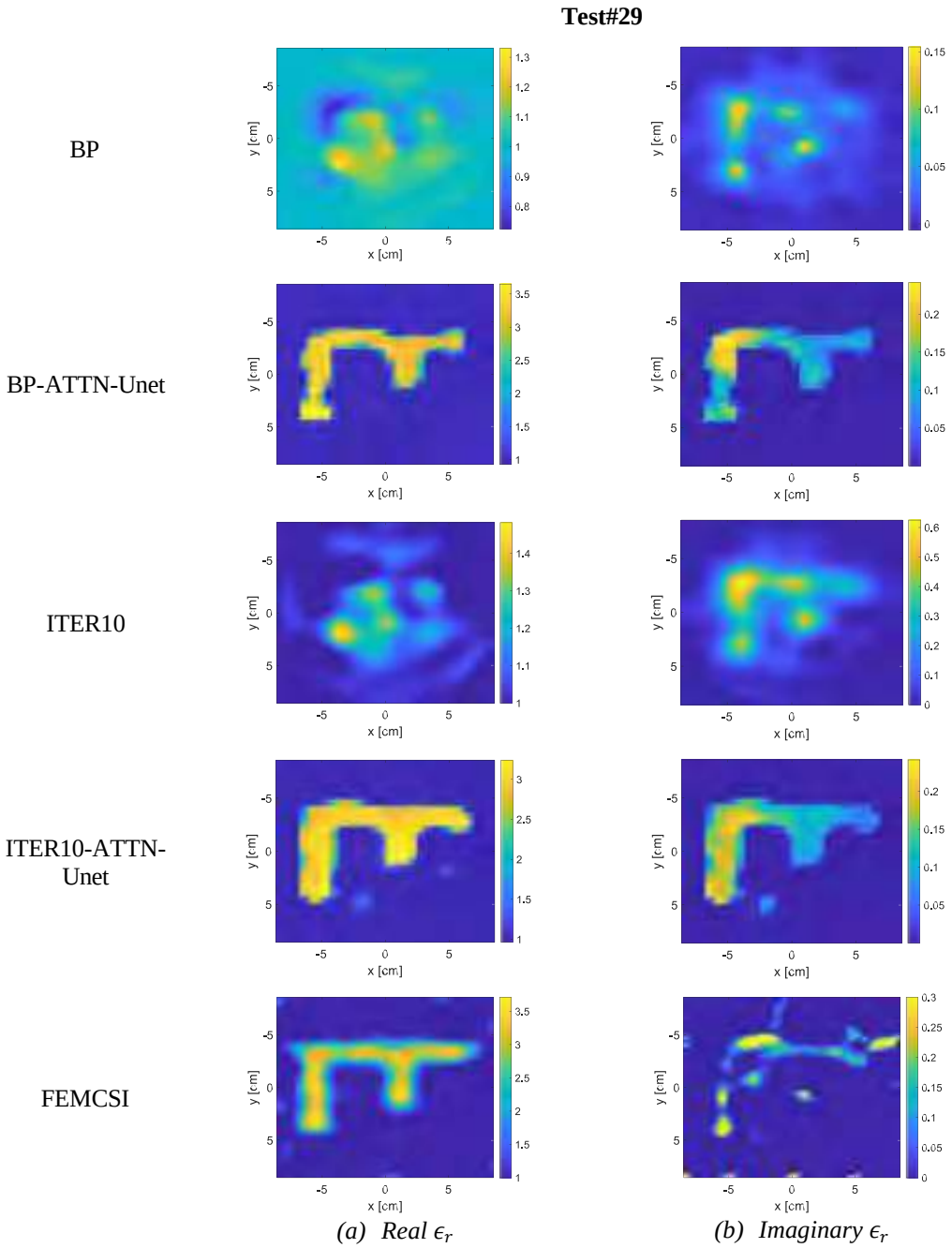

Figure 72. Reconstruction results of (a) real and (b) imaginary components of relative permittivity ϵ_r of Tilted-F with 10% added noise.

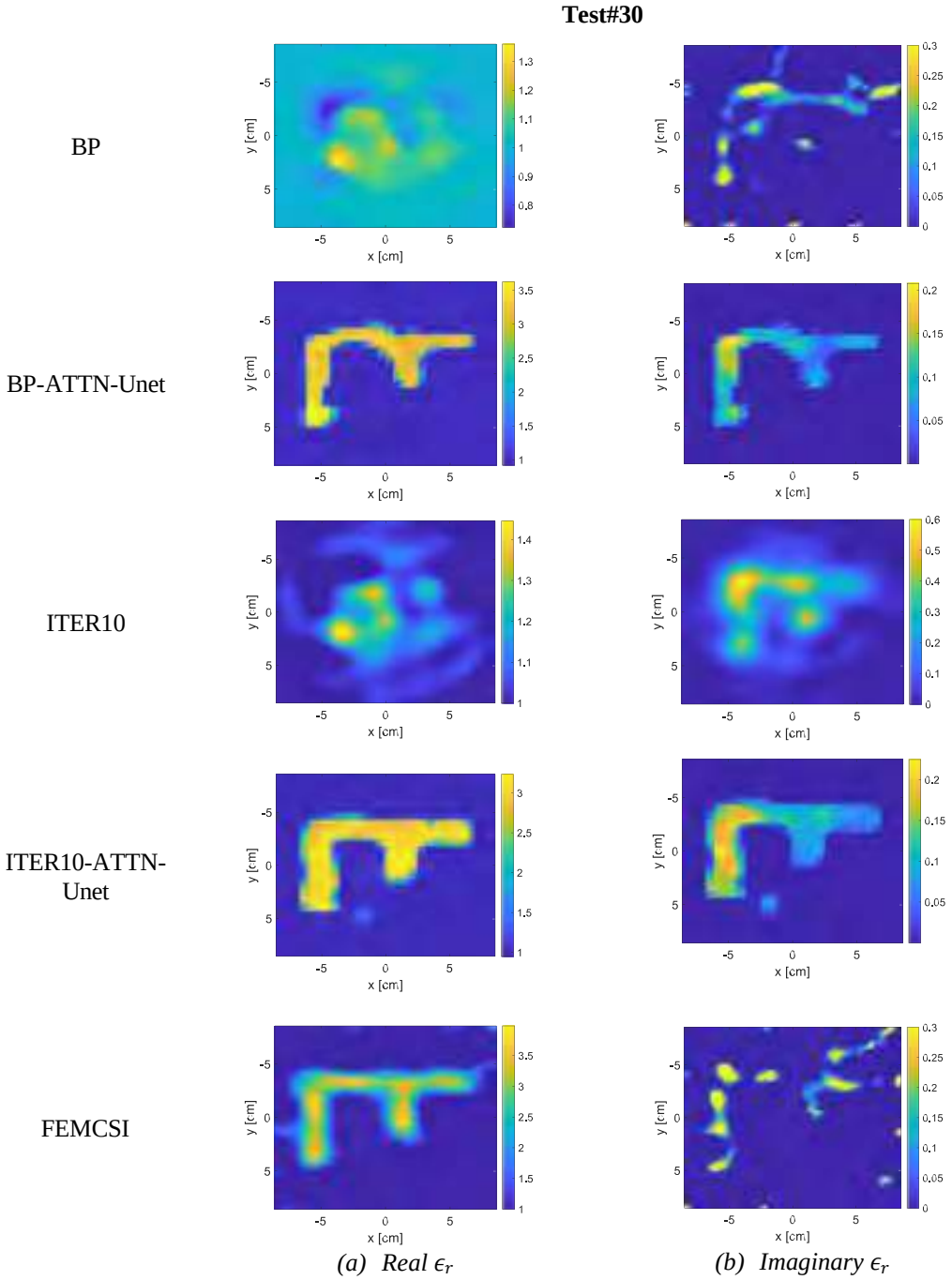

Figure 73. Reconstruction results of (a) real and (b) imaginary components of relative permittivity ϵ_r of Tilted-F with 15% added noise.

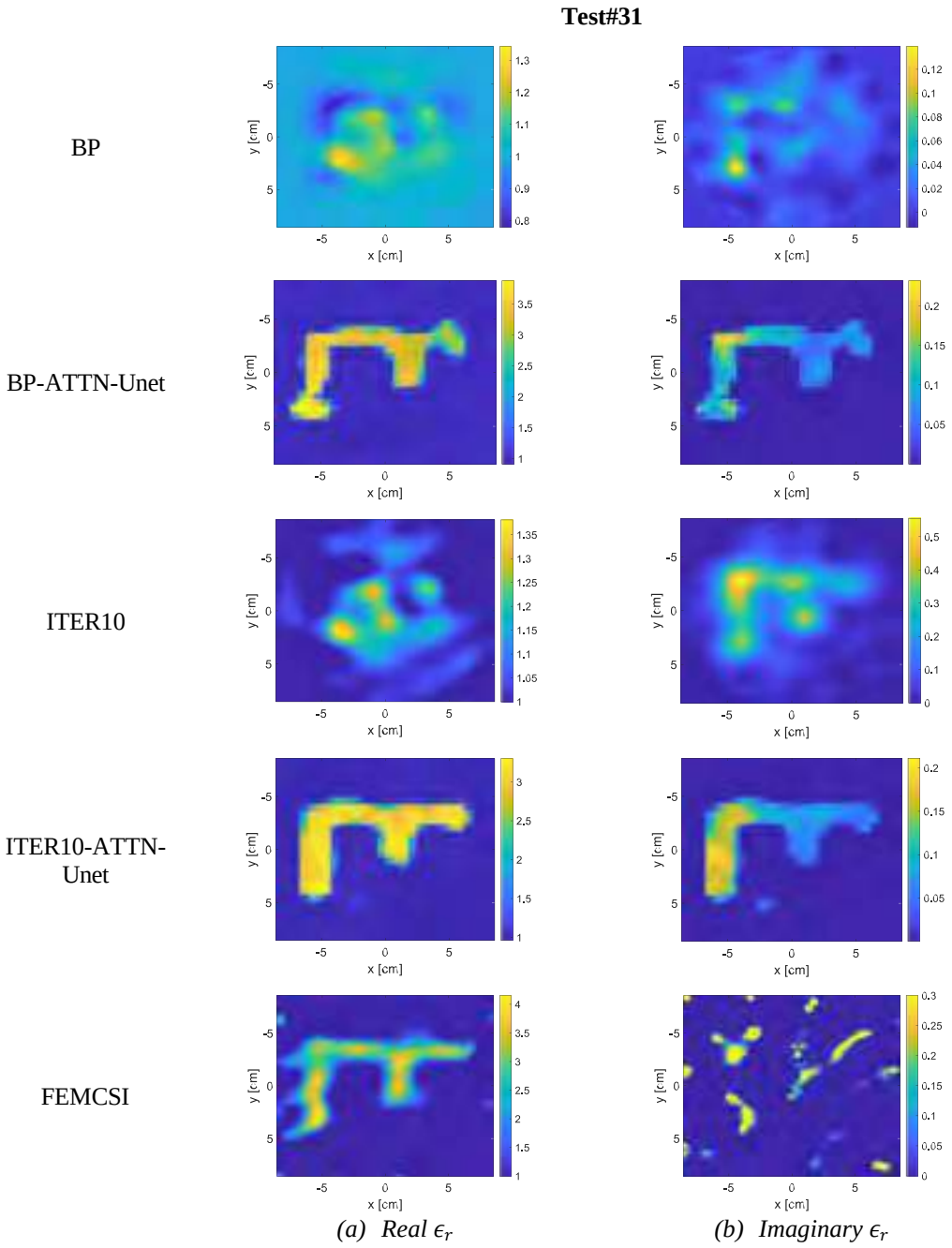

Figure 74. Reconstruction results of (a) real and (b) imaginary components of relative permittivity ϵ_r of Tilted-F with 20% added noise.

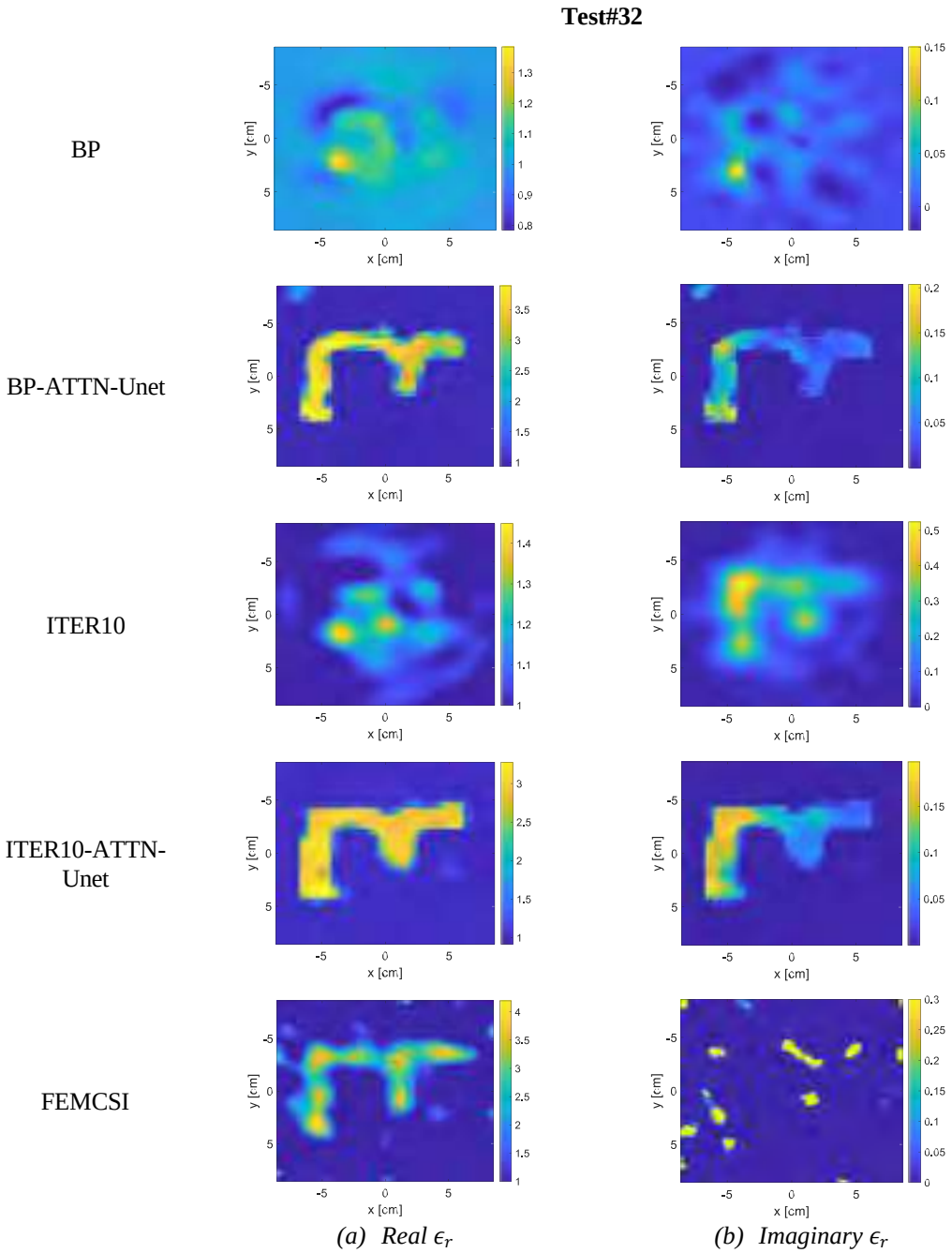

Figure 75. Reconstruction results of (a) real and (b) imaginary components of relative permittivity ϵ_r of Tilted-F with 25% added noise.

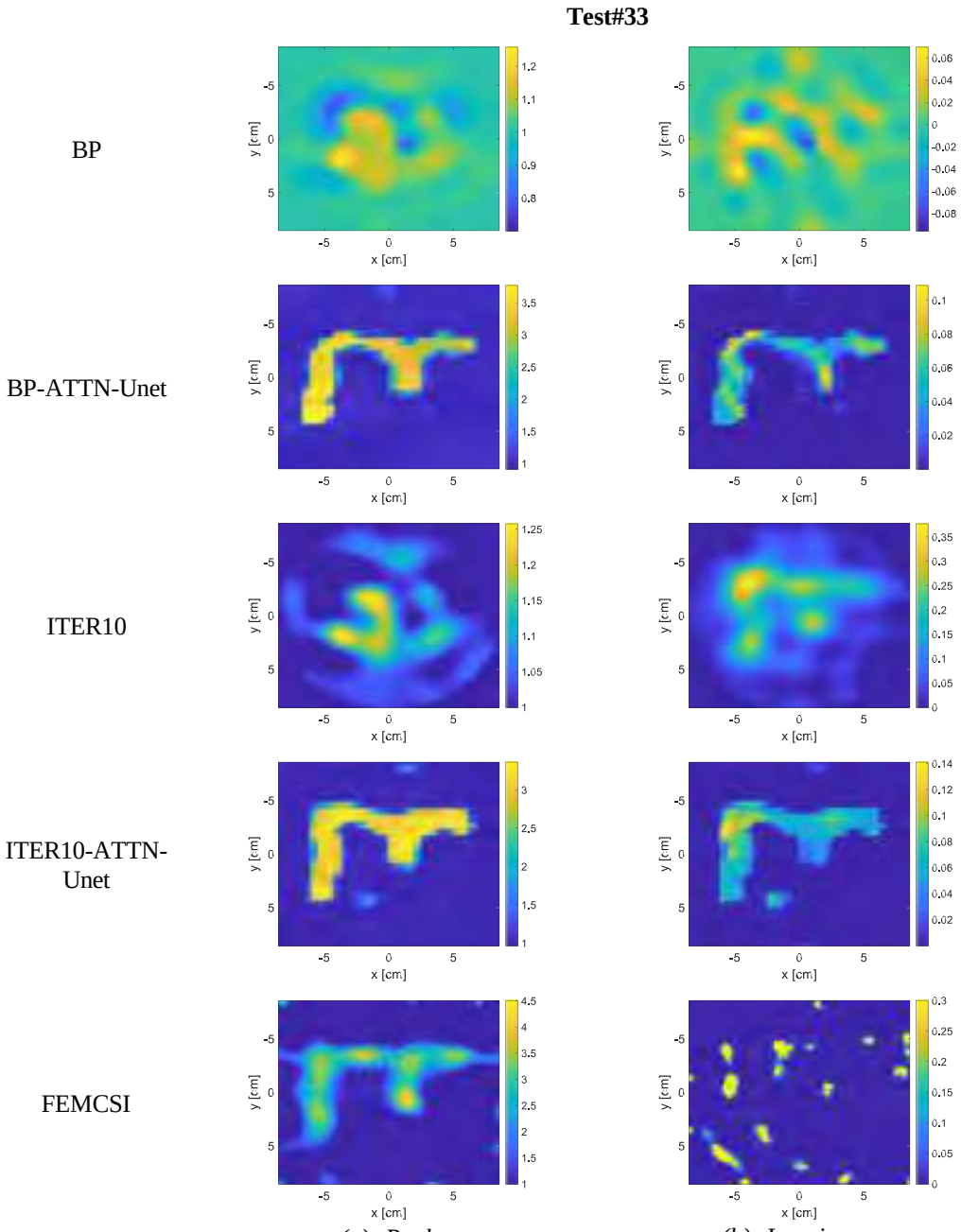

Figure 76. Reconstruction results of (a) real and (b) imaginary components of relative permittivity ϵ_r of Tilted-F with 30% added noise.

Table 21. MSE of the real ϵ_r Reconstructions for Test#28-Test#33 under different Noise levels

Method	**MSE-Real**					
	Test#28	Test#29	Test#30	Test#31	Test#32	Test#33
BP-ATTN-Unet	0.1580	0.1604	0.2190	0.2083	0.1969	0.1765
ITER10-ATTN-Unet	0.0536	0.0789	0.0845	0.0750	0.0956	0.1993
FEMCSI	0.0519	0.0596	0.0643	0.1066	0.1303	0.0987

Table 22. MSE of the imaginary ϵ_r Reconstructions for Test#28-Test#33 under different Noise levels

Method	**MSE-Imaginary**					
	Test#28	Test#29	Test#30	Test#31	Test#32	Test#33
BP-ATTN-Unet	0.0006	0.0008	0.0006	0.0006	0.0007	0.0007
ITER10-ATTN-Unet	0.0009	0.0010	0.0006	0.0005	0.0005	0.0006
FEMCSI	0.0016	0.0047	0.0073	0.0109	0.0136	0.0102

Table 23. MSE of the ϵ_r Reconstructions for Test#28-Test#33 under different Noise levels

Method	**MSE**					
	Test#28	Test#29	Test#30	Test#31	Test#32	Test#33
BP-ATTN-Unet	0.0793	0.0806	0.1098	0.1045	0.0988	0.0886
ITER10-ATTN-Unet	0.0273	0.0399	0.0426	0.0378	0.0481	0.1000
FEMCSI	0.0267	0.0322	0.0358	0.0588	0.0719	0.0545

5.4 Configuration 4: Lossy Targets with Relative Permittivity of High Dynamic Range

In this configuration setup, lossy targets with relative permittivity of high dynamic range (HDR) have been implemented.

5.4.1 Configuration of the Forward Problem

The target is positioned inside a square imaging domain D with side-length of 17 cm. The imaging domain is centered in the middle of the microwave imaging system and is illuminated by 24 transmitters at a frequency of 3 GHz. For each transmitter, the scattered data are collected at 24 receivers. The transmitting and receiving points are co-located and evenly spaced on a circular surface S of radius of 13 cm. The problem domain is bounded and enclosed by a circular absorbing boundary with a radius of 18 cm.

Since deep CNNs training requires a large number of input samples, the first 10000 MNIST handwritten digits are selected as targets. The scattered data are obtained for these 10000 MNIST digit-like targets in the imaging domain *D* that are randomly assigned a complex relative permittivity ϵ_r of high dynamic range (HDR). The HDR for the real component is from 1 to 10 and the imaginary component is from 0 to 2. The target is surrounded in a homogeneous lossless background medium with relative permittivity $\epsilon_b = 1$. Both the input and the ground truth image pairs are interpolated into square grids of 128×128.

The HDR distribution is implemented randomly as well as with weights providing two different types of ITER10 inputs as discussed below.

5.4.1.1 ITER10 input type 1: Random HDR Distribution (ITER10-HDR-r)

In this ITER10 input type, the HDR complex relative permittivity ϵ_r is randomly distributed between 1 and 10 for the real component and between 0 and 2 for the imaginary component for the 10000 MNIST targets.

5.4.1.2 ITER10 input type 2: Weighted HDR Distribution (ITER10-HDR-w)

In this ITER10 input type, the HDR complex relative permittivity ϵ_r is distributed with weights. Since most of the test targets have ϵ_r of low dynamic range (LDR), 70% of the ϵ_r values are distributed between 1 and 4 and remaining 30% of the ϵ_r values are distributed for HDR between 4 and 10 for the real component. This resulted in 7000 MNIST targets with ϵ_r of LDR while remaining 3000 MNIST targets with ϵ_r beyond LDR. This weighted distribution is implemented only in the real

component. As for the imaginary component, ϵ_r values are randomly distributed between 0 and 2 with no weights.

5.4.2 Training Details

For this configuration setup, ATTN-Unet that is found to be the best performing model from previous results, is trained and tested with both the ITER10 inputs and the results are compared with each other as well as the corresponding FEMCSI.

Similar to previous configurations, from the 10000 pairs generated using the MNIST targets, 7000 pairs are selected as training data, 1000 for validation, and 2000 as testing data. The input data for training and validation are the ITER10-HDR and ITER-HDR-w estimates successively, while the corresponding complex ground truth pairs served as the output data for training and validation labels in the ATTN-Unet architecture.

The loss function used is the standard mean-square error (MSE). Furthermore, the Adaptive moment estimation (Adam) optimizer is used for optimizing the MSE loss function. Early stopping with a patience parameter of 10 is implemented during the training. Both ITER10-ATTN-Unet-HDR-r and ITER10-ATTN-Unet-HDR-w are trained with a batch size of 8. The ITER10-ATTN-Unet-HDR-r effectively trained for 28 epochs and took about 6.31 hours, while the ITER10-ATTN-Unet-HDR-w effectively trained for 20 epochs and took about 4.52 hours.

The code is developed using Python 3.7 within the Conda environment in the Spyder IDE version 5.3.3. The machine for training and testing the models is equipped with an Intel® X®(R) E-2124 CPU operating at 3.30 GHz, equipped with 32GB of RAM and an NVIDIA Quadro P620 GPU with 2GB of VRAM.

5.4.3 Synthetic Data Results

After the models are trained, they are tested both within the MNIST database as well as with cross-database samples that include synthetic complex profiles. In the cross-database testing, the models are tested for robustness against noise as well as large permittivity range. In order to quantitatively evaluate the reconstruction accuracy, the MSE in Equation (5.1) is calculated between the ground truth and the reconstruction for all the numerical samples.

5.4.3.1 Within-Database Test

Both the trained models are first tested with 2000 MNIST testing data. The reconstruction results of Test#34 with $\epsilon_r = 7.1 - j0.52$ is shown in Figure 77 while

the MSEs for the real, imaginary and combined parts are shown in Table 24, Table 25, and Table 26.

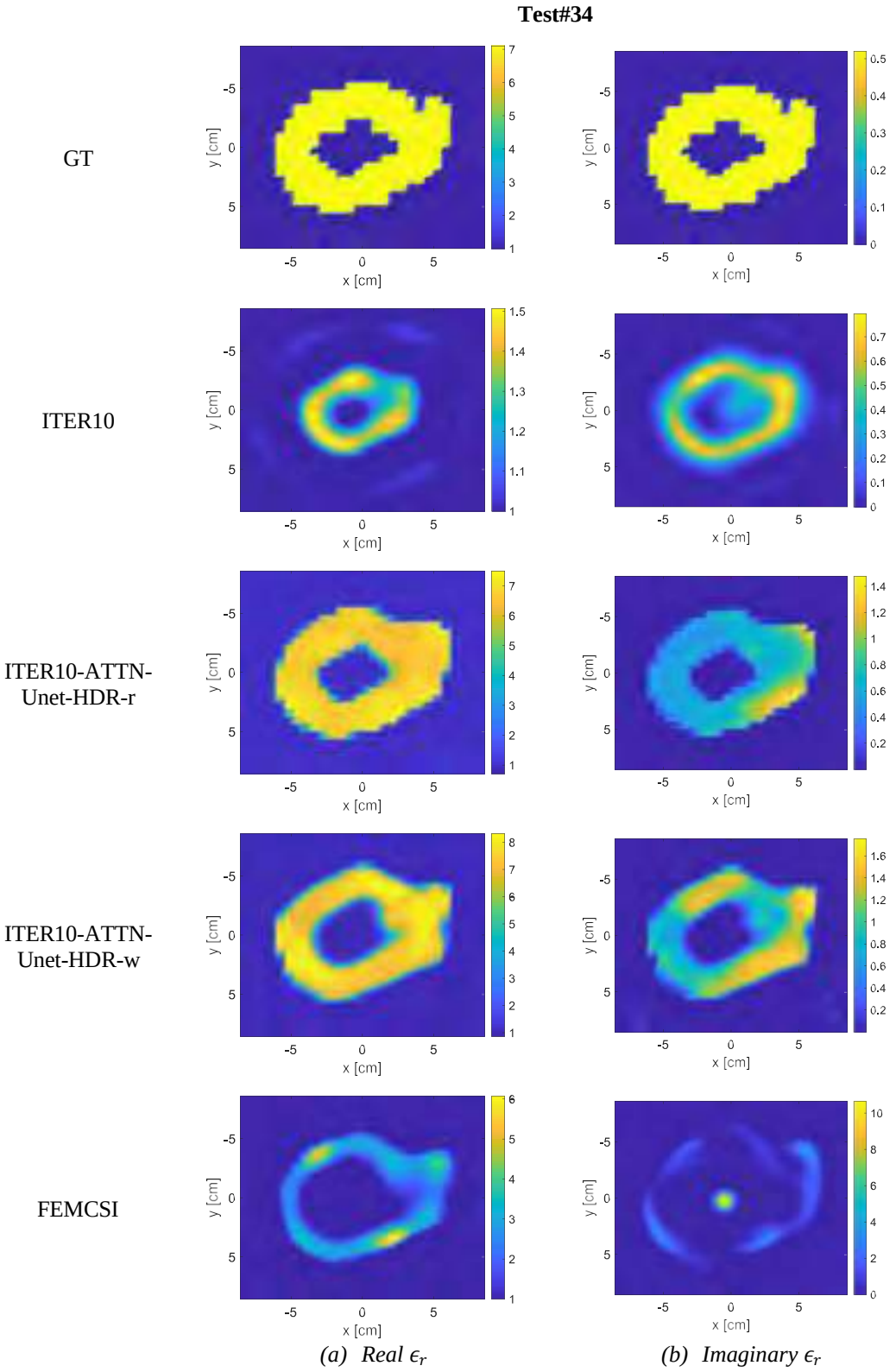

Figure 77. Reconstruction results of (a) real and (b) imaginary components of ϵ_r of Test#34.

Table 24. MSE between Ground Truth and Reconstructions of the real ϵ_r for Test#34

Method	**MSE-Real**
	Test#34
ITER10-ATTN-Unet-HDR-r	0.6866
ITER10-ATTN-Unet-HDR-w	1.1360
FEMCSI	7.0439

Table 25. MSE between Ground Truth and Reconstructions of the imaginary ϵ_r for Test#34

Method	**MSE-Imaginary**
	Test#34
ITER10-ATTN-Unet-HDR-r	0.3575
ITER10-ATTN-Unet-HDR-w	0.1180
FEMCSI	0.5740

Table 26. MSE between Ground Truth and Reconstructions for the ϵ_r for Test#34

Method	**MSE**
	Test#34
ITER10-ATTN-Unet-HDR-r	0.6866
ITER10-ATTN-Unet-HDR-w	0.6270
FEMCSI	3.8090

The reconstructed results of Test#34 in Figure 77 clearly show that both the ITER10 trained ATTN-Unet models outperform the FEMCSI in both real and imaginary component of the complex relative permittivity. This makes sense because high permittivities degrade the performance of FEMCSI. Nonetheless, the permittivity output values from the ATTN-Unets closely match the ground truth values, achieving excellent quality and accuracy. The HDR-r trained model performed better than the HDR-w trained model.

This is one of the first studies to provide acceptable quality reconstructions in high complex relative permittivities, despite the fact that researchers in low relative permittivities have produced a great deal of effort and satisfactory findings.

5.4.3.2 Cross-Database Test

The tests carried out in Configuration 3 with the complex profiles have always been utilized here to test the performance and validate the trained ITER-ATTN-Unet models' generalization capacity. However, as the main objective of this section is to display the reconstructions of profiles with high relative permittivities, the test results that include profiles with low permittivities are displayed in Appendix A.

5.4.3.2.1 Complex Profiles

Both the ITER10-ATTN-Unets with HDR-r and HDR-w are tested with the 'Tilted-F' and '2-Circles' complex profiles in Test#35 and Test#36 shown in Figure 47 and Figure 48 respectively to validate the generalization capability of the network. Since both profiles have permittivities that belong to the LDR and the results obtained are not found better than the ITER10-ATTN-Unet in configuration 3, they can be found in Appendix A in Figure 106 and Figure 107 with their MSE values in Table 36 to Table 38.

5.4.3.2.2 High Permittivity

To validate the performance of HDR trained models, the complex profile 'Tilted-F' is assigned three different relative permittivity; 'moderate' $\epsilon_r = 4.0 - j1.0$, 'high' $\epsilon_r = 6.0 - j1.2$, and 'very high' $\epsilon_r = 8.0 - j2.0$. With the exception of a name change, the 'moderate' profile and the 'maximum' profile depicted in Figure 64 are identical. Figure 78 and Figure 79 show the 'high' and 'very high' permittivity profiles. All the other forward problem configurations setup are kept the same. Their respective ITER10 inputs for the ATTN-Unet are obtained in the same procedure that is used to obtain the ITER10 data for the 10000 MNIST targets.

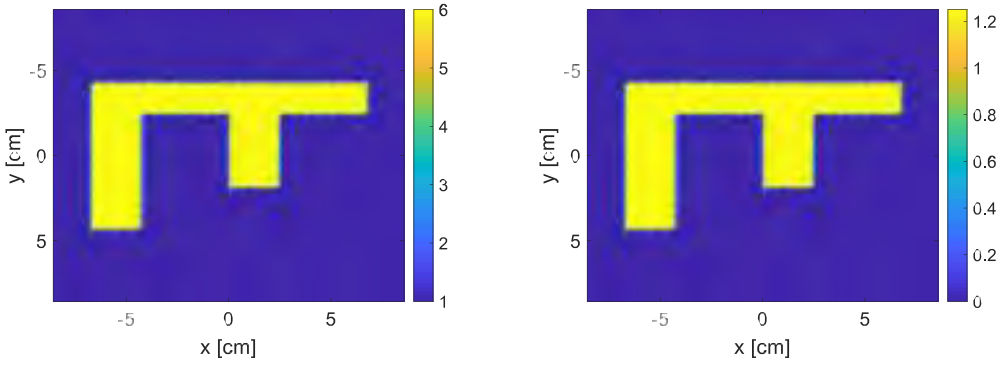

(a) GT-Real ϵ_r *(b) GT-Imaginary ϵ_r*

Figure 78. (a) Real and (b) imaginary components of the 'high' permittivity for the ground truth of Tilted-F.

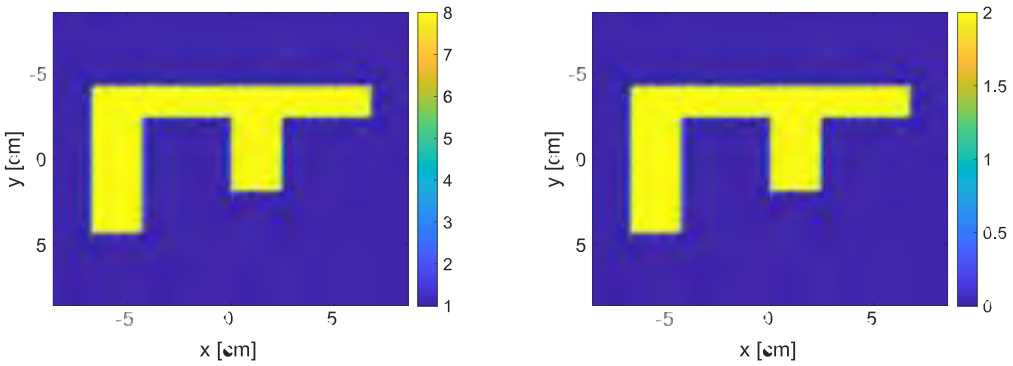

(a) GT-Real ϵ_r *(b) GT-Imaginary ϵ_r*

Figure 79. (a) Real and (b) imaginary components of the 'very high' relative permittivity for the ground truth of Tilted-F.

Since the 'moderate' profile is nothing but the 'maximum' profile from the LDR, its reconstruction results are shown in Figure 108 in Test#37 and its MSE values are summarized from Table 39 to Table 41 in Appendix A. Test#38 and Test#39 reconstruction results are depicted in Figure 80 and Figure 81 and their MSE values are summarized in Table 27 to Table 29. The results show that the ITER-ATTN-Unets achieve reasonable accuracy with the HDR-r model outperforming the HDR-w model, whereas the FEMCSI fails to offer satisfactory results and breaks down drastically.

On a significant note, the real permittivity values of the Test#39 reconstructions of the models go as high 8 without being capped off. This is due to the fact that they have been trained with HDR whose maximum real $\epsilon_r = 10$. As previously mentioned, this type of performance at high permittivities is among the novel research findings.

Further, it significantly took much lesser computational time to obtain the ITER10-ATTN-Unet-HDR results than the FEMCSI. It only took about 13 seconds to obtain a single reconstruction in the testing phase. In detail, the ITER10-HDR took about 11 seconds, while the ATTN-Unet took only about 2 seconds. On the other hand, running the FEMCSI for 300 iterations to reconstruct a single testing sample took about 58 seconds.

5.4.3.2.3 High Noise Interference

To further test the robustness of the HDR trained models, they are tested under different noise levels. White Gaussian noise of 5%, 10%, 15% and 20% are added to the scattered data of the 'Tilted-F' profile in Figure 47 along with its 'moderate', 'high' and 'very high' profiles in Figure 64, Figure 78, and Figure 79 respectively, prior to the ITER10 input generation for testing.

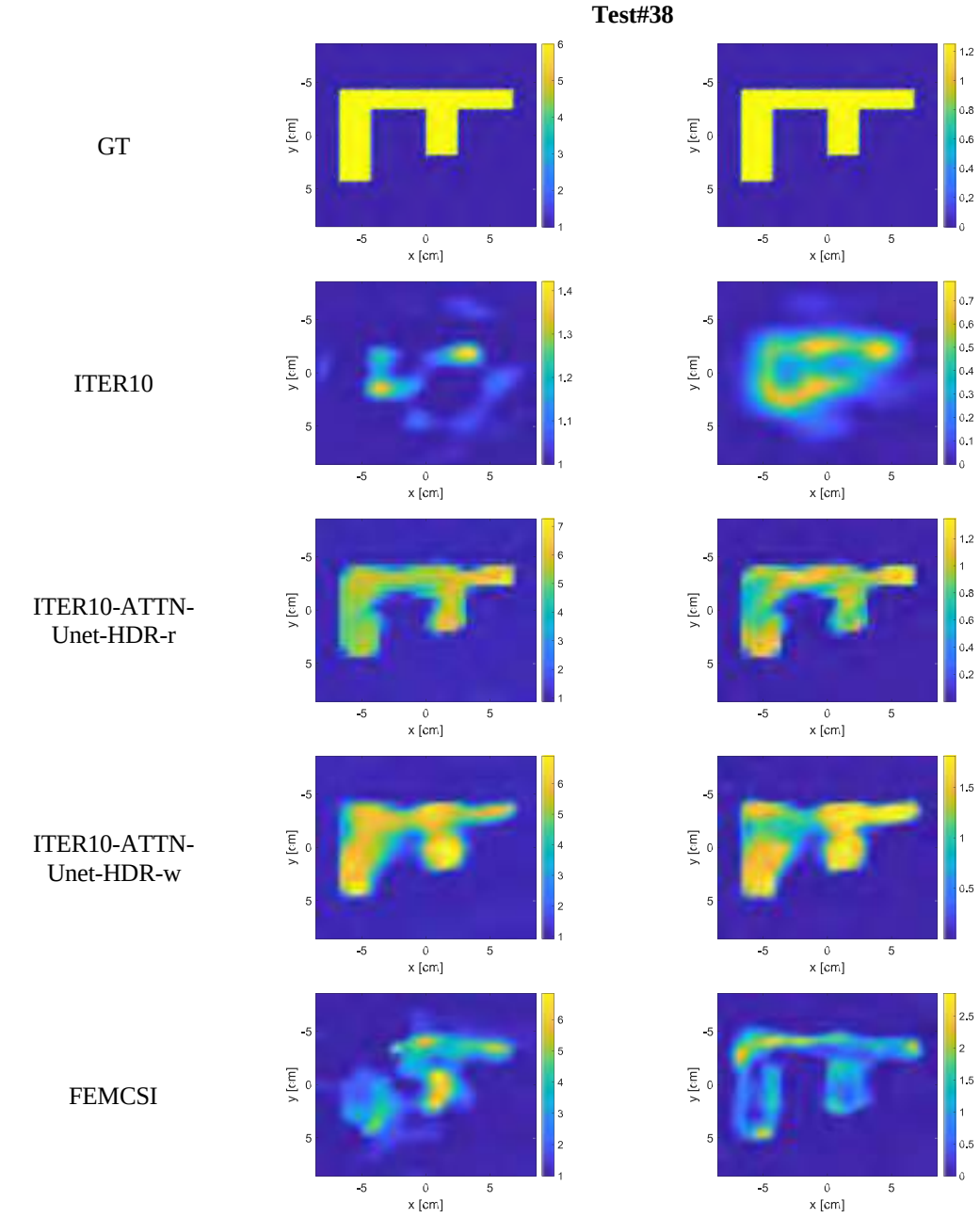

Figure 80. Reconstruction results of (a) real and (b) imaginary components of 'high' ϵ_r of Tilted-F.

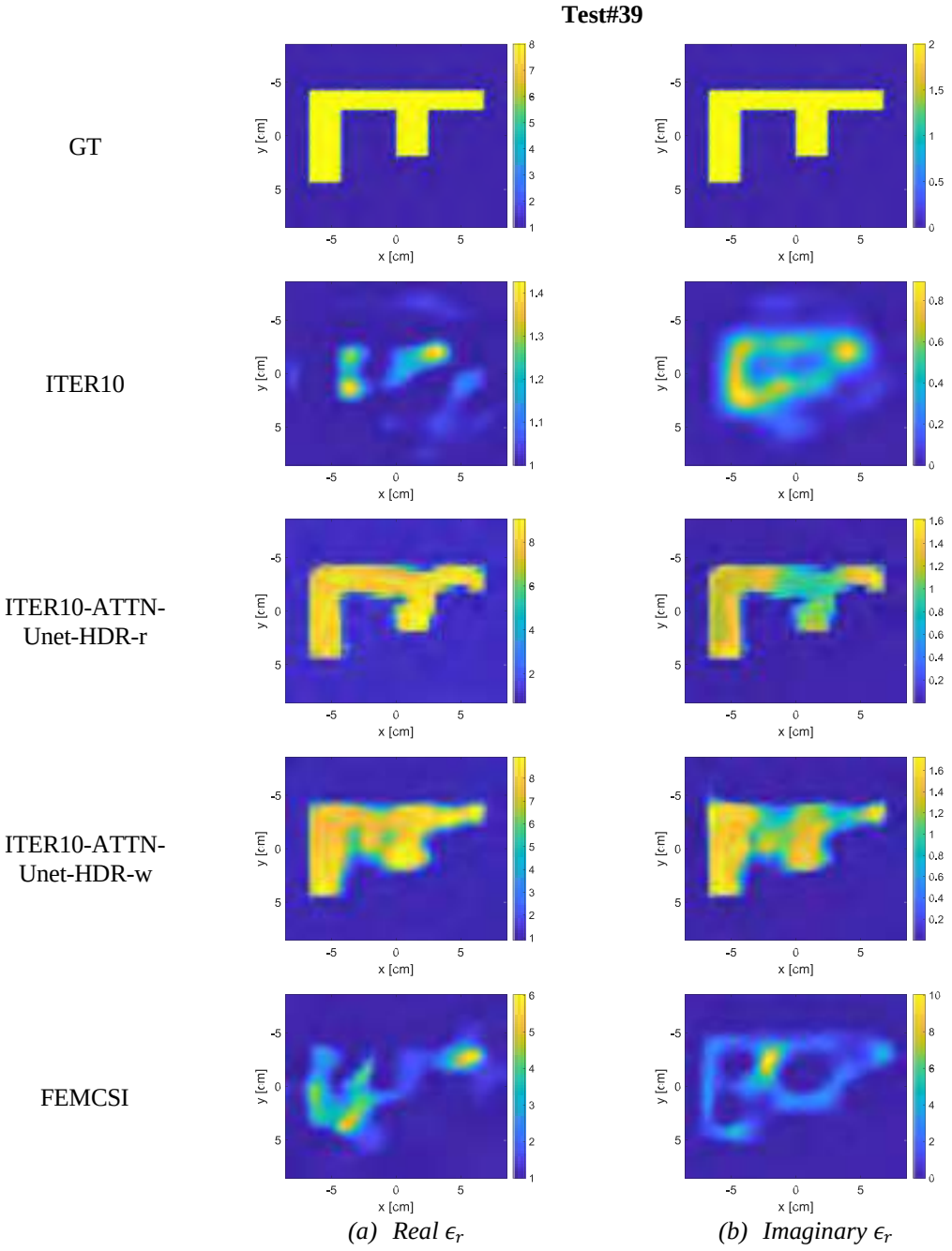

Figure 81. Reconstructions of (a) real and (b) imaginary components of 'very high' ϵ_r of Tilted-F.

Table 27. MSE between Ground Truth and Reconstructions of the real ϵ_r for Test#38-Test#39

Method	**MSE-Real**	
	Test#38	Test#39
ITER10-ATTN-Unet-HDR-r	0.7204	1.2350
ITER10-ATTN-Unet-HDR-w	0.9528	2.2284
FEMCSI	2.3485	6.6060

Table 28. MSE between Ground Truth and Reconstructions of the imaginary ϵ_r for Test#38-Test#39

Method	**MSE-Imaginary**	
	Test#38	Test#39
ITER10-ATTN-Unet-HDR-r	0.0465	0.1609
ITER10-ATTN-Unet-HDR-w	0.0936	0.1839
FEMCSI	1.8981	1.5933

Table 29. MSE between Ground Truth and Reconstructions for the ϵ_r for Test#38-Test#39

Method	**MSE**	
	Test#38	Test#39
ITER10-ATTN-Unet-HDR-r	0.3835	0.6979
ITER10-ATTN-Unet-HDR-w	0.5232	1.2061
FEMCSI	2.1233	4.0996

The Test#40 to Test#47 from Figure 109 to Figure 116 that depict the reconstructions of 'Tilted-F' and its 'moderate' profile, are shown in the Appendix A as these profiles belong to the LDR and the results achieved are not better than the ones obtained in configuration 3 with ITER10-ATTN-Unet.

Test#15 to Test#22 depicted in Figure 82 to Figure 89 show the reconstructions of the 'high' and very high' complex profile whose MSE values are summarized in Table 30 to Table 35. It can be clearly seen that the ITER10-ATTN-HDR-r stays strong even at high noise levels without breaking down much. This proves the robustness of the ITER10-ATTN-HDR-r at high permittivities under high noise levels.

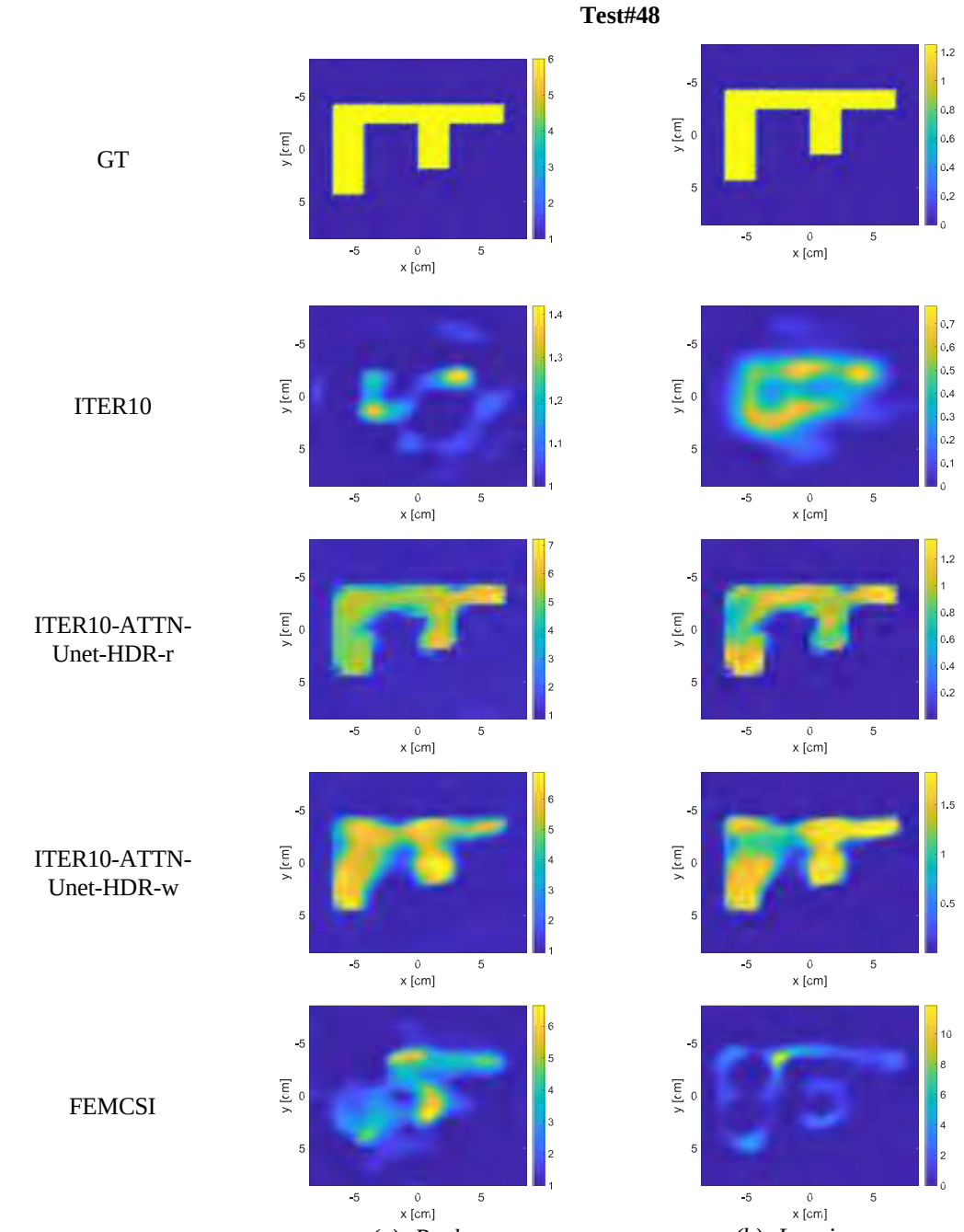

Figure 82. Reconstruction results of (a) real and (b) imaginary components of 'high' ϵ_r of Tilted-F with 5% noise.

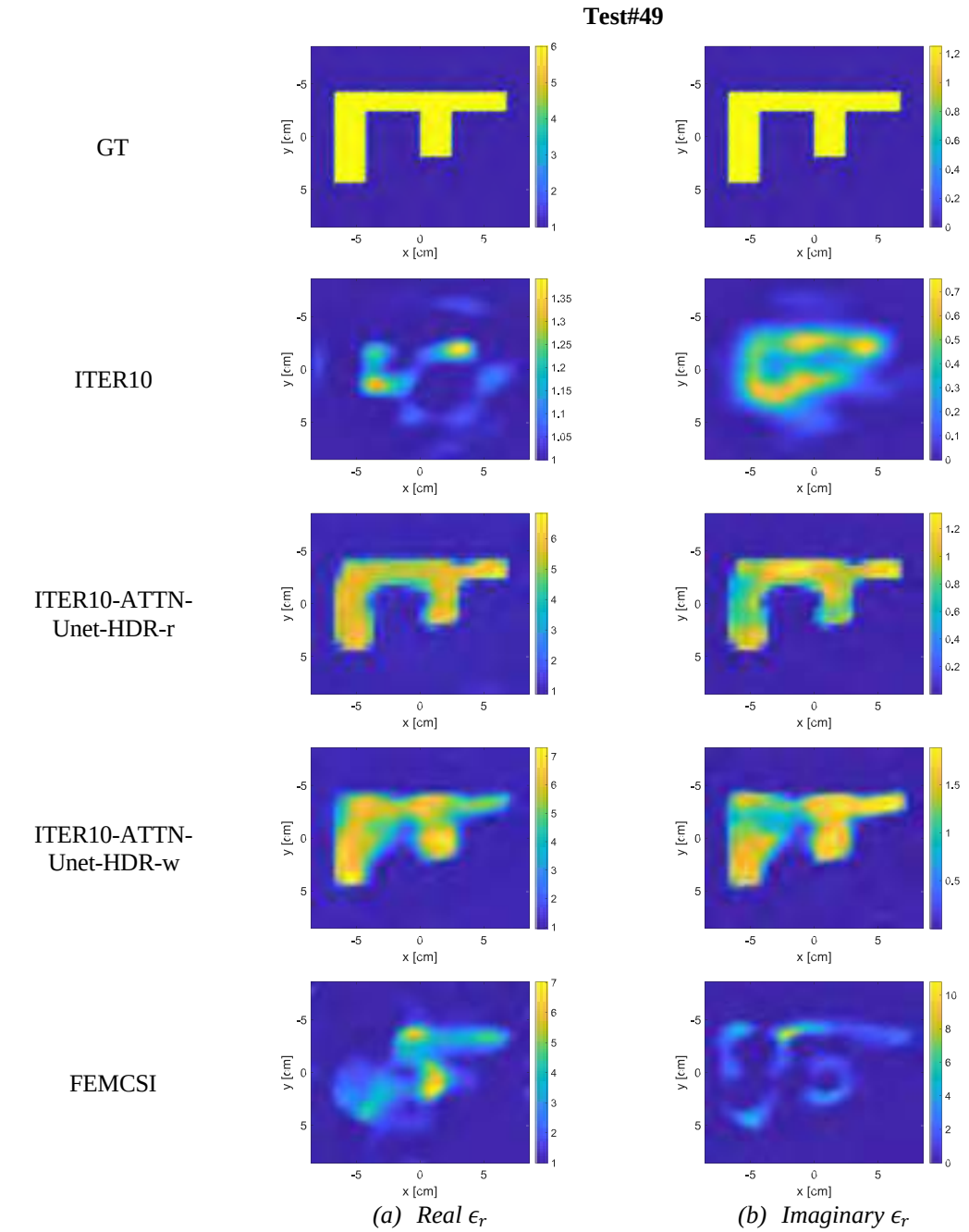

Figure 83. Reconstruction results of (a) real and (b) imaginary components of 'high' ϵ_r of Tilted-F with 10% noise.

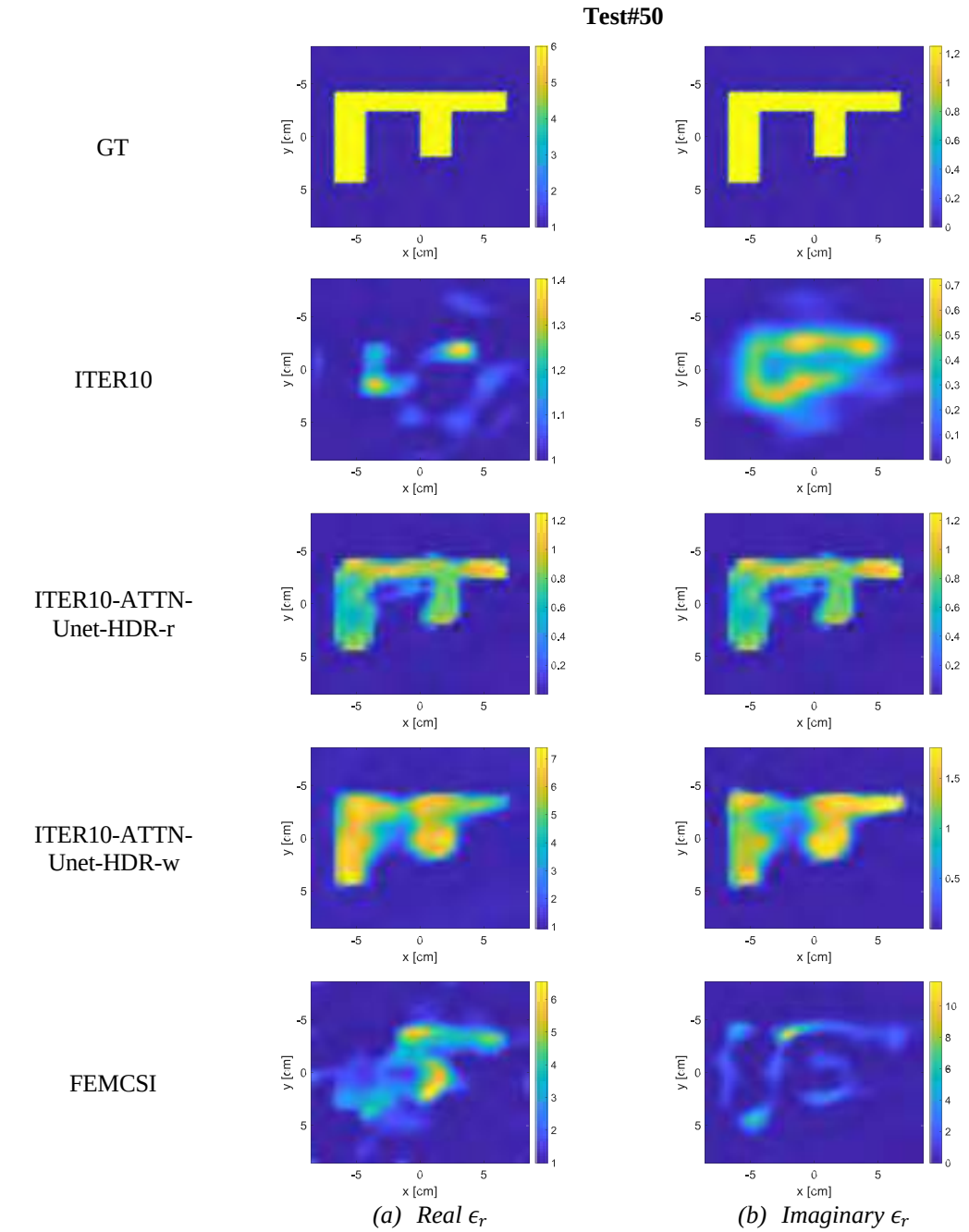

Figure 84. Reconstruction results of (a) real and (b) imaginary components of 'high' ϵ_r of Tilted-F with 15% noise.

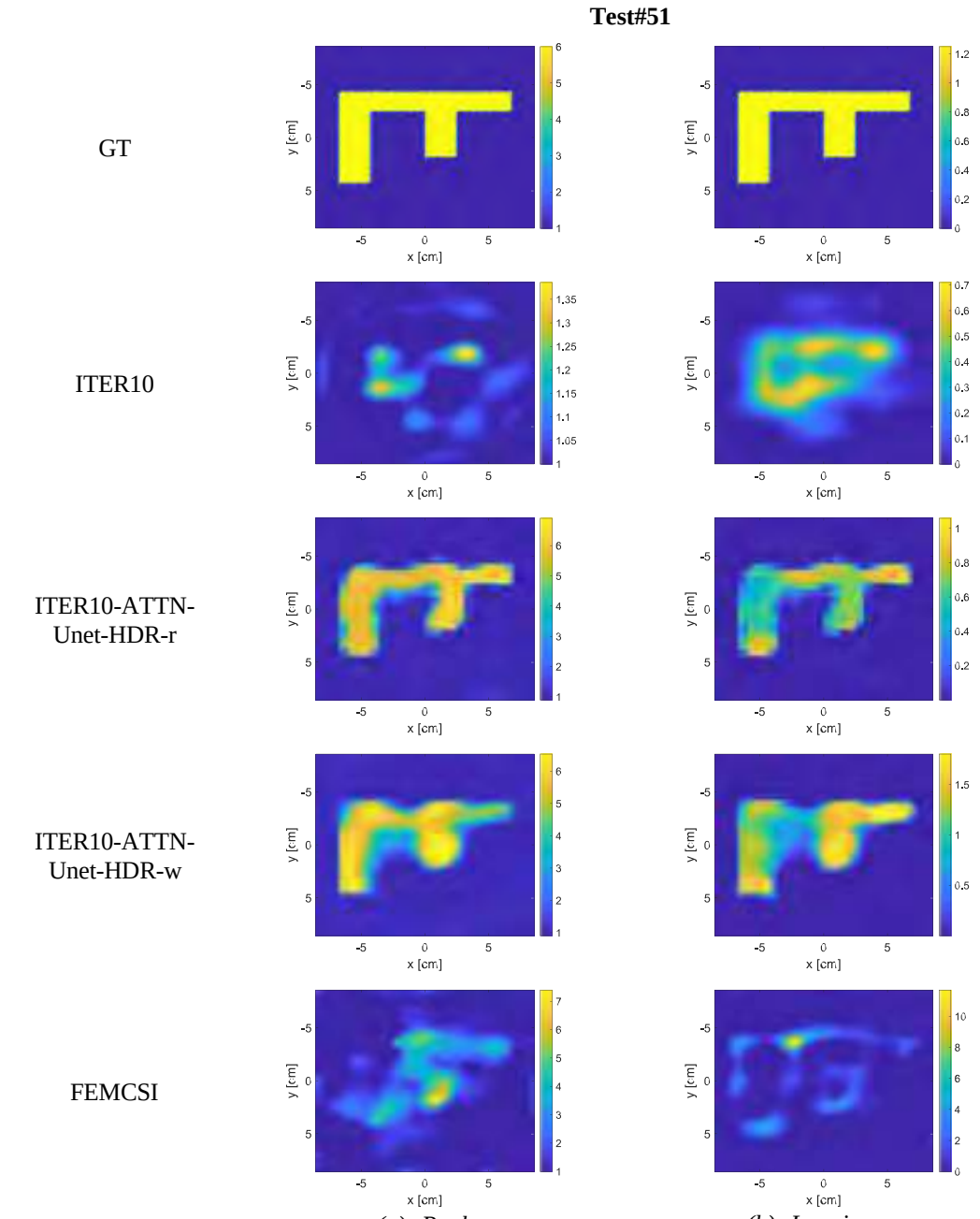

Figure 85. Reconstruction results of (a) real and (b) imaginary components of 'high' ϵ_r of Tilted-F with 20% noise.

Table 30. MSE of the real ϵ_r Reconstructions for Test#48-Test#51 under different Noise levels

Method	MSE-Real			
	Test#48	Test#49	Test#50	Test#51
ITER10-ATTN-Unet-HDR-r	0.6464	0.6583	0.6617	0.9554
ITER10-ATTN-Unet-HDR-w	0.9482	0.9813	0.9756	0.9855
FEMCSI	2.4284	2.4649	2.5097	2.7423

Table 31. MSE of the imaginary ϵ_r Reconstructions for Test#48-Test#51 under different Noise levels

Method	MSE-Imaginary			
	Test#48	Test#49	Test#50	Test#51
ITER10-ATTN-Unet-HDR-r	0.0426	0.0437	0.0504	0.0789
ITER10-ATTN-Unet-HDR-w	0.0937	0.0894	0.0665	0.0775
FEMCSI	0.9298	0.8135	0.8917	0.9767

Table 32. MSE of the ϵ_r Reconstructions for Test#48-Test#51 under different Noise levels

Method	MSE			
	Test#48	Test#49	Test#50	Test#51
ITER10-ATTN-Unet-HDR-r	0.3445	0.3510	0.3560	0.5171
ITER10-ATTN-Unet-HDR-w	0.5210	0.5353	0.5211	0.5315
FEMCSI	1.6791	1.6392	1.7007	1.8595

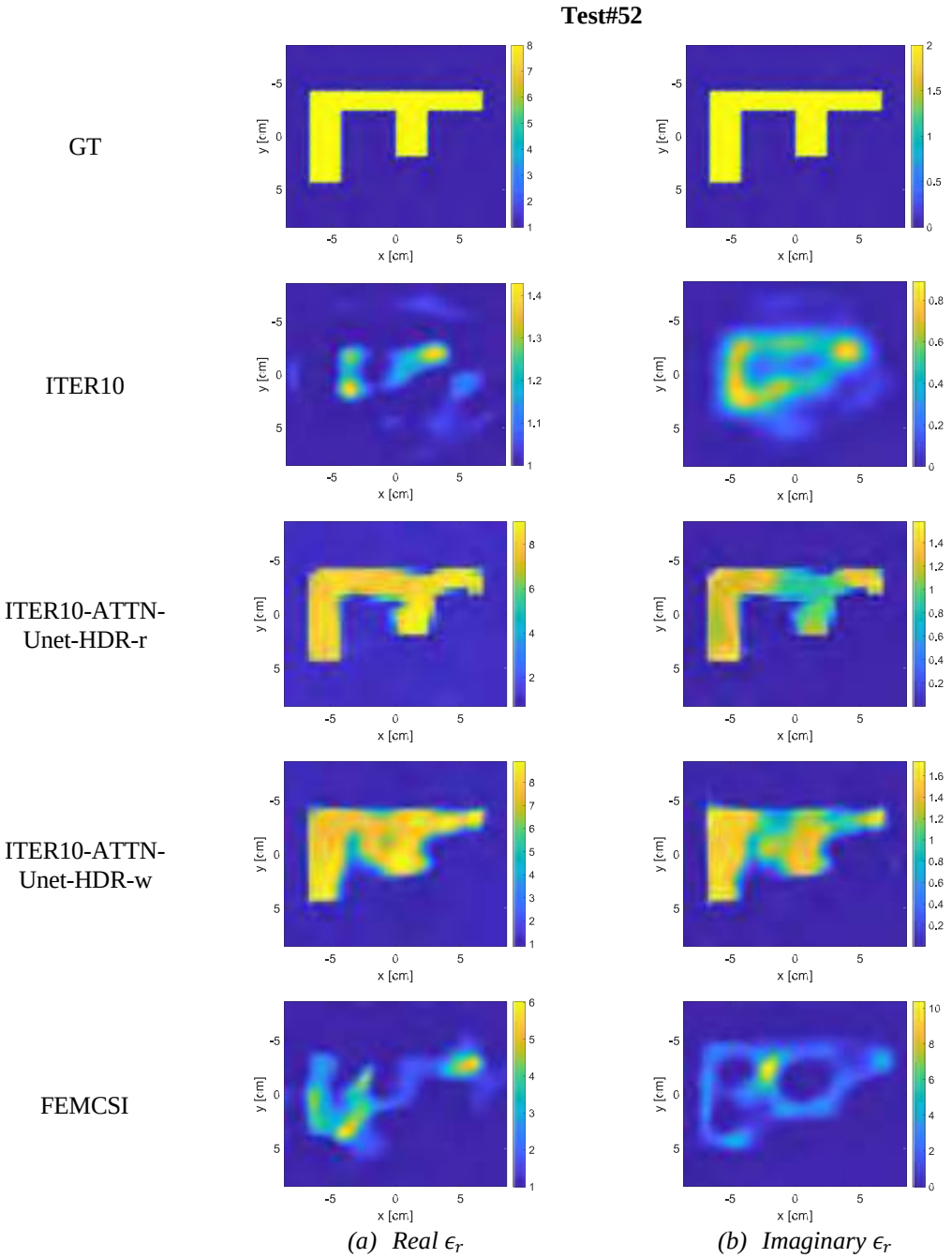

Figure 86. Reconstruction results of (a) real and (b) imaginary components of 'very high' ϵ_r of Tilted-F with 5% noise.

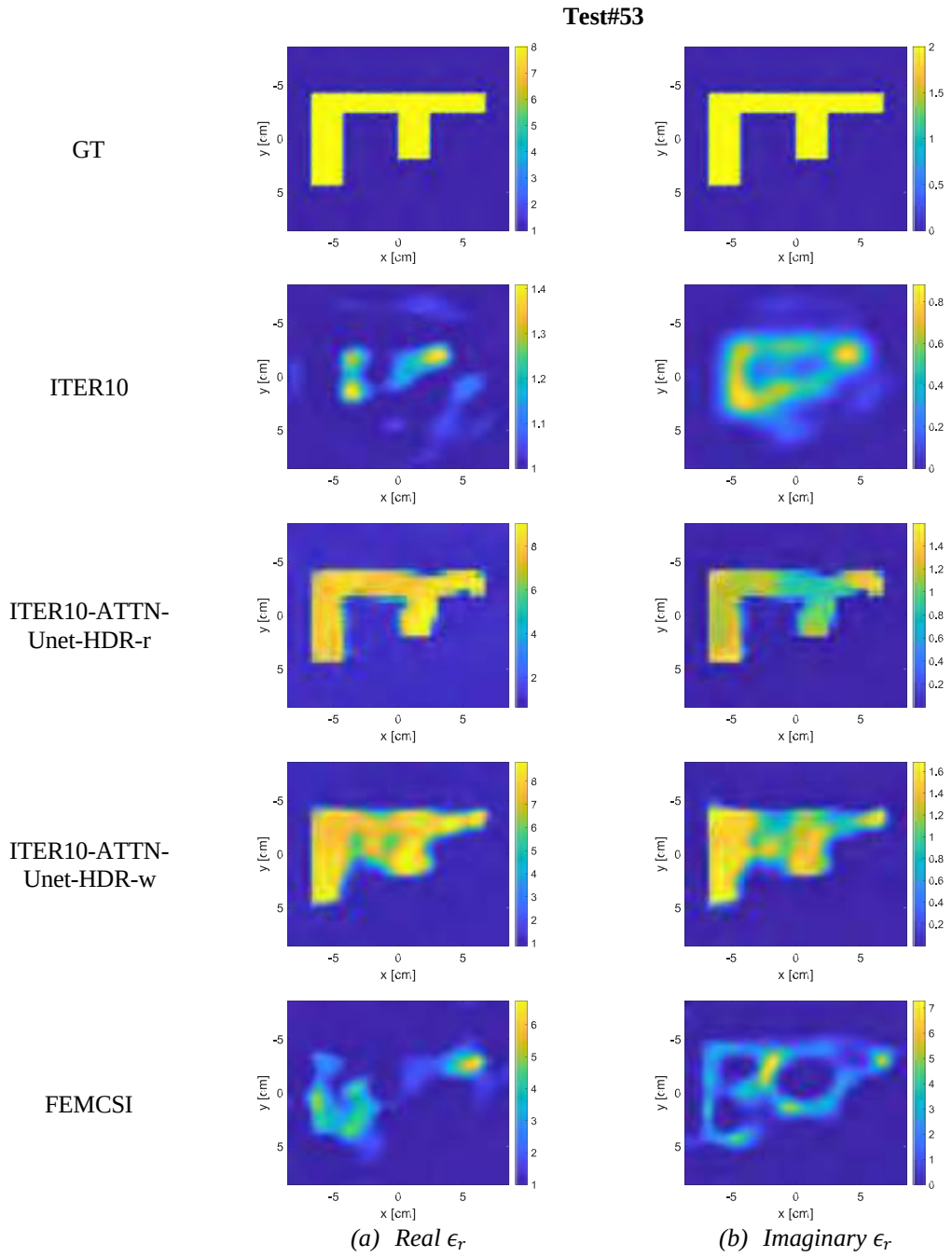

Figure 87. Reconstruction results of (a) real and (b) imaginary components of 'very high' ϵ_r of Tilted-F with 10% noise.

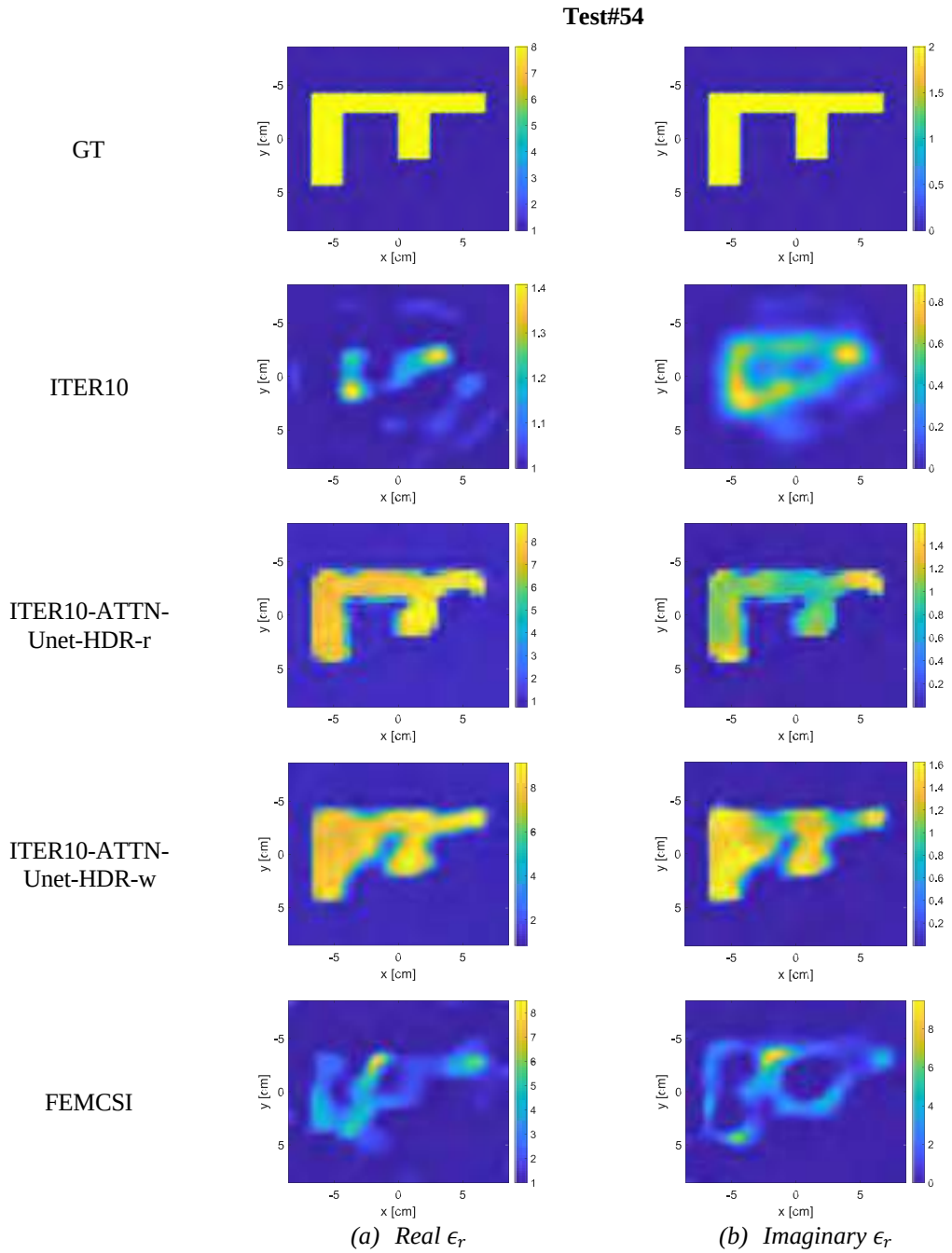

Figure 88. Reconstruction results of (a) real and (b) imaginary components of 'very high' ϵ_r of Tilted-F with 15% noise

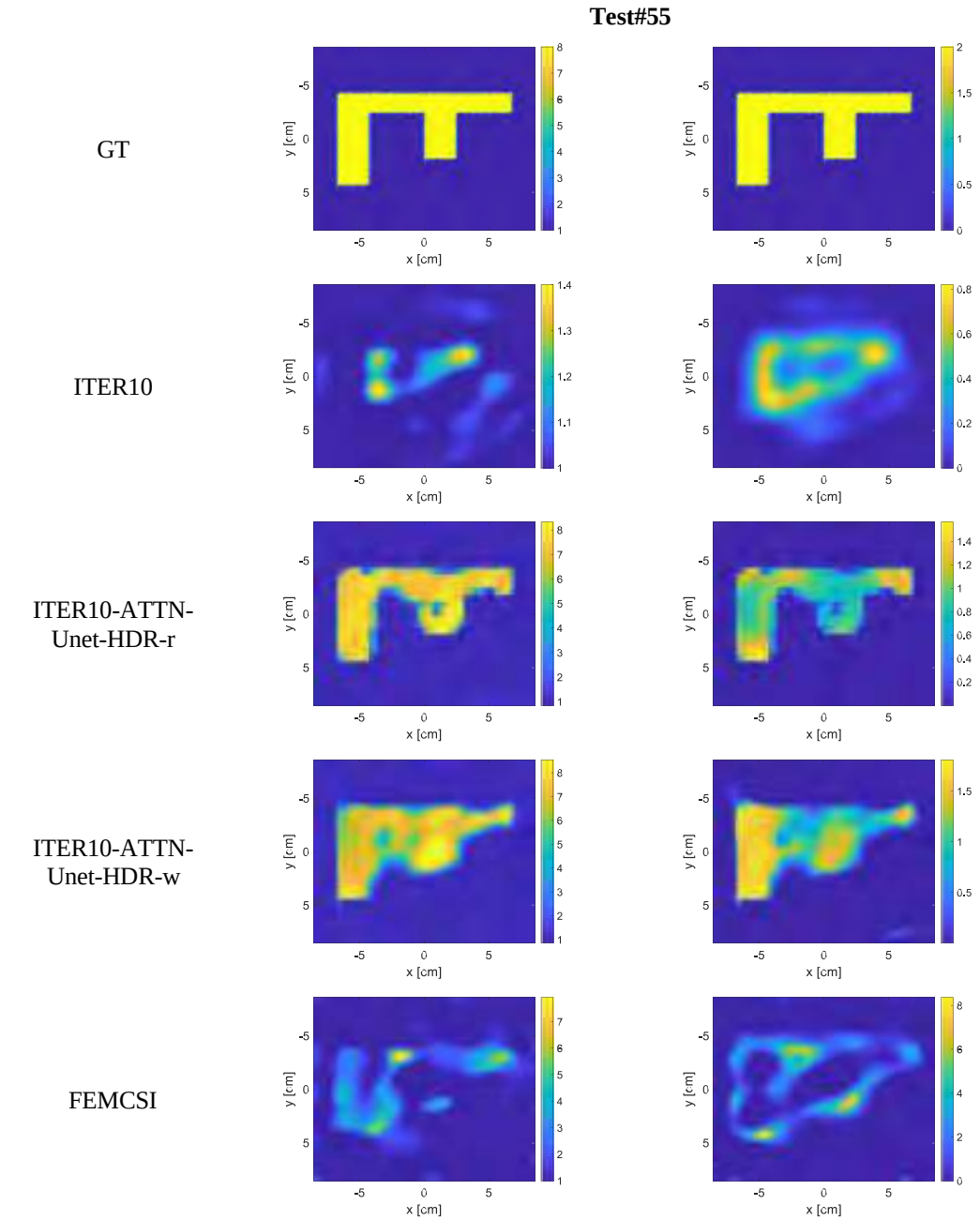

Figure 89. Reconstruction results of (a) real and (b) imaginary components of 'very high' ϵ_r of Tilted-F with 20% noise.

Table 33. MSE of the real ϵ_r Reconstructions for Test#52-Test#55 under different Noise levels

Method	MSE-Real			
	Test#52	Test#53	Test#54	Test#55
ITER10-ATTN-Unet-HDR-r	1.1263	1.1868	1.4413	1.2873
ITER10-ATTN-Unet-HDR-w	2.1995	2.2090	2.2704	2.2576
FEMCSI	6.6037	6.5652	6.2949	5.8497

Table 34. MSE of the imaginary ϵ_r Reconstructions for Test#52-Test#55 under different Noise levels

Method	MSE-Imaginary			
	Test#52	Test#53	Test#54	Test#55
ITER10-ATTN-Unet-HDR-r	0.1655	0.1733	0.1970	0.2125
ITER10-ATTN-Unet-HDR-w	0.1764	0.1883	0.1835	0.1921
FEMCSI	1.6014	1.3040	1.4402	1.3919

Table 35. MSE of the ϵ_r Reconstructions for Test#52-Test#55 under different Noise levels

Method	MSE			
	Test#52	Test#53	Test#54	Test#55
ITER10-ATTN-Unet-HDR-r	0.6459	0.6801	0.8191	0.7499
ITER10-ATTN-Unet-HDR-w	1.1880	1.1987	1.2269	1.2249
FEMCSI	4.1025	3.9346	3.8676	3.6208

5.5 Experimental Data Results

After demonstrating the ITER10-ATTN-Unet's effectiveness in reconstructing cross-database synthetic data with respect to quality, generalization, and durability, it is chosen to reconstruct the University of Manitoba's (UM) experimental data [37].

5.5.1 Forward Problem Configuration

Retraining the model was not necessary because the forward problem configuration for all of the UM experimental data was the same as for configurations 3 and 4. The imaging domain D was selected to be a square centered in the middle of the microwave imaging system with a side-length of 17 cm and is illuminated by 24 transmitters. For each transmitter, the scattered data are collected at 24 receivers. The transmitting and receiving points are co-located and evenly spaced on a circular surface S of radius of 13 cm [37].

5.5.2 Wood-Nylon Target – UM1

The first University of Manitoba experimental data referred as UM1 is a lossy dielectric target that consists of nylon-66 cylinder next to a square wooden block as depicted in Figure 90. The wooden block has dimensions of 8.7×8.8 cm and the nylon-66 cylinder has a diameter of 3.81 cm. Their relative complex permittivities are $\epsilon_r^{wood} = 2.0 - j0.2$ and $\epsilon_r^{nylon} = 3.0 - j0.03$ at a frequency $f = 3$ GHz [37]. In the same process used to obtain the inputs for the complex profiles, the BP and ITER10 inputs are also produced from the UM1 scattered data.

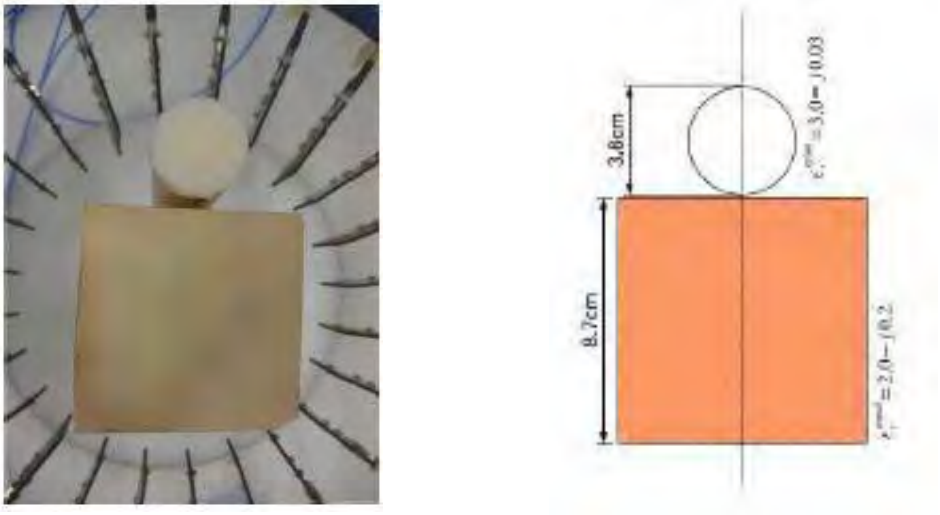

(a) (b)

Figure 90. The UM1 target of a wooden block and a nylon cylinder [8].

5.5.3 Two-Nylon Cylinders – UM2 to UM11

The second University of Manitoba experimental data consists of two nylon-66 cylinders each with a diameter of 3.8 cm and a complex relative permittivity $\epsilon_r^{nylon} = 3.0 - j0.03$ at 3 GHz [37]. The MWI setup of the two cylinders is shown in Figure 91. The two cylinders that made up the target were positioned at two distinct angles in the imaging domain. In the first angle setup, the separation of the two cylinders was varied from 0 to 5 mm in 1-mm steps. This led to obtaining the scattered data for UM2 to UM7. Then with the second angle setup, the two cylinders were separated by 2 mm, 4 mm, 7 mm, and 10 mm producing the UM8 to UM11 scattered data. Similar to UM1, the BP and ITER10 input data of UM2 to UM11 were produced using their scattered data.

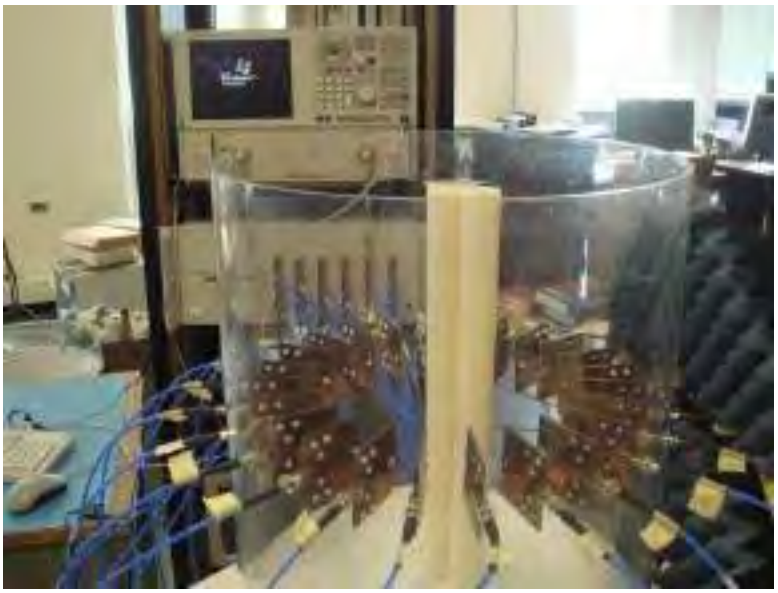

Figure 91. The MWI system with two nylon cylinders [39].

5.5.4 Butternut Squash – UM12

The third University of Manitoba experimental data UM12 is a butternut squash, which is technically a fruit. Figure 92 shows a sample of the butternut squash that was used in the MWI system in the University of Manitoba Lab. Though a proper picture of the setup isn't available, the scattered data obtained from the MWI system is available from the lab at 3 GHz. The complex relative permittivity of the butternut squash at 3 GHz is unknown. In the same process used to obtain the inputs for the complex profiles, the BP and ITER10 inputs are also produced from the UM1 scattered data.

Figure 92. A sample of the Butternut squash target UM12

5.5.5 LDR Network Results

The trained BP-ATTN-Unet and the optimal ITER10-ATTN-Unet from configuration 3 were used to test the UM experimental data. Though, the primary focus was on the optimal ITER10-ATTN-Unet results, the BP-ATTN-Unet was also tested for the purpose of comparison.

5.5.5.1 UM1

The Test#56 reconstructed results of UM1 are shown in Figure 93 along with its FEMCSI results. It can be clearly seen that the ITER10-ATTN-Unet achieves much better image quality than the BP-ATTN-Unet and the FEMCSI.

5.5.5.2 UM2 – UM11

The trained BP-ATTN-Unet and the ITER10-ATTN-Unet were both tested with their respective inputs. Test#58 to Test#67 shown in Figure 94 to Figure 103 display the reconstructed results of the networks along with its FEMCSI results. It can be clearly seen that the ITER10-ATTN-Unet reconstructions are of high accuracy and resolution when compared with the BP-trained model and the FEMCSI. Moreover, the resolution tends to improve with the increase in the separation of the two cylinders. About 3mm is when the separation gap starts to become visible, revealing the two separate cylinders. High resolution is reached at 7 and 10 mm, allowing for a clear and accurate visualization of the two cylinders.

5.5.5.3 UM12

The Test#68 reconstructed results of UM12 are shown in Figure 104 along with its FEMCSI results. It can be clearly seen that the ITER10-ATTN-Unet achieves much better image quality than the BP-ATTN-Unet and the FEMCSI. But one important finding from the FEMCSI's real ϵ_r is that the value goes as high as 10. This indicates that the permittivity range of butternut squash is quite high. Though the reconstruction image of the ITER10-ATTN-Unet is of superior quality, its maximum training limit caps the true ϵ_r value at 4, which isn't accurate.

So, in order to accurately reconstruct the high permittivity UM12, it needs to be tested with the HDR network that has been trained and tested in configuration 4.

Therefore, as discussed earlier, a separate model needs to be trained with high dynamic range (HDR) of complex relative permittivity in order to reconstruct the targets with high permittivities more accurately.

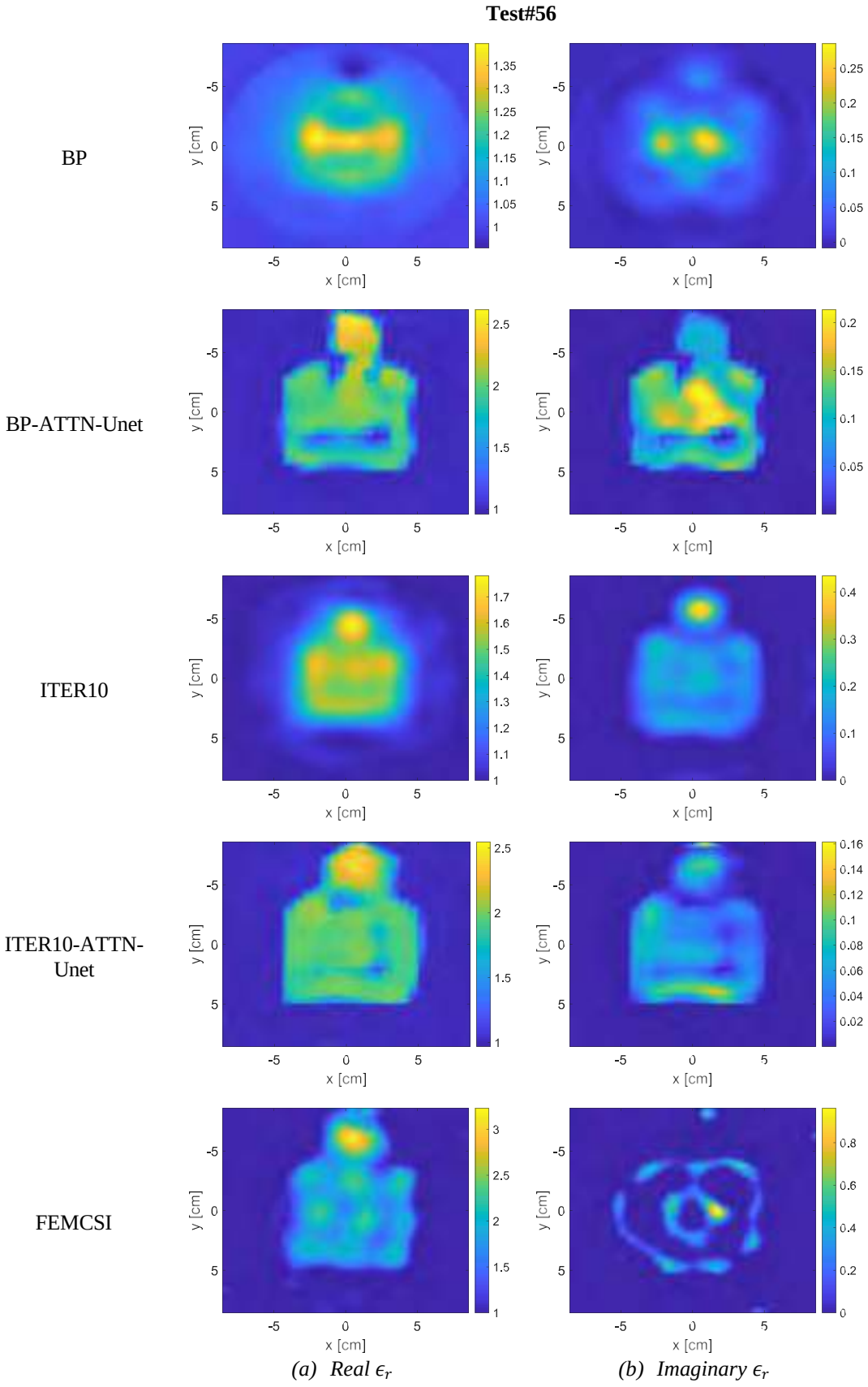

Figure 93. Reconstruction results of (a) real and (b) imaginary components of ϵ_r of UM1.

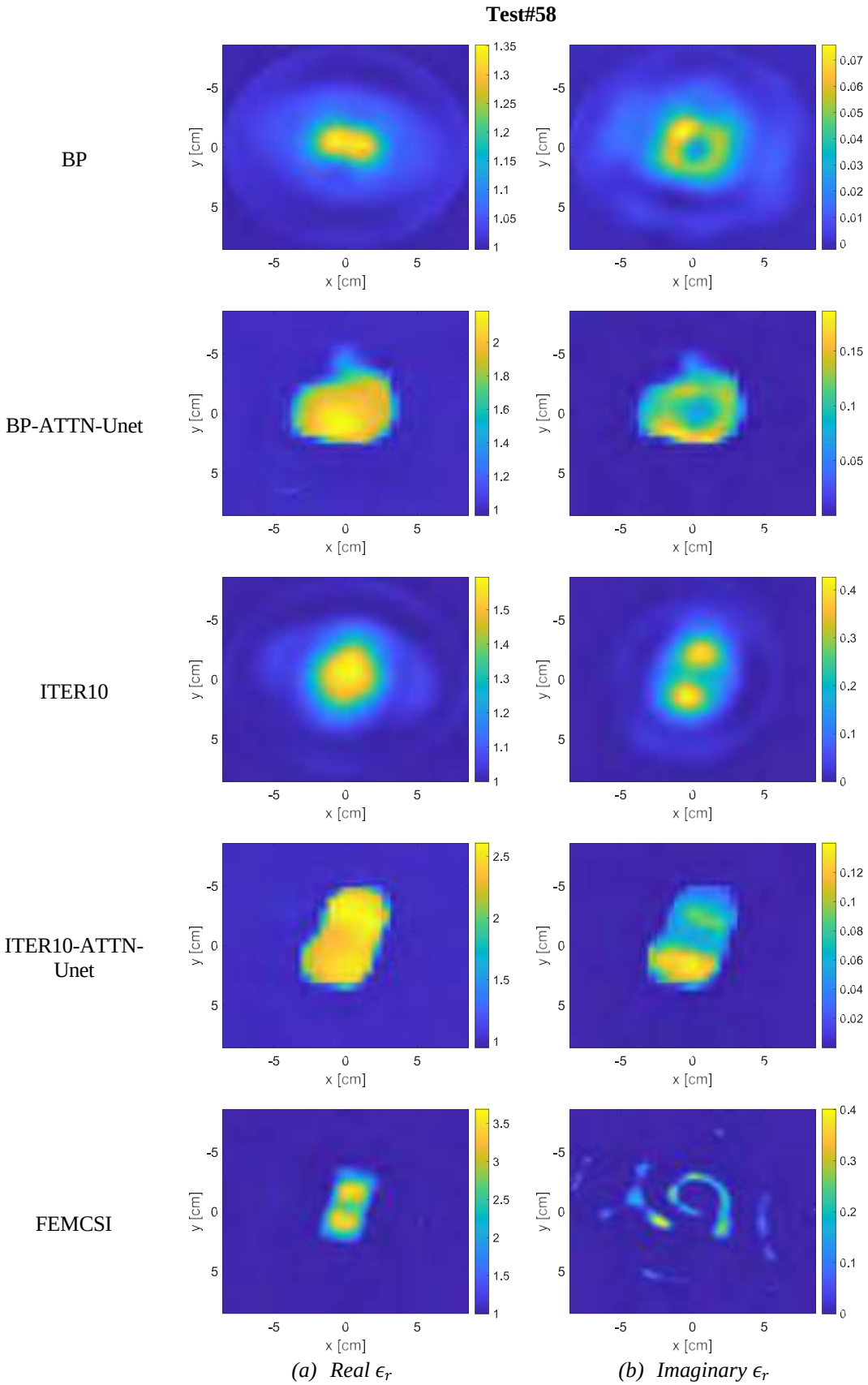

Figure 94. Reconstruction results of (a) real and (b) imaginary components of ϵ_r of UM2 with 0mm separation.

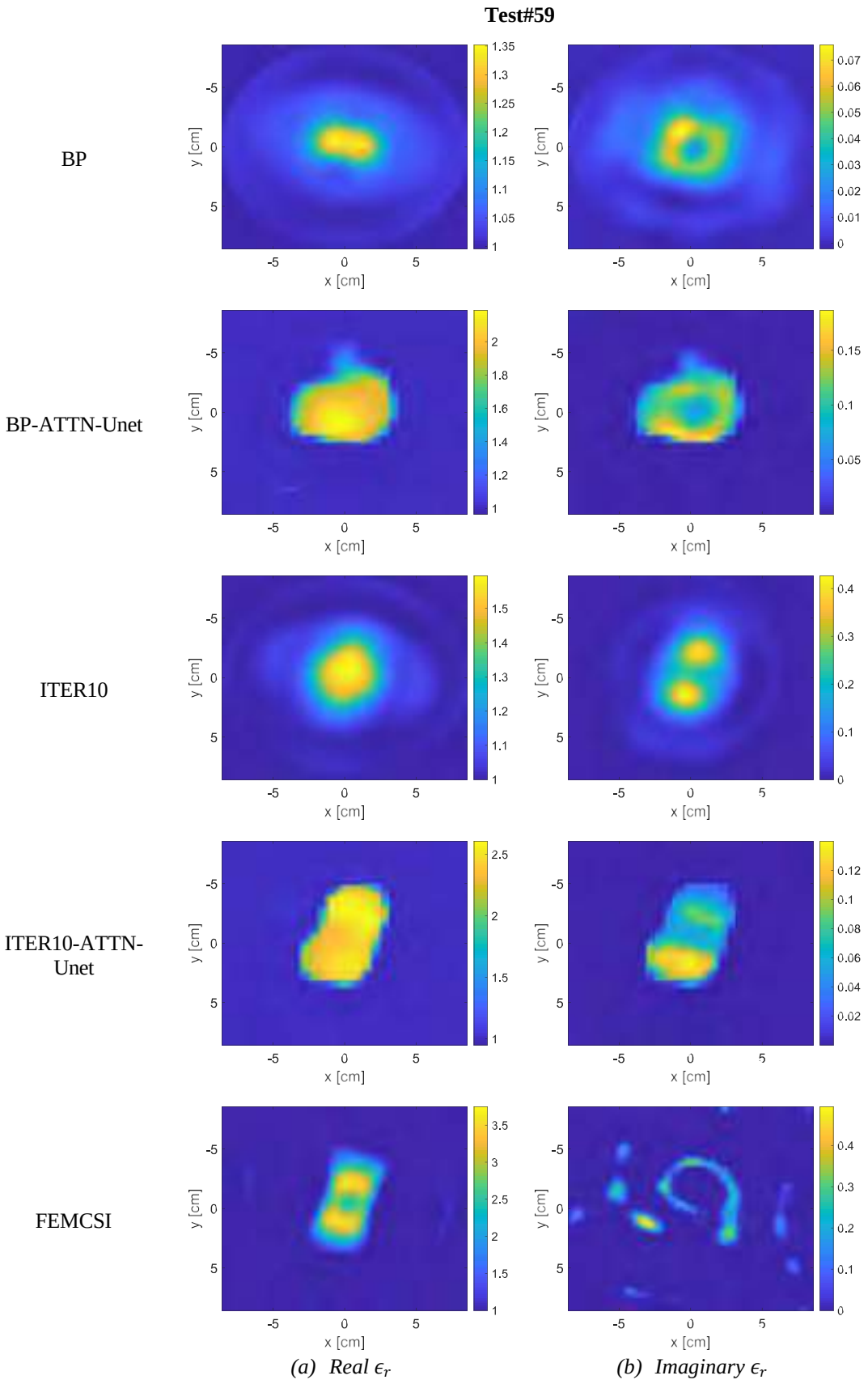

Figure 95. Reconstruction results of (a) real and (b) imaginary components of ϵ_r of UM3 with 1mm separation.

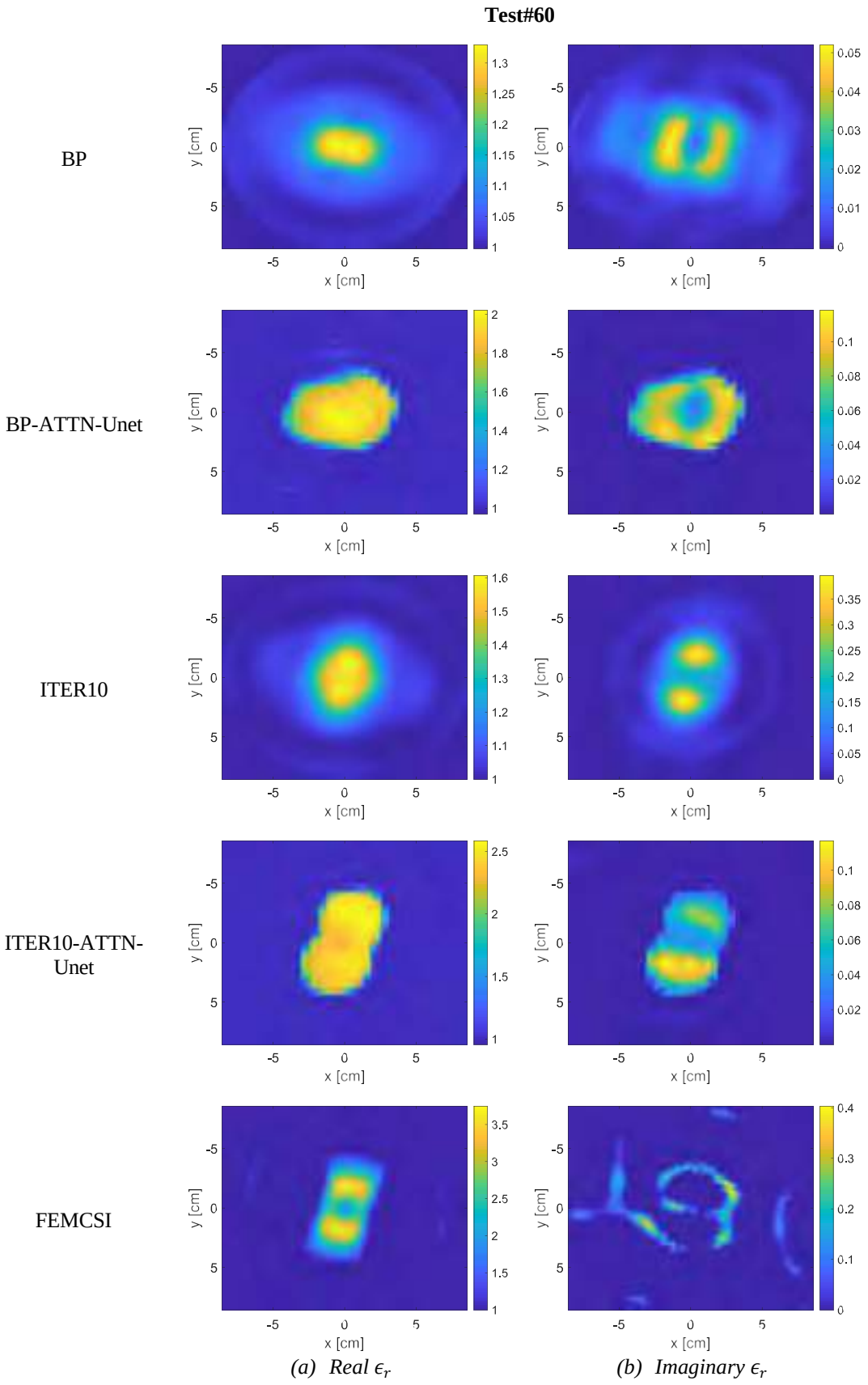

Figure 96. Reconstruction results of (a) real and (b) imaginary components of ϵ_r of UM4 with 2mm separation.

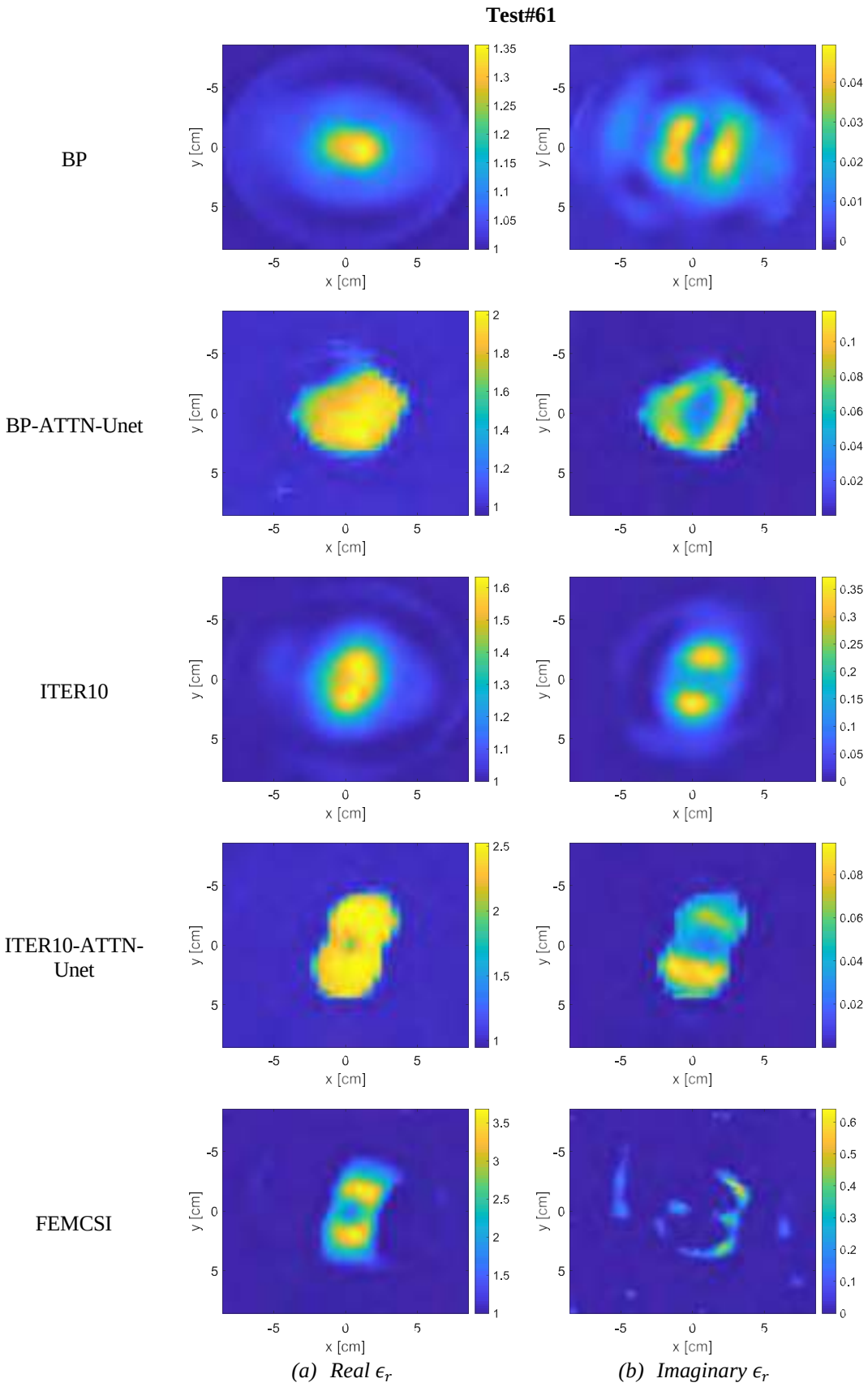

Figure 97. Reconstruction results of (a) real and (b) imaginary components of ϵ_r of UM5 with 3mm separation.

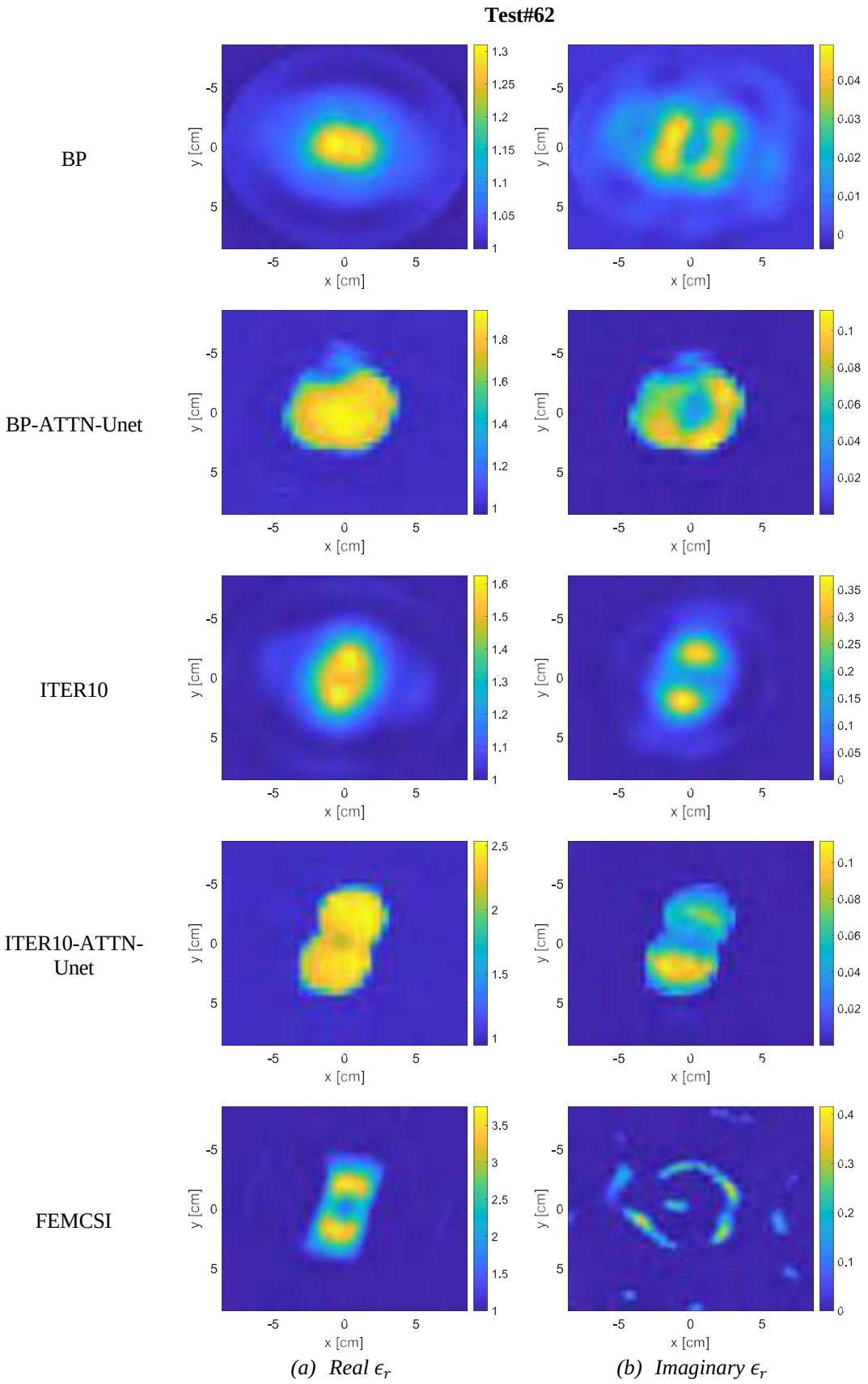

Figure 98. Reconstruction results of (a) real and (b) imaginary components of ϵ_r of UM6 with 4mm separation.

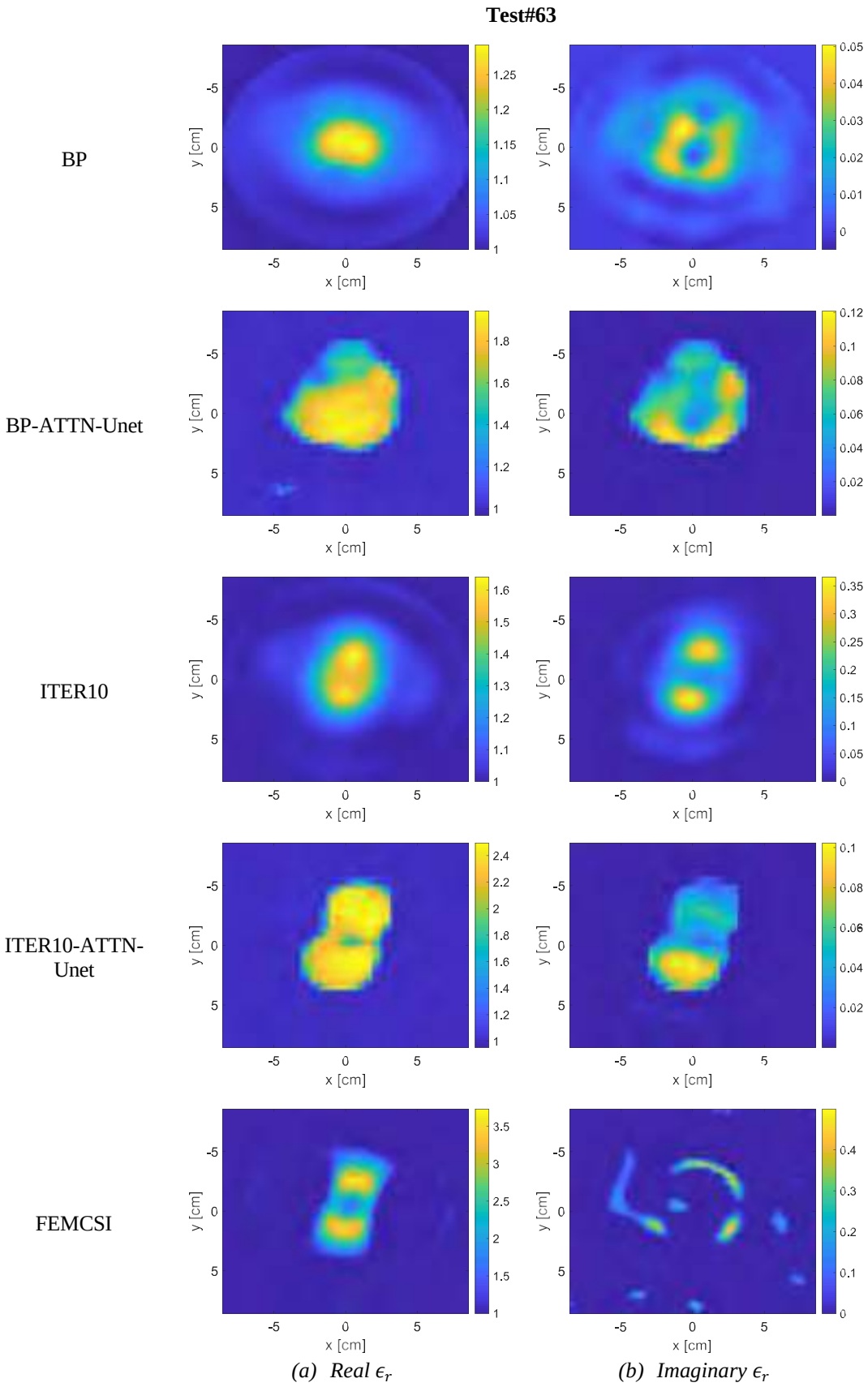

Figure 99. Reconstruction results of (a) real and (b) imaginary components of ϵ_r of UM7 with 5mm separation.

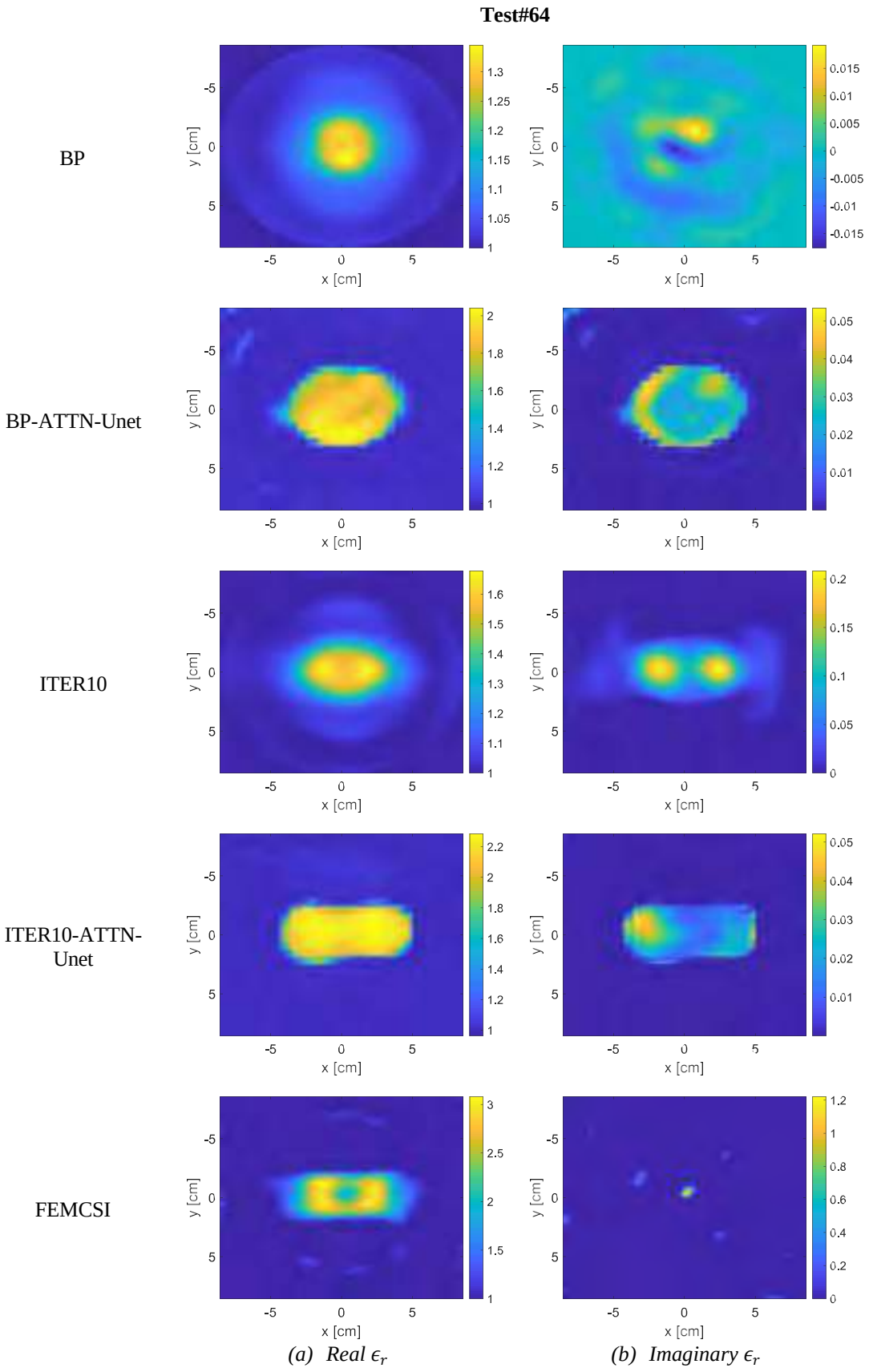

Figure 100. Reconstruction results of (a) real and (b) imaginary components of ϵ_r of UM8 with 2mm separation.

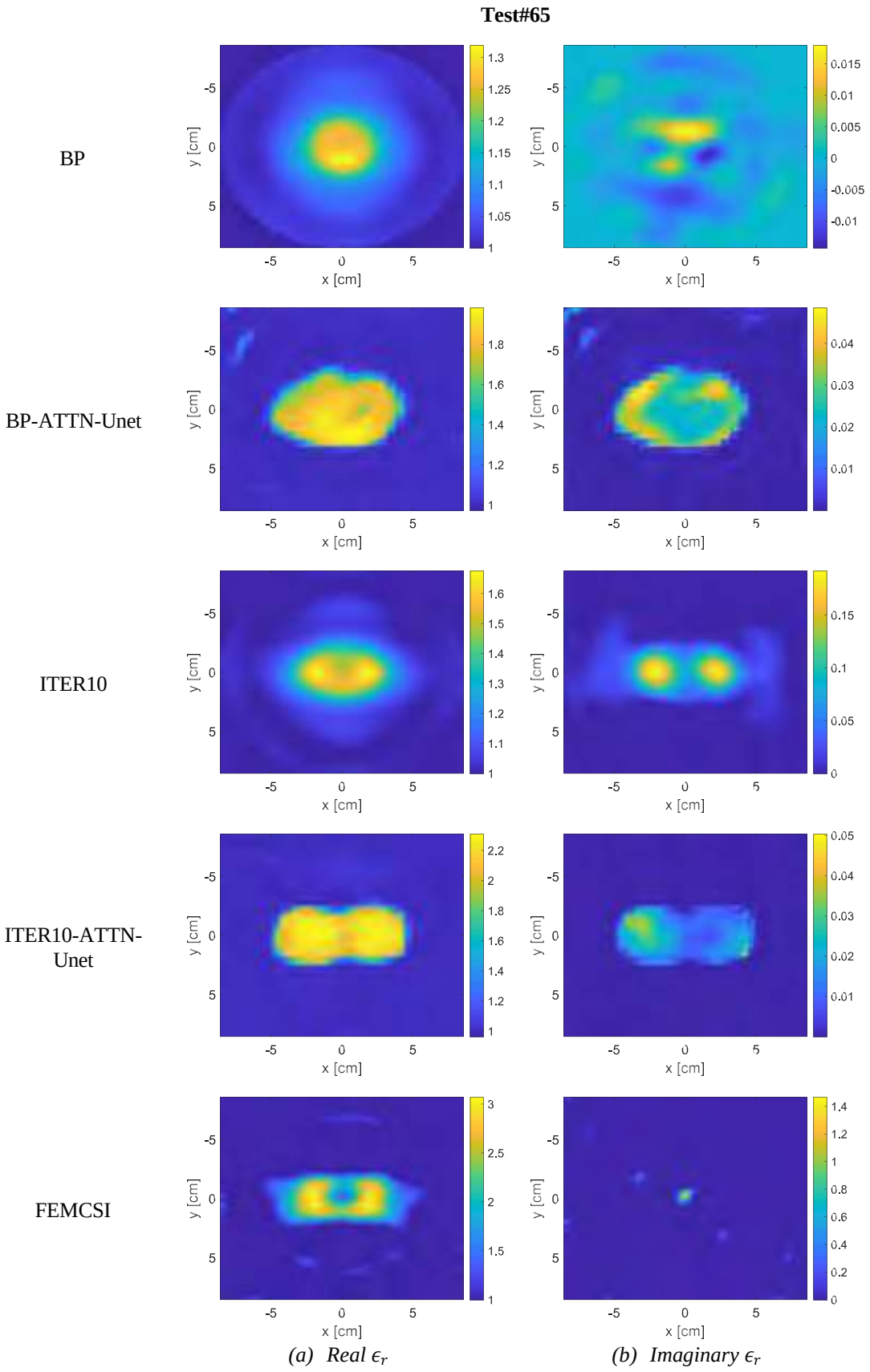

Figure 101. Reconstruction results of (a) real and (b) imaginary components of ϵ_r of UM9 with 4mm separation.

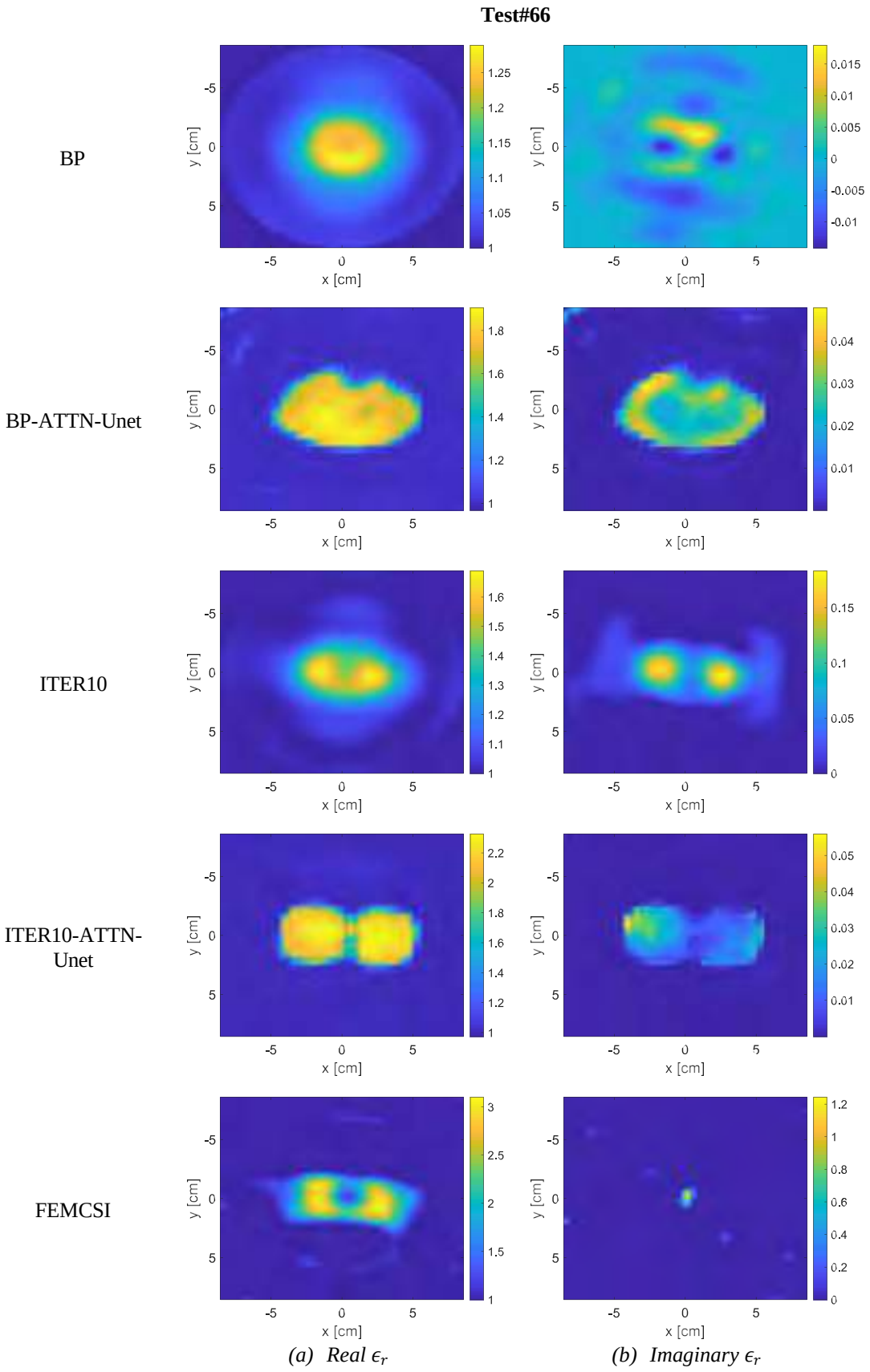

Figure 102. Reconstruction results of (a) real and (b) imaginary components of ϵ_r of UM10 with 7mm separation.

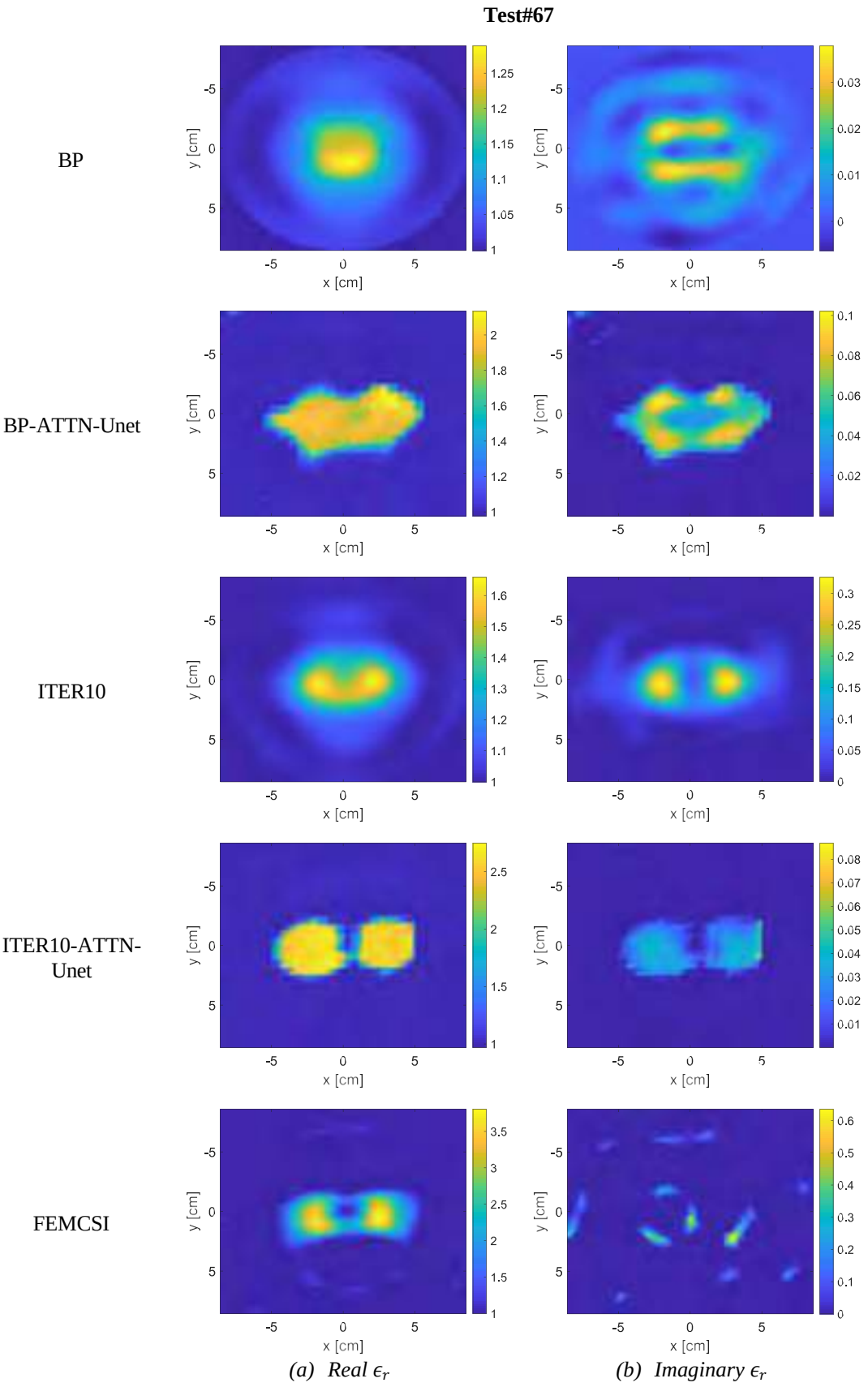

Figure 103. Reconstruction results of (a) real and (b) imaginary components of ϵ_r of UM11 with 10mm separation.

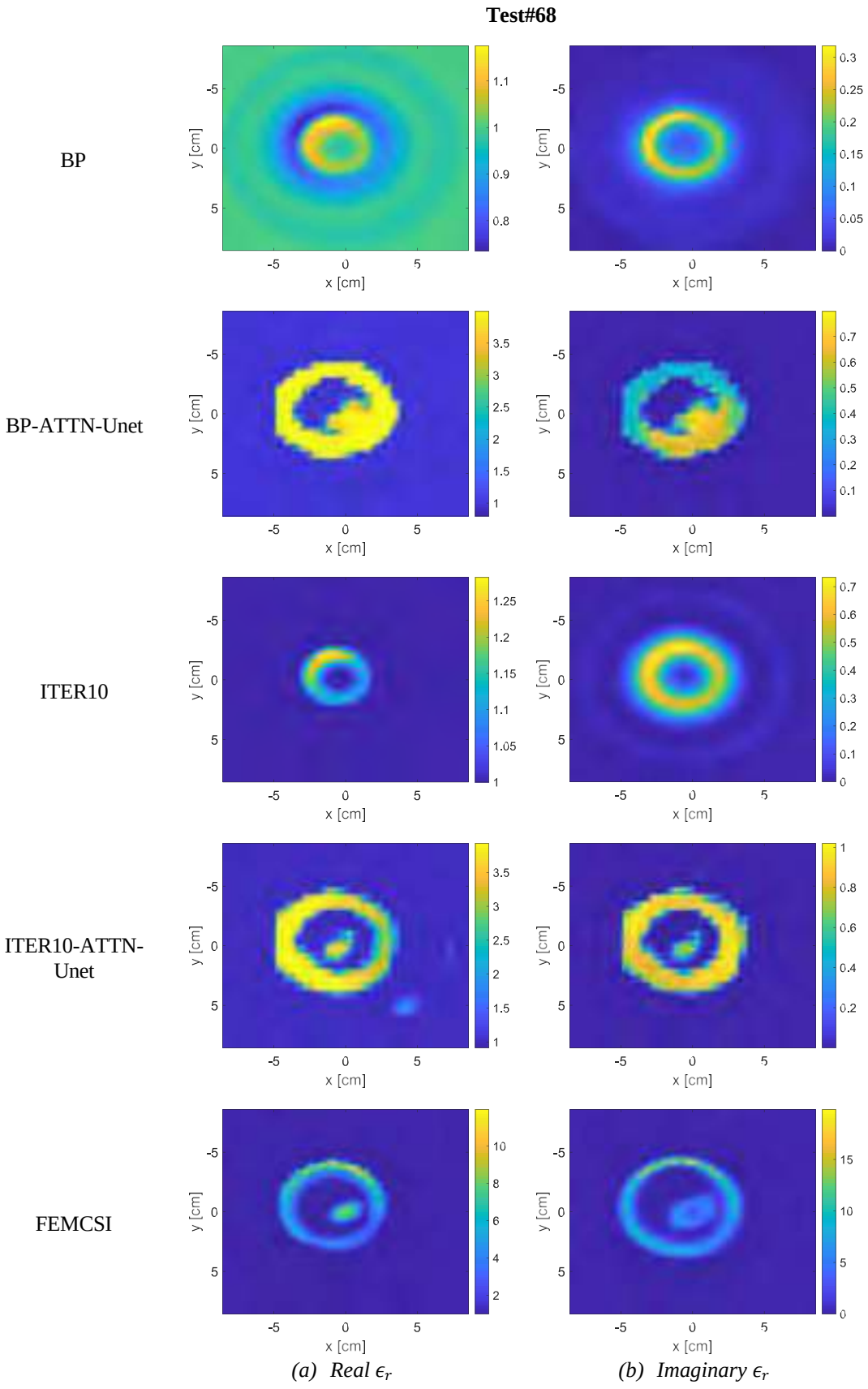

Figure 104. Reconstruction results of (a) real and (b) imaginary components of ϵ_r of UM12.

5.5.6 HDR Network Results

To further validate the generalization capability of the HDR trained models, they are tested with the University of Manitoba experimental data consisting of UM1 to UM12. Test#69 to Test#79 results for UM1 through UM11 are displayed in Appendix B in Figure 117 to Figure 127 since they fall inside the LDR of permittivities and their reconstruction results with the HDR trained models are not better than the ones achieved in configuration 3 with ITER10-ATTN-Unet.

5.5.6.1 UM12

UM12 is the only experimental data that has high relative permittivity which is seen in FEMCSI results in configuration 3. Therefore, the HDR trained models are tested with UM12. Test#80 in Figure 105 depict the reconstruction results obtained with the HDR trained models along with the ITER10 input and FEMCSI results. It can be seen that the HDR trained models provide reconstructions of better quality and accuracy than the FEMCSI which fails drastically due to the high permittivity of the butternut squash. However, this time ITER10-ATTN-Unet-HDR-w produced reconstructions of higher quality and resolution than the ITER10-ATTN-Unet-HDR-r. This fluctuation in the performance of the ITER10-ATTN-Unet-HDR-r is due to the limited input size of 10000 MNIST targets during training. These 10000 targets proved sufficient in the LDR setup where the ITER-ATTN-Unet provided high quality results throughout its permittivity range. However, with the permittivity range increasing by three times in the HDR setup, the 10000 MNIST targets proved insufficient for efficiently training the ITER10-ATTN-Unet across all permittivities.

5.6 Computational Limitations

Limited GPU memory of only 2GB is the reason for not being able to select beyond 10000 MNIST targets for the HDR model training. With more GPU memory, the input size for the HDR models can be extended at the minimum by three times to make it 30000 MNIST targets. With this increase in input size, the ITER10-ATTN-Unet-HDR can effectively train with sufficient input data to produce consistent high-quality reconstructions similar to the ITER10-ATTN-Unet across the entire HDR of permittivities. Moreover, the small batch size of 4 selected for the ITER10-ATTN-Unet is also due to the limited GPU memory. Larger batch sizes can be studied to provide even better results with additional GPU memory.

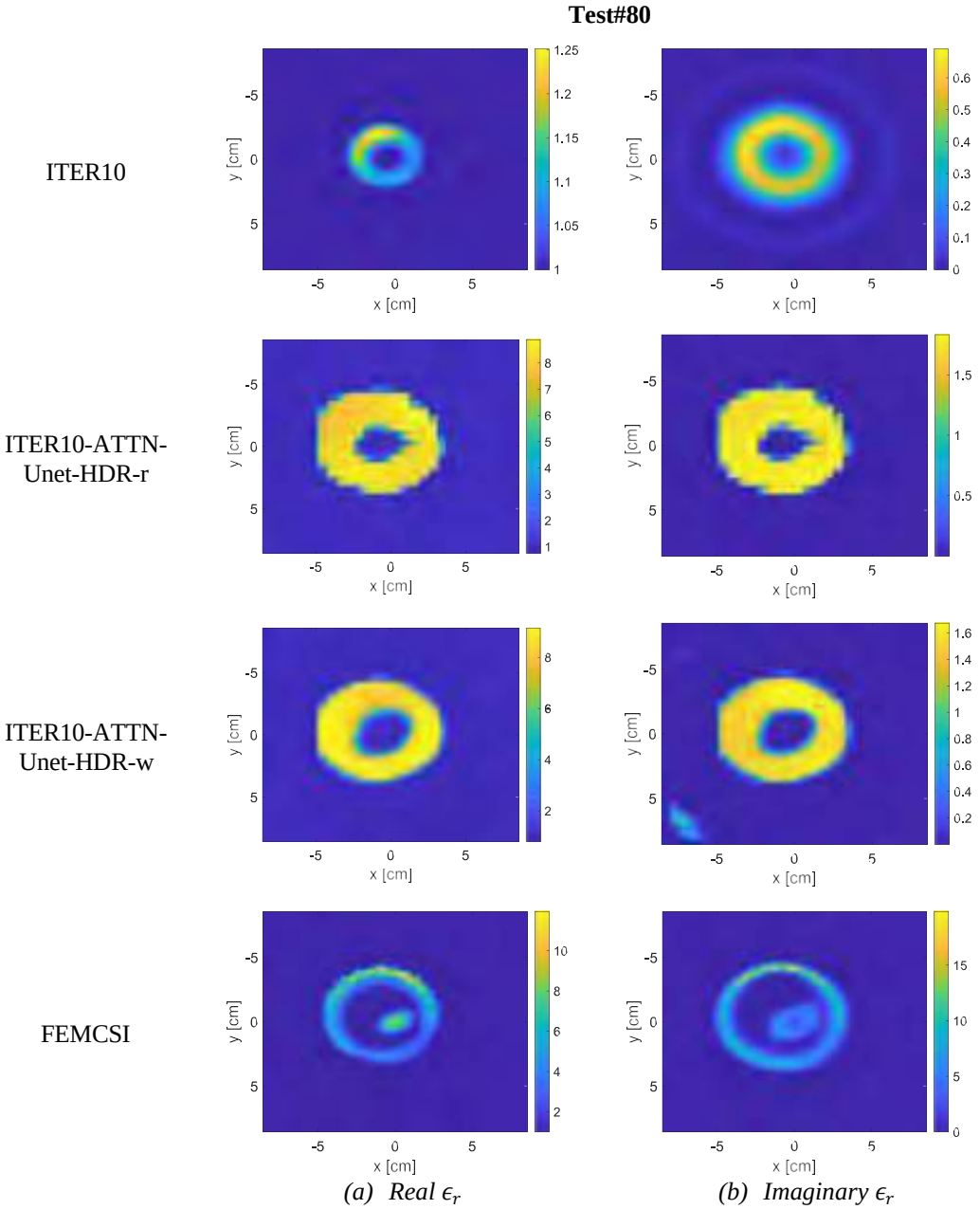

Figure 105. Reconstruction results of (a) real and (b) imaginary components of ϵ_r of UM12.

Chapter 6. Conclusions and Future Work

In the initial phase, two convolutional neural network architectures based on the encoder-decoder: Baseline-AE and DCEDnet were designed, implemented and tested to resolve the EMIS problem. Baseline-AE was designed mainly for functionality test, while the DCEDnet was a much deeper model with more layers and parameters designed to resolve the nonlinear EMIS problem. The readily available MNIST digits that were selected as the targets were assigned a static complex relative permittivity in the forward problem. The $\vec{E}_{\text{meas}}^{sct}$ of the targets obtained provided to two different input types to the DNNs: BP and $\vec{E}_{\text{meas}}^{sct}$. Upon training and testing with the MNIST targets, both the DNNs produced reconstruction results. However, the results obtained by the BP-DCEDnet were of much higher precision and image quality than the other networks. In addition, the reconstructions produced by the BP-DCEDnet were more accurate and closer to the ground truth than the conventional FEMCSI, especially in the imaginary component of ϵ_r. In addition, the computational time for the BP-DCEDnet was significantly much less than for FEMCSI.

In the secondary phase, three more DNNs based on the Unet architecture were added to training and testing in addition to the DCEDnet. They include the Unet-Lite, Unet and the ATTN-Unet. The MNIST lossy targets were assigned a low dynamic range of complex permittivities in the forward problem. The $\vec{E}_{\text{meas}}^{sct}$ of these targets obtained led to two different input types to the DNNs: BP and ITER10. However, initially the four DNNs were trained and tested with the BP input in order to filter out the best network for the physics-incorporated ITER10 input. The four DNNs namely DCEDnet, Unet-Lite, Unet and ATTN-Unet were trained and tested both within the MNIST database, as well with cross-database synthetic complex profiles like the 'Tilted-F' and '2-Circles' to validate the generalization capability of the networks. In addition, the BP-trained models were tested with the complex profiles under different noise levels and large permittivity range to verify the robustness and durability of the networks. Upon successful testing, the BP-ATTN-Unet was found to outperform the other networks and also dominate the FEMCSI in the reconstruction of the imaginary component of ϵ_r. Also, it just took about 10 seconds to produce a single reconstruction in comparison to the FEMCSI which took about 58 seconds to for its 300 iterations. However, the real component of the FEMCSI was still better than the ATTN-Unet especially at the low noise levels.

In order to address this issue and optimize the ATTN-Unet performance further, it was re-trained under the same configuration with the novel physics-incorporated input 'ITER10'. All the tests performed on the BP-ATTN-Unet were done on the ITER10-ATTN-Unet in order to verify its durability and generality. The test results clearly showed that, in addition to outperforming the BP-ATTN-Unet and the FEMCSI imaginary component along with getting closer to the ground truth values, the ITER10-ATTN-Unet reconstructions improved significantly getting extremely near to the real component of the FEMCSI. Moreover, it just took about 13 seconds for the ITER10-ATTN-Unet to produce a single reconstruction unlike the FEMCSI which took about 58 seconds for its 300 iterations.

With the successful cross-testing with synthetic data, the ITER10-ATTN-Unet was put to test with the more challenging experimental data measured by the University of Manitoba Electromagnetic Imaging Group [37]. The reconstructions produced were of high quality and resolution and much better than the FEMCSI reconstructions both in the real and imaginary components. However, since the ϵ_r of UM12 belonged to the HDR, the permittivity values of the ITER10-ATTN-Unet were seen to be capped off at its maximum limit. This shows that neural networks are not as good in extrapolating as they are interpolating.

In the final phase, a HDR version of the ITER10-ATTN-Unet was developed to address the testing data with high ϵ_r similar to the UM12. This was done by assigning the MNIST training targets with high dynamic range of ϵ_r for building the ITER10 input to the ATTN-Unet. This HDR of ϵ_r assignment was done randomly as well as in a weighted manner to create to two versions of the HDR inputs; ITER10-HDR-r and ITER10-HDR-w. Two different models of the ATTN-Unet were trained with these inputs and were tested with high permittivity synthetic as well as experimental data. The results clearly show the HDR versions of the ITER-ATTN-Unet outperforms the FEMCSI both in the real as well as the imaginary component and display reasonable image quality with high permittivity accuracy even for profiles with large permittivity values.

Regarding future work, the input size for the ITER10-ATTN-HDR model can be adequately enlarged with the update of the GPU with larger memory in order to attain good quality and resolution throughout all of the HDR's permittivity values.

References

[1] A. Abubakar, P. M. Van den Berg and J. J. Mallorqui, "Imaging of biomedical data using a multiplicative regularized contrast source inversion method," *IEEE Trans. Microwave Theory Tech.,* vol. 50, *(7),* pp. 1761-1771, 2002.

[2] S. Y. Semenov and D. R. Corfield, "Microwave tomography for brain imaging: Feasibility assessment for stroke detection," *International Journal of Antennas and Propagation,* vol. 2008, 2008.

[3] A. Abubakar *et al*, "2.5 D forward and inverse modeling for interpreting low-frequency electromagnetic measurements," *Geophysics,* vol. 73, *(4),* pp. F165-F177, 2008.

[4] L. Song, C. Yu and Q. H. Liu, "Through-wall imaging (TWI) by radar: 2-D tomographic results and analyses," *IEEE Trans. Geosci. Remote Sens.,* vol. 43, *(12),* pp. 2793-2798, 2005.

[5] S. Kharkovsky and R. Zoughi, "Microwave and millimeter wave nondestructive testing and evaluation-Overview and recent advances," *IEEE Instrumentation & Measurement Magazine,* vol. 10, *(2),* pp. 26-38, 2007.

[6] H. M. Yao, L. Jiang and E. I. Wei, "Enhanced deep learning approach based on the deep convolutional encoder–decoder architecture for electromagnetic inverse scattering problems," *IEEE Antennas and Wireless Propagation Letters,* vol. 19, *(7),* pp. 1211-1215, 2020.

[7] P. M. Meaney *et al*, "A clinical prototype for active microwave imaging of the breast," *IEEE Trans. Microwave Theory Tech.,* vol. 48, *(11),* pp. 1841-1853, 2000.

[8] A. Zakaria, *The Finite-Element Contrast Source Inversion Method for Microwave Imaging Applications.* 2012.

[9] W. C. Chew and Y. Wang, "Reconstruction of two-dimensional permittivity distribution using the distorted Born iterative method," *IEEE Trans. Med. Imaging,* vol. 9, *(2),* pp. 218-225, 1990.

[10] P. M. Van Den Berg and R. E. Kleinman, "A contrast source inversion method," *Inverse Problems,* vol. 13, *(6),* pp. 1607, 1997.

[11] Y. Zhong and X. Chen, "Twofold subspace-based optimization method for solving inverse scattering problems," *Inverse Problems,* vol. 25, *(8),* pp. 085003, 2009.

[12] Y. Huang *et al*, "Deep learning-based inverse scattering with structural similarity loss functions," *IEEE Sensors Journal,* vol. 21, *(4),* pp. 4900-4907, 2020.

[13] R. Song *et al*, "Electromagnetic inverse scattering with perceptual generative adversarial networks," *IEEE Transactions on Computational Imaging,* vol. 7, pp. 689-699, 2021.

[14] A. Massa *et al*, "DNNs as applied to electromagnetics, antennas, and propagation—A review," *IEEE Antennas and Wireless Propagation Letters,* vol. 18, *(11),* pp. 2225-2229, 2019.

[15] M. T. McCann, K. H. Jin and M. Unser, "Convolutional neural networks for inverse problems in imaging: A review," *IEEE Signal Process. Mag.,* vol. 34, *(6),* pp. 85-95, 2017.

[16] L. G. Wang *et al*, "Complex-valued deep convolutional networks for nonlinear electromagnetic inverse scattering," in *2018 IEEE International Conference on Computational Electromagnetics (ICCEM),* 2018, .

[17] S. Caorsi and P. Gamba, "Electromagnetic detection of dielectric cylinders by a neural network approach," *IEEE Trans. Geosci. Remote Sens.,* vol. 37, *(2),* pp. 820-827, 1999.

[18] I. T. Rekanos, "Neural-network-based inverse-scattering technique for online microwave medical imaging," *IEEE Trans. Magn.,* vol. 38, *(2),* pp. 1061-1064, 2002.

[19] L. Li *et al*, "DeepNIS: Deep neural network for nonlinear electromagnetic inverse scattering," *IEEE Transactions on Antennas and Propagation,* vol. 67, *(3),* pp. 1819-1825, 2018.

[20] W. Shao and Y. Du, "Microwave imaging by deep learning network: Feasibility and training method," *IEEE Transactions on Antennas and Propagation,* vol. 68, *(7),* pp. 5626-5635, 2020.

[21] O. Ronneberger, P. Fischer and T. Brox, "U-net: Convolutional networks for biomedical image segmentation," in *International Conference on Medical Image Computing and Computer-Assisted Intervention,* 2015, pp. 234-241.

[22] P. Isola *et al*, "Image-to-image translation with conditional adversarial networks," in *Proceedings of the IEEE Conference on Computer Vision and Pattern Recognition,* 2017, pp. 1125-1134.

[23] J. Geffrin, P. Sabouroux and C. Eyraud, "Free space experimental scattering database continuation: experimental set-up and measurement precision," *Inverse Problems,* vol. 21, *(6),* pp. S117, 2005.

[24] W. Shao *et al*, "A phase confocal method for near-field microwave imaging," *IEEE Trans. Microwave Theory Tech.,* vol. 65, *(7),* pp. 2508-2515, 2017.

[25] T. Shan *et al*, "Physics-informed supervised residual learning for electromagnetic modeling," *IEEE Transactions on Antennas and Propagation,* vol. 71, *(4),* pp. 3393-3407, 2023.

[26] Y. Liu *et al*, "SOM-net: Unrolling the subspace-based optimization for solving full-wave inverse scattering problems," *IEEE Trans. Geosci. Remote Sens.,* vol. 60, pp. 1-15, 2022.

[27] Z. Wei and X. Chen, "Physics-inspired convolutional neural network for solving full-wave inverse scattering problems," *IEEE Transactions on Antennas and Propagation,* vol. 67, *(9),* pp. 6138-6148, 2019.

[28] X. Chen *et al*, "A review of deep learning approaches for inverse scattering problems (invited review)," *Electromagnetic Waves,* vol. 167, pp. 67-81, 2020.

[29] D. Bahdanau, K. Cho and Y. Bengio, "Neural machine translation by jointly learning to align and translate," *arXiv Preprint arXiv:1409.0473,* 2014.

[30] A. Vaswani *et al*, "Attention is all you need," *Advances in Neural Information Processing Systems,* vol. 30, pp. 1-11, 2017.

[31] P. Anderson *et al*, "Bottom-up and top-down attention for image captioning and visual question answering," in *Proceedings of the IEEE Conference on Computer Vision and Pattern Recognition,* 2018, pp. 6077-6086.

[32] S. Jetley *et al*, "Learn to pay attention," *arXiv Preprint arXiv:1804.02391,* 2018.

[33] P. Veličković *et al*, "Graph attention networks," *arXiv Preprint arXiv:1710.10903,* 2017.

[34] F. Wang *et al*, "Residual attention network for image classification," in *Proceedings of the IEEE Conference on Computer Vision and Pattern Recognition,* 2017, pp. 3156-3164.

[35] V. Mnih, N. Heess and A. Graves, "Recurrent models of visual attention," *Advances in Neural Information Processing Systems,* vol. 27, pp. 1-9, 2014.

[36] O. Oktay *et al*, "Attention u-net: Learning where to look for the pancreas," *arXiv Preprint arXiv:1804.03999,* 2018.

[37] C. Gilmore *et al*, "The University of Manitoba Microwave Imaging Repository: A Two-Dimensional Microwave Scattering Database for Testing Inversion and Calibration Algorithms [Measurements Corner]," *IEEE Antennas and Propagation Magazine,* vol. 53, *(5),* pp. 126-133, 2011. . DOI: 10.1109/MAP.2011.6138442.

[38] G. James *et al*, *An Introduction to Statistical Learning.* Springer, 2013, vol. 112.

[39] C. Gilmore *et al*, "On super-resolution with an experimental microwave tomography system," *IEEE Antennas and Wireless Propagation Letters,* vol. 9, pp. 393-396, 2010.

Appendix

Appendix A HDR Results – Synthetic Data

A.1 Cross-Database Test

A.1.1 Complex Profiles

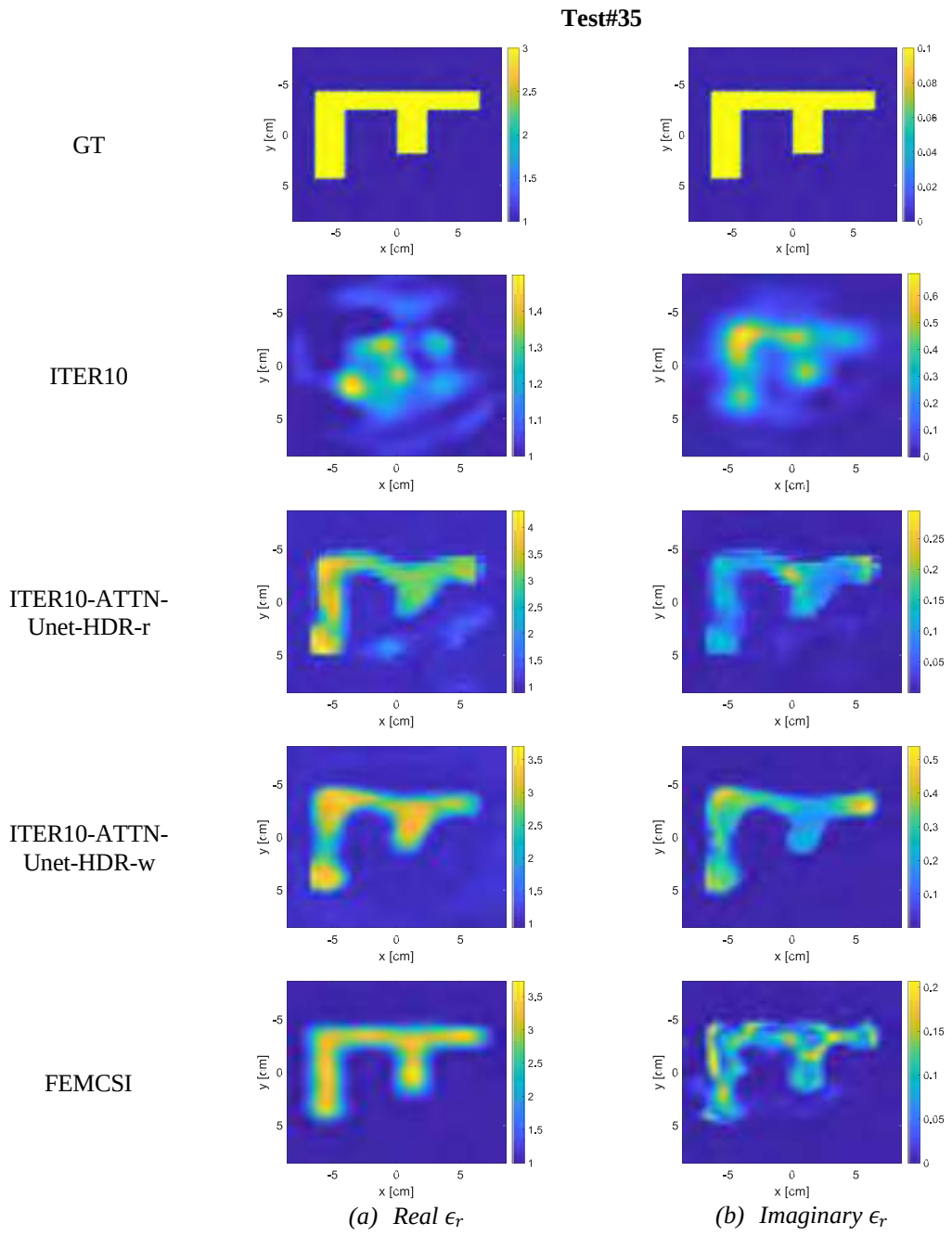

Figure 106. Reconstruction results of (a) real and (b) imaginary components of ϵ_r of Tilted-F.

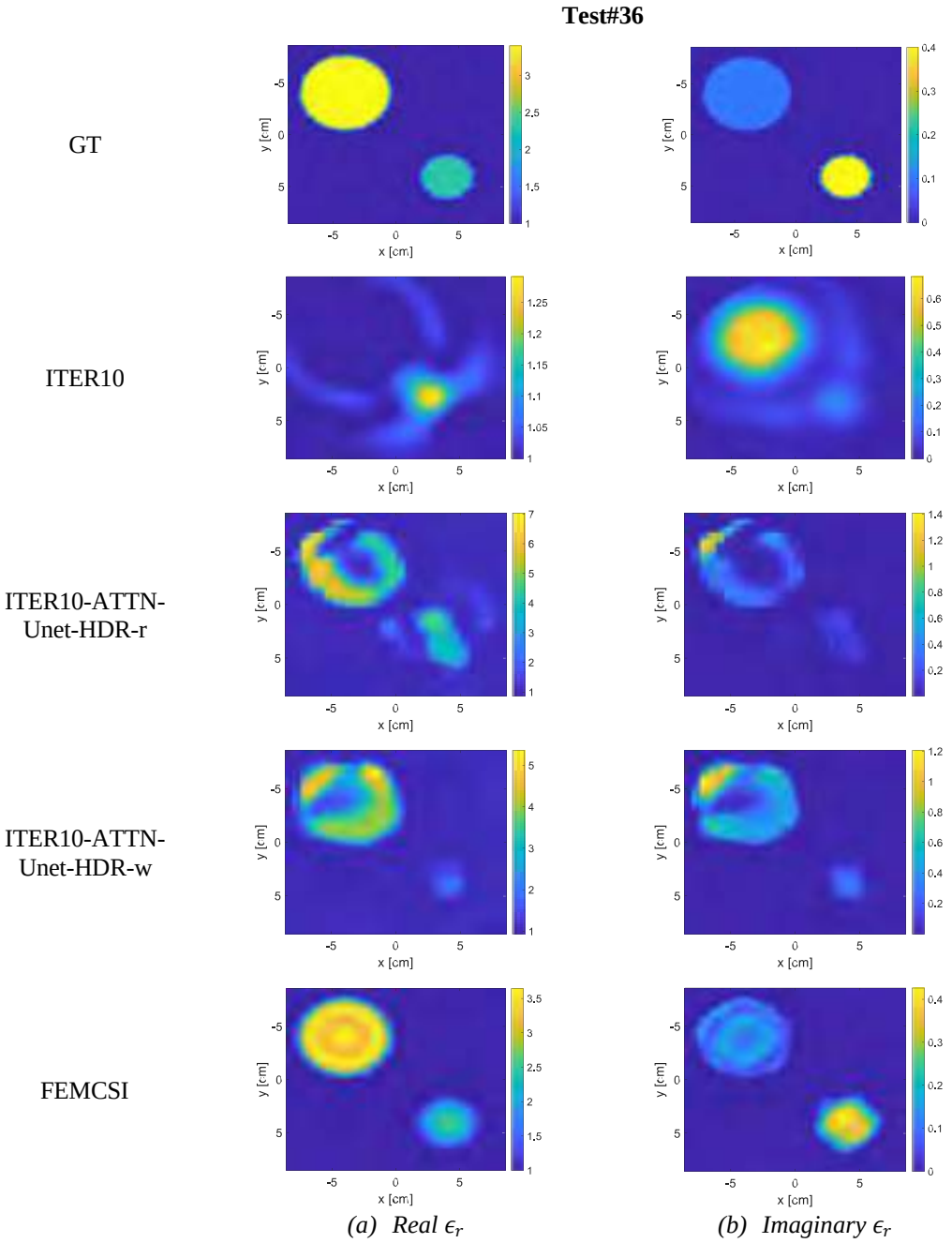

Figure 107. Reconstruction results of (a) real and (b) imaginary components of ϵ_r of 2-Circles.

Table 36. MSE between Ground Truth and Reconstructions of the real ϵ_r for Test#35-Test#36

Method	**MSE-Real**	
	Test#35	Test#36
ITER10-ATTN-Unet-HDR-r	0.2111	0.9597
ITER10-ATTN-Unet-HDR-w	0.1535	0.3550
FEMCSI	0.0491	0.0160

Table 37. MSE between Ground Truth and Reconstructions of the imaginary ϵ_r for Test#35-Test#36

Method	**MSE-Imaginary**	
	Test#35	Test#36
ITER10-ATTN-Unet-HDR-r	0.0007	0.0201
ITER10-ATTN-Unet-HDR-w	0.0073	0.0355
FEMCSI	0.0004	0.0007

Table 38. MSE between Ground Truth and Reconstructions for the ϵ_r for Test#35-Test#36

Method	**MSE**	
	Test#35	Test#36
ITER10-ATTN-Unet-HDR-r	0.1059	0.4899
ITER10-ATTN-Unet-HDR-w	0.0804	0.1943
FEMCSI	0.0248	0.0083

A.1.2 Large Permittivity Range

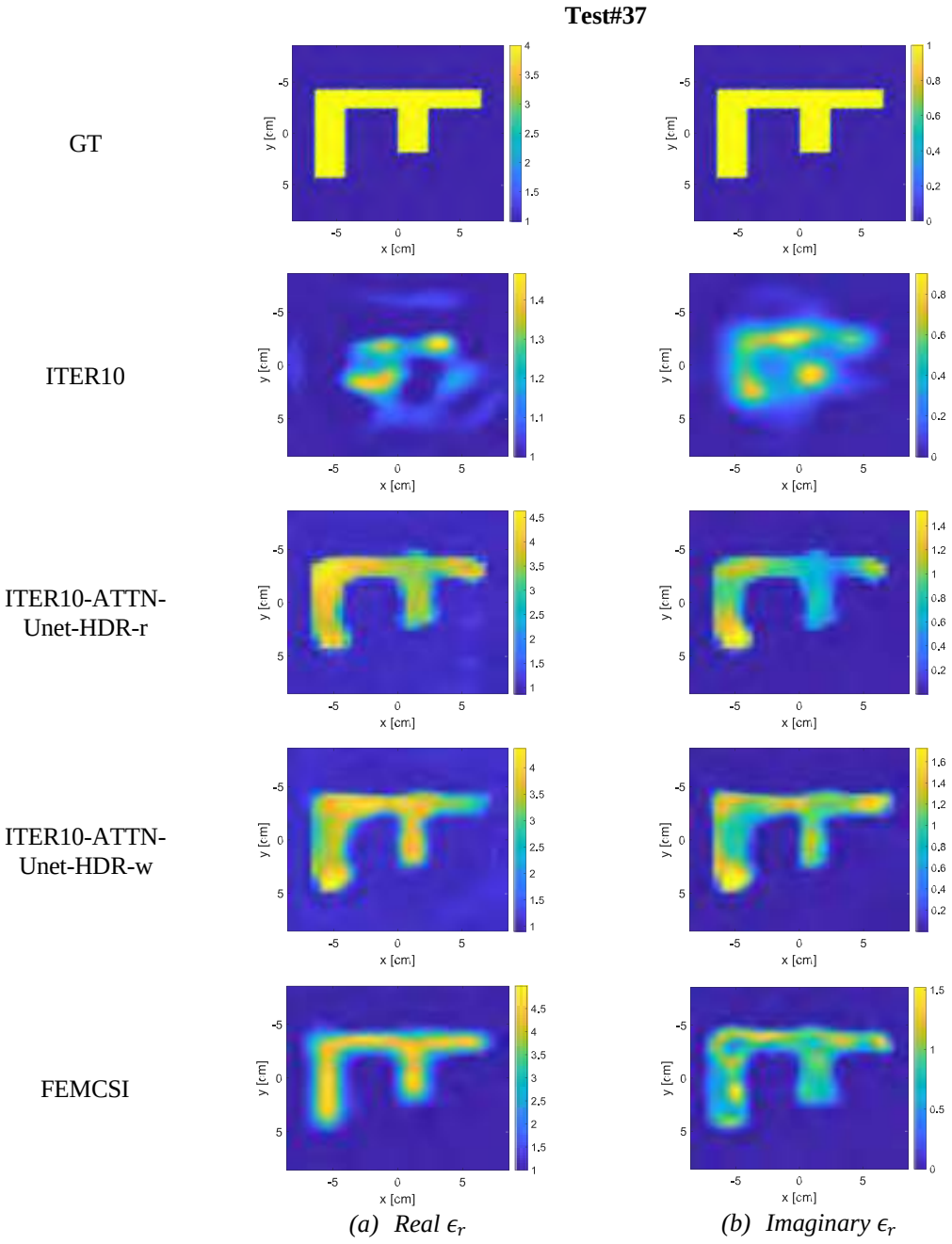

Figure 108. Reconstruction results of (a) real and (b) imaginary components of ϵ_r 4 of Tilted-F.

Table 39. MSE between Ground Truth and Reconstructions of the real ϵ_r for Test#37

Method	**MSE-Real**
	Test#37
ITER10-ATTN-Unet-HDR-r	0.1533
ITER10-ATTN-Unet-HDR-w	0.2295
FEMCSI	0.1353

Table 40. MSE between Ground Truth and Reconstructions of the imaginary ϵ_r for Test#37

Method	**MSE-Imaginary**
	Test#37
ITER10-ATTN-Unet-HDR-r	0.0259
ITER10-ATTN-Unet-HDR-w	0.0393
FEMCSI	0.0284

Table 41. MSE between Ground Truth and Reconstructions for the ϵ_r for Test#37

Method	**MSE**
	Test#37
ITER10-ATTN-Unet-HDR-r	0.0906
ITER10-ATTN-Unet-HDR-w	0.1344
FEMCSI	0.0818

A.1.3 High Noise Interference

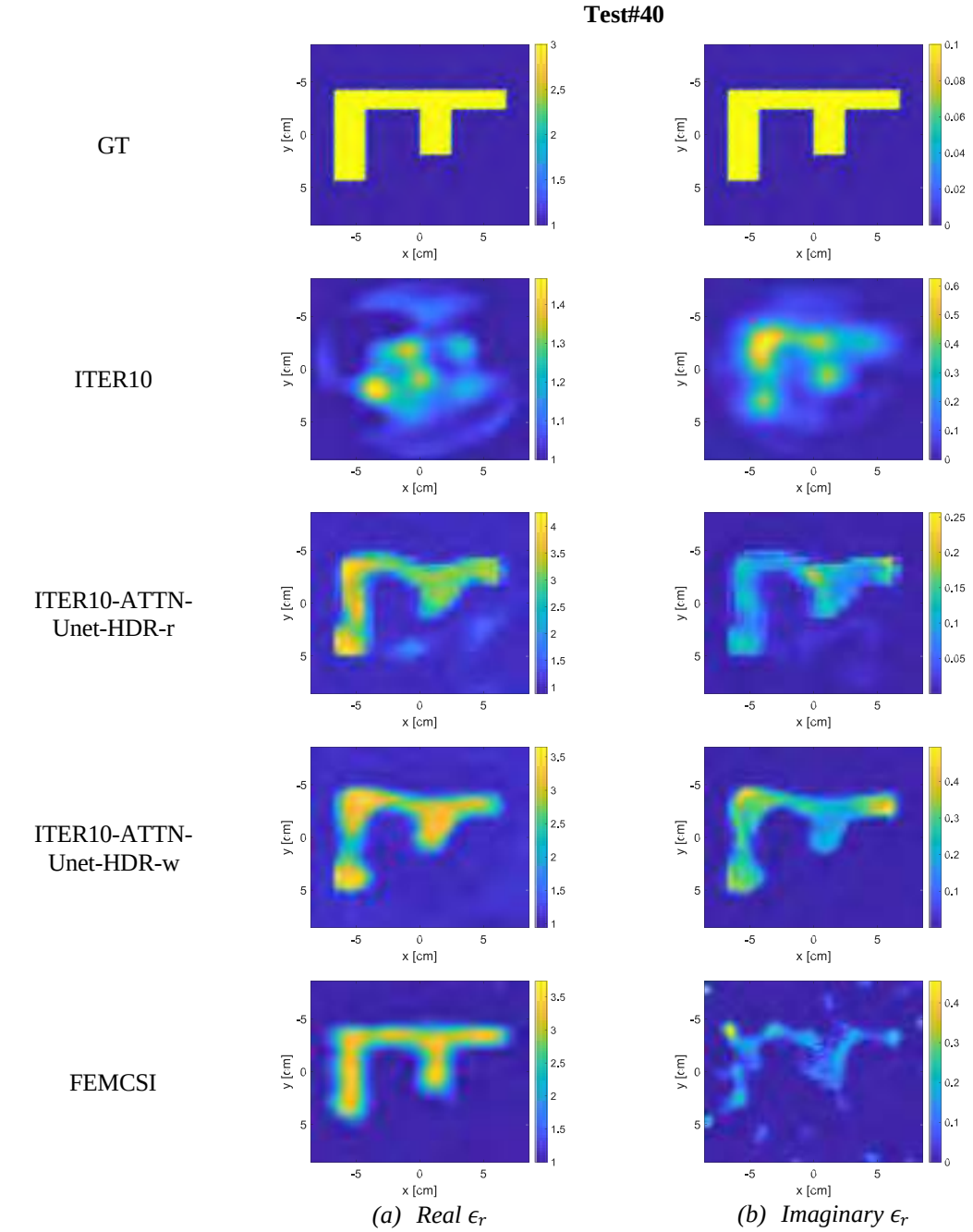

Figure 109. Reconstruction results of (a) real and (b) imaginary components of ϵ_r of Tilted-F with 5% noise.

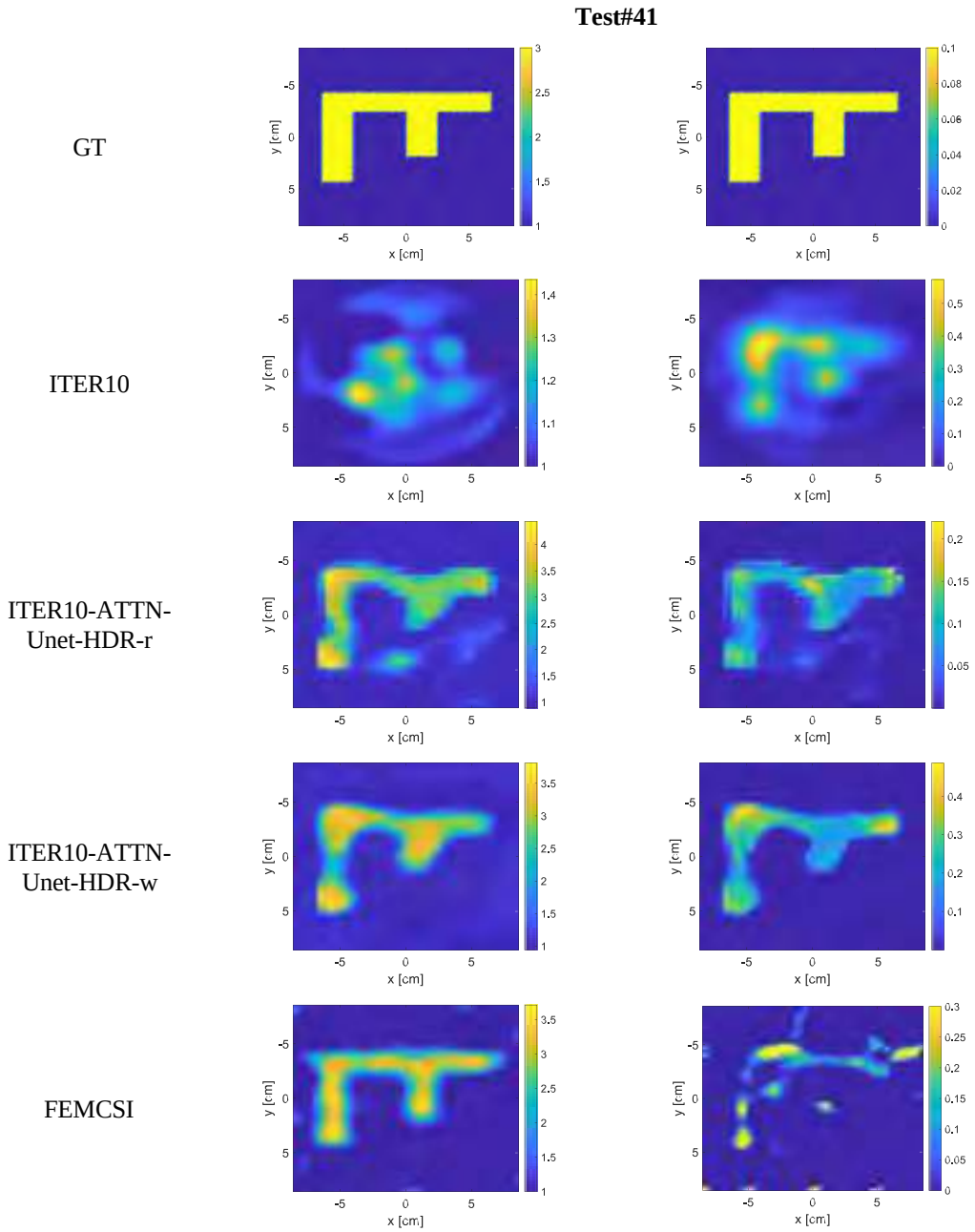

Figure 110. Reconstruction results of (a) real and (b) imaginary components of ϵ_r of Tilted-F with 10% noise.

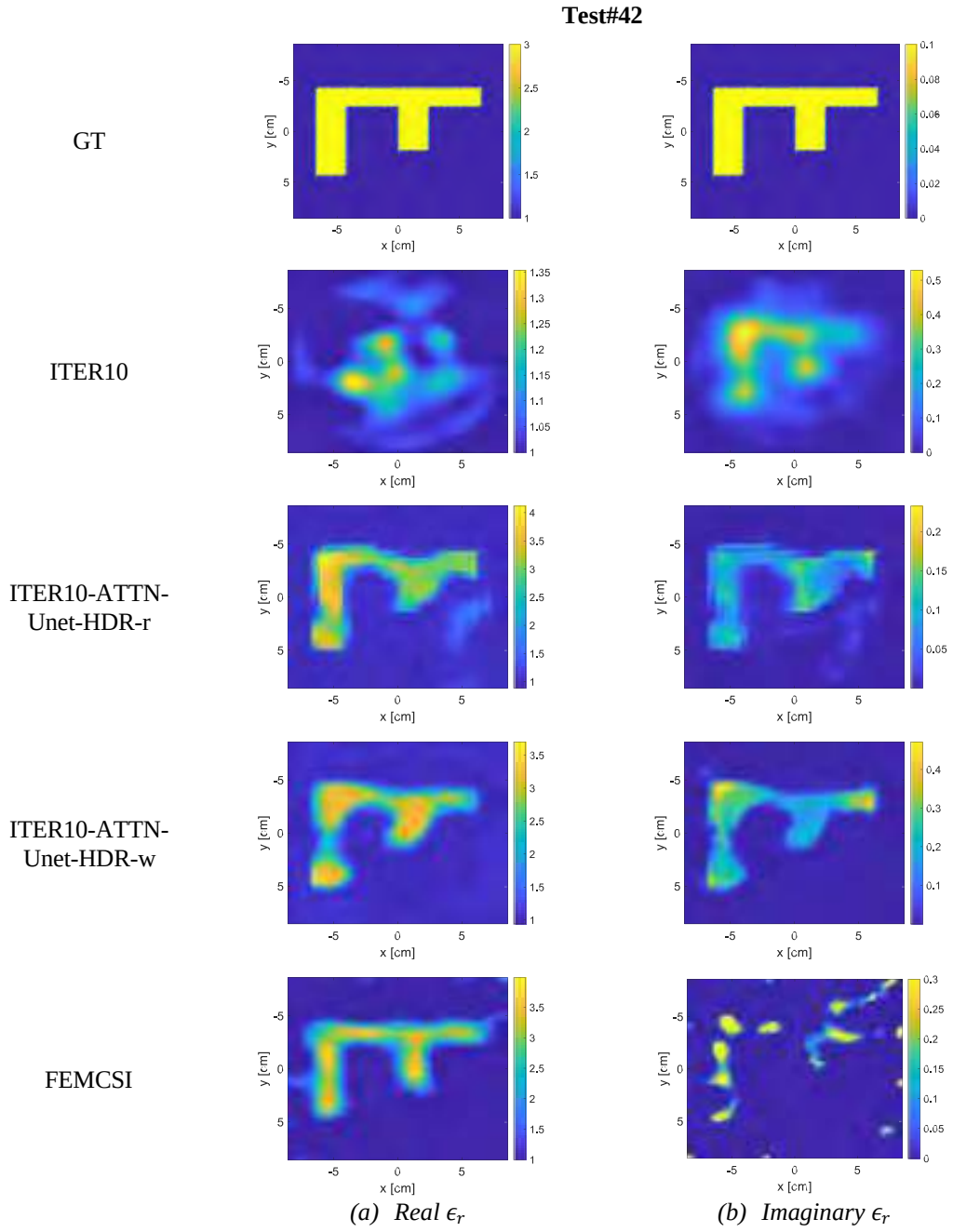

Figure 111. Reconstruction results of (a) real and (b) imaginary components of ϵ_r of Tilted-F with 15% noise.

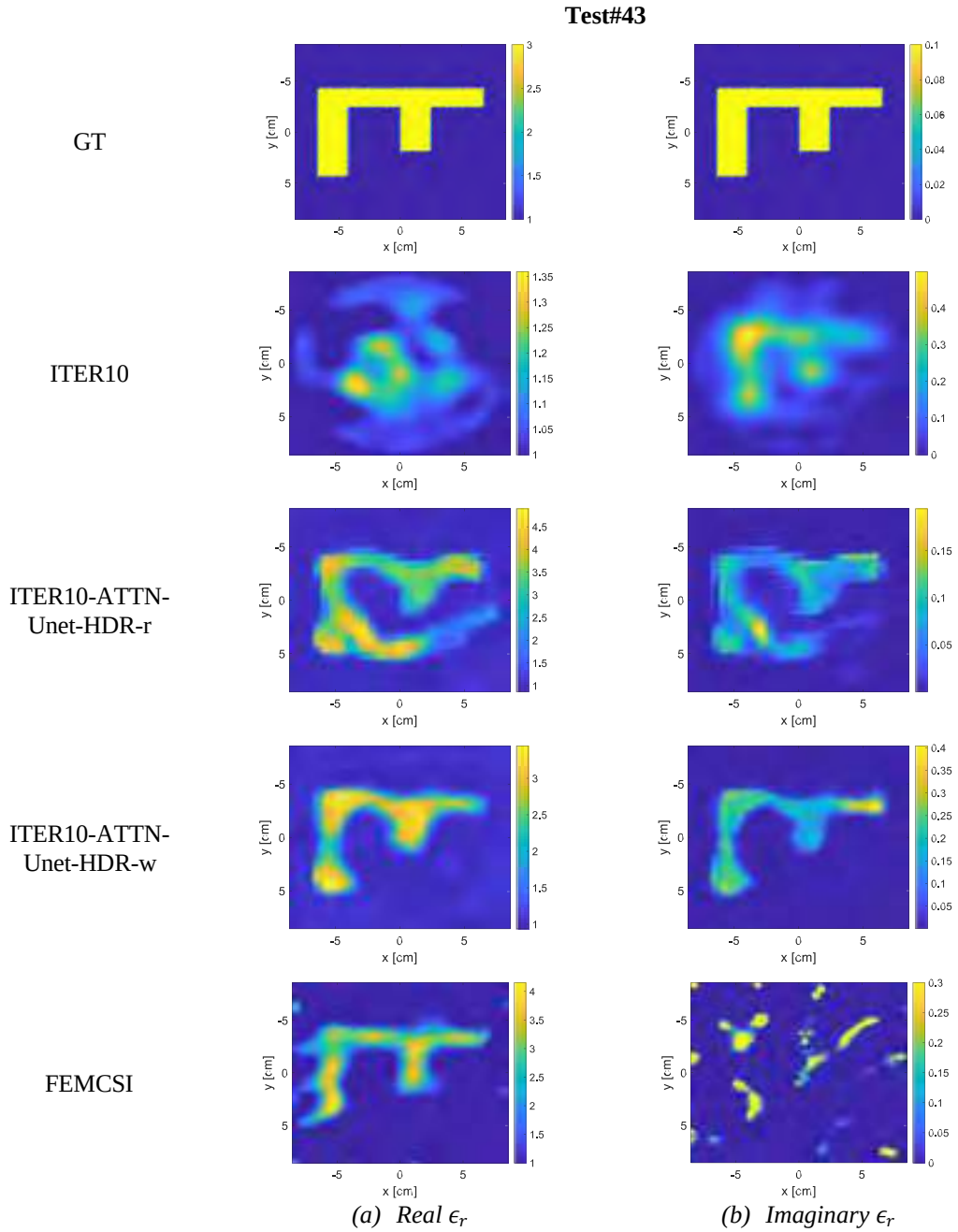

Figure 112. Reconstruction results of (a) real and (b) imaginary components of ϵ_r of Tilted-F with 20% noise.

Table 42. MSE of the real ϵ_r Reconstructions for Test#40-Test#43 under different Noise levels

Method	**MSE-Real**			
	Test#40	Test#41	Test#42	Test#43
ITER10-ATTN-Unet-HDR-r	0.2170	0.2508	0.1864	0.7371
ITER10-ATTN-Unet-HDR-w	0.1651	0.1777	0.1872	0.1828
FEMCSI	0.0172	0.0273	0.0398	0.0439

Table 43. MSE of the imaginary ϵ_r Reconstructions for Test#40-Test#43 under different Noise levels

Method	**MSE-Imaginary**			
	Test#40	Test#41	Test#42	Test#43
ITER10-ATTN-Unet-HDR-r	0.0006	0.0005	0.0005	0.0009
ITER10-ATTN-Unet-HDR-w	0.0059	0.0054	0.0046	0.0026
FEMCSI	0.0020	0.0046	0.0085	0.0111

Table 44. MSE of the ϵ_r Reconstructions for Test#40-Test#43 under different Noise levels

Method	**MSE**			
	Test#40	Test#41	Test#42	Test#43
ITER10-ATTN-Unet-HDR-r	0.1088	0.2508	0.0934	0.3690
ITER10-ATTN-Unet-HDR-w	0.0855	0.0916	0.0959	0.0927
FEMCSI	0.0096	0.0160	0.0242	0.0275

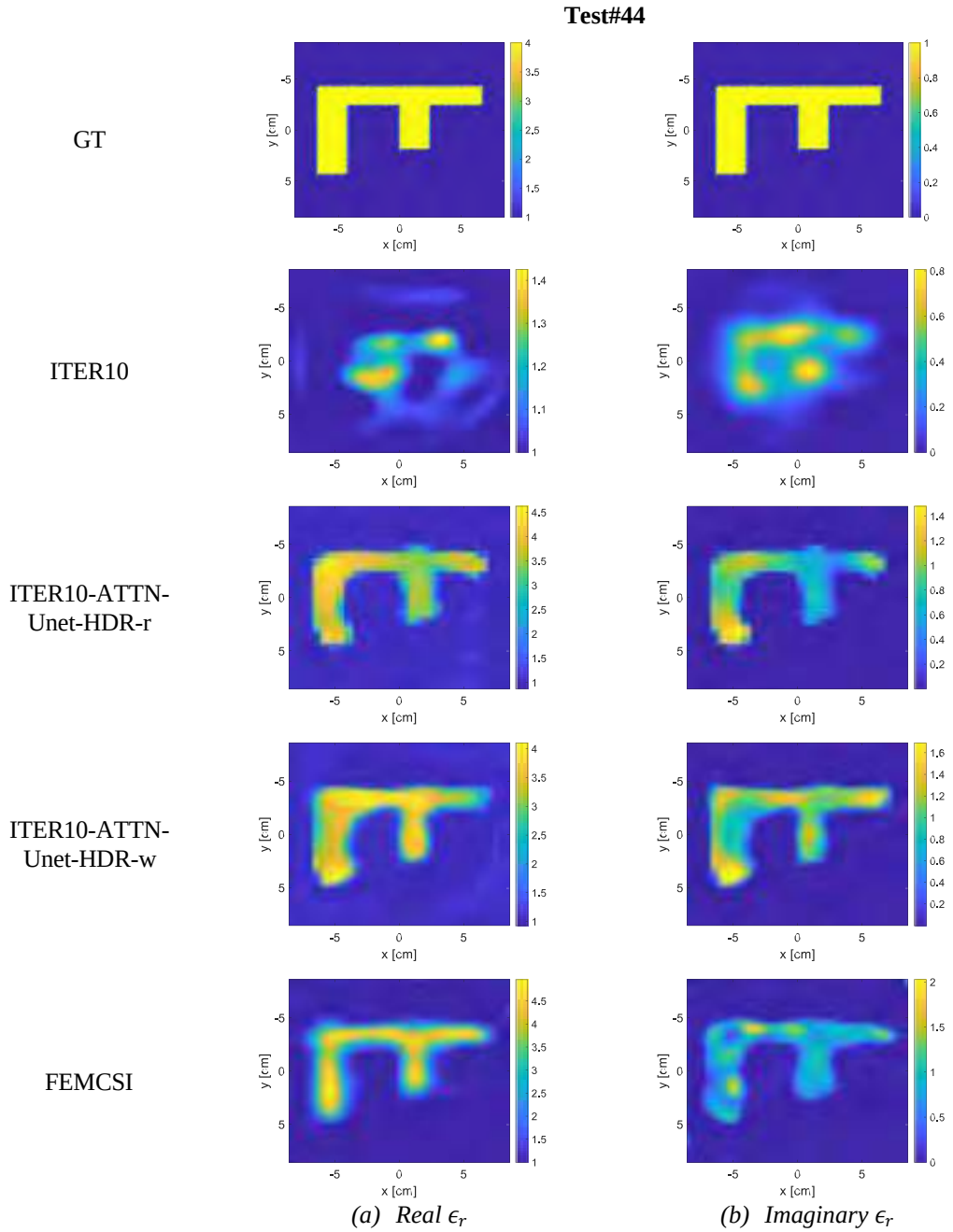

Figure 113. Reconstruction results of (a) real and (b) imaginary components of 'moderate' ϵ_r of Tilted-F with 5% noise.

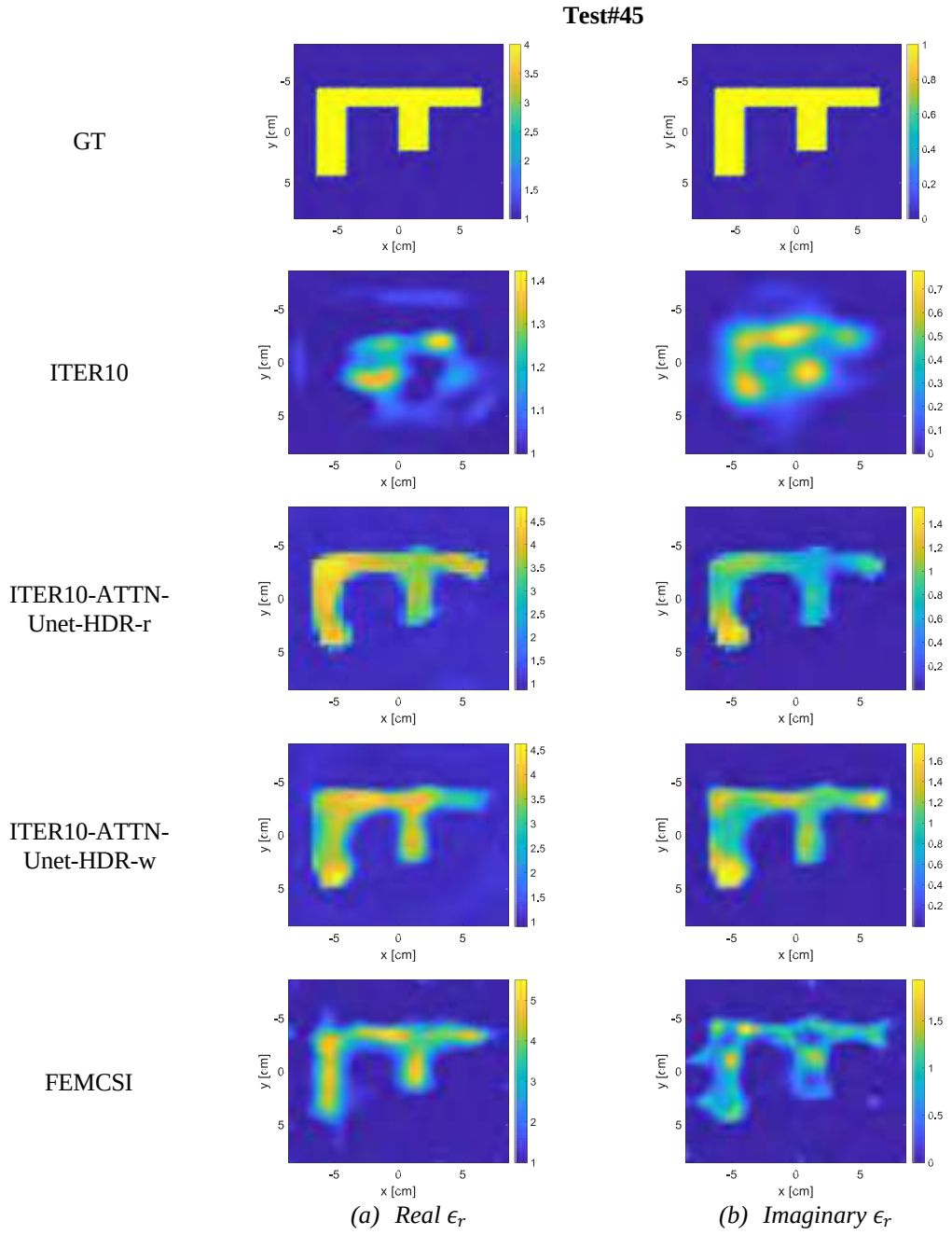

Figure 114. Reconstruction results of (a) real and (b) imaginary components of 'moderate' ϵ_r of Tilted-F with 10% noise.

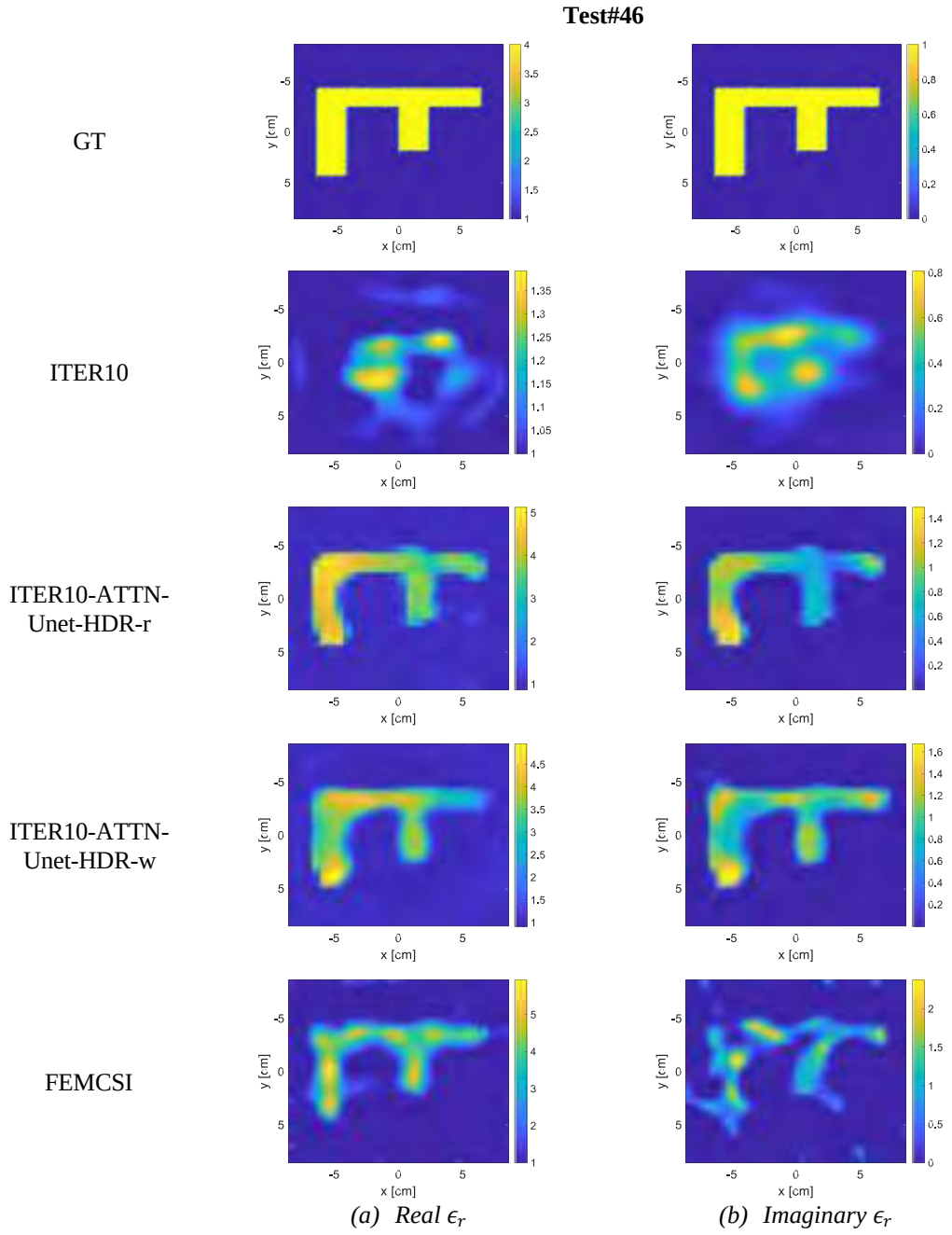

Figure 115. Reconstruction results of (a) real and (b) imaginary components of 'moderate' ϵ_r of Tilted-F with 15% noise.

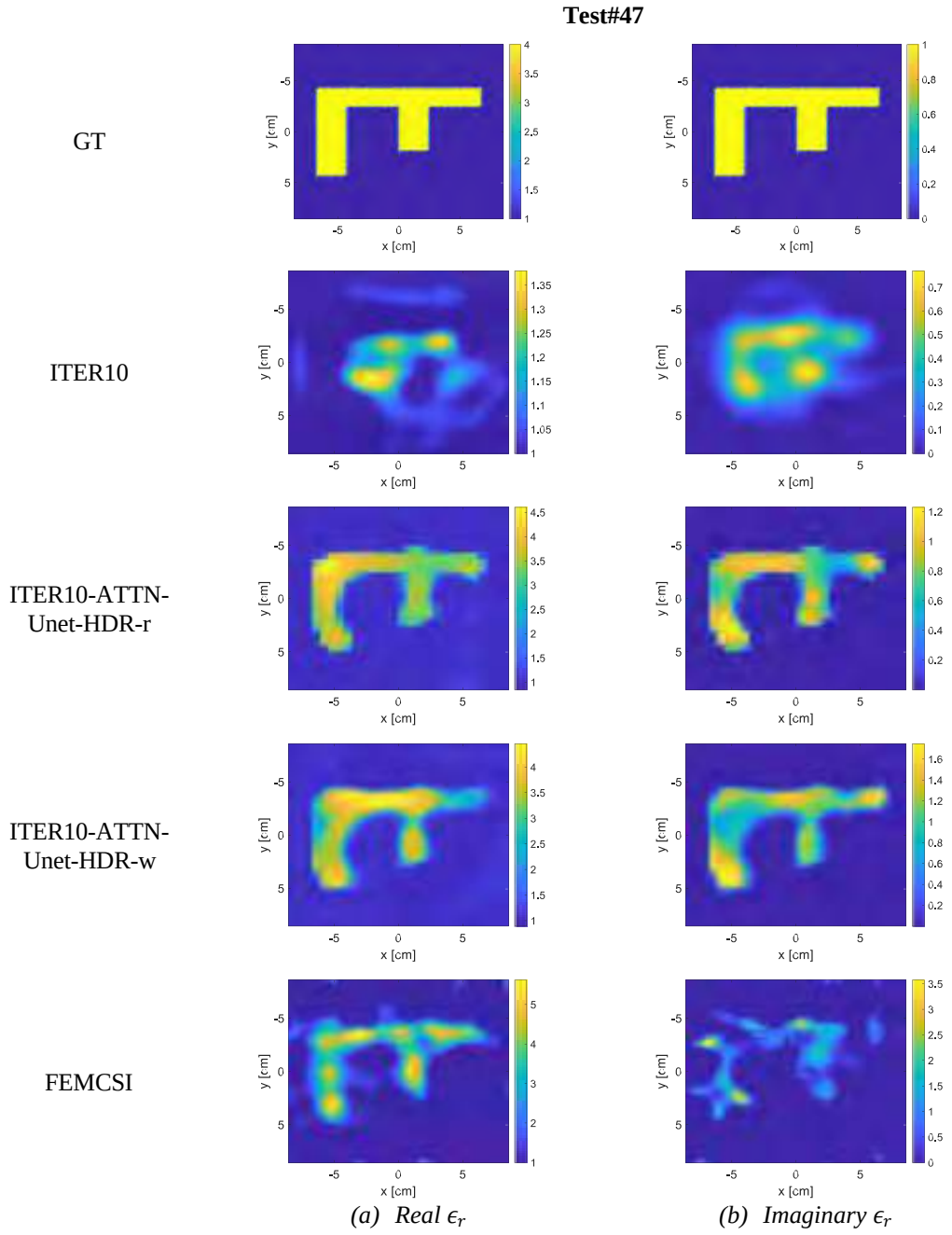

Figure 116. Reconstruction results of (a) real and (b) imaginary components of 'moderate' ϵ_r of Tilted-F with 20% noise.

Table 45. MSE of the real ϵ_r Reconstructions for Test#44-Test#47 under different Noise levels

Method	**MSE-Real**			
	Test#44	Test#45	Test#46	Test#47
ITER10-ATTN-Unet-HDR-r	0.1612	0.1877	0.1982	0.2199
ITER10-ATTN-Unet-HDR-w	0.2324	0.2693	0.2399	0.3434
FEMCSI	0.1456	0.1712	0.2026	0.2625

Table 46. MSE between Ground Truth and Reconstructions for Test#44-Test#47 under different Noise levels

Method	**MSE-Imaginary**			
	Test#44	Test#45	Test#46	Test#47
ITER10-ATTN-Unet-HDR-r	0.0277	0.0306	0.0311	0.0278
ITER10-ATTN-Unet-HDR-w	0.0341	0.0450	0.0294	0.0492
FEMCSI	0.0361	0.0529	0.0832	0.1479

Table 47. MSE between Ground Truth and Reconstructions for Test#44-Test#47 under different Noise levels

Method	**MSE**			
	Test#44	Test#45	Test#46	Test#47
ITER10-ATTN-Unet-HDR-r	0.0945	0.1091	0.1147	0.1238
ITER10-ATTN-Unet-HDR-w	0.1333	0.1572	0.1346	0.1963
FEMCSI	0.0909	0.1121	0.1429	0.2052

Appendix B HDR Results – Experimental Data

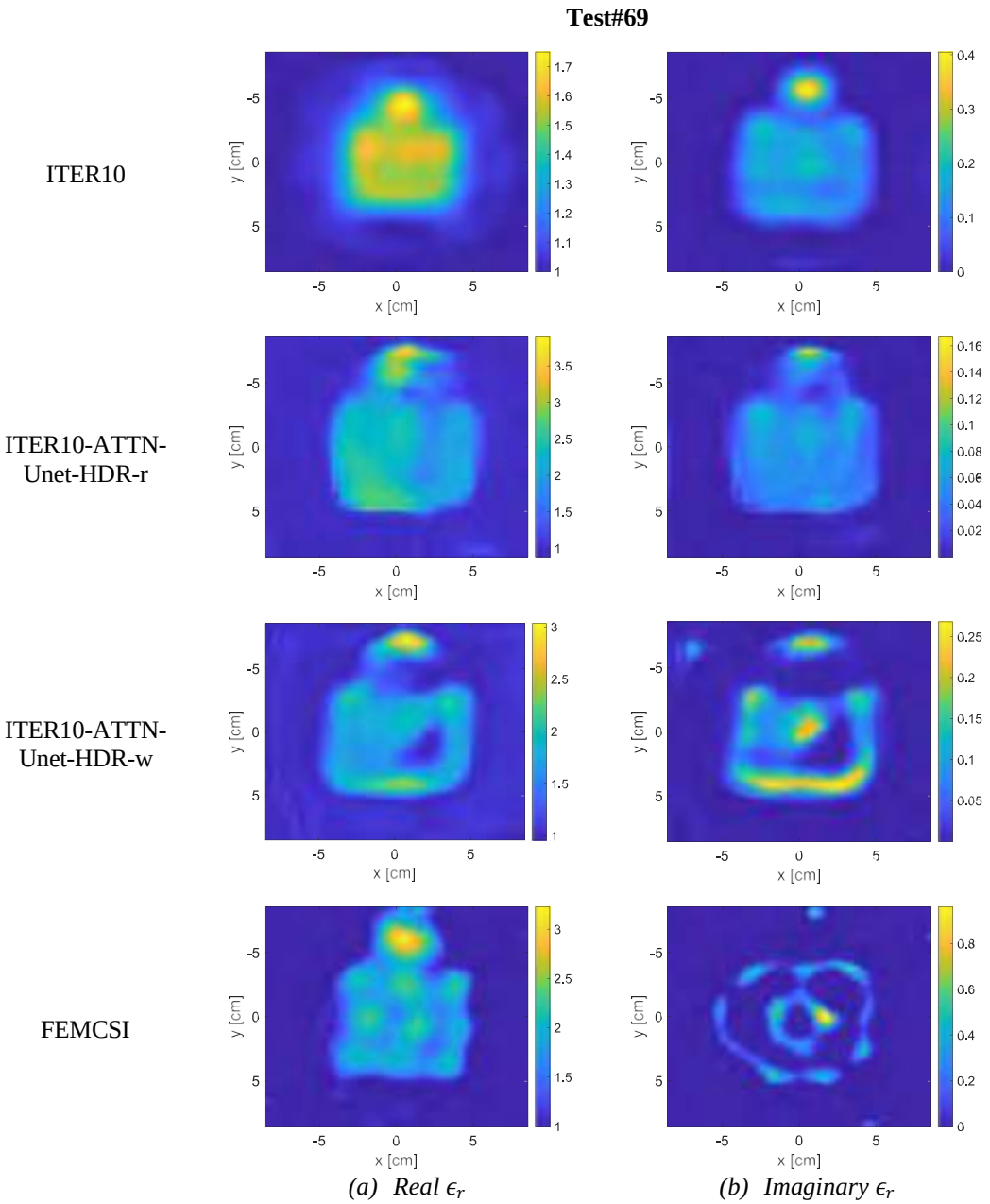

Figure 117. Reconstruction results of (a) real and (b) imaginary components of ϵ_r of UM1.

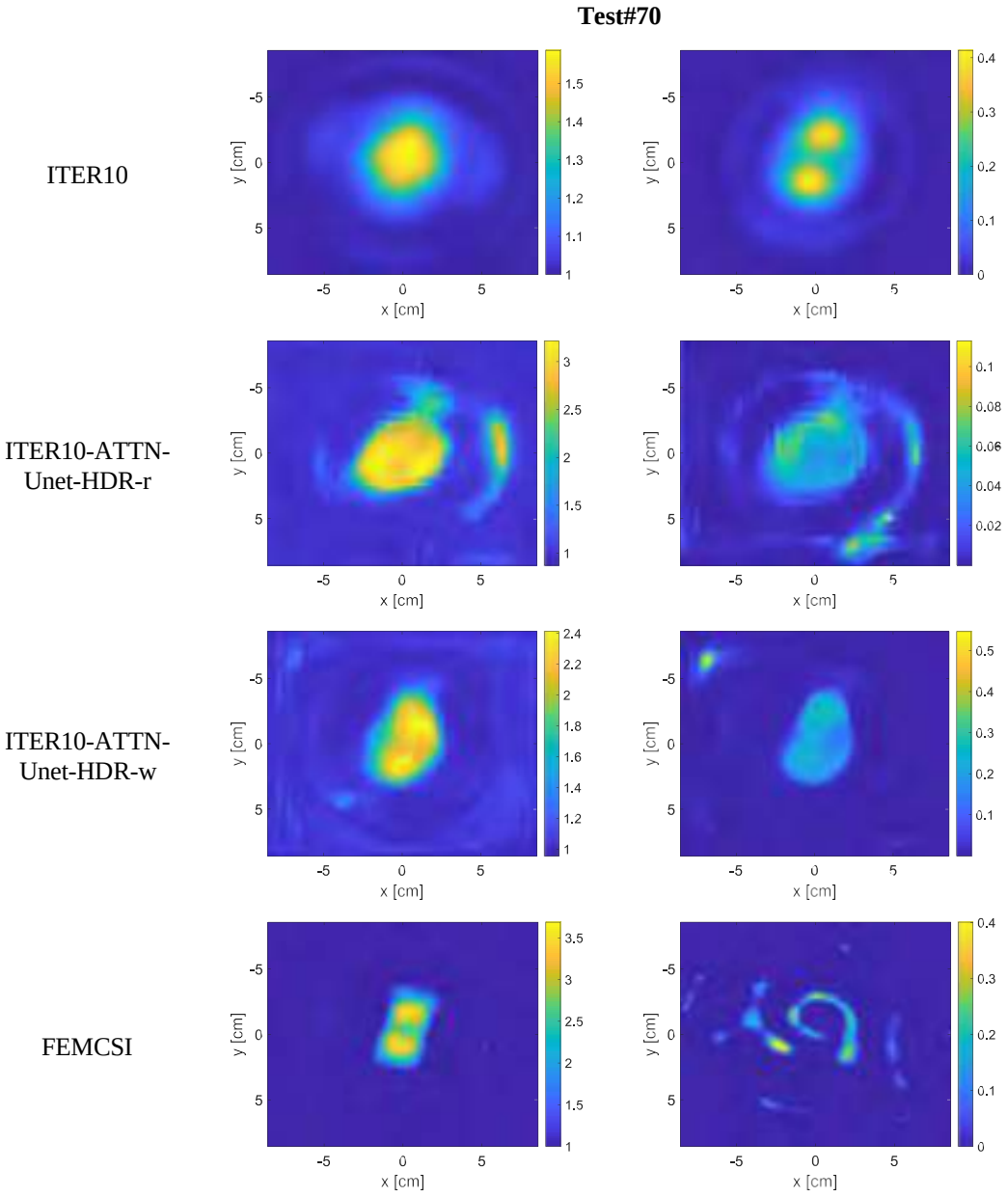

Figure 118. Reconstruction results of (a) real and (b) imaginary components of ϵ_r of UM2.

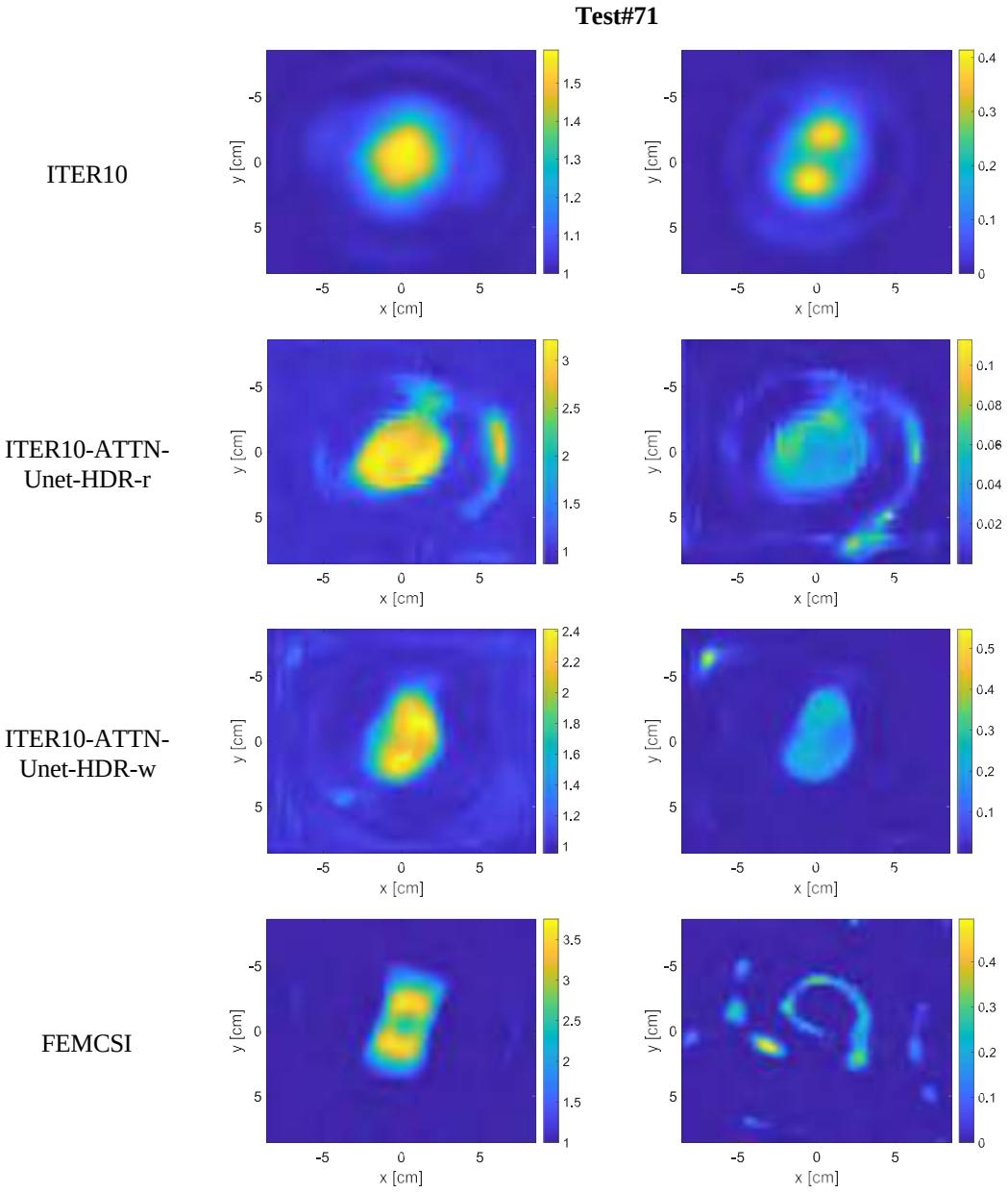

Figure 119. Reconstruction results of (a) real and (b) imaginary components of ϵ_r of UM3.

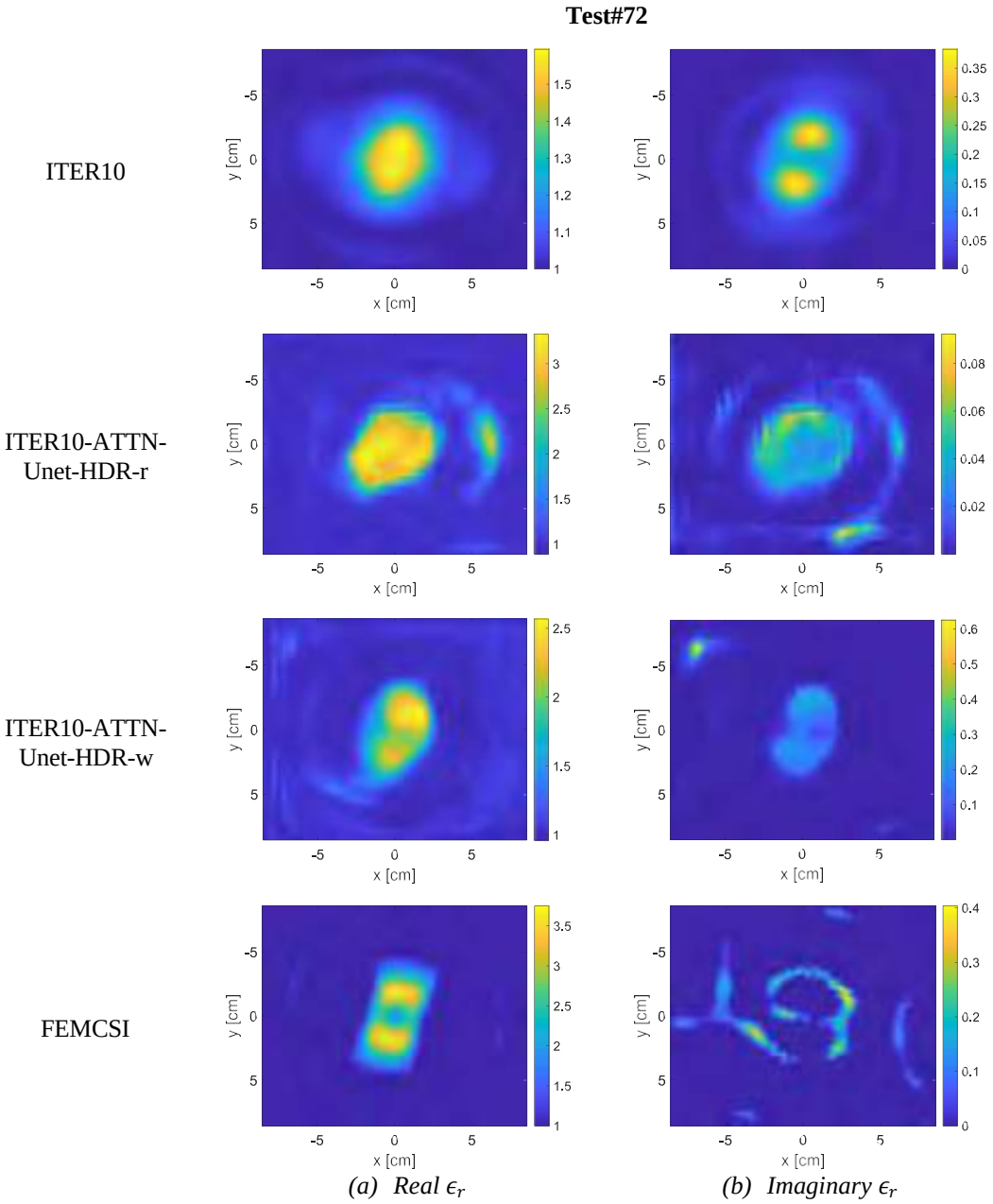

Figure 120. Reconstruction results of (a) real and (b) imaginary components of ϵ_r of UM4.

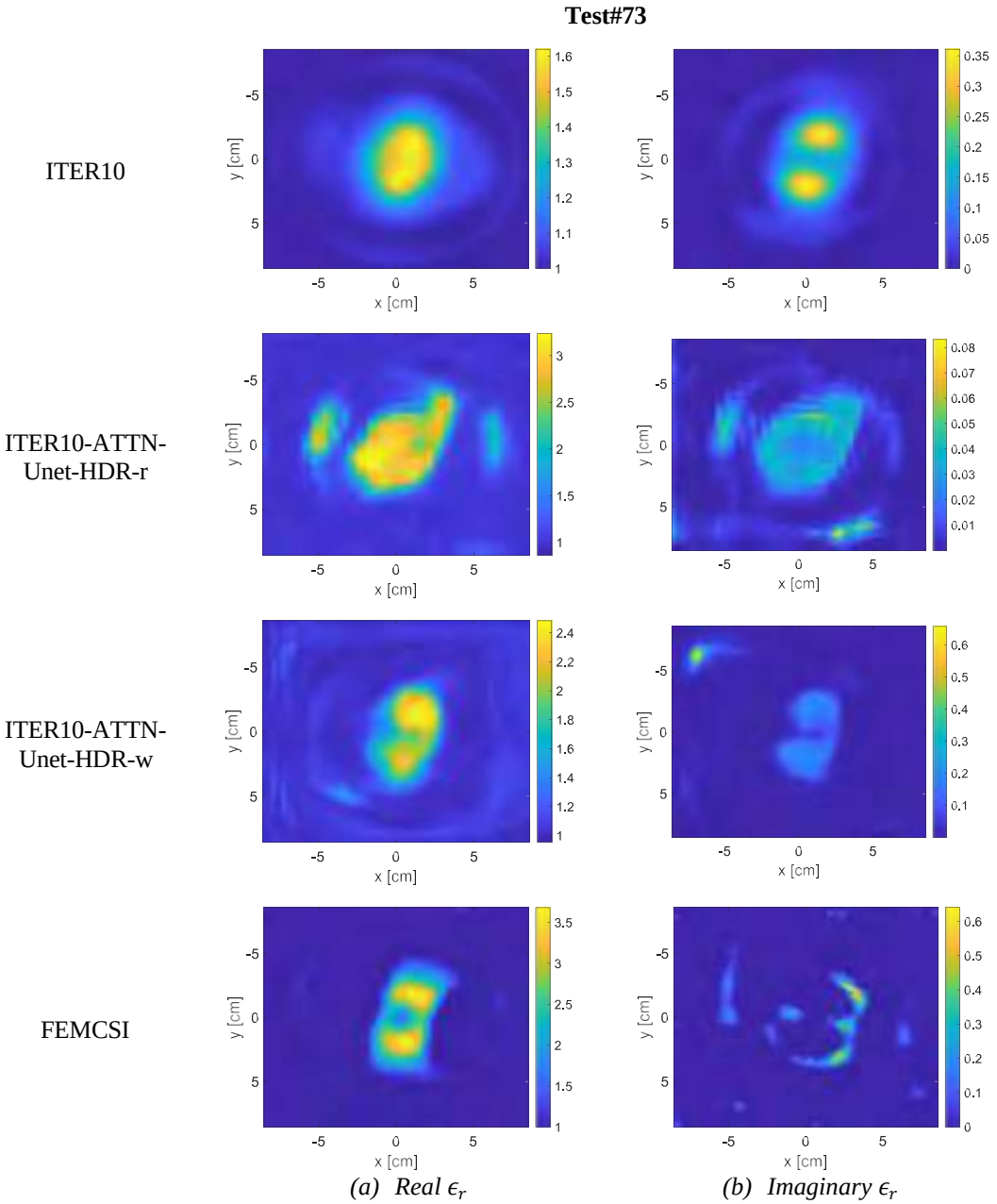

Figure 121. Reconstruction results of (a) real and (b) imaginary components of ϵ_r of UM5.

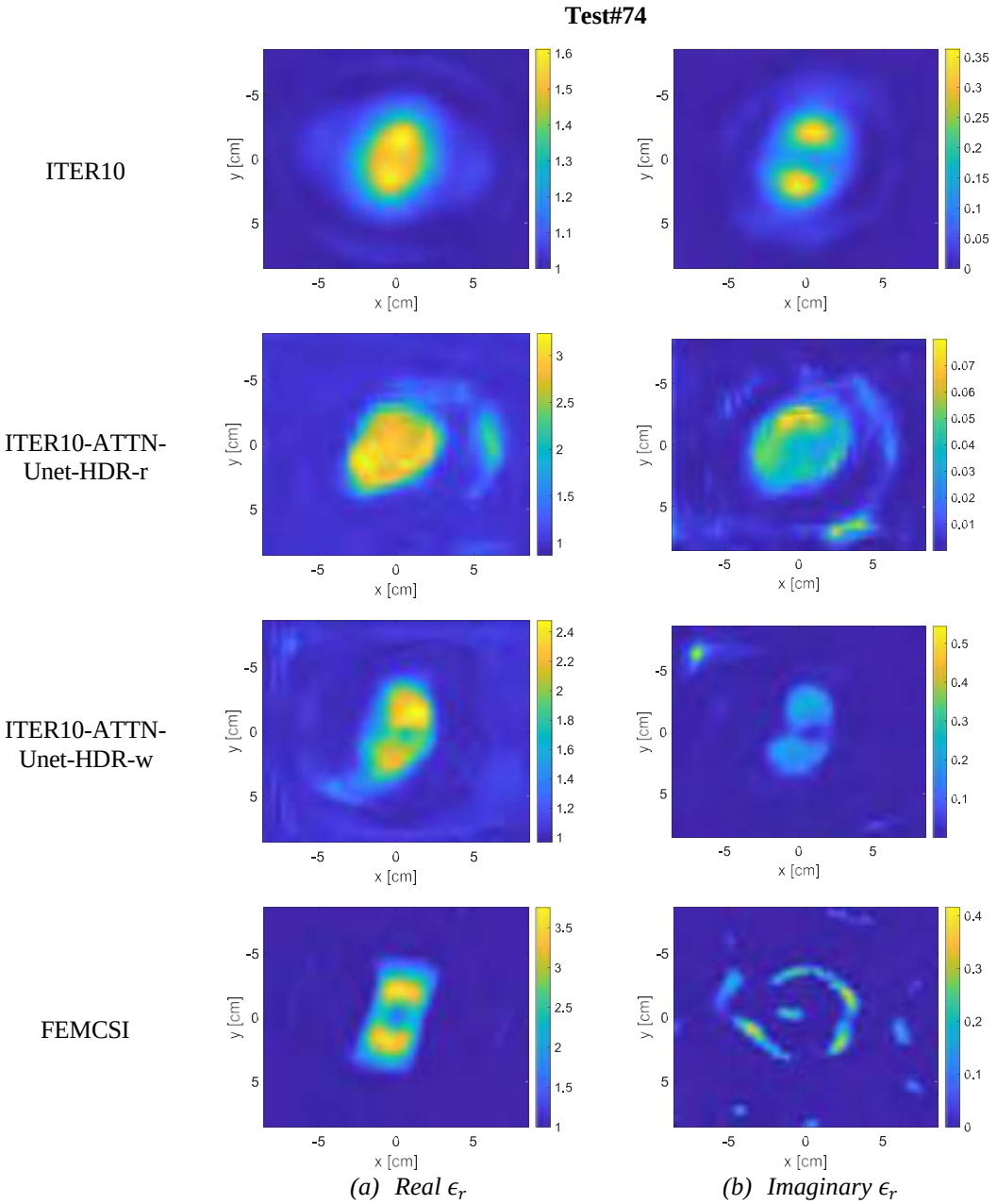

Figure 122. Reconstruction results of (a) real and (b) imaginary components of ϵ_r of UM6.

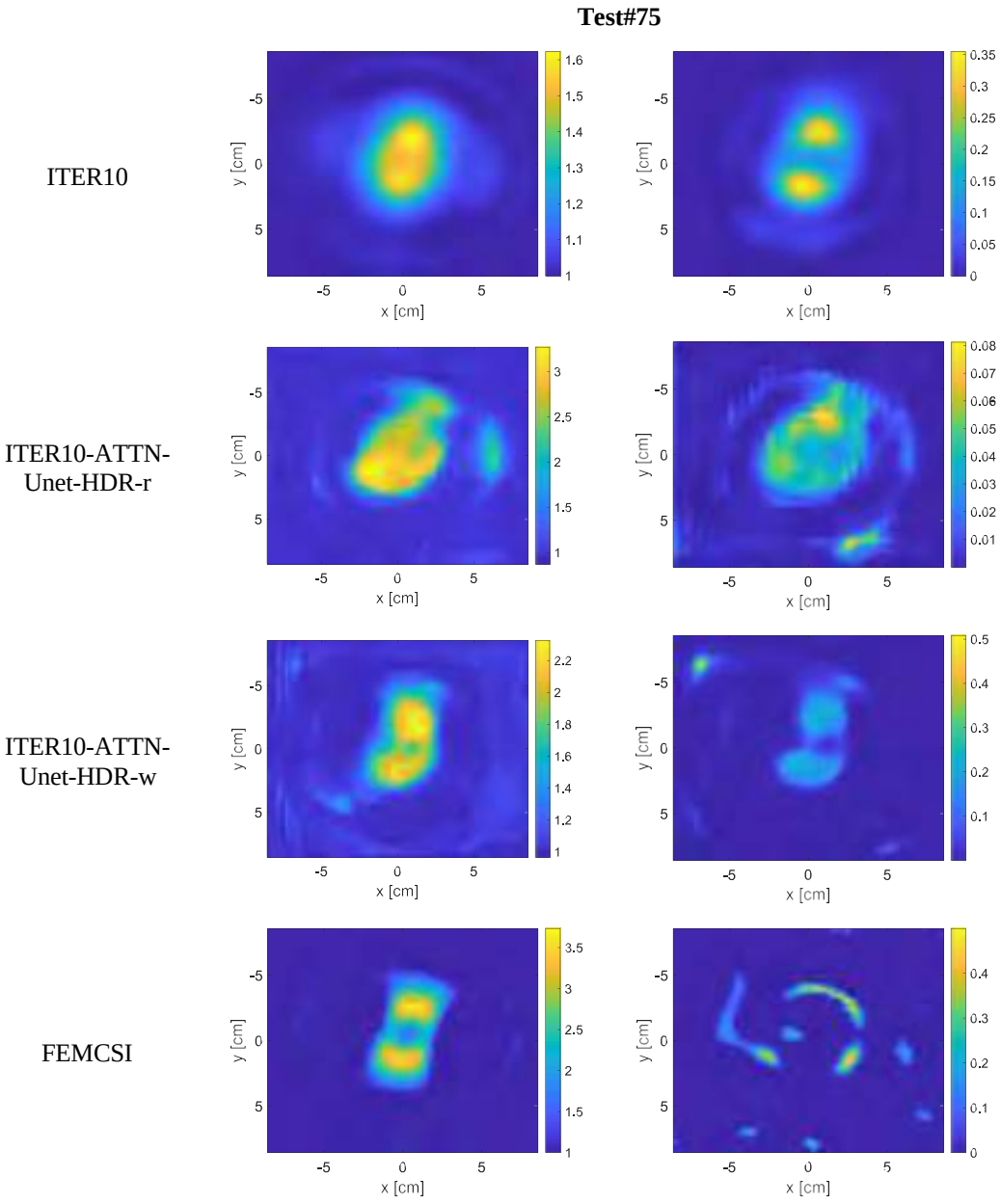

Figure 123. Reconstruction results of (a) real and (b) imaginary components of ϵ_r of UM7.

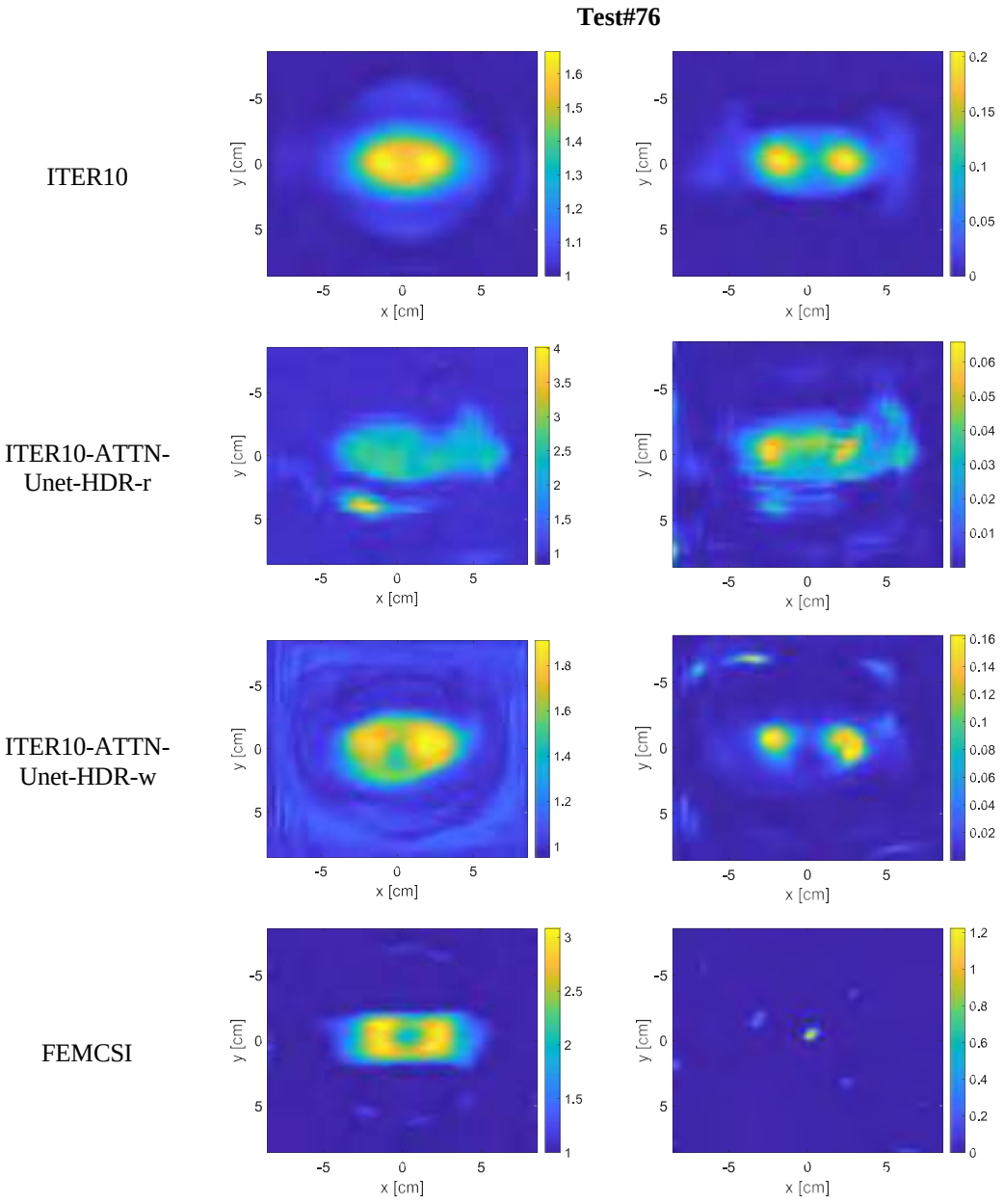

Figure 124. Reconstruction results of (a) real and (b) imaginary components of ϵ_r of UM8.

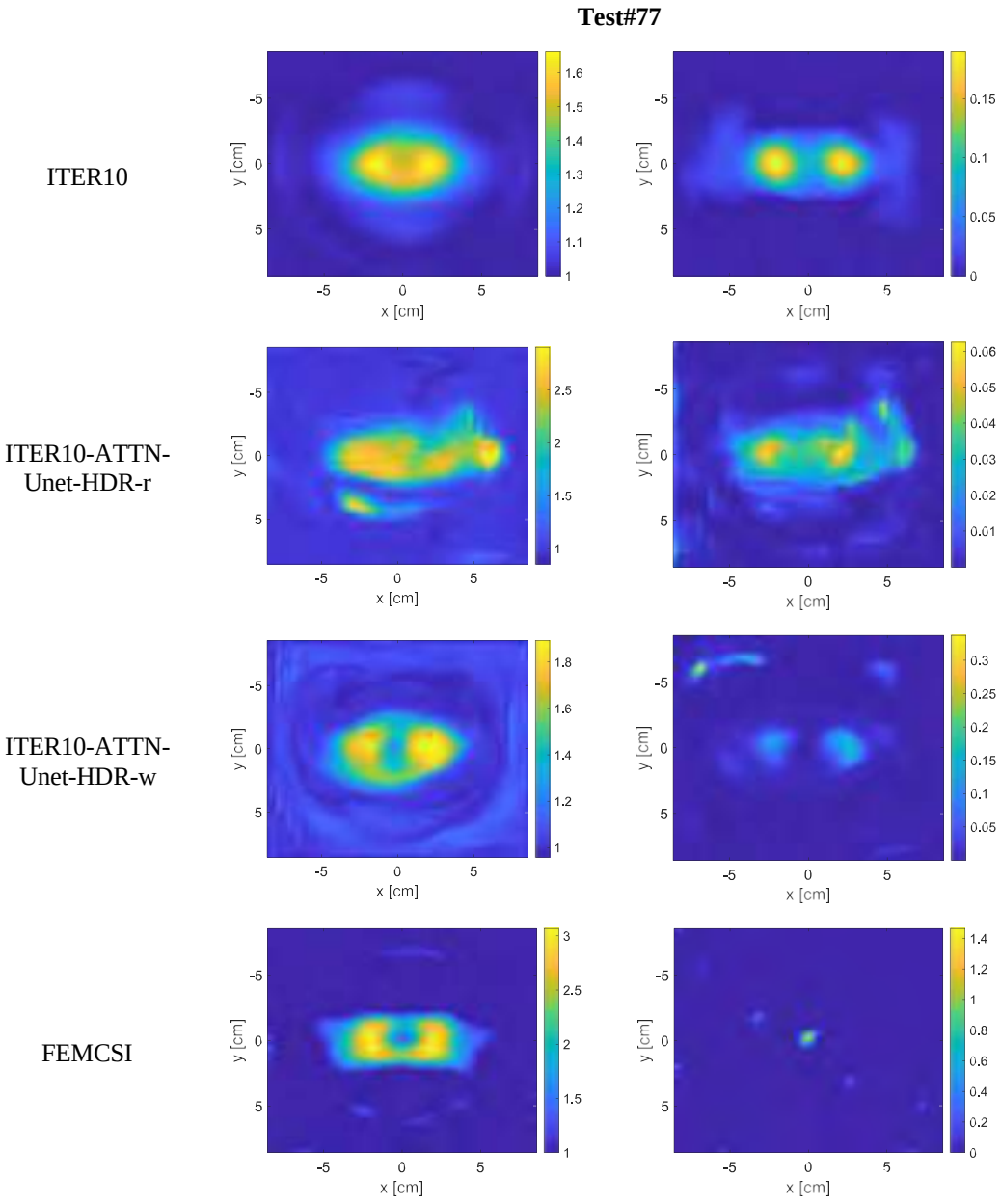

Figure 125. Reconstruction results of (a) real and (b) imaginary components of ϵ_r of UM9.

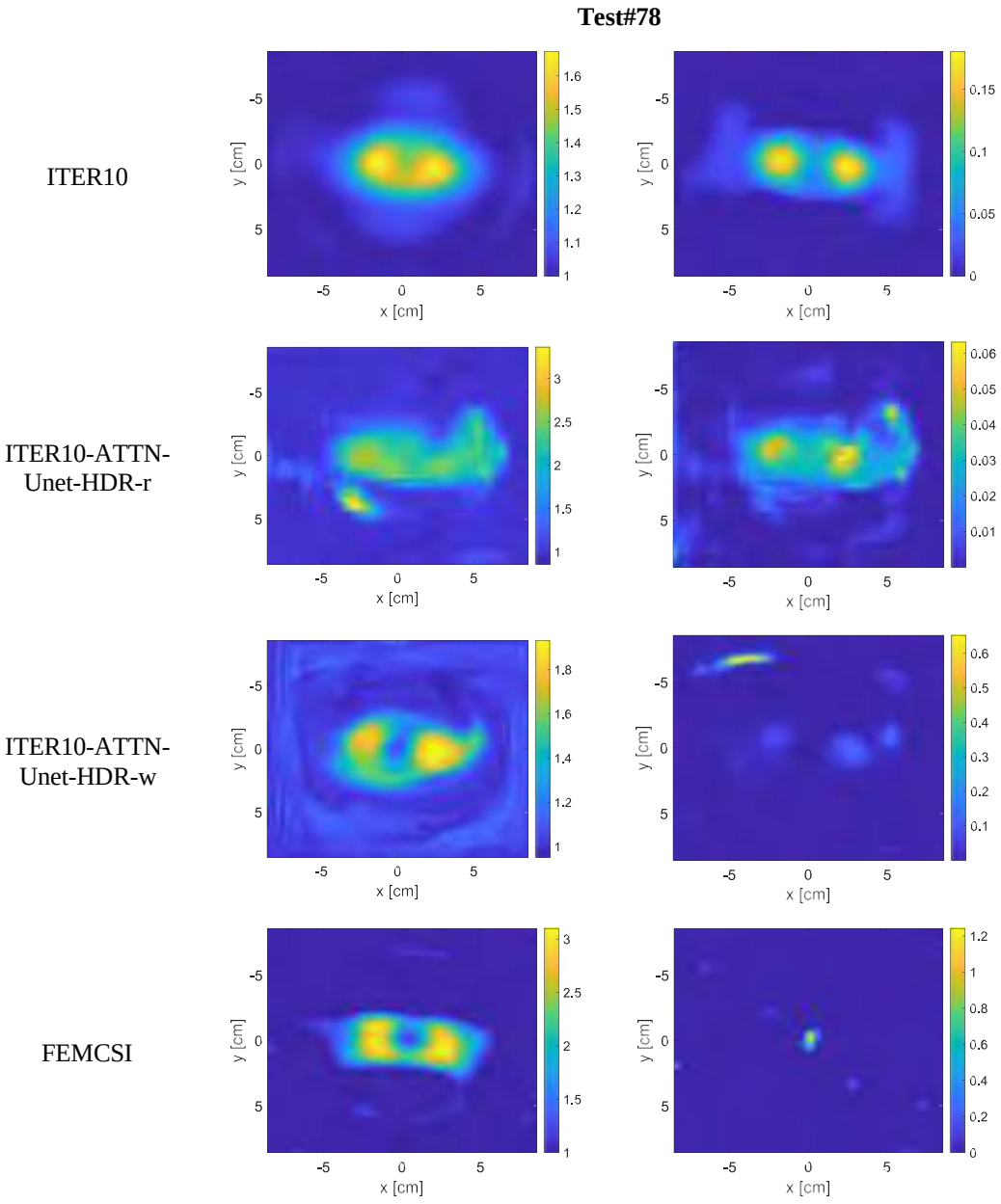

Figure 126. Reconstruction results of (a) real and (b) imaginary components of ϵ_r of UM10.

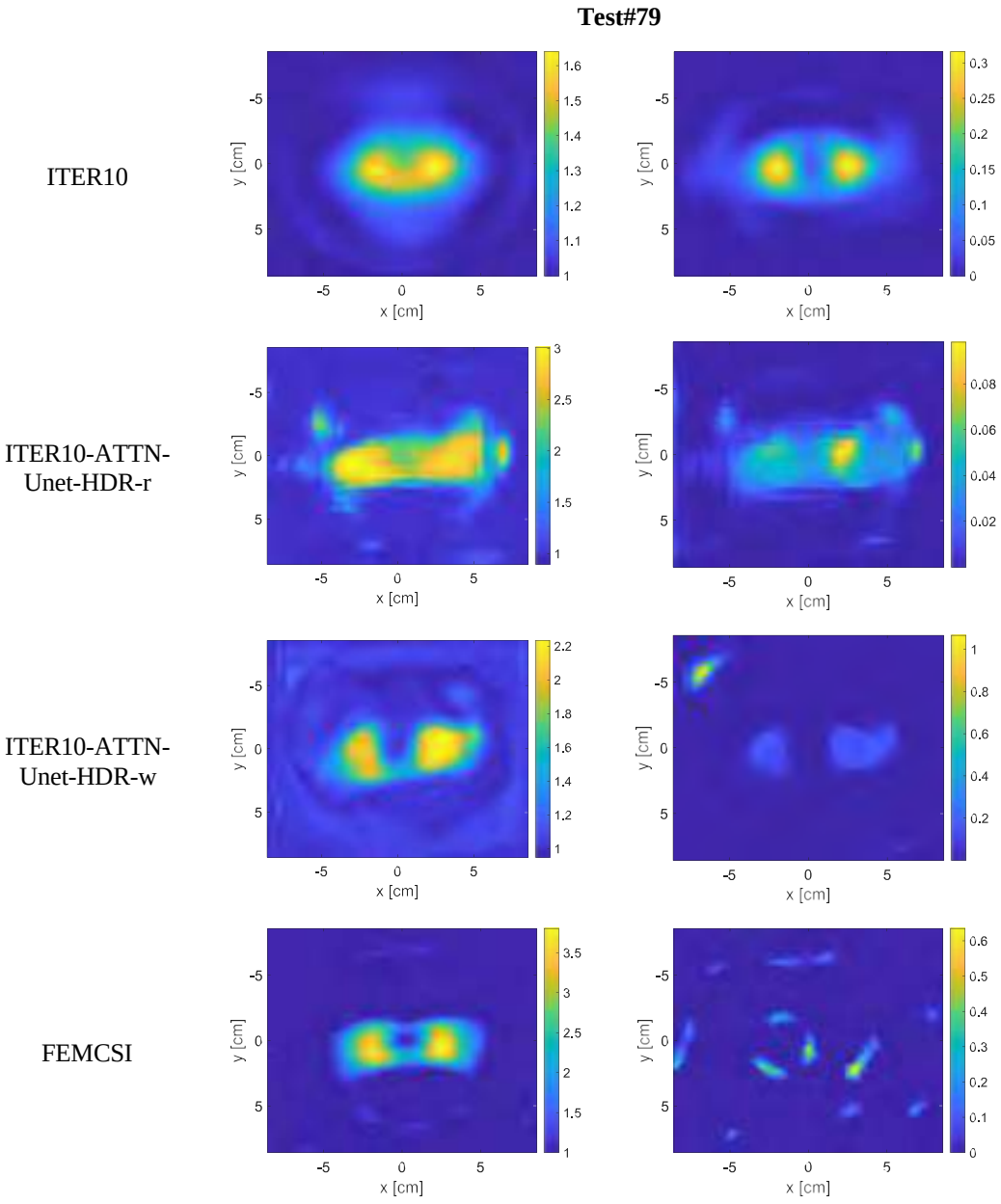

Figure 127. Reconstruction results of (a) real and (b) imaginary components of ϵ_r of UM11.

Vita

Mohammed Farook Maricar was born in 1982 in Abu Dhabi, United Arab Emirates (UAE). He earned his bachelor's degree with magna cum laude in Electrical and Electronics Engineering from the American University of Sharjah (AUS), UAE, in 2004. He was working in the industry before returning to academia in 2021. He is currently a teaching/research assistant in the College of Engineering at the American University of Sharjah (AUS), UAE, where he is pursuing his Master of Science degree in Electrical Engineering with a full scholarship granted by the university to distinguished students. As an undergraduate student, Farook conducted his senior design project on Intelligent Cell Phone Jammers. His current research interests include the implementation of deep learning in microwave imaging.